

Air Force Institute of Technology

**AFIT Scholar**

---

Theses and Dissertations

Student Graduate Works

---

9-9-2009

## Pulsed Film Cooling on a Turbine Blade Leading Edge

James L. Rutledge

Follow this and additional works at: <https://scholar.afit.edu/etd>



Part of the [Aerospace Engineering Commons](#)

---

### Recommended Citation

Rutledge, James L., "Pulsed Film Cooling on a Turbine Blade Leading Edge" (2009). *Theses and Dissertations*. 2388.

<https://scholar.afit.edu/etd/2388>

This Dissertation is brought to you for free and open access by the Student Graduate Works at AFIT Scholar. It has been accepted for inclusion in Theses and Dissertations by an authorized administrator of AFIT Scholar. For more information, please contact [richard.mansfield@afit.edu](mailto:richard.mansfield@afit.edu).



**PULSED FILM COOLING ON A TURBINE  
BLADE LEADING EDGE**

DISSERTATION

James L. Rutledge, Captain, USAF

AFIT/DS/ENY/09-S03

**DEPARTMENT OF THE AIR FORCE  
AIR UNIVERSITY**

***AIR FORCE INSTITUTE OF TECHNOLOGY***

---

**Wright-Patterson Air Force Base, Ohio**

APPROVED FOR PUBLIC RELEASE; DISTRIBUTION UNLIMITED

*The views expressed in this thesis are those of the author and do not reflect the official policy or position of the United States Air Force, Department of Defense, or the United States Government.*

AFIT/DS/ENY/09-S03

PULSED FILM COOLING ON A TURBINE BLADE LEADING EDGE

DISSERTATION

Presented to the Faculty

Graduate School of Engineering and Management

Air Force Institute of Technology

Air University

Air Education and Training Command

In Partial Fulfillment of the Requirements for the

Degree of Doctor of Philosophy

James L. Rutledge, B.S., M.S.

Captain, USAF

September 2009

APPROVED FOR PUBLIC RELEASE; DISTRIBUTION UNLIMITED

PULSED FILM COOLING ON A TURBINE BLADE LEADING EDGE

James Lloyd Rutledge, BS, MS  
Captain, USAF

Approved:

  
\_\_\_\_\_  
Paul I. King, PhD (Chairman)

8 Aug 09  
date

  
\_\_\_\_\_  
David J. Bunker, PhD (Member)

8/11/09  
date

  
\_\_\_\_\_  
Mark F. Reeder, PhD (Member)

8/11/09  
date

  
\_\_\_\_\_  
Richard B. Rivir, PhD (Member)

8/11/09  
date

Accepted:

  
\_\_\_\_\_  
M. U. Thomas, PhD  
Dean, Graduate School of  
Engineering and Management

8/25/09  
date

**Abstract**

Unsteadiness in gas turbine film cooling jets may arise due to inherent unsteadiness of the flow through an engine or may be induced as a means of flow control. The traditional technique used to evaluate the performance of a steady film cooling scheme is demonstrated to be insufficient for use with unsteady film cooling and is modified to account for the cross coupling of the time dependent adiabatic effectiveness and heat transfer coefficient. The addition of a single term to the traditional steady form of the net heat flux reduction equation with time averaged quantities accounts for the unsteady effects. An experimental technique to account for the influence of the new term was devised and used to measure the influence of a pulsating jet on the net heat flux in the leading edge region of a turbine blade. High spatial resolution data was acquired in the near-hole region using infrared thermography coupled with experimental techniques that allowed application of the appropriate thermal boundary conditions immediately adjacent to the film cooling hole. The turbine blade leading edge was simulated by a half cylinder in cross flow with a blunt afterbody. The film cooling geometry consisted of a coolant hole located  $21.5^\circ$  from the leading edge, angled  $20^\circ$  to the surface and  $90^\circ$  from the streamwise direction. Investigated parameters include pulsation frequency, duty cycle, and waveform shape. Separate experiments were conducted in a water channel to provide visualization of the unsteady coolant propagation behavior. Further insight into the flow physics was obtained through computational simulations of the experimental apparatus. The computational results afforded time resolved flow field and net heat flux reduction data unobtainable with the experimental techniques. A technique to predict the performance of an unsteady film cooling scheme through knowledge of only the steady film cooling behavior was developed and demonstrated to be effective.

AFIT/DS/ENY/09-S03

*To My Wife*

## Acknowledgements

This dissertation would not have been possible without the help and support of many along the way. Dr. Paul King lent his broad expertise with countless hours discussing even the finest details of this research. He has been a source of inspiration and motivation and has had a positive impact on my career as an engineer and an officer.

I thank my other committee members, Dr. Mark Reeder, Dr. David Bunker, and Dr. Richard Rivir for their guidance. Dr. Rivir was especially helpful with his enthusiasm and facilitation of financial support.

There have been a number of fellow students who have helped me in countless ways. Jon McCall spent many hours in the lab helping me run experiments. He also served as a reviewer of seeds of ideas scribbled on napkins during our weekly lunch meetings. Isaac Roland and Dan Carroll were great help with the preparation and performance of experiments.

The people of the Air Force Research Laboratory Propulsion Directorate, especially Dr. Shichuan Ou and others in Test Cell 21, were generous by allowing me to use their wind tunnel facilities. I am also grateful for the time with a water channel facilitated by Dr. Michael Ol of the Air Force Research Laboratory Air Vehicles Directorate.

The skill and expertise of the AFIT model shop crew managed to turn my abstract drawings into physical hardware. Dan Ryan and Jan LeValley were never intimidated by the prospect of fabricating anything, no matter how bizarre the combination of material and geometry.

Finally, I thank my family for their encouragement and support. Practically since birth, my parents made sure that I had the opportunities available to me to pursue an education, the importance of which they instilled. My wife has been patient and understanding. I could not imagine this course of study without her always cheerful smile.

## Table of Contents

	Page
<b>Abstract</b> .....	<b>iv</b>
<b>Acknowledgements</b> .....	<b>vi</b>
<b>Table of Contents</b> .....	<b>vii</b>
<b>List of Figures</b> .....	<b>x</b>
<b>List of Tables</b> .....	<b>xix</b>
<b>Nomenclature</b> .....	<b>xx</b>
<b>Acronyms</b> .....	<b>xxiii</b>
<b>1. Introduction</b> .....	<b>1</b>
1.1 Uniqueness of the Current Study .....	3
1.2 Research Objectives .....	3
<b>2. Literature Review</b> .....	<b>5</b>
2.1 Film Cooling Flow Rate Parameters .....	5
2.2 Steady Film Cooling Heat Transfer .....	6
2.3 Rotor-Stator Interaction .....	7
2.4 Pulsed Jet Fluid Dynamics .....	8
2.5 Flat Plate Film Cooling .....	9
2.6 Leading Edge Film Cooling .....	12
<b>3. Unsteady Film Cooling Performance Determination</b> .....	<b>15</b>
3.1 Unsteady Film Cooling Heat Transfer .....	15
3.2 Unsteady Net Heat Flux Reduction .....	17
3.3 Experimental Determination of NHFR .....	19
3.4 Surface Temperature Fluctuations .....	24
3.4.1 Zero Applied Heat Flux .....	25
3.4.2 Nonzero Applied Heat Flux .....	34
3.5 The Physical Significance of the $h$ - $\eta$ Coupling Term .....	38
3.6 Unsteady Film Cooling Behavior at Low Frequency .....	39
<b>4. Experimental Methodology for Leading Edge Pulsed Film Cooling Net Heat Flux Reduction</b> .....	<b>44</b>
4.1 Leading Edge Model .....	44
4.2 Wind Tunnel Facility .....	46
4.3 Gamma Experiments .....	50
4.3.1 Conduction Correction .....	50
4.4 Heat Transfer Experiments .....	54
4.4.1 Buss Bar Voltage Drop Analysis .....	55
4.4.2 Nonuniform Current Density Considerations .....	57

4.4.3.	Data Reduction Procedure .....	64
4.5	Spanwise and Area Averaging of the Net Heat Flux Reduction and Heat Transfer Coefficient Ratios.....	67
4.6	Uncertainty Analysis .....	69
4.6.1.	Freestream Reynolds Number .....	70
4.6.2.	Blowing Ratio.....	71
4.6.3.	Temperature Measurements .....	72
4.6.4.	Gamma .....	73
4.6.5.	Heat Transfer Coefficient .....	75
4.6.6.	Net Heat Flux Reduction .....	79
<b>5.</b>	<b>Net Heat Flux Reduction Results.....</b>	<b>82</b>
5.1	Steady Jet Results.....	82
5.1.1.	Influence of Freestream Turbulence and Reynolds Number on Adiabatic Effectiveness ....	86
5.1.2.	Influence of Freestream Turbulence and Reynolds Number on Frössling Number .....	95
5.1.3.	Influence of Freestream Turbulence and Reynolds Number on Net Heat Flux Reduction	102
5.2	Pulsed Jet Results .....	107
5.2.1.	The Baseline Condition: Low Freestream Turbulence, $Re_D = 60k$ .....	109
5.2.2.	The Influence of Freestream Turbulence and Reynolds Number on Pulsed Film Cooling	120
5.3	Validity of the Low Frequency Prediction Technique .....	130
5.3.1.	Net Heat Flux Reduction Performance Prediction .....	130
5.3.2.	Frössling Number Augmentation Performance Prediction.....	133
5.3.3.	Performance Prediction with Hypothetical Waveforms .....	134
<b>6.</b>	<b>Experimental Methodology for Flow Visualization .....</b>	<b>138</b>
6.1	Water Channel Facility.....	138
6.2	Parameter Space .....	140
6.3	Pulsed Jet Waveforms .....	140
6.4	Flow Visualization Technique.....	143
6.5	Uncertainty Analysis .....	144
6.5.1.	Freestream Reynolds Number .....	144
6.5.2.	Blowing Ratio.....	145
6.5.3.	Timing .....	145
<b>7.</b>	<b>Flow Visualization Results .....</b>	<b>146</b>
7.1	Steady Jet Results.....	146
7.2	Pulsed Jet Results .....	158
<b>8.</b>	<b>Computational Fluid Dynamics Methodology.....</b>	<b>173</b>
8.1	Grid Convergence .....	175

8.2	Time Step Convergence .....	180
<b>9.</b>	<b>Computational Results .....</b>	<b>183</b>
9.1	Steady Jet Results .....	183
9.2	Pulsed Jet Results .....	189
9.2.1.	Low Frequency Pulsed Jet Results .....	189
9.2.2.	Low Frequency Performance Prediction .....	200
9.2.3.	The Frequency Dependence of Pulsed Jets .....	203
9.3	Computational Simulation of a Row of Holes.....	212
<b>10.</b>	<b>Conclusion .....</b>	<b>215</b>
10.1	Summary of Work.....	215
10.2	Recommendations for Future Work .....	220
10.2.1.	Low Frequency Predictions with Steady Data Sets from Other Configurations .....	220
10.2.2.	Pulsed Film Cooling from Multiple Rows of Film Cooling Holes.....	220
10.2.3.	Full Coverage Pulsed Film Cooling .....	221
10.2.4.	Modulation of Film Cooling Flow.....	222
10.2.5.	Examination of Other Sources of Unsteadiness .....	222
<b>Appendix A</b>	<b>Pulsed Jet Waveforms for Net Heat Flux Reduction Experiments .....</b>	<b>223</b>
A.1	Partial Valve Closure, 20 Hz, DC = 25% .....	224
A.2	Partial Valve Closure, 20 Hz, DC = 50% .....	226
A.3	Partial Valve Closure, 20 Hz, DC = 75% .....	229
A.4	Partial Valve Closure, 40 Hz, DC = 50% .....	231
A.5	Complete Valve Closure, 20 Hz, DC = 50%.....	234
A.6	Complete Valve Closure, 20 Hz, DC = 75%.....	238
A.7	Complete Valve Closure, 80 Hz, DC = 50%.....	241
<b>Appendix B</b>	<b>Multiple Row Superposition Theory for Pulsed Film Cooling.....</b>	<b>243</b>
<b>References</b>	<b>.....</b>	<b>246</b>
<b>Vita</b>	<b>.....</b>	<b>250</b>

## List of Figures

	Page
Fig. 3.1 Temperature distribution for semi-infinite slab with oscillating adiabatic wall temperature ( $C = 5.85$ ).....	28
Fig. 3.2 Maximum relative deviation of surface temperature.....	29
Fig. 3.3 Temperature response at surface with no applied heat flux for $C = 5.85$ , $h_{fluc} / \bar{h} = 0.333$ , and $\theta = \pi$ rad.....	33
Fig. 3.4 Temperature response at surface with nonzero applied heat flux for $C = 5.85$ , $h_{fluc} / \bar{h} = 0.333$ .	37
Fig. 3.5 Two hypothetical $Z(M)$ curves sharing a common pair of points used in a hypothetical pulsing scheme.....	42
Fig. 4.1 Leading edge model.....	45
Fig. 4.2 Leading edge model cross-section along plane oriented $21.5^\circ$ from stagnation line and intersecting cylinder centerline.....	45
Fig. 4.3 Right handed coordinate system ( $y$ into page) (figure not to scale).....	46
Fig. 4.4 Schematic of Coolant Feed Line for Wind Tunnel Experiments.....	48
Fig. 4.5 Heat flux plate schematic (not to scale).....	55
Fig. 4.6 Electrical heat flux relative to average heat flux at $y/d = 0$ and 2.....	62
Fig. 4.7 Frössling number distributions attained using local heat flux method and hole covered; low turbulence, $Re_D = 60k$ .....	63
Fig. 4.8 Repeatability of $\eta$ within a test and between tests; $M = 0.75$ (steady); low $Tu$ ; $Re_D = 60k$ . Trial 2 was conducted 17 days after Trial 1.....	74
Fig. 4.9 Area averaged $\gamma$ , low $Tu$ , $Re_D = 60k$ , steady. Trial 2 was conducted 17 days after Trial 1.....	75
Fig. 4.10 Repeatability of $h_f / h_0$ within a test and between tests; $M = 1.0$ (steady); high $Tu$ ; $Re_D = 60k$ . Trial 2 was conducted 16 days after Trial 1.....	78
Fig. 4.11 Area averaged $h_f / h_0$ , high $Tu$ , $Re_D = 60k$ , steady. Trial 2 was conducted 16 days after Trial 1. .....	79
Fig. 4.12 Repeatability of $\Delta q_r$ with a test and between tests; $M = 1.0$ (steady); high $Tu$ ; $Re_D = 60k$ .....	80
Fig. 4.13 Area averaged $\Delta q_r$ , high $Tu$ , $Re_D = 60k$ , steady.....	81
Fig. 5.1 Spanwise averaged adiabatic effectiveness for steady film cooling, low $Tu$ , $Re_D = 60k$ .....	83
Fig. 5.2 Spanwise averaged heat transfer coefficient augmentation for steady film cooling, low $Tu$ , $Re_D = 60k$ .....	84
Fig. 5.3 Spanwise averaged Frössling number for steady film cooling, low $Tu$ , $Re_D = 60k$ .....	85
Fig. 5.4 Spanwise averaged net heat flux reduction for steady film cooling, low $Tu$ , $Re_D = 60k$ .....	86
Fig. 5.5 Area averaged $\eta$ for steady film cooling.....	87

Fig. 5.6	Adiabatic effectiveness contours for steady film cooling, $\gamma = \eta$ , $M = 1.5$ , low $Tu$ , $Re_D = 60k$ ....	88
Fig. 5.7	Adiabatic effectiveness contours for steady film cooling, $\gamma = \eta$ , $M = 1.5$ , high $Tu$ , $Re_D = 60k$ ....	88
Fig. 5.8	Adiabatic effectiveness contours for steady film cooling, $\gamma = \eta$ , $M = 1.5$ , low $Tu$ , $Re_D = 30k$ ....	88
Fig. 5.9	Adiabatic effectiveness contours for steady film cooling, $\gamma = \eta$ , $M = 1.5$ , high $Tu$ , $Re_D = 30k$ ....	88
Fig. 5.10	Adiabatic effectiveness contours for steady film cooling, $\gamma = \eta$ , $M = 0.5$ , low $Tu$ , $Re_D = 60k$ ...	90
Fig. 5.11	Adiabatic effectiveness contours for steady film cooling, $\gamma = \eta$ , $M = 0.5$ , high $Tu$ , $Re_D = 60k$ ..	90
Fig. 5.12	Adiabatic effectiveness contours for steady film cooling, $\gamma = \eta$ , $M = 0.5$ , low $Tu$ , $Re_D = 30k$ ...	90
Fig. 5.13	Adiabatic effectiveness contours for steady film cooling, $\gamma = \eta$ , $M = 0.5$ , high $Tu$ , $Re_D = 30k$ ..	90
Fig. 5.14	Adiabatic effectiveness contours for steady film cooling, $\gamma = \eta$ , $M = 1.0$ , low $Tu$ , $Re_D = 30k$ ...	91
Fig. 5.15	Adiabatic effectiveness contours for steady film cooling, $\gamma = \eta$ , $M = 0.25$ , low $Tu$ , $Re_D = 60k$ .	94
Fig. 5.16	Adiabatic effectiveness contours for steady film cooling, $\gamma = \eta$ , $M = 0.25$ , high $Tu$ , $Re_D = 60k$	94
Fig. 5.17	Adiabatic effectiveness contours for steady film cooling, $\gamma = \eta$ , $M = 0.25$ , low $Tu$ , $Re_D = 30k$ .	94
Fig. 5.18	Adiabatic effectiveness contours for steady film cooling, $\gamma = \eta$ , $M = 0.25$ , high $Tu$ , $Re_D = 30k$	94
Fig. 5.19	Adiabatic effectiveness contours for steady film cooling, $\gamma = \eta$ , $M = 0.1$ , low $Tu$ , $Re_D = 60k$ ...	95
Fig. 5.20	Frössling number distribution with no film cooling and no influence of film cooling hole.....	97
Fig. 5.21	$Fr_f / Fr_0$ contours for steady film cooling, $M = 1.5$ , low $Tu$ , $Re_D = 60k$ .....	99
Fig. 5.22	$Fr_f / Fr_0$ contours for steady film cooling, $M = 1.5$ , high $Tu$ , $Re_D = 60k$ .....	99
Fig. 5.23	$Fr_f / Fr_0$ contours for steady film cooling, $M = 1.5$ , low $Tu$ , $Re_D = 30k$ .....	99
Fig. 5.24	$Fr_f / Fr_0$ contours for steady film cooling, $M = 1.5$ , high $Tu$ , $Re_D = 30k$ .....	99
Fig. 5.25	$Fr_f / Fr_0$ contours for steady film cooling, $M = 0.5$ , low $Tu$ , $Re_D = 60k$ .....	100
Fig. 5.26	$Fr_f / Fr_0$ contours for steady film cooling, $M = 0.5$ , high $Tu$ , $Re_D = 60k$ .....	100
Fig. 5.27	$Fr_f / Fr_0$ contours for steady film cooling, $M = 0.5$ , low $Tu$ , $Re_D = 30k$ .....	100
Fig. 5.28	$Fr_f / Fr_0$ contours for steady film cooling, $M = 0.5$ , high $Tu$ , $Re_D = 30k$ .....	100
Fig. 5.29	$Fr_f / Fr_0$ contours for steady film cooling, $M = 0.25$ , low $Tu$ , $Re_D = 60k$ .....	101
Fig. 5.30	$Fr_f / Fr_0$ contours for steady film cooling, $M = 0.25$ , high $Tu$ , $Re_D = 60k$ .....	101
Fig. 5.31	$Fr_f / Fr_0$ contours for steady film cooling, $M = 0.25$ , low $Tu$ , $Re_D = 30k$ .....	101
Fig. 5.32	$Fr_f / Fr_0$ contours for steady film cooling, $M = 0.25$ , high $Tu$ , $Re_D = 30k$ .....	101
Fig. 5.33	Area averaged $Fr_f / Fr_0$ for steady film cooling.....	102
Fig. 5.34	Net heat flux reduction, $\Delta q_r$ , contours for steady film cooling, $M = 1.5$ , low $Tu$ , $Re_D = 60k$ ...	104
Fig. 5.35	Net heat flux reduction, $\Delta q_r$ , contours for steady film cooling, $M = 1.5$ , high $Tu$ , $Re_D = 60k$ ..	104

Fig. 5.36	Net heat flux reduction, $\Delta q_r$ , contours for steady film cooling, $M = 1.5$ , low $Tu$ , $Re_D = 30k$ ...	104
Fig. 5.37	Net heat flux reduction, $\Delta q_r$ , contours for steady film cooling, $M = 1.5$ , high $Tu$ , $Re_D = 30k$ ..	104
Fig. 5.38	Net heat flux reduction, $\Delta q_r$ , contours for steady film cooling, $M = 0.5$ , low $Tu$ , $Re_D = 60k$ ...	105
Fig. 5.39	Net heat flux reduction, $\Delta q_r$ , contours for steady film cooling, $M = 0.5$ , high $Tu$ , $Re_D = 60k$ ..	105
Fig. 5.40	Net heat flux reduction, $\Delta q_r$ , contours for steady film cooling, $M = 0.5$ , low $Tu$ , $Re_D = 30k$ ...	105
Fig. 5.41	Net heat flux reduction, $\Delta q_r$ , contours for steady film cooling, $M = 0.5$ , high $Tu$ , $Re_D = 30k$ ..	105
Fig. 5.42	Net heat flux reduction, $\Delta q_r$ , contours for steady film cooling, $M = 0.25$ , low $Tu$ , $Re_D = 60k$ .	106
Fig. 5.43	Net heat flux reduction, $\Delta q_r$ , contours for steady film cooling, $M = 0.25$ , high $Tu$ , $Re_D = 60k$	106
Fig. 5.44	Net heat flux reduction, $\Delta q_r$ , contours for steady film cooling, $M = 0.25$ , low $Tu$ , $Re_D = 30k$ .	106
Fig. 5.45	Net heat flux reduction, $\Delta q_r$ , contours for steady film cooling, $M = 0.25$ , high $Tu$ , $Re_D = 30k$	106
Fig. 5.46	Area averaged $\Delta q_r$ for steady film cooling .....	107
Fig. 5.47	$\gamma$ contours for $\bar{M} = 0.25$ , low $Tu$ , $Re_D = 60k$ , $F = 0.148$ , $DC = 50\%$ , partial VC.....	111
Fig. 5.48	$\gamma$ contours for $\bar{M} = 0.25$ , low $Tu$ , $Re_D = 60k$ , $F = 0.148$ , $DC = 75\%$ , partial VC.....	111
Fig. 5.49	$\gamma$ contours for $\bar{M} = 0.25$ , low $Tu$ , $Re_D = 60k$ , $F = 0.148$ , $DC = 50\%$ , complete VC .....	111
Fig. 5.50	$\gamma$ contours for $\bar{M} = 0.25$ , low $Tu$ , $Re_D = 60k$ , $F = 0.148$ , $DC = 75\%$ , complete VC .....	111
Fig. 5.51	$\overline{Fr_f} / Fr_0$ contours for $\bar{M} = 0.25$ , low $Tu$ , $Re_D = 60k$ , $F = 0.148$ , $DC = 50\%$ , partial VC .....	112
Fig. 5.52	$\overline{Fr_f} / Fr_0$ contours for $\bar{M} = 0.25$ , low $Tu$ , $Re_D = 60k$ , $F = 0.148$ , $DC = 75\%$ , partial VC .....	112
Fig. 5.53	$\overline{Fr_f} / Fr_0$ contours for $\bar{M} = 0.25$ , low $Tu$ , $Re_D = 60k$ , $F = 0.148$ , $DC = 50\%$ , complete VC .....	112
Fig. 5.54	$\overline{Fr_f} / Fr_0$ contours for $\bar{M} = 0.25$ , low $Tu$ , $Re_D = 60k$ , $F = 0.148$ , $DC = 75\%$ , complete VC .....	112
Fig. 5.55	$\overline{\Delta q_r}$ contours for $\bar{M} = 0.25$ , low $Tu$ , $Re_D = 60k$ , $F = 0.148$ , $DC = 50\%$ , partial VC.....	114
Fig. 5.56	$\overline{\Delta q_r}$ contours for $\bar{M} = 0.25$ , low $Tu$ , $Re_D = 60k$ , $F = 0.148$ , $DC = 75\%$ , partial VC.....	114
Fig. 5.57	$\overline{\Delta q_r}$ contours for $\bar{M} = 0.25$ , low $Tu$ , $Re_D = 60k$ , $F = 0.148$ , $DC = 50\%$ , complete VC .....	114
Fig. 5.58	$\overline{\Delta q_r}$ contours for $\bar{M} = 0.25$ , low $Tu$ , $Re_D = 60k$ , $F = 0.148$ , $DC = 75\%$ , complete VC .....	114
Fig. 5.59	$\gamma$ contours for $M = 1.25$ , low $Tu$ , $Re_D = 60k$ , steady.....	115
Fig. 5.60	$\gamma$ contours for $\bar{M} = 1.25$ , low $Tu$ , $Re_D = 60k$ , $F = 0.148$ , $DC = 50\%$ , partial VC.....	115
Fig. 5.61	$\gamma$ contours for $\bar{M} = 1.25$ , low $Tu$ , $Re_D = 60k$ , $F = 0.148$ , $DC = 50\%$ , complete VC .....	115
Fig. 5.62	$\gamma$ contours for $\bar{M} = 2.0$ , low $Tu$ , $Re_D = 60k$ , steady.....	116
Fig. 5.63	$\gamma$ contours for $\bar{M} = 2.0$ , low $Tu$ , $Re_D = 60k$ , $F = 0.148$ , $DC = 50\%$ , partial VC.....	116

Fig. 5.64	$Fr_f / Fr_0$ contours for $\bar{M} = 2.0$ , low $Tu$ , $Re_D = 60k$ , steady .....	117
Fig. 5.65	$\overline{Fr_f} / Fr_0$ contours for $\bar{M} = 2.0$ , low $Tu$ , $Re_D = 60k$ , $F = 0.148$ , $DC = 50\%$ , partial VC .....	117
Fig. 5.66	$\Delta q_r$ contours for $M = 2.0$ , low $Tu$ , $Re_D = 60k$ , steady .....	117
Fig. 5.67	$\overline{\Delta q_r}$ contours for $\bar{M} = 2.0$ , low $Tu$ , $Re_D = 60k$ , $F = 0.148$ , $DC = 50\%$ , partial VC.....	117
Fig. 5.68	Difference in $\gamma$ between pulsed and steady cases as a function of $\bar{M}$ ; low $Tu$ ; $Re_D = 60k$ .....	118
Fig. 5.69	Ratio of $\overline{Fr}$ between pulsed and steady cases as a function of $\bar{M}$ ; low $Tu$ ; $Re_D = 60k$ .....	119
Fig. 5.70	Net heat flux reduction due to pulsing as a function of $\bar{M}$ ; low $Tu$ ; $Re_D = 60k$ .....	120
Fig. 5.71	Area averaged $\gamma$ for pulsed film cooling; $F \approx 0.15$ and $0.30$ , $DC = 50\%$ , partial VC.....	122
Fig. 5.72	Area averaged $\overline{Fr_f} / Fr_0$ for pulsed film cooling; $F \approx 0.15$ and $0.30$ , $DC = 50\%$ , partial VC...	123
Fig. 5.73	Area-averaged $\overline{\Delta q_r}$ for pulsed film cooling; $F \approx 0.15$ and $0.30$ , $DC = 50\%$ , partial VC .....	124
Fig. 5.74	Area averaged $\gamma$ for pulsed film cooling; $F \approx 0.60$ and $1.20$ , $DC = 50\%$ .....	125
Fig. 5.75	Area averaged $\overline{Fr_f} / Fr_0$ for pulsed film cooling; $F \approx 0.60$ and $1.20$ , $DC = 50\%$ .....	126
Fig. 5.76	Area-averaged $\overline{\Delta q_r}$ for pulsed film cooling; $F \approx 0.60$ and $1.20$ , $DC = 50\%$ .....	127
Fig. 5.77	Net Heat flux reduction due to pulsing as a function of $\bar{M}$ , high $Tu$ , $Re_D = 60k$ .....	128
Fig. 5.78	Net Heat flux reduction due to pulsing as a function of $\bar{M}$ , low $Tu$ , $Re_D = 30k$ .....	129
Fig. 5.79	Net Heat flux reduction due to pulsing as a function of $\bar{M}$ , high $Tu$ , $Re_D = 30k$ .....	129
Fig. 5.80	Net heat flux reduction due to pulsing as a function of $\bar{M}$ ; low $Tu$ ; $Re_D = 60k$ ; low frequency prediction vs. actual results .....	131
Fig. 5.81	Frössling number augmentation due to pulsing as a function of $\bar{M}$ ; low $Tu$ ; $Re_D = 60k$ ; low frequency prediction vs. actual results .....	134
Fig. 5.82	Area averaged $\overline{\Delta q_{r,pulsed}}$ performance prediction for sinusoidal $M(t)$ waveforms of various average blowing ratio and amplitude. Max $\overline{\Delta q_{r,pulsed}} = 6.6\%$ at $\bar{M} = 1.88$ , amplitude = 1.62 ....	135
Fig. 5.83	Area averaged $\overline{\Delta q_{r,pulsed}}$ performance prediction for sawtooth $M(t)$ waveforms of various average blowing ratio and amplitude. $M$ ramps up linearly and drops instantly. Max $\overline{\Delta q_{r,pulsed}} = 5.0\%$ at $\bar{M} = 1.96$ , amplitude = 1.54.....	136
Fig. 5.84	Area averaged $\overline{\Delta q_{r,pulsed}}$ performance prediction for square wave $M(t)$ waveforms of various average blowing ratio and amplitude. Max $\overline{\Delta q_{r,pulsed}} = 10.9\%$ at $\bar{M} = 1.88$ , amplitude = 1.62 ..	136

Fig. 5.85 Area averaged $\overline{\Delta q_{r,pulsed}}$ performance prediction for triangle wave $M(t)$ waveforms of various average blowing ratio and amplitude. $M$ ramps up and down linearly. $\text{Max } \overline{\Delta q_{r,pulsed}} = 5.0\%$ at $\overline{M} = 1.98$ , amplitude = 1.52.....	137
Fig. 6.1 Schematic of Coolant Feed Line for Water Channel Experiments.....	140
Fig. 6.2 Approximate $M(t)$ for $\overline{M} = 1.0$ , $F = 0.148$ , $DC = 50\%$ .....	142
Fig. 6.3 Approximate $M(t)$ for $\overline{M} = 0.25$ , $F = 0.590$ , $DC = 50\%$ .....	142
Fig. 6.4 Leading edge model and camera positions.....	143
Fig. 7.1 Near surface normal view of coolant at several points in time, steady $M = 0.25$ . (Camera Angle 1) .....	147
Fig. 7.2 Near parallel to surface view of coolant, steady $M = 0.25$ . (Camera Angle 2).....	148
Fig. 7.3 Near parallel to surface view, steady $M = 0$ . (Camera Angle 2) .....	148
Fig. 7.4 Off-surface view of coolant at $M = 0.25$ . Left edge of model is at $x/d = 1.5$ . (Camera Angle 3).....	149
Fig. 7.5 Near surface normal view of coolant at several points in time, steady $M = 0.50$ . (Camera Angle 1) .....	151
Fig. 7.6 Near parallel to surface view of coolant, steady $M = 0.50$ . (Camera Angle 2).....	152
Fig. 7.7 Off-surface view of coolant at $M = 0.5$ . Two images taken at two random times. Left edge of model is at $x/d = 1.5$ . (Camera Angle 3) .....	152
Fig. 7.8 Near surface normal view of coolant at several points in time, steady $M = 1.0$ . .....	154
Fig. 7.9 Near parallel to surface view of coolant, steady $M = 1.0$ . (Camera Angle 2).....	155
Fig. 7.10 Near surface normal view of coolant at several points in time, steady $M = 2.0$ . (Camera Angle 1) .....	156
Fig. 7.11 Near parallel to surface view of coolant, steady $M = 2.0$ . (Camera Angle 2).....	157
Fig. 7.12 Off-surface view of coolant at $M = 2.0$ . Left edge of model is at $x/d = 1.5$ . (Camera Angle 3).....	158
Fig. 7.13 Near surface normal view of coolant startup event, $\overline{M} = 0.25$ , $F = 0.148$ . (Camera Angle 1) ..	160
Fig. 7.14 Near surface normal view of coolant shutdown event, $\overline{M} = 0.25$ , $F = 0.148$ . .....	161
Fig. 7.15 Near surface normal view of coolant startup event, $\overline{M} = 1.0$ , $F = 0.148$ . (Camera Angle 1) ...	162
Fig. 7.16 Near parallel to surface view of coolant startup event, $\overline{M} = 1.0$ , $F = 0.148$ . (Camera Angle 2).....	163
Fig. 7.17 Near surface normal view of coolant cycle, $\overline{M} = 0.25$ , $F = 0.590$ . (Camera Angle 1) .....	165
Fig. 7.18 Near parallel to surface view of coolant startup event, $\overline{M} = 0.25$ , $F = 0.590$ . .....	166
Fig. 7.19 Near surface normal view of coolant cycle, $\overline{M} = 0.25$ , $F = 1.195$ . (Camera Angle 1) .....	168
Fig. 7.20 Near parallel to surface view of coolant cycle, $\overline{M} = 0.25$ , $F = 1.195$ . (Camera Angle 2).....	169
Fig. 7.21 Near surface normal view of coolant cycle, $\overline{M} = 0.75$ , $F = 1.195$ . (Camera Angle 1) .....	171
Fig. 7.22 Near parallel to surface view of coolant cycle, $\overline{M} = 0.75$ , $F = 1.195$ . (Camera Angle 2).....	172

Fig. 8.1 Computational domain .....	174
Fig. 8.2 Adiabatic effectiveness plots for several grids at $x/d = 1$ .....	176
Fig. 8.3 Adiabatic effectiveness plots for several grids at $x/d = 4$ .....	177
Fig. 8.4 Adiabatic effectiveness plots for several grids at $x/d = 9$ .....	177
Fig. 8.5 Surface mesh on leading edge in vicinity of coolant hole .....	179
Fig. 8.6 Fluid region mesh on streamwise plane bisecting intersection of the coolant hole with the leading edge .....	179
Fig. 8.7 Surface points used in establishment of time step convergence .....	181
Fig. 8.8 Adiabatic effectiveness histories at Point E obtained using two different time steps .....	182
Fig. 9.1 Steady $M = 0.50$ adiabatic effectiveness, $\eta$ (arrows indicate direction of coolant and freestream) .....	185
Fig. 9.2 Steady $M = 0.50$ heat transfer coefficient ratio, $h_f / h_0$ .....	185
Fig. 9.3 Steady $M = 0.50$ net heat flux reduction, $\Delta q_r$ .....	186
Fig. 9.4 Steady $M = 0.25$ adiabatic effectiveness, $\eta$ .....	186
Fig. 9.5 Comparison of computational and experimental steady spanwise averaged adiabatic effectiveness .....	188
Fig. 9.6 Steady $M = 0.25$ adiabatic effectiveness, $\eta$ , acquired through LES simulation .....	189
Fig. 9.7 Temporally resolved adiabatic effectiveness for several points on leading edge .....	190
Fig. 9.8 Nondimensional temperature distribution, $\theta$ , for fluid in plane intersecting surface at $x/d = 1$ for transient jet startup for the case of pulsed coolant between $M = 1$ and $M = 0$ , $\overline{M} = 0.50$ .....	192
Fig. 9.9 Adiabatic effectiveness contours for transient jet startup for the case of pulsed coolant between $M = 1$ and $M = 0$ , $\overline{M} = 0.50$ (arrows indicate direction of coolant and freestream) .....	194
Fig. 9.10 $h_f/h_0$ contours for transient jet startup for the case of pulsed coolant between $M = 1$ and $M = 0$ , $\overline{M} = 0.50$ (arrows indicate direction of coolant and freestream) .....	195
Fig. 9.11 Average net heat flux reduction, $\overline{\Delta q_r}$ , for the case of pulsed coolant between $M = 1$ and $M = 0$ , $\overline{M} = 0.50$ , $\overline{M} = 0.50$ .....	196
Fig. 9.12 Influence of cross coupling term alone, $\overline{h_f' \eta'} / (h_0 \phi)$ , on average net heat flux reduction for the case of pulsed coolant between $M = 1$ and $M = 0$ , $\overline{M} = 0.50$ .....	197
Fig. 9.13 Average net heat flux reduction, $\overline{\Delta q_r}$ , for the case of pulsed coolant between $M = 0.5$ and $M = 0$ , $\overline{M} = 0.25$ .....	198
Fig. 9.14 Heat transfer coefficient ratio, $\overline{h_f} / h_0$ , pulsed coolant between $M = 0.5$ and $M = 0$ , $F = 0.151$ , $\overline{M} = 0.25$ .....	198

Fig. 9.15 Spanwise averaged $\bar{\eta}$ ; $M = A, B$ indicates pulsing between $M = A$ and $M = B$ .....	199
Fig. 9.16 Net spanwise heat flux reduction $\overline{\Delta q_{r,span}}$ ; $M = A, B$ indicates pulsing between $M = A$ and $M = B$ .....	200
Fig. 9.17 Spanwise averaged $\bar{\eta}$ for the case of a jet pulsed between $M = A$ and $M = B$ (indicated by $M = A, B$ ) at $F = 0.151$ compared to the prediction from Eq. (3.77). .....	202
Fig. 9.18 Square and sawtooth waves used for pulsing between $M = 1$ and $M = 0$ at $F = 0.755$ . Both have average blowing ratio, $\bar{M} = 0.5$ .....	204
Fig. 9.19 Spanwise net heat flux reduction, $\overline{\Delta q_{r,span}}$ , for $\bar{M} = 0.5$ at several $F$ . $M = A, B$ indicates pulsing between $M = A$ and $M = B$ . Steady $M = 1$ results also shown. ....	204
Fig. 9.20 Average net heat flux reduction, $\overline{\Delta q_r}$ , for pulsed coolant between $M = 1$ and $M = 0$ , $F = 3.02$ , $\bar{M} = 0.50$ .....	206
Fig. 9.21 Average net heat flux reduction, $\overline{\Delta q_r}$ , for pulsed coolant between $M = 1$ and $M = 0$ , $F = 6.04$ , $\bar{M} = 0.50$ .....	206
Fig. 9.22 Adiabatic effectiveness contours through a cycle for $F = 6.04$ jet pulsed in square wave, $DC = 50\%$ . Total cycle time is $1/F = 0.166$ . Jet turns off at $T = \pm 0.083$ and on at $T = 0$ . ....	207
Fig. 9.23 Nondimensional temperature distribution, $\theta$ , of fluid in plane intersecting surface at $x/d = 0$ for several points in time for pulsed coolant between $M = 1$ and $M = 0$ at $F = 6.04$ . Total cycle time is $1/F = 0.166$ . Jet turns off at $T = \pm 0.083$ and on at $T = 0$ .....	208
Fig. 9.24 Spanwise net heat flux reduction, $\overline{\Delta q_{r,span}}$ , for $\bar{M} = 0.25$ at several frequencies. $M = A, B$ indicates pulsing between $M = A$ and $M = B$ . ....	209
Fig. 9.25 Average net heat flux reduction, $\overline{\Delta q_r}$ , pulsed coolant between $M = 0.5$ and $M = 0$ , $F = 3.02$ , $\bar{M} = 0.25$ .....	210
Fig. 9.26 Heat transfer coefficient ratio, $\bar{h}_f / h_0$ , pulsed coolant between $M = 0.5$ and $M = 0$ , $F = 3.02$ , $\bar{M} = 0.25$ .....	210
Fig. 9.27 Spanwise net heat flux reduction, $\overline{\Delta q_{r,span}}$ , for $\bar{M} = 1.0$ at $F = 6.04$ . $M = A, B$ indicates pulsing between $M = A$ and $M = B$ . ....	212
Fig. 9.28 Spanwise averaged $\bar{\eta}$ for a row of holes compared with a single hole with pulsed coolant between $M = 1$ and $M = 0$ , $\bar{M} = 0.5$ , $F = 6.04$ .....	214
Fig. A.1 $M(t)$ for $\bar{M} = 0.25$ , 20 Hz, $DC = 25\%$ , partial VC ( $M$ calculated based on $Re_D = 60000$ ; double $M$ for $Re_D = 30000$ ) .....	224

Fig. A.2 $M(t)$ for $\bar{M} = 0.50$ , 20 Hz, $DC = 25\%$ , partial VC ( $M$ calculated based on $Re_D = 60000$ ; double $M$ for $Re_D = 30000$ ) .....	225
Fig. A.3 $M(t)$ for $\bar{M} = 1.0$ , 20 Hz, $DC = 25\%$ , partial VC ( $M$ calculated based on $Re_D = 60000$ ; double $M$ for $Re_D = 30000$ ) .....	225
Fig. A.4 $M(t)$ for $\bar{M} = 2.0$ , 20 Hz, $DC = 25\%$ , partial VC ( $M$ calculated based on $Re_D = 60000$ ; double $M$ for $Re_D = 30000$ ) .....	226
Fig. A.5 $M(t)$ for $\bar{M} = 0.25$ , 20 Hz, $DC = 50\%$ , partial VC ( $M$ calculated based on $Re_D = 60000$ ; double $M$ for $Re_D = 30000$ ) .....	227
Fig. A.6 $M(t)$ for $\bar{M} = 0.50$ , 20 Hz, $DC = 50\%$ , partial VC ( $M$ calculated based on $Re_D = 60000$ ; double $M$ for $Re_D = 30000$ ) .....	227
Fig. A.7 $M(t)$ for $\bar{M} = 1.0$ , 20 Hz, $DC = 50\%$ , partial VC ( $M$ calculated based on $Re_D = 60000$ ; double $M$ for $Re_D = 30000$ ) .....	228
Fig. A.8 $M(t)$ for $\bar{M} = 2.0$ , 20 Hz, $DC = 50\%$ , partial VC ( $M$ calculated based on $Re_D = 60000$ ; double $M$ for $Re_D = 30000$ ) .....	228
Fig. A.9 $M(t)$ for $\bar{M} = 0.25$ , 20 Hz, $DC = 75\%$ , partial VC ( $M$ calculated based on $Re_D = 60000$ ; double $M$ for $Re_D = 30000$ ) .....	229
Fig. A.10 $M(t)$ for $\bar{M} = 0.50$ , 20 Hz, $DC = 75\%$ , partial VC ( $M$ calculated based on $Re_D = 60000$ ; double $M$ for $Re_D = 30000$ ) .....	230
Fig. A.11 $M(t)$ for $\bar{M} = 1.0$ , 20 Hz, $DC = 75\%$ , partial VC ( $M$ calculated based on $Re_D = 60000$ ; double $M$ for $Re_D = 30000$ ) .....	230
Fig. A.12 $M(t)$ for $\bar{M} = 2.0$ , 20 Hz, $DC = 75\%$ , partial VC ( $M$ calculated based on $Re_D = 60000$ ; double $M$ for $Re_D = 30000$ ) .....	231
Fig. A.13 $M(t)$ for $\bar{M} = 0.25$ , 40 Hz, $DC = 50\%$ , partial VC ( $M$ calculated based on $Re_D = 60000$ ; double $M$ for $Re_D = 30000$ ) .....	232
Fig. A.14 $M(t)$ for $\bar{M} = 0.50$ , 40 Hz, $DC = 50\%$ , partial VC ( $M$ calculated based on $Re_D = 60000$ ; double $M$ for $Re_D = 30000$ ) .....	232
Fig. A.15 $M(t)$ for $\bar{M} = 1.0$ , 40 Hz, $DC = 50\%$ , partial VC ( $M$ calculated based on $Re_D = 60000$ ; double $M$ for $Re_D = 30000$ ) .....	233
Fig. A.16 $M(t)$ for $\bar{M} = 2.0$ , 40 Hz, $DC = 50\%$ , partial VC ( $M$ calculated based on $Re_D = 60000$ ; double $M$ for $Re_D = 30000$ ) .....	233
Fig. A.17 $M(t)$ for $\bar{M} = 0.25$ , 20 Hz, $DC = 50\%$ , complete VC ( $M$ calculated based on $Re_D = 60000$ ; double $M$ for $Re_D = 30000$ ) .....	235
Fig. A.18 $M(t)$ for $\bar{M} = 0.50$ , 20 Hz, $DC = 50\%$ , complete VC ( $M$ calculated based on $Re_D = 60000$ ; double $M$ for $Re_D = 30000$ ) .....	236

Fig. A.19 $M(t)$ for $\bar{M} = 1.0$ , 20 Hz, $DC = 50\%$ , complete VC ( $M$ calculated based on $Re_D = 60000$ ; double $M$ for $Re_D = 30000$ ) .....	236
Fig. A.20 Approximate locations of hot-film probe .....	238
Fig. A.21 $M(t)$ for $\bar{M} = 0.25$ , 20 Hz, $DC = 75\%$ , complete VC ( $M$ calculated based on $Re_D = 60000$ ; double $M$ for $Re_D = 30000$ ) .....	239
Fig. A.22 $M(t)$ for $\bar{M} = 0.50$ , 20 Hz, $DC = 75\%$ , complete VC ( $M$ calculated based on $Re_D = 60000$ ; double $M$ for $Re_D = 30000$ ) .....	239
Fig. A.23 $M(t)$ for $\bar{M} = 1.0$ , 20 Hz, $DC = 75\%$ , complete VC ( $M$ calculated based on $Re_D = 60000$ ; double $M$ for $Re_D = 30000$ ) .....	240
Fig. A.24 $M(t)$ for $\bar{M} = 1.75$ , 20 Hz, $DC = 75\%$ , complete VC ( $M$ calculated based on $Re_D = 60000$ ; double $M$ for $Re_D = 30000$ ) .....	240
Fig. A.25 $M(t)$ for $\bar{M} = 0.25$ , 80 Hz, $DC = 50\%$ , complete VC ( $M$ calculated based on $Re_D = 60000$ ; double $M$ for $Re_D = 30000$ ) .....	241
Fig. A.26 $M(t)$ for $\bar{M} = 0.50$ , 80 Hz, $DC = 50\%$ , complete VC ( $M$ calculated based on $Re_D = 60000$ ; double $M$ for $Re_D = 30000$ ) .....	242
Fig. A.27 $M(t)$ for $\bar{M} = 1.0$ , 80 Hz, $DC = 50\%$ , complete VC ( $M$ calculated based on $Re_D = 60000$ ; double $M$ for $Re_D = 30000$ ) .....	242

## List of Tables

	Page
Table 4.1 Wind Tunnel Freestream Conditions.....	47
Table 4.2 Illustration of Pitfall with Spanwise Averaged NHFR.....	68
Table 5.1 Dimensional Frequencies and Corresponding Nondimensional Frequencies Used in Net Heat Flux Reduction Experiments.....	109

## Nomenclature

### ***Symbols***

- $A$  = area,  $m^2$ , or a constant of integration  
 $b$  = thickness, m  
 $c$  = specific heat, J / (kg K)  
 $C$  = resistance to surface temperature fluctuations,  $\frac{k}{\bar{h}\sqrt{\alpha/\omega}}$ , see Eq. (3.47)  
 $D$  = leading edge diameter, m  
 $d$  = film cooling hole diameter, m  
 $DC$  = duty cycle (fraction of time spent “on”)  
 $DR$  = density ratio,  $\frac{\rho_c}{\rho_\infty}$   
 $E$  = voltage, V  
 $F$  = nondimensional frequency,  $\frac{fD}{U_\infty}$   
 $Fr$  = Frössling number,  $Nu / \sqrt{Re_D}$   
 $f$  = frequency, Hz  
 $h$  = convective heat transfer coefficient, W / ( $m^2$  K), Eq. (3.1)  
 $I$  = momentum flux ratio,  $\frac{\rho_c U_j^2}{\rho_\infty U_\infty^2}$ , or electrical current, A  
 $\hat{I}$  = electrical current density, A /  $m^2$   
 $i$  =  $\sqrt{-1}$   
 $k$  = thermal conductivity, W / (m K), or specific turbulence kinetic energy,  $m^2 / s^2$   
 $k$  =  $\times 1000$   
 $L$  = length, often hole length, m  
 $M$  = blowing ratio,  $\frac{\rho_c U_j}{\rho_\infty U_\infty}$   
 $m$  = order of curve fit  
 $N$  = number of measurements  
 $Nu$  = Nusselt number,  $hD / k$   
 $n_i$  = unit normal vector  
 $Pr$  = Prandtl number,  $\nu\rho c_p / k$   
 $P$  = hole-to-hole pitch, m  
 $q$  = charge density, C /  $m^3$   
 $q''$  = convective heat flux into a surface, W /  $m^2$   
 $q_{elec}''$  = electrical heat dissipation per unit area, W /  $m^2$   
 $R$  = electrical resistance,  $\Omega$   
 $\mathfrak{R}$  = electrical resistivity,  $\Omega \cdot m$   
 $r$  = recovery factor or radius, m

- $Re_D$  = Reynolds number base on leading edge diameter,  $U_\infty D / \nu$   
 $St$  = Stanton number,  $\frac{h}{\rho c_p U_{in}}$   
 $s$  = entropy, J / (kg K)  
 $t$  = time, s  
 $T$  = temperature, K or nondimensional time,  $\frac{tU_\infty}{D}$   
 $Tu$  = turbulence intensity,  $\frac{u'_{rms}}{u}$   
 $U$  = flow velocity, m / s or nondimensional temperature (Eq. (3.40))  
 $u$  = local velocity, m / s  
 $VR$  = velocity ratio,  $U_j / U_\infty$   
 $w$  = velocity, m / s or probability density function  
 $W$  = nondimensional temperature (Eq. (3.67))  
 $X$  = arbitrary performance parameter that does not depend on unsteady fluctuations, or nondimensional distance into wall (Eq. (3.42))  
 $x$  = distance, usually in streamwise direction, into wall, or along a buss bar, m  
 $y$  = distance, usually normal to the surface, m  
 $Z$  = arbitrary performance parameter that does not depend on unsteady fluctuations  
 $z$  = distance, usually in the spanwise direction, m

### Greek

- $\alpha$  = thermal diffusivity,  $\frac{k}{\rho c}$ ,  $m^2 / s$   
 $\Delta$  = change in a quantity  
 $\Delta q_r$  = net heat flux reduction due to film cooling, Eq. (3.10)  
 $\Delta q_{r,pulsed}$  = net heat flux reduction due to pulsing an otherwise steady coolant flow, Eq. (5.2)  
 $\delta$  = Dirac delta function, Eq. (3.76)  
 $\varepsilon$  = emissivity, turbulence dissipation,  $m^2 / s^3$ , uncertainty, or error  
 $\Lambda_f$  = turbulence integral length scale, m  
 $\eta$  = adiabatic effectiveness,  $(T_\infty - T_{aw}) / (T_\infty - T_c)$   
 $\phi$  = overall effectiveness,  $(T_\infty - T_s) / (T_\infty - T_c)$   
 $\gamma$  = unsteady coupled adiabatic effectiveness, Eq. (3.29)  
 $\nu$  = kinematic viscosity,  $m^2 / s$   
 $\theta$  = phase shift, rad, nondimensional internal wall temperature,  $(T_\infty - T_{wi}) / (T_\infty - T_c)$ , or nondimensional fluid temperature,  $(T_\infty - T) / (T_\infty - T_c)$   
 $\rho$  = density,  $kg / m^3$   
 $\lambda$  = nondimensional surface temperature with applied heat flux,  $(T_\infty - T_{s,HFP}) / (T_\infty - T_c)$   
 $\sigma$  = Stefan-Boltzmann constant,  $5.6704 \times 10^{-8} W / (m^2 K^4)$  or standard deviation

$\omega$  = frequency, rad / s

### ***Subscripts***

0 = without film cooling, or another baseline condition as described in the context

*aw* = adiabatic wall

*b* = buss bar

*c* = coolant

*D* = quantity based on leading edge diameter

*f* = with film cooling

*HFP* = heat flux plate

*i* = initial, internal, a summation index, or a vector index

*j* = coolant jet

*meas* = directly measured- no conduction correction applied

*o* = out

*p* = constant pressure

*rms* = root mean squared

*s* = surface

*span* = spanwise averaged or relating to the spanwise direction

*w* = wall

$\infty$  = freestream

### ***Superscripts***

$\bar{\quad}$  = temporal average

$\prime$  = fluctuating component

## Acronyms

AFIT	=	Air Force Institute of Technology
CFD	=	computational fluid dynamics
DNS	=	direct numerical simulation
ER	=	electrical region (a region through which no charge may pass)
HVAC	=	heating, ventilation, and air conditioning
IR	=	infrared
LES	=	large eddy simulation
NHFR	=	net heat flux reduction
RMS	=	root mean squared
RPM	=	revolutions per minute
RTV	=	room temperature vulcanized
USAF	=	United States Air Force
VC	=	valve closure

# **PULSED FILM COOLING ON A TURBINE BLADE LEADING EDGE**

## **1. Introduction**

Gas turbine engines are based on the Brayton cycle in which atmospheric air is compressed, heated via combustion, and expanded through a turbine prior to being exhausted back to the atmosphere, perhaps through a nozzle in the case of an engine used for thrust generation. Because the working fluid is in an open loop, a cooling process is absent from the Brayton cycle. The ideal Brayton cycle (one in which the working fluid experiences total pressure changes only over isentropic compression and isentropic expansion stages) has an efficiency dictated only by the pressure ratio across the compressor or turbine. However, increasing the turbine inlet temperature has a direct effect of increasing the thermal efficiency of an actual, non-isentropic engine. In fact, early gas turbine engines were incapable of producing a net work output due to low firing temperatures and non-isentropic compressors and turbines, in part, a consequence of the thermodynamics resulting in the divergence of lines of constant pressure on a temperature-entropy diagram. In fact, the isentropic efficiencies of early compressors were generally less than 50% (Wilson and Korakianitis (1998)). Just as important as efficiency, higher firing temperatures lead to an increase in specific power output.

Historically and presently, the limit on the combustor firing temperature has been the temperature limits of the hot gas path components, particularly the first stage nozzle guide vanes. Early engines were limited to a turbine inlet temperature of about 1200 K. Simple cooling schemes in place by 1960 allowed higher temperatures, whereas modern cooling schemes allow turbine inlet temperatures of 1755 K (2700 °F) in the case of the F100-PW-229 engine used with F-15 and F-16 aircraft (Mattingly, 2002). In addition to simply allowing the engine to operate at all, cooling the hot gas path components allows them to last longer in the high temperature, corrosive, erosive, high stress environment of

the turbine. Han et al. (2000) claim that the life of a turbine blade may be doubled by reducing its temperature by a mere 30 K.

Cooling the turbine components is a thermodynamically expensive process. Air is bled from the compressor stage and routed through serpentine channels within the hot gas path components before ejection out through coolant holes. The coolant holes are engineered to provide film cooling to protect the surfaces from the hot freestream gas. The first thermodynamic tax is paid when air is bled from the compressor stage. Energy is added into the coolant by the compressor, but it does not gain heat in the combustor. The next tax is paid when the coolant is introduced into turbine section. Ideally, the decrease in total temperature of the fluid through the turbine section would correspond to the energy extracted by the turbine. The very introduction of coolant to the turbine section reduces the bulk total temperature of the working fluid. The engineering challenge is to use as little coolant as possible and place it wisely in the turbine section. That is, we desire to cool only the components and avoid mixing coolant with the freestream unnecessarily.

Film cooling schemes have found potential secondary use in boundary layer control. Military aircraft are increasingly being used at low velocities in high-altitude, low density atmosphere. The resulting low Reynolds numbers of the flow over the low pressure turbine lends itself to boundary layer separation. Passive and active means of flow control in such cases have been studied with the passive ones being detrimental when the engine is operating at higher Reynolds numbers. Active flow control measures naturally allow the control mechanism to be turned off when it is no longer beneficial. Steady vortex generator jets with compound angle injection in a turbulent boundary layer have been shown (Compton and Johnston, 1992) to produce streamwise vortices. McManus et al. (1994) demonstrated that the ability of a vortex generator jet to delay boundary layer separation can be greater for a pulsed jet than a steady jet with the same average mass flow rate. Gompertz et al. (2009) found that synchronization of a pulsed vortex generator jet with the upstream wake passage frequency such that the jet pulsed between wake passage events provided even greater flow control.

## **1.1 Uniqueness of the Current Study**

The dual use of pulsed vortex generator jets as film cooling jets leaves the question of how pulsing the film cooling flow affects the ability of the film cooling scheme to protect a hot gas path component. Besides the requirement for an understanding of a potential thermal cost of using the film cooling jets as pulsed vortex generators, the possibility of potential thermal benefit of pulsing film cooling jets must also be explored. Although pulsed vortex generator jets served as inspiration for the present study, there is also inherent unintentional unsteadiness in film cooling flows. Perhaps the most dominant source of these fluctuations is through the rotor-stator interaction, which has been shown to result in coolant fluctuations of up to  $\pm 100\%$  of the mean blowing ratio (Abhari, 1996). The requisite techniques for the prediction and measurement of the thermal impact of pulsing are developed in the present study. These techniques are applied to the special case of film cooling jets on the leading edge of a turbine blade through computational and experimental simulations.

## **1.2 Research Objectives**

The overall objective of the research is to determine how pulsed jets affect film cooling behavior in the leading edge region of a turbine blade and why pulsed jets perform differently than steady jets. The spectrum of the investigation includes examination of the flow structures to determine coolant propagation behavior. Experimental facilities used in the investigation include the open circuit low speed wind tunnel located at the Air Force Research Laboratory Propulsion Directorate Test Cell 21 and the free surface water channel at the Air Force Research Laboratory Air Vehicles Directorate. Computational simulations were performed at the Air Force Institute of Technology parallel computing facility.

Following a brief review of existing literature in Chapter 2, Chapter 3 develops the theory of thermal performance evaluation for unsteady film cooling flows. The traditional technique by which one predicts the net benefit of film cooling on a turbine component is shown to be inadequate to describe the performance of unsteady film cooling schemes. In order to accomplish the primary objective, a new form of the net heat flux reduction equation is derived and a methodology for its experimental

determination is developed for unsteady film cooling. The experimental techniques developed as part of this research may be applied to virtually any geometry to determine the influence of pulsed film cooling (or any other film cooling situation in which  $T_{aw}$  and  $h$  are unsteady) on the heat flux to a hot gas path component. In Chapter 3, a method is also developed with which a wealth of existing performance data for steady film cooling schemes on any geometry may be used to obtain at least a rough prediction of the influence of pulsing an otherwise steady film cooling jet.

Chapter 4 will present the particular experimental methodology used to employ the techniques of Chapter 3 on a model of a turbine blade leading edge. Although the techniques for evaluating unsteady film cooling flows have general application, the turbine blade leading edge region was selected due to its very high heat load and consequently, the importance of protecting it. The results of this experimental regimen to determine how pulsed film cooling influences the heat load to the leading edge region are presented in Chapter 5. The prediction technique developed in Chapter 3 is shown to be quite effective in Chapter 5 as well.

Although the thermal benefit of film cooling is the ultimate test of a film cooling scheme's ability to protect an engine component, additional insight into the behavior of film cooling jets can be obtained through flow visualization. Chapters 6 and 7 present the methodology and results, respectively, of an experimental regimen to visualize pulsed film coolant with the same geometry and some of the same flow conditions as used in Chapter 5.

Chapters 8 and 9 present the methodology and results, respectively, of a computational study to determine both the flow behavior and thermal performance of pulsed film cooling schemes. In addition to time resolved flow field data, the computational study afforded time resolved thermal properties of the flow. The computational approach also allowed for the use of pulsed jet waveforms that are virtually impossible to achieve in the laboratory.

## 2. Literature Review

A great deal of research related to gas turbine film cooling has been performed, but only a few of them deal directly with pulsed film cooling. This section presents an overview of prior research that is relevant to the current study, beginning with a description of the various flow rate parameters that are in use and moving on to performance parameters. Then significant experimental and computational studies are discussed.

### 2.1 Film Cooling Flow Rate Parameters

Engine designers must pay close attention to the amount of coolant that is being used. The coolant to freestream density ratio in an actual engine can be greater than two. In order to match density ratio, the experimentalist must either use an appropriate temperature ratio or a foreign gas as the coolant. The considerable expense required to match density ratio has led to the development of several ways to normalize the coolant flow rate against the freestream flow rate in a fashion such that the film cooling behavior is not dependent upon the density ratio. The mass flux ratio, or blowing ratio, is the ratio of the coolant to freestream mass fluxes defined as:

$$M \equiv \frac{\rho_c U_j}{\rho_\infty U_\infty} \quad (2.1)$$

where  $U_\infty$  is the freestream velocity at the hole and  $U_j$  is the coolant velocity at the hole exit. In the case of showerhead cooling (cooling near the stagnation point), we take  $U_\infty$  to be the approach velocity. The blowing ratio is the most common way of expressing coolant injection rates perhaps due to its physical significance in that it is linearly proportional to the amount of bleed air that is used and therefore represents the thermodynamic “cost” of the coolant. Another method of characterizing blowing rates is the velocity ratio. The velocity ratio ( $VR$ ) is defined as:

$$VR \equiv \frac{U_j}{U_\infty} \quad (2.2)$$

Ammari et al. (1990) suggested using  $VR$  for characterizing the heat transfer behavior of inclined jets at nonrealistic density ratios. Another widely used method of characterizing coolant flow rate is through the momentum flux ratio defined as:

$$I \equiv \frac{\rho_c U_j^2}{\rho_\infty U_\infty^2} \quad (2.3)$$

Ekkad et al. (1998) suggested that  $I$  scaled adiabatic effectiveness and heat transfer coefficient well in the leading edge region. Despite this finding, it remains commonplace in the literature to use blowing ratio (Eq. (2.1)) solely. For that reason along with the fact that the blowing ratio gives direct indication of the coolant mass flow rate, the blowing ratio is the primary coolant flow rate parameter used in the present study. Density ratios of approximately  $DR = 1.0$  for the heat transfer experiments and  $DR = 1.08$  for the adiabatic effectiveness and unsteady coupled adiabatic effectiveness experiments (described in Chapter 3) allow the reader to compare this data to other data obtained at different density ratios with whatever means deemed most appropriate.

## 2.2 Steady Film Cooling Heat Transfer

Although an in-depth discussion of unsteady film cooling heat transfer is reserved for Chapter 3, it is useful to give an introduction to steady film cooling heat transfer at this point. The heat flux into or out of a surface is given by Newton's Law of Cooling. Generalizing the equation for an adiabatic wall temperature that is not necessarily equal to the freestream temperature, we have

$$q'' = h(T_{aw} - T_s) \quad (2.4)$$

with heat flux defined as positive into the surface. Equation (2.4) implies that the surface would assume the adiabatic wall temperature in the absence of heat transfer. This, of course, would be expected due to the name "adiabatic wall temperature."

The adiabatic wall temperature,  $T_{aw}$ , is the edge temperature of the film and is not uniform, simply because the film coolant is not uniform everywhere and the coolant mixes with the hot freestream gas. The adiabatic effectiveness is the nondimensional adiabatic wall temperature defined as:

$$\eta \equiv \frac{T_{\infty} - T_{aw}}{T_{\infty} - T_c} \quad (2.5)$$

The adiabatic effectiveness,  $\eta$ , is unaffected by changes in the coolant or freestream temperatures. It depends only on flow conditions and geometry. In the event that an experiment is performed with high speed flow such that viscous dissipation is significant, the  $T_{\infty}$  in Eq. (2.5) would be replaced with the freestream recovery temperature. Sometimes called the adiabatic wall temperature in non-film cooling contexts, this freestream recovery temperature is simply the freestream temperature added to the quantity,  $r \frac{U_{\infty}^2}{2c_p}$  where  $r$  is the recovery factor which is  $r \approx Pr^{1/2}$  for a turbulent boundary layer, to account for viscous dissipation (Mills, 1999).

### 2.3 Rotor-Stator Interaction

Abhari (1996) performed a study of rotor-stator interaction using a full engine scale facility with a blow-down wind tunnel. The blade passing frequency was 6 kHz. Temporally resolved measurements were made of the unsteady Nusselt number as well as time averaged adiabatic effectiveness. Two plenums fed suction side and pressure side coolant holes on the test stator; however, no showerhead cooling was present. A companion CFD study examined the pressure fluctuations that were expected during the experiment and computed the expected coolant blowing rates as a function of time. In some regions, especially the row closest to the leading edge on the suction side, blowing rates dropped to zero as a consequence of elevated external pressure. This row of holes experienced fluctuations of  $\pm 100\%$  of the average coolant consumption. Smaller, but still very significant fluctuations occurred for the other rows of coolant holes. Simulations were also performed without the unsteady blade passage. The average coolant consumption from individual rows of holes was also influenced by the unsteadiness.

Adami et al. (2004) performed a computational study of the interaction between unsteady wakes and leading edge region film cooling. The computational simulation replicated the experimental configuration of Wolff et al. (2002) in which cylindrical bars moved perpendicular to the freestream flow upstream of a simulated cascade. As a wake

passed over the stagnation region, the coolant velocity dropped 6.5% from the value it attained between wakes. The wake influenced the jet for approximately 50% of the cycle time.

## **2.4 Pulsed Jet Fluid Dynamics**

A limited number of flow visualization experiments have been performed on pulsed jets in cross flow. One such study is that by M'Closkey et al. (2002). The M'Closkey team excited a round normal jet in cross flow using a forced jet actuator. Flow visualization was performed by generating smoke in the upstream of the nozzle in the jet flow. Experiments were performed at an average velocity ratio of  $\overline{V}R = 2.58$  and the average jet velocity was 3.1 m/s. The experiments were performed with sinusoidal and square wave input and the RMS of the velocity perturbations was maintained at 1.7 m/s. A square wave excitation at 110 Hz and  $DC = 31\%$  (for which the high and low velocities were nominally approximately 5.6 m/s and 2.0 m/s, respectively) was found to produce a jet with a remarkably effective penetration into the freestream—about 2.5 times the penetration of the steady jet at a distance of about 10 hole diameters downstream of the hole. In all cases, the unsteady jet had greater penetration than the steady jet. Also apparent from the flow visualization imagery is the formation of distinct vortex structures that penetrate farther into the flow than the remainder of the jet fluid. At 110 Hz, nearly all of the jet fluid is contained in these vortices, but at lower frequencies, a sizeable (approximately half at 73.5 Hz,  $DC = 24\%$ ) portion of the jet fluid resides in a stream much closer to the wall than the vortices.

The production of ring vortices is well documented for unsteady jets. Their behavior in complex geometries and cross flow conditions continues to receive some well-deserved attention. Webster and Longmire (1997) performed flow visualization experiments with vortex rings emitted from cylinders with inclined exits, but no cross flow. The relevance of this fundamental research lies in the fact that film cooling holes generally have exits inclined with respect to the axis of the hole. Indeed, the geometry of Ekkad et al. (2006) used such a hole geometry. Webster and Longmire (1997) demonstrated not only that the inclination of a vortex ring is less than the inclination of the exit, but also that the circulation strength appears to vary around the vortex tube.

Maximum circulation was found at the short side of the tube and minimum circulation was  $180^\circ$  from that location, at the long side of the tube. This striking observation may at first appear to be in conflict with the Helmholtz vortex theorem, but close examination of the flow field revealed two additional vortex cores emanating from the region with the high circulation and extending into the hole. Summation of the circulations of those branched cores and the primary core agrees with the maximum circulation at the short end of the hole. As time progresses, the branched vortex tubes break free of the hole and form a closed loop that eventually passes through the primary ring.

## **2.5 Flat Plate Film Cooling**

Leylek and Zerkle (1994) performed a computational analog to the experiments of Pietrzyk et al. (1989) in which a flat plate was film-cooled with cylindrical jets angled at  $35^\circ$  in the streamwise direction with no compound angle. The relatively low hole  $L/d$  ratios of 3.5 and 1.75 resulted in a strong coupling between the external flow, coolant hole flow, and the flow within the plenum. A counter-rotating vortex pair was located in the coolant hole along with higher velocities toward the upstream side of the hole than the downstream side. This jetting effect was increasingly pronounced at higher blowing ratios. The researchers also discovered that the flow within the coolant hole was the major source of turbulence at the exit plane of the hole.

Walters and Leylek (1997) performed further refinements on the computational model of Leylek and Zerkle (1994). They located a separation region at the downstream edge of the coolant hole inlet and recommended the use of second order discretization. The researchers also stressed the importance of accurately modeling the physical problem with an appropriate grid. The  $k-\varepsilon$  turbulence model with wall functions was used. The wall functions were invalid in the viscous sublayer, so near-wall grid resolution was limited. The computational results, although decent, tended to overpredict centerline adiabatic effectiveness and underpredict lateral coolant spreading when compared to experimental data.

Coulthard et al. (2007, 1 and 2) performed an experimental study of the effects of jet pulsing on film cooling effectiveness and heat transfer coefficient on a flat plate. The researchers used a single row of five holes spaced  $3D$  apart, inclined  $35^\circ$  to the surface

and with no compound angle (parallel to the streamwise direction). Adiabatic effectiveness and heat transfer coefficients were reportedly measured in separate experiments using the steady-state techniques. An electrical heat flux plate was used to generate a uniform heat flux. A separate heat flux plate upstream of the row of coolant holes was used to develop a thermal boundary layer upstream of the coolant holes. Pulsing the coolant was found to decrease adiabatic effectiveness compared to a steady jet, whether one made the comparison to a steady jet with the blowing ratio equal the “on” value of the pulsed jet or a steady jet with the time averaged blowing ratio of the unsteady jet. The researchers observed that pulsing the coolant jet induced a high startup velocity prior to the jet reaching steady state. This high startup velocity may be responsible for increased jet lift-off with the pulsed jet. The Stanton number augmentation was increased for a pulsed jet compared to a steady jet with the blowing ratio equal the “on” value of the pulsed jet. However, when compared to a steady jet with the time-averaged blowing ratio of the pulsed jet, the heat transfer coefficient was not necessarily higher than with the steady jet. At the highest pulsing frequencies, the heat transfer coefficient was higher than the steady jet, but as pulsing frequency was decreased, the heat transfer coefficient dropped lower than with the steady jet. At the lowest nondimensional frequency of 0.0119 (based on hole diameter<sup>a</sup>) and a duty cycle of  $DC = 0.5$ , the heat transfer coefficient augmentation was about 25% lower than with a steady jet with the same average blowing ratio of  $M = 0.25$ .

Recently, Kartuzova et al. (2008) performed CFD simulations of pulsed film cooling on a flat plate using the realizable  $k-\varepsilon$  model after having confirmed that the realizable  $k-\varepsilon$  model outperformed the standard  $k-\varepsilon$ ,  $k-\omega$ , and  $k-\varepsilon-v^2$  models, using the adiabatic effectiveness data of Coulthard et al. (2006, 1) as the benchmark. Although heat transfer simulations were not performed, film cooling adiabatic effectiveness was the pulsed schemes was compared to steady film cooling at blowing ratios of  $M = 0.5$ , 1.25, and 1.5 for a laterally diffused film cooling hole and at  $M = 0.5$  and 1.5 for a cylindrical film cooling hole. The duty cycle for all pulsed cases was 50% and the nondimensional

---

<sup>a</sup> The nondimensional frequency,  $F$ , used in this document is based on leading edge diameter. As discussed in Section 4.1,  $D/d = 18.67$  in the present study, thus nondimensional frequencies reported in this document may be directly compared to those based on hole diameter by simply dividing the former by 18.67.

frequency (based on hole diameter) ranged from 0.0119 to 1.0. The authors reach the conclusion that pulsing generally resulted in a reduction in temporally averaged adiabatic effectiveness, but a case did exist in which pulsing increased  $\bar{\eta}$ . This interesting case occurred with the cylindrical film cooling hole at  $M = 1.5$  and the highest nondimensional pulsing frequency of 0.38, yielding area averaged  $\bar{\eta}$  15% higher than the steady case, although the magnitude of the difference was only  $\Delta\bar{\eta} = 0.0065$ . Lower frequencies resulted in performance poorer than the steady  $M$  case. Unfortunately, the authors compared their steady  $M$  results to pulsed results with matched peak  $M$ , not  $\bar{M}$ . Thus, the pulsed case in question that performed better than the steady case was actually running at an average blowing ratio of  $\bar{M} = 0.75$ , half that of the steady case to which it was compared. No steady case was performed at  $M = 0.75$  for a more complete comparison. Although the improved  $\bar{\eta}$  with half the coolant consumption may sound interesting, consider that steady film cooling at an even lower blowing ratio of only  $M = 0.5$  from the same coolant hole yielded an adiabatic effectiveness 262% higher ( $\Delta\bar{\eta} = 0.116$ ) than the steady  $M = 1.5$  case.

Muldoon and Acharya (2007) performed a direct numerical simulation (DNS) of a pulsed coolant jet on a flat plate. The coolant jet was cylindrical, aligned in the streamwise direction and inclined at  $35^\circ$  relative to the plate. The flow was assumed to be incompressible; furthermore, the density of the coolant was assumed to be the same as the density of the freestream. Because the computation relied on direct simulation of the turbulence, the cell size was necessarily quite small. Hence, the authors chose to use a domain that did not include the coolant hole. Instead, the elliptic hole exit was set as a boundary condition. This boundary condition used a temporally averaged velocity profile obtained from a separate experiment in which the blowing ratio  $M = 1.5$  was simulated. The velocity profiles used for blowing ratios other than  $M = 1.5$  were obtained via scaling the  $M = 1.5$  velocity profile. A steady jet at  $M = 1.5$  was found to contain large scale turbulent structures of approximately the same size as the hole diameter beginning at about  $x/d = 4$ . These structures also happen to be of a scale that is nearly equal to the distance that the jet resides above the surface for this lifted-off jet; therefore, these

unsteady structures may play a very important role in the time averaged adiabatic effectiveness. The authors noted the absence of these large scale turbulent structures in the near field of the coolant jet exit, but the present author notes this as a dubious assertion due to the imperfection of the boundary condition (i.e. laminar and unable to interact with the exterior flow) at the jet exit. An additional problem with this study is the observation of strong horseshoe vortices that entrain coolant and are very evident on spatial adiabatic effectiveness plots. One wonders if this may also be attributable to the imperfect hole exit boundary condition since this strong horseshoe vortex coolant entrainment is unobserved in experimental studies (see for example, Coulthard et al. (2007a)). Pulsing the coolant between  $M = 1.5$  and  $M = 0$  was found to generally improve adiabatic effectiveness compared to the steady jet at  $M = 1.5$ . On the other hand, pulsing was found to be detrimental to adiabatic effectiveness compared to the steady jet with the average blowing ratio of the pulsed jet. Pulsing was generally found to destroy the beneficial horseshoe vortex detected with the simulations of the steady jet, but downward vortex induction of the starting vortex was found to cause the coolant to reattach.

## **2.6 Leading Edge Film Cooling**

Mick and Mayle (1988) performed a study of film cooling effectiveness and heat transfer on the leading edge of a half cylinder with a blunt afterbody. The model had four rows of coolant holes located at  $\pm 15^\circ$  and  $\pm 44^\circ$ . The holes were oriented  $90^\circ$  to the direction of flow and were angled  $30^\circ$  to the surface. The researchers used an electrical heat flux plate with holes cut in it to facilitate the coolant flow. Three separate experiments were run in order to determine the influence of the nonuniform heat flux distribution in the vicinity of the holes. Adiabatic effectiveness and heat transfer coefficients were plotted for the entire leading edge, including within the hole pattern. Heat transfer coefficients were found to be increased by the film cooling. The authors reported local increases in the heat transfer coefficient of up to a factor of two, except in the vicinity of the very edge of the coolant holes where the initiation of new thermal boundary layers results in even higher heat transfer coefficient augmentation. The researchers warn that data very near the holes is unreliable to due three dimensional

conduction effects that were not accounted. Aside from the region within one hole diameter of the injection sites, the regions of highest heat transfer coefficient lie between regions of the highest and lowest adiabatic effectiveness; however, these regions move closer to the regions of low adiabatic effectiveness as blowing ratio is increased. An implication of this is that film cooling might be expected to increase the heat load to the component at these regions in a real engine.

Ekkad et al. (2006) studied the effects of jet pulsation and duty cycle on film cooling from a single jet on a leading edge model. Heat transfer coefficient distributions and adiabatic effectiveness distributions were determined simultaneously through the use of a transient experiment. In their experiment the model was soaked at an initial temperature  $T_i$  prior to the simultaneous (and nearly instantaneous) startup of both the coolant flow and the freestream flow. Temperatures were selected such that the initial model temperature, coolant temperature and freestream temperature all differ. The partial differential equation modeling convective heat transfer into a semi-infinite slab for which lateral conduction is negligible may be written:

$$k \frac{\partial^2 T}{\partial y^2} = \rho c \frac{\partial T}{\partial t} \quad (2.6)$$

$$-k \left. \frac{\partial T}{\partial y} \right|_{y=0} = h(T_{aw} - T_s) \quad (2.7)$$

$$T|_{t=0} = T_i \quad (2.8)$$

$$T|_{y \rightarrow \infty} = T_i \quad (2.9)$$

The solution for the temperature response was described by Incropera and DeWitt (1996) among other heat transfer texts. At the surface ( $y = 0$ ), the solution can be written:

$$\frac{T_w - T_i}{T_{aw} - T_i} = 1 - \exp\left(\frac{h^2 \alpha t}{k^2}\right) \operatorname{erfc}\left(\frac{h\sqrt{\alpha t}}{k}\right) \quad (2.10)$$

By measuring the wall temperature at any two moments in time after test initiation but prior to thermal wave penetration through the model walls, the above equation can be solved simultaneously for  $h$  and  $T_{aw}$ . Spatial  $h$  and  $\eta$  data can be obtained through this technique, although only spanwise averaged data was reported. Using the two-point

transient methodology, Ekkad et al. found that pulsing a jet at a particular peak blowing ratio tended to increase the adiabatic effectiveness compared to a steady jet at the same blowing ratio, but the effect on heat transfer coefficient was small. Results were independent of pulsing frequency for all three pulsing frequencies studied for which all  $F \ll 1$ . When compared to a steady jet at the same average blowing ratio, some pulsed jets were found to have higher adiabatic effectiveness, but at the cost of higher heat transfer coefficient. This effect was most notable at an average blowing ratio of  $\overline{M} = 0.5$ , for which pulsing increased the spanwise averaged adiabatic effectiveness between 0.03 and 0.05, with the greater gains farther from the film cooling hole. Similar results occurred with the  $\overline{M} = 1$  jet pulsed at  $DC = 50\%$  compared to the steady  $M = 1$  jet since spanwise averaged adiabatic effectiveness for steady jets at  $M = 0.5$  and  $M = 1$  happen to be nearly identical. Pulsing increased the heat transfer coefficient by approximately 20% compared to the continuous coolant flow at the same average blowing ratio of  $\overline{M} = 0.5$ .

A shortcoming with the aforementioned transient experimental technique with pulsed film cooling is that the solution to the differential equation assumes that both the heat transfer coefficient and the adiabatic effectiveness are constant. This is not true with unsteady film cooling; however, the measurement technique directly measures heat load, which is essentially the bottom line when it comes to engine design. So although details regarding the behavior of  $h$  and  $\eta$  may be somewhat murky for pulsed film cooling cases, the measurements do suggest that there are cases in which pulsing the film coolant decreases the heat load if the average blowing ratios are held constant.

In the following pages, a rigorous approach to the treatment of unsteady  $h$  and  $\eta$  measurements rectify the aforementioned shortcoming in the work of Ekkad et al. (2006) as well as shortcomings with the methodology used by researchers such as Coulthard et al. (2007, 1 and 2). Furthermore, an in-depth look at pulsed film cooling reveals insight into why it behaves differently from steady film cooling and a way to predict the behavior of certain pulsed schemes.

### 3. Unsteady Film Cooling Performance Determination

Steady film cooling jets have been studied extensively and a wealth of literature and mature techniques are available for evaluating the performance of steady film cooling flows. The variations in adiabatic wall temperature and heat transfer coefficient that are consequences of unsteady film cooling must be treated carefully; any use of steady film cooling evaluation techniques with unsteady flows must be applied with caution. In this section, I consider the fundamental equations of convective heat transfer with unsteady variables and derive the appropriate equations for evaluating the performance of unsteady film cooling flows. I then devise a theoretical experimental methodology for determining the necessary parameters in these equations. This methodology will have general application for any unsteady film cooling flow. The particular methodology used to demonstrate these techniques with a specific geometry and flow conditions is presented in Chapter 4.

#### 3.1 Unsteady Film Cooling Heat Transfer

As introduced in Section 2.2, the heat flux into or out of a surface is given by Newton's Law of Cooling in Eq. (2.4). Generalizing the equation for time dependent parameters and an adiabatic wall temperature that is not necessarily equal to the freestream temperature, we have

$$q''(t) = h(t)(T_{aw}(t) - T_s(t)) \quad (3.1)$$

with heat flux defined as positive into the surface. In the absence of film cooling the adiabatic wall temperature would be the freestream temperature. With unsteady film cooling, we must recognize that the adiabatic effectiveness varies in time due to variation in blowing ratio, even though the coolant temperature remains constant. Temporally resolved adiabatic effectiveness is then defined as

$$\eta(t) \equiv \frac{T_\infty - T_{aw}(t)}{T_\infty - T_c} \quad (3.2)$$

and is therefore the nondimensional temperature distribution that would occur if no heat transfer takes place. Unsteady film cooling naturally leads to unsteady adiabatic effectiveness. Substitute Eq. (3.2) into Eq. (3.1) to eliminate  $T_{aw}$  :

$$q''(t) = h(t)(T_\infty(t) - \eta(t)(T_\infty - T_c) - T_s) \quad (3.3)$$

$$q''(t) = h(t)T_\infty - h(t)\eta(t)(T_\infty - T_c) - h(t)T_s(t) \quad (3.4)$$

We shall employ the standard notation of the temporal average of an arbitrary property,  $z$ , defined by

$$\bar{z} = \lim_{\Delta t \rightarrow \infty} \frac{1}{\Delta t} \int_t^{t+\Delta t} z(t) dt \quad (3.5)$$

We temporally average Eq. (3.4).

$$\bar{q}'' = \lim_{\Delta t \rightarrow \infty} \frac{1}{\Delta t} \int_t^{t+\Delta t} (h(t)T_\infty - h(t)\eta(t)(T_\infty - T_c) - h(t)T_s(t)) dt \quad (3.6)$$

$$\bar{q}'' = \lim_{\Delta t \rightarrow \infty} \frac{1}{\Delta t} \int_t^{t+\Delta t} (h(t)T_\infty) dt - \lim_{\Delta t \rightarrow \infty} \frac{1}{\Delta t} \int_t^{t+\Delta t} (h(t)\eta(t)(T_\infty - T_c)) dt - \quad (3.7)$$

$$\lim_{\Delta t \rightarrow \infty} \frac{1}{\Delta t} \int_t^{t+\Delta t} (h(t)T_s(t)) dt$$

$$\bar{q}'' = \bar{h}T_\infty - \bar{h}\eta(T_\infty - T_c) - \bar{h}T_s \quad (3.8)$$

Although the surface temperature may generally vary, the impending development of the unsteady net heat flux reduction equation in Section 3.2 will require the special case of constant surface temperature. If the surface temperature is held constant, Eq. (3.8) reduces to

$$\bar{q}'' = \bar{h}(T_\infty - T_s) - \bar{h}\eta(T_\infty - T_c) \quad (3.9)$$

Equations (3.8) and (3.9) are significant in that they show the coupling between the time dependent heat transfer coefficient with the adiabatic effectiveness and surface temperature. Indeed, we expect more than simple independence of the temporally averaged adiabatic effectiveness and temporally averaged heat transfer coefficient to be important. As an illustration, consider a case in which coolant pulsing causes both the heat transfer coefficient and adiabatic effectiveness to oscillate between high values and low values. If oscillations are in phase, we would expect a lower heat flux into the surface than if they fluctuated out of phase since less efficient heat transfer occurs during times of low  $\eta$  than during high  $\eta$ .

### 3.2 Unsteady Net Heat Flux Reduction

To predict the reduction of heat flux into a real film cooled surface with steady film cooling, the net benefit of film cooling on the heat flux is sometimes described by the “net heat flux reduction” or NHFR,  $\Delta q_r$ , defined as

$$\Delta q_r \equiv 1 - \frac{q_f''}{q_0''} = 1 - \frac{h_f(T_{aw} - T_s)}{h_0(T_\infty - T_s)} \quad (3.10)$$

where  $T_{aw}$  represents the cooling film edge temperature. The subscript,  $f$ , refers to the quantity with film cooling and the subscript,  $0$ , refers to the quantity without film cooling<sup>b</sup>. With this model,  $\Delta q_r$  gives the fraction that the heat flux into the component is reduced if the component is maintained (perhaps by internal cooling) at a fixed temperature. A negative net heat flux reduction indicates that the heat flux is increased by film cooling and is clearly undesirable. Some algebraic manipulation will show

$$\Delta q_r = 1 - \frac{h_f}{h_0} \left(1 - \frac{\eta}{\phi}\right) \quad (3.11)$$

where  $\phi$  is the nondimensionalized local surface temperature, or overall effectiveness, defined as

$$\phi \equiv \frac{T_\infty - T_s}{T_\infty - T_c} \quad (3.12)$$

Typically, we set  $\phi = 0.6$  (see, for example, Sen et al., 1996) for evaluation of Eq. (3.11).

The steady form of this equation has been used in the literature, but I propose a generalized form applicable to unsteady film cooling as well.

To develop a suitable form of the net heat flux reduction equation for unsteady film cooling, we begin by writing an equation for the temporal average of the net heat flux reduction:

$$\overline{\Delta q_r} \equiv 1 - \frac{\overline{q_f''}}{\overline{q_0''}} \quad (3.13)$$

<sup>b</sup> The NHFR equation may be adapted to show the effect of any change in conditions, not just film cooling on the net heat flux into a surface (dimples, surface roughness, pulsed film cooling vs. steady, etc.)

$q_0''$  is for the inherently steady non-film-cooled case ( $\overline{q_0''} = q_0''$ ). In the evaluation of  $\Delta q_r$ , we assume that the surface temperature is constant. This assumption that the fluctuations in surface temperature are small is valid due to the dampening effect of the thermal capacity of the material,  $\rho c$ , particularly at the high pulsation frequencies that would be likely in an engine. The applicability of neglecting surface temperature fluctuations is treated thoroughly in Section 3.4.

Continuing with the development of the NHFR equation, we shall employ Eq. (3.9) in Eq. (3.13) since we assume a constant surface temperature.

$$\overline{\Delta q_r} = 1 - \frac{\overline{h_f}(T_\infty - T_s) - \overline{h_f \eta}(T_\infty - T_c)}{h_0 \phi (T_\infty - T_c)} \quad (3.14)$$

$$\overline{\Delta q_r} = 1 - \frac{\overline{h_f}(T_\infty - T_\infty + \phi(T_\infty - T_c)) - \overline{h_f \eta}(T_\infty - T_c)}{h_0 \phi (T_\infty - T_c)} \quad (3.15)$$

$$\overline{\Delta q_r} = 1 - \frac{\overline{h_f \phi} - \overline{h_f \eta}}{h_0 \phi} \quad (3.16)$$

If we define a time dependent parameter as the sum of a temporal mean and a zero-mean fluctuating component,

$$Z(t) = \bar{Z} + Z'(t) \quad (3.17)$$

Then for any two such parameters,  $Z$  and  $X$ ,

$$\overline{XZ} = \overline{(\bar{X} + X')(\bar{Z} + Z')} \quad (3.18)$$

$$\overline{XZ} = \overline{\bar{X}\bar{Z}} + \overline{\bar{X}Z'} + \overline{X'\bar{Z}} + \overline{X'Z'} \quad (3.19)$$

$$\overline{XZ} = \overline{\bar{X}\bar{Z}} + \overline{\bar{X}Z'} + \overline{X'\bar{Z}} + \overline{X'Z'} \quad (3.20)$$

$$\overline{XZ} = \overline{\bar{X}\bar{Z}} + \overline{\bar{X}Z'} + \overline{X'\bar{Z}} + \overline{X'Z'} \quad (3.21)$$

The average of the zero-mean fluctuating component is, by definition, zero, so the expression reduces to

$$\overline{XZ} = \overline{\bar{X}\bar{Z}} + \overline{X'Z'} \quad (3.22)$$

Applying this to Eq. (3.16), we obtain the following.

$$\overline{\Delta q_r} = 1 - \frac{\overline{h_f \phi} - \overline{h_f \eta} - \overline{h_f' \eta'}}{h_0 \phi} \quad (3.23)$$

$$\overline{\Delta q_r} = 1 - \frac{\overline{h_f}(\phi - \overline{\eta}) - \overline{h_f' \eta'}}{h_0 \phi} \quad (3.24)$$

$$\overline{\Delta q_r} = 1 - \frac{\overline{h_f} \left( 1 - \frac{\overline{\eta}}{\phi} \right) + \frac{\overline{h_f' \eta'}}{h_0 \phi}}{\quad} \quad (3.25)$$

Equation (3.25) is similar to the steady state NHFR equation used in existing literature, Eq. (3.11), but with time averaged parameters and an additional term accounting for the fluctuations in the heat transfer coefficient and adiabatic effectiveness. Equation (3.25) shows that if the heat transfer coefficient and adiabatic effectiveness fluctuate more or less in phase, then the  $\frac{\overline{h_f' \eta'}}{h_0 \phi}$  term is positive, improving  $\overline{\Delta q_r}$  if  $\overline{h_f}$  and  $\overline{\eta}$  are unchanged by pulsing the coolant. There is good reason to believe that such in-phase fluctuations are likely, in particular if the film cooling is cycled on and off. It is well documented that film cooling increases both adiabatic effectiveness (since  $\eta = 0$  when the jet is off) and the heat transfer coefficient relative to the non-film-cooled case. (See, for example, Mick and Mayle, 1988.)

### 3.3 Experimental Determination of NHFR

It appears from Eq. (3.25) that in addition to an assumed value for the overall effectiveness,  $\phi$ , we must experimentally measure  $\overline{\eta}$ ,  $\overline{h_f' \eta'}$ ,  $\overline{h_f}$ , and  $h_0$  to determine the net heat flux reduction,  $\overline{\Delta q_r}$ . In order to directly measure  $\overline{h_f' \eta'}$ , one would need to perform time resolved surface temperature measurements on a very low heat capacity model, i.e., a model for which surface temperature fluctuations would be undamped. We restrict our discussion of experimental techniques to those available in a lab in which only time averaged surface temperature measurements are practical. Further, it will be shown that  $\overline{\eta}$  and  $\overline{h_f' \eta'}$  can be replaced by a single parameter,  $\gamma$ , which is relatively simple to measure. Following the development of  $\gamma$  and the experimental technique to measure  $\gamma$ , a technique to measure  $\overline{h_f}$  and  $h_0$  is presented, thereby completing the information needed to compute the net heat flux reduction with unsteady film cooling.

In order to understand the utility of the combined parameter,  $\gamma$ , and the role of  $\overline{h_f' \eta'}$  in influencing our experimental measurements, we first consider how one might attempt to measure  $\overline{\eta}$ . The temporal average of adiabatic effectiveness,  $\overline{\eta}$ , can be written by averaging Eq. (3.2) to obtain:

$$\overline{\eta} = \frac{T_\infty - \overline{T_{aw}}}{T_\infty - T_c} \quad (3.26)$$

It would seem that an unsteady adiabatic wall experiment could be performed to determine  $\overline{\eta}$  on a model of an engine component in which the coolant flow is held at a known constant temperature,  $T_c$ , different from the known freestream temperature,  $T_\infty$ . With a perfectly adiabatic wall, the measured average surface temperature would, by definition, equal the average adiabatic wall temperature, i.e.,  $\overline{T_s} = \overline{T_{aw}}$ . However, in a laboratory setting a wall can only be nearly adiabatic at best. A real material with heat capacity,  $\rho c$ , and thermal conductivity,  $k$ , will undergo cyclic heat transfer into and out of the surface.  $T_{aw}(t)$ , which is synonymous with the film edge temperature (dictated by flow conditions which vary periodically), will not be the temperature measured on the conducting surface,  $T_s(t)$ , per Eq. (3.1), and we do not have assurance that  $\overline{T_s} = \overline{T_{aw}}$ . In need of more information regarding the response of the surface temperature to the adiabatic wall temperature, we abandon Eq. (3.26) for experimental use and instead solve for  $\overline{\eta}$  from Eqs. (3.8) and (3.22).

$$\overline{\eta} = \frac{T_\infty - \overline{T_s}}{T_\infty - T_c} - \frac{\overline{h_f' \eta'}}{\overline{h_f}} - \frac{\overline{q''}}{\overline{h_f} (T_\infty - T_c)} - \frac{\overline{h_f' T_s'}}{\overline{h_f} (T_\infty - T_c)} \quad (3.27)$$

It will be shown that Eq. (3.27) reduces to Eq. (3.26) for the theoretical adiabatic wall, but Eq. (3.27) has utility for determining the net heat flux reduction for the more usual conducting wall. Although the average adiabatic effectiveness,  $\overline{\eta}$ , is a flow property unaffected by the thermal state of the surface, the behavior of  $\eta$  influences the thermal state of the surface, the response of which we can measure but which depends on the material properties. We shall investigate two limiting cases in material selection. First is

the perfectly adiabatic surface ( $k = 0$ ) and second is a conducting material with infinite thermal capacity ( $\rho c \rightarrow \infty$ ).

In the trivial case of a perfectly adiabatic surface ( $k = 0$ ), the surface temperature fluctuations will match the fluctuations in the adiabatic wall temperature, i.e.,  $T_s' = T_{aw}'$ . From Eqs. (3.2) and (3.17),

$$\eta' = \frac{-T_{aw}'}{T_\infty - T_c}, \quad (3.28)$$

and the second and fourth terms on the right hand side of Eq. (3.27) cancel. Furthermore, since  $q_f'' = 0$ , the second term on the right hand side of Eq. (3.27) is zero. Therefore, as previously stated, in the case of  $k = 0$ , only the average surface temperature measurement is required to determine  $\bar{\eta}$ . Although this hypothetical experimental technique with  $k = 0$  yields  $\bar{\eta}$ ,  $\overline{h_f' \eta'}$  would still be required to calculate NHFR with Eq. (3.25). Since we are unable to directly measure  $\overline{h_f' \eta'}$  with an averaging technique, the first limiting case of  $k = 0$ , even if achievable in the lab, would not provide the necessary data to compute NHFR.

Before we direct our attention to the second limiting case of a conducting surface with  $\rho c \rightarrow \infty$ , we define a new film cooling parameter,  $\gamma$ :

$$\gamma \equiv \bar{\eta} + \frac{\overline{h_f' \eta'}}{\bar{h}_f} \quad (3.29)$$

Since  $\gamma$  is only a function of the behavior of  $\eta$  and  $h$ ,  $\gamma$  is a flow parameter unaffected by the thermal condition of the film cooled surface. Equation (3.29) combined with Eq. (3.27) yields

$$\gamma = \frac{T_\infty - \bar{T}_s}{T_\infty - T_c} - \frac{\overline{q_f''}}{\bar{h}_f (T_\infty - T_c)} - \frac{\overline{h_f' T_s'}}{\bar{h}_f (T_\infty - T_c)} \quad (3.30)$$

Substitution of Eq. (3.29) into Eq. (3.25) results in

$$\overline{\Delta q_r} = 1 - \frac{\bar{h}_f}{h_0} \left( 1 - \frac{\gamma}{\phi} \right) \quad (3.31)$$

It will be shown that  $\gamma$  is measurable in the second limiting case and, thus, will lead to determination of  $\overline{\Delta q_r}$  in Eq. (3.31). We note that  $\gamma = \eta$  for the case of steady film cooling, and may be thought of as an unsteady coupled adiabatic effectiveness.

In the second limiting case of  $\rho c \rightarrow \infty$ , the thermal capacitance of the material does not allow the surface temperature to respond to fluctuations in the adiabatic wall temperature. Therefore,  $T_s'$  is zero and the last term on the right hand side of Eq. (3.30) is zero. Alternatively, if  $\omega \rightarrow \infty$ , the surface will not have the time required to respond to a change in adiabatic wall temperature, thereby also causing  $T_s' \rightarrow 0$ .

For real materials ( $k \neq 0$ ,  $\rho c \neq \infty$ ), the magnitude of  $T_s'$  can be made small through proper choice of wall material and fluctuation frequency. We reserve discussion on the criteria for an experimental model that will accomplish this objective for Section 3.4. For now, suffice it to say that  $T_s'$  can be made small to within an arbitrary tolerance. Choosing materials for negligible  $T_s'$  and for which  $\overline{q_f''} = 0$  allows reduction of Eq. (3.30) to a simple term:<sup>c</sup>

$$\gamma = \frac{T_\infty - T_s}{T_\infty - T_c}, \quad (3.32)$$

noting that  $\overline{T_s} = T_s$  with the assumption that  $T_s' = 0$ . In summary, an unsteady experiment in which  $T_s'$  is negligible and  $\overline{q_f''} \approx 0$  allows for the measurement of  $\gamma$  for use in Eq. (3.31).

Before discussing  $\overline{h_f}$  and  $h_0$ , we can now quantify the difference between  $T_s$  and  $\overline{T_{aw}}$  on the perfectly damped ( $T_s' \rightarrow 0$ ) conducting wall. Substitution of Eqs. (3.26) and (3.32) into Eq. (3.29) yields

$$T_s = \overline{T_{aw}} - \frac{(T_\infty - T_c) \overline{h_f' \eta'}}{\overline{h_f}} \quad (3.33)$$

<sup>c</sup> Note that  $\overline{q_f''}$  can be zero even on a conducting surface since  $\overline{q_f''}$  is the average heat flux. Heat flux into the surface during a cycle need only match the heat flux out later in the cycle.

Equation (3.33) shows that for a conducting surface (including that for which  $\overline{q_f''} = 0$  in developing Eq. (3.32)), the average surface temperature does not equal the average adiabatic wall temperature. The reason is due to an unsteady heat transfer coefficient along with the thermal capacitance of the wall which dampens the reaction of the wall to changes in the adiabatic wall temperature. This capacitance (taken to be infinite in the assumption that  $T_s' = 0$  with the properly designed model) causes the surface temperature to differ from the adiabatic wall temperature, thereby creating a temperature difference across which cyclic convective heat transfer occurs.<sup>d</sup>

As shown in Eq. (3.31),  $\overline{h_f}$  and  $h_0$  are still needed to calculate the net heat flux reduction. To determine  $\overline{h_f}$ , consider a second unsteady experiment with a known average convective heat flux applied at the surface via an electrical heater such that  $\overline{q_f''} \neq 0$ , and with arbitrary (constant) coolant and freestream temperatures. Equation (3.8) with Eq. (3.22) yields

$$\overline{q_f''} = \overline{h_f} T_\infty - \overline{h_f'} T_s' - \overline{h_f} \cdot \overline{T_s} - \overline{h_f} \cdot \overline{\eta} (T_\infty - T_c) - \overline{h_f'} \eta' (T_\infty - T_c) \quad (3.34)$$

By the same reasoning as described for the first experiment for  $\gamma$ , the material and scaling can be selected such that  $T_s'$  is negligible. That is, the material used for the measurement of  $\gamma$  would also be appropriate for the measurement of  $\overline{h_f}$  since this method also relies on small  $T_s'$ .

Again, note that  $\overline{T_s} = T_s$  with the assumption that  $T_s' = 0$ . We shall nondimensionalize the resulting surface temperature distribution,  $\lambda = (T_\infty - T_s) / (T_\infty - T_c)$  this time with  $\overline{q_f''} \neq 0$ . Substitution of Eq. (3.29) into Eq. (3.34) yields

$$\overline{h_f} = \frac{-\overline{q_f''}}{(T_\infty - T_c)(\gamma - \lambda)} \quad (3.35)$$

<sup>d</sup> A thorough analysis and discussion of this phenomenon is presented in Section 3.4.1.1.

Unlike  $\gamma$ ,  $\lambda$  is not a flow property by itself;  $\lambda$  depends on the arbitrary value of  $\overline{q_f}''$  imposed by the electrical heater and is meaningful only when used in conjunction with a particular value of  $\overline{q_f}''$  as in Eq. (3.35). Any nonzero value of  $\overline{q_f}''$  would be permissible, with larger values generally yielding lower experimental uncertainty due to larger measurable differences between  $T_s$  and  $T_{aw}$ . Note that due to the definition of  $\lambda$ , Eq. (3.35) is defined in the limit as  $(T_\infty - T_c) \rightarrow 0$  in the  $\overline{q_f}'' \neq 0$  experiment. That is, the discontinuity at  $T_\infty = T_c$  is removable. Given that  $\gamma$  is simply a predetermined value in Eq. (3.35), the denominator in Eq. (3.35) would simply become  $-(T_\infty - T_c)\lambda$ , or  $T_s - T_\infty$ , if  $T_\infty = T_c$ . The same  $\overline{q_f}'' \neq 0$  experiment and Eq. (3.35) can also be used with a non-film-cooled surface to determine  $h_0$ . For the non-film-cooled surface,  $\eta = 0$  by definition and by examination of Eq. (3.29), it follows that  $\gamma = 0$  for a non-film-cooled surface.

### 3.4 Surface Temperature Fluctuations

The preceding development of measurement techniques requires that  $T_s'$  is small with the test article. The fluctuations in surface temperature are related to the thermal properties of the material as well as the frequency of the unsteadiness. This section presents an analysis of the relationship between the design of the experimental model and the surface temperature fluctuations that would be expected on the model. More specifically, we lay out the requirements on the experimental design in order to yield the desired data discussed in Section 3.3. We first discuss the requirements for the  $\overline{q_f}'' = 0$  experiment to determine  $\gamma$  and then discuss the requirements for the known  $\overline{q_f}'' \neq 0$  experiment used to determine  $\overline{h_f}$ .

### 3.4.1. Zero Applied Heat Flux

For real materials ( $k \neq 0$ ,  $\rho c \neq \infty$ ), the magnitude of  $T_s'$  in Eq. (3.30) can be made small through proper choice of wall material and fluctuation frequency.<sup>e</sup> We desire sufficiently small  $T_s'$  such that the final term on the right hand side of Eq. (3.30),  $\overline{h_f' T_s'} / (\overline{h_f} (T_\infty - T_c))$ , is negligible. To determine a value of  $T_s'$  that causes the term to be small, one must estimate  $\overline{h_f}$  and the extreme values of  $h_f'$  which appear in the final term on the right hand side of Eq. (3.30). With knowledge of the value of  $T_\infty - T_c$  to be used during the experiment, one can then estimate the maximum permissible value of  $T_s'$  such that the final term on the right hand side of Eq. (3.30) is negligible to within a desired tolerance.

With a particular maximum permissible value of  $T_s'$ , the criteria for choices in wall material and fluctuation frequency can be determined by examining the unsteady surface conduction. For the simple case of a sinusoidally varying adiabatic effectiveness over a semi-infinite uniform material with heat transfer coefficient,  $h$ , assumed to be constant for the moment, the conduction can be modeled with the following differential equation and boundary conditions (noting positive  $x$  is into the wall):

$$\rho c \frac{\partial T}{\partial t} = k \frac{\partial^2 T}{\partial x^2} \quad (3.36)$$

$$T_{aw} = T_{fluc} \sin(\omega t) + \overline{T_{aw}} \quad (3.37)$$

We impose a Robin boundary condition at the surface that specifies that the convective heat transfer into the surface is equal to the conduction into the substrate. For the purposes of this analysis, we shall assume that the heat transfer coefficient is constant.

$$h(T_{aw}(t) - T_s(t)) = -k \left. \frac{\partial T}{\partial x} \right|_{x=0} \quad (3.38)$$

<sup>e</sup> Although a goal of an experiment may be to test a particular pulsing frequency, the frequency must only be matched in the nondimensional sense just as velocity, for instance, must only be matched through the Reynolds number (and possibly other nondimensional parameters depending on the governing flow physics.) Thus, the pulsing frequency at which the desired experiment must be performed is flexible, provided appropriate scaling is performed.

We shall further assume that the solid is semi-infinite—valid if during the course of a cycle, the thermal wave (proportional to  $\sqrt{\alpha t}$ ) cannot penetrate the model material. We expect that as  $x \rightarrow \infty$ ,  $T \rightarrow T_{aw}$ , that is, the temperature fluctuations at the surface are damped as we look deeper into the solid and at an infinite distance away from the surface, the fluctuations are zero. For our initial condition, we shall set the temperature of the entire solid at  $\overline{T_{aw}}$ ,

$$T(x, t = 0) = \overline{T_{aw}} \quad (3.39)$$

Introducing the non-dimensional variables,

$$U = \frac{T - \overline{T_{aw}}}{T_{fluc}} \quad (3.40)$$

$$\tau = \omega t \quad (3.41)$$

$$X = \frac{x}{(\alpha / \omega)^{1/2}} \quad (3.42)$$

The differential equation in the nondimensional variables is then written,

$$\frac{\partial U}{\partial \tau} - \frac{\partial^2 U}{\partial X^2} = 0 \quad (3.43)$$

$$U(X, \tau = 0) = 0 \quad (3.44)$$

$$U(X \rightarrow \infty, \tau) = 0 \quad (3.45)$$

$$U(X = 0, \tau) = \sin \tau + C \left. \frac{\partial U}{\partial X} \right|_{X=0} = \text{Im}(e^{i\tau}) + C \left. \frac{\partial U}{\partial X} \right|_{X=0} \quad (3.46)$$

where 
$$C = \frac{k}{\bar{h} \sqrt{\alpha / \omega}} \quad (3.47)$$

Note that  $\bar{h}$  is used in the definition of  $C$  in Eq. (3.47) in order to maintain generality for the eventual use of variable  $h$ . This differential equation with its associated boundary conditions is similar in formulation to the viscous flow problem known as “Stokes’s oscillating plate” with the exception of the Robin boundary condition given by Eq. (3.46) in lieu of the Neumann boundary condition associated with Stokes’s oscillating plate. A solution methodology for the Stokes oscillating plate is given by Panton (1996).

The solution that follows was inspired by that technique in that we consider the solution,  $U$ , as a complex variable and take the imaginary part as the answer as was written in the formulation of Eq. (3.46). We seek the periodic steady state solution obtained by dispensing with the initial condition in Eq. (3.44) and forcing the time dependence of the solution to be an oscillation. We shall assume that the solution has the form

$$U = f(X)e^{i\tau} \quad (3.48)$$

Substitution of Eq. (3.48) into Eq. (3.43) imposes the differential equation,

$$(f'' - if')e^{i\tau} = 0 \quad (3.49)$$

or

$$f'' - if' = 0 \quad (3.50)$$

from which we may assume a solution of the form

$$f = Ae^{\pm \frac{1+i}{\sqrt{2}}X} \quad (3.51)$$

Therefore, a solution to Eq. (3.43) is given by

$$U = Ae^{\pm \frac{1+i}{\sqrt{2}}X} e^{i\tau} \quad (3.52)$$

Since the solution must be bounded as  $X \rightarrow \infty$  per Eq. (3.45), the negative sign must be selected. Satisfaction of the Robin boundary condition given by Eq. (3.46) forces the requirement on the constant,  $A$ .

$$A = \frac{1}{1 + \frac{C(1+i)}{\sqrt{2}}} \quad (3.53)$$

The imaginary part of the solution may be written as

$$U = \text{Im} \left[ \frac{1}{1 + \frac{C(1+i)}{\sqrt{2}}} e^{\pm \frac{1+i}{\sqrt{2}}X} e^{i\tau} \right] \quad (3.54)$$

or, after some algebraic manipulation,

$$U = \frac{e^{-X/\sqrt{2}}}{1 + C\sqrt{2} + C^2} \left[ \left( 1 + \frac{C}{\sqrt{2}} \right) \sin \left( \tau - \frac{X}{\sqrt{2}} \right) - \frac{C}{\sqrt{2}} \cos \left( \tau - \frac{X}{\sqrt{2}} \right) \right] \quad (3.55)$$

A plot of the response for a particular value of  $C = 5.85$  is shown in Fig. 3.1. For this  $C$  value (selected for its importance in the experiments described in Chapter 4), there is a lag in the surface temperature response of  $0.216\pi$  rad behind the adiabatic wall temperature. The amplitude of the temperature oscillations at the surface is only 15% of the oscillations in the adiabatic wall temperature. Also notable is the fact that the thermal wave penetrates to approximately  $X = 6$ , where for this case the oscillation amplitude is only 0.002% of the adiabatic wall temperature oscillation.

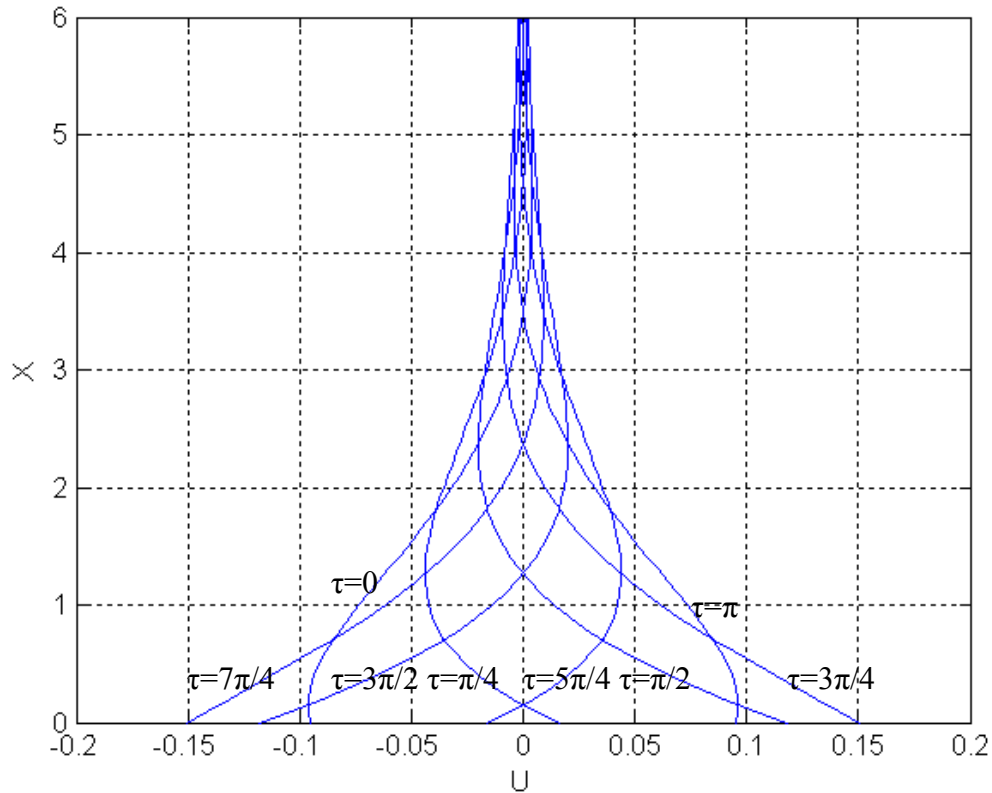


**Fig. 3.1 Temperature distribution for semi-infinite slab with oscillating adiabatic wall temperature ( $C = 5.85$ )**

The response at the surface would then be

$$U_{x=0} = \frac{\left(1 + \frac{C}{\sqrt{2}}\right) \sin(\tau) - \frac{C}{\sqrt{2}} \cos(\tau)}{1 + C\sqrt{2} + C^2} \quad (3.56)$$

or in dimensional terms,

$$T_s = \overline{T_{av}} + T_{fluc} \frac{\left(1 + \frac{C}{\sqrt{2}}\right) \sin(\omega t) - \frac{C}{\sqrt{2}} \cos(\omega t)}{1 + C\sqrt{2} + C^2} \quad (3.57)$$

The parameter  $C$  controls the magnitude of the surface temperature fluctuations. For high frequency or large  $k\rho c$ ,  $C \rightarrow \infty$  and  $T_s' \rightarrow 0$  as shown in Fig. 3.2. The parameter,  $C$ , may be determined for actual engine conditions to check the assumption of  $\phi' = 0$  ( $T_s' = 0$ ) used in the formulation of Eq. (3.25). Hastelloy C-276, a superalloy of the class used in hot turbine sections, has  $c = 427$  J/(kg K),  $\rho = 8890$  kg/m<sup>3</sup>, and  $k = 19$  W/(m K) (ASM, 2000). A turbine blade operating at 10000 RPM with 30 upstream nozzles would have unsteadiness at 5 kHz, or 31400 rad/s. Han et al. (2000) indicate that a typical conservative estimate for heat transfer coefficient is  $h = 1000$  W/(m<sup>2</sup> K). With Eq. (3.47), the  $C$  value for an actual engine component would be  $C \approx 1700$ , a very high value, particularly in the context of Fig. 3.2.

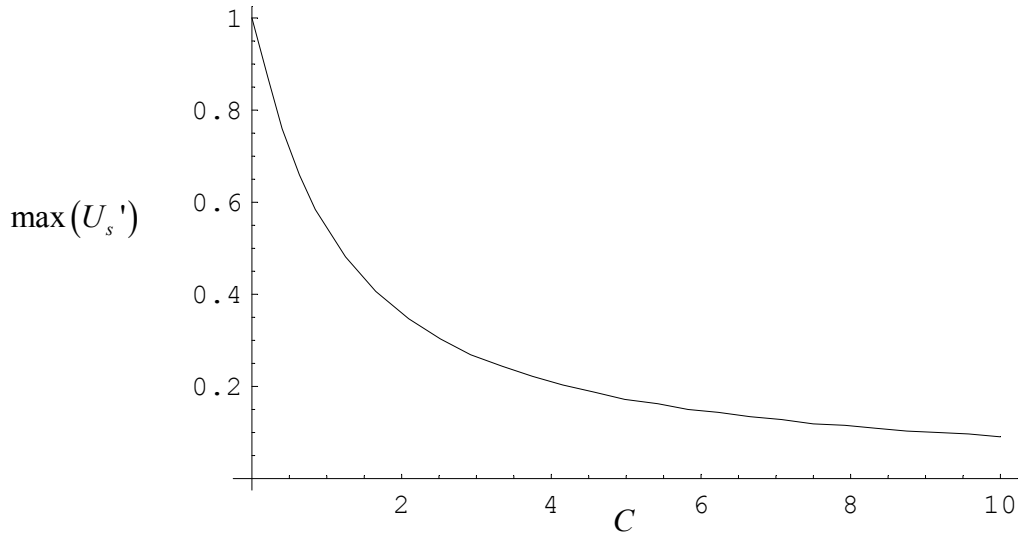


Fig. 3.2 Maximum relative deviation of surface temperature

There is no requirement to match  $C$  with an experimental model used to determine the net heat flux reduction (Eq. (3.25)). Only scaled geometry and the relevant nondimensional flow conditions (e.g., Reynolds number and a nondimensionalized pulsing frequency, in the form of a Strouhal number) of the model must match those of the engine component. By estimating  $\overline{h_f}$  and the extreme values of  $h_f'$  (perhaps through the use of non-pulsed experiments at the extreme blowing rates) that would appear in the final term on the right hand side of Eq. (3.30), one can estimate the maximum permissible value of  $T_s'$  such that the final term on the right hand side of Eq. (3.30) is negligible to within a desired tolerance. Further estimates of the extreme values of  $T_{aw}$  may be used to determine that maximum permissible fraction of  $T_{aw,fluc}$  that the surface temperature is allowed to vary. From this fraction, Fig. 3.2 may be used to determine the minimum value of  $C$  that will force the final term on the right hand side of Eq. (3.30) to be negligible. In addition to carefully selecting the material to influence  $k$ ,  $\rho$ , and  $c$ , one may arbitrarily select  $\omega$  while scaling the geometry accordingly in order to maintain a matched nondimensional frequency. Since the result in Eq. (3.57) assumes constant  $h$  and we recognize that  $h$  generally varies over the course of a cycle, a conservative (i.e., high) estimate of  $h$  should be used in  $C$  to determine the requirements on  $k$ ,  $\rho$ ,  $c$ , and  $\omega$  in order to ensure that the actual value of  $C$  exceeds the minimum required value.

We shall depart briefly from the discussion of general experimental design applicable to any unsteady film cooling experiment to consider the geometry of interest in the present experimental campaign—a half cylinder in cross flow. An uncooled cylinder in cross flow at  $Re_D=71000$  has a maximum heat transfer coefficient of approximately  $77 \text{ W}/(\text{m}^2 \text{ K})$  (Incropera and DeWitt (1996)), which is fairly uniform in the region of the film cooling holes. Per the results of Mick and Mayle (1988), let us multiply our heat transfer coefficient of  $h_0=77 \text{ W}/(\text{m}^2 \text{ K})$  by a factor of 2 to give an approximate value for the maximum heat transfer coefficient in the presence of film

cooling so that  $h_f = 154 \text{ W}/(\text{m}^2 \text{ K})$ .<sup>f</sup> In essence, we shall suppose for the sake of this analysis that the heat transfer coefficient fluctuates between 154 and 77  $\text{W}/(\text{m}^2 \text{ K})$  as the jet is pulsed on and off. We shall further suppose that the heat transfer coefficient for the purpose of this analysis is steady and at the average of the high and low values, or  $\bar{h} = 115.5 \text{ W}/(\text{m}^2 \text{ K})$ .

As described in Section 4.1, the model is constructed of General Plastics Last-A-Foam FR-7106, in part due to the analysis presented in this section. The properties of the material are as follows:  $k = 0.030 \text{ W}/(\text{m K})$ ,  $\rho = 96 \text{ kg}/\text{m}^3$ ,  $c = 1260 \text{ J}/(\text{kg K})$ . Thermal conductivity and density were obtained directly from General Plastics; the specific heat is given by Keith (1998).<sup>g</sup> Having benefited from performing the following analysis with several pulsing frequencies, we shall restrict ourselves *a posteriori* to a minimum pulsation frequency 20 Hz, or  $\omega = 125.7 \text{ rad/s}$ . With these values, we find that  $C = 5.85$  (Fig. 3.1 represents our experimental conditions) and the thermal wave penetration of  $X = 6$  corresponds to 0.27 mm, validating the semi-infinite slab assumption since the foam model is 1.92 cm thick.

Ultimately, we wish to determine the magnitude of the final term on the right hand side of Eq. (3.30), repeated here:

$$\gamma = \frac{T_\infty - \bar{T}_s}{T_\infty - T_c} - \frac{\overline{q_f''}}{\bar{h}_f (T_\infty - T_c)} - \frac{\overline{h_f' T_s'}}{\bar{h}_f (T_\infty - T_c)} \quad (3.30)$$

We shall assume conservatively that  $h_f$  and  $T_s$  are always at their extremes. Using the preceding estimates for the behavior of  $h_f$  and a location where the adiabatic effectiveness varies between 0 and 0.7, we find

$$\frac{\overline{h_f' T_s'}}{\bar{h}_f (T_\infty - T_c)} \approx 0.0175 \quad (3.58)$$

<sup>f</sup> These predicted estimates of  $h$  were used in this analysis prior to execution of the present set of experiments since this analysis was essential to proper design of the experiments. Although the large parameter space of the current study resulted in wide variations in the measurements of  $h$ , it has been verified that the values of  $h$  used in this section are conservative for the purposes of this analysis. Thus no repetition of the analysis and subsequent iteration of the experimental design was necessary.

<sup>g</sup> Although the values of  $c$  given in the literature for polyurethane vary, the value used in this analysis is among the lower values yielding a more conservative (lower) value for  $C$  than would higher values of  $c$ .

This value is within the experimental uncertainty of 0.02 on measurements of  $\eta$  and represents a worst-case situation within a conservative analysis. Higher pulsation frequencies than  $\omega = 125.7$  rad/s would serve to reduce this value even further. We shall also see in Section 3.4.1.1 that the introduction of unsteady  $h$  in the analysis further reduces the error caused by the real material as opposed to the ideal  $\rho c \rightarrow \infty$  material.

### 3.4.1.1 The Influence of Unsteady Heat Transfer Coefficient

Due to the use of a constant heat transfer coefficient in the analytical model of Eq. (3.55), one may call into question the applicability of that model to determine the requirements on the wind tunnel model materials and pulsation frequency. Instead of a constant heat transfer coefficient, we now allow the heat transfer coefficient to vary sinusoidally with an arbitrary phase shift,  $\theta$ :

$$h(t) = \bar{h} + h_{fluc} \sin(\omega t + \theta) \quad (3.59)$$

The boundary condition, Eq. (3.46) may then be reposed as

$$U(X = 0, \tau) = \sin \tau + \left( \frac{C}{\frac{h_{fluc}}{\bar{h}} \sin(\tau + \theta) + 1} \right) \frac{\partial U}{\partial X} \Big|_{X=0} \quad (3.60)$$

where as before,

$$C = \frac{k}{\bar{h} \sqrt{\alpha / \omega}} \quad (3.42)$$

The analytical solution methodology used to solve the original problem with the constant heat transfer coefficient is no longer applicable. Instead, the problem was solved numerically using a time marching algorithm programmed using Matlab. We shall continue use of the value  $C = 5.85$  with  $\bar{h} = 115.5$  W/(m<sup>2</sup> K). We indicated earlier that a reasonable assumption is that the heat transfer coefficient fluctuates between 154 and 77 W/(m<sup>2</sup> K) as the jet is pulsed on and off. We find that  $h_{fluc} / \bar{h} = 0.333$  with  $h_{fluc} = 38.5$  W/(m<sup>2</sup> K). Since the maximum heat transfer coefficient is expected to coincide with the time at which the adiabatic effectiveness is at its max (coolest temperature), we shall use a phase shift of  $\theta = \pi$  rad. Figure 3.3 presents the temperature response of the surface for

the first ten cycles after initiation of the simulation starting with a uniform solid temperature equal to the average adiabatic effectiveness temperature. The surface temperature immediately biases to the negative side of the mean due to more efficient heat transfer when the adiabatic wall temperature is low than when it is high.

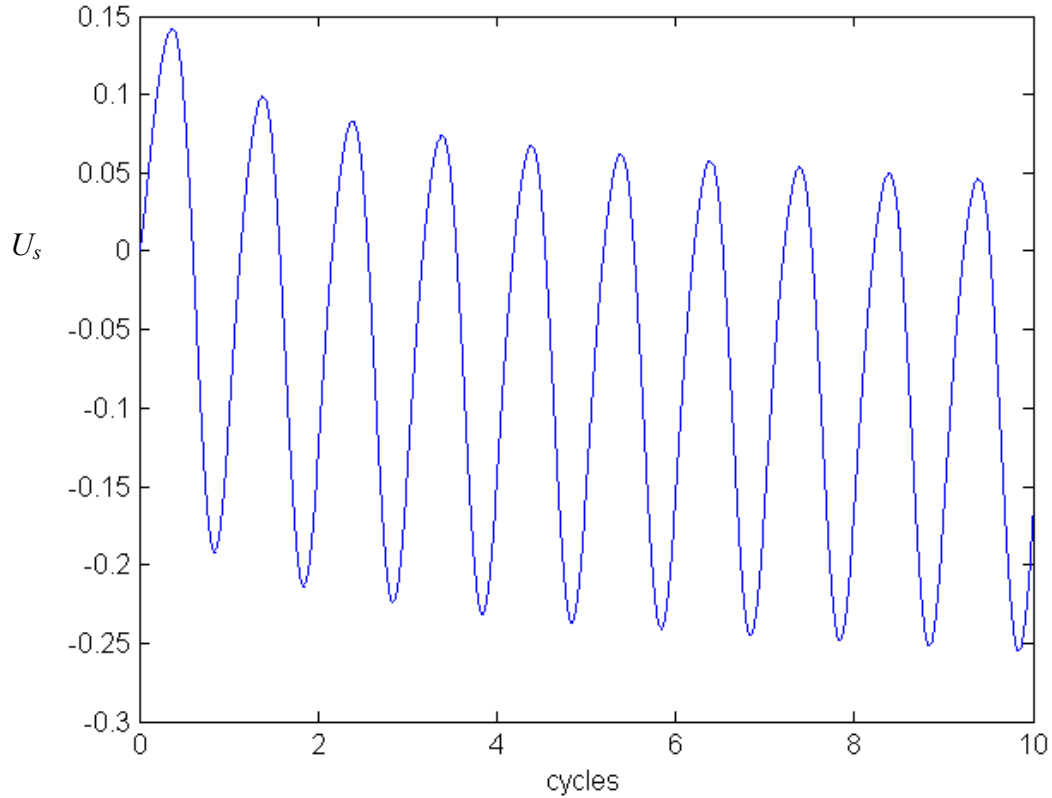


**Fig. 3.3 Temperature response at surface with no applied heat flux for  $C = 5.85$ ,  $h_{fluc}/\bar{h} = 0.333$ , and  $\theta = \pi$  rad**

The computational model was run for a total of 300 cycles at which point the temperature response had reached periodic steady state (confirmed by comparing adjacent peaks and troughs and by calculating the total heat transfer into the surface over the course of the cycle and ensuring that  $\overline{q''} = 0$ ). The average nondimensional surface temperature was computed to be  $\overline{U_{surf}} = -0.1582$  at periodic steady state as opposed to the average nondimensional adiabatic wall temperature of zero. To determine what the steady state nondimensional temperature would be for infinite  $C$ , we can write the energy balance for the surface undergoing the varying adiabatic effectiveness and heat transfer coefficient,

but with constant surface temperature. At steady state, no bulk heat transfer takes place into or out of the surface so we can write:

$$0 = \int_0^{2\pi} \left( 1 + \frac{h_{fluc}}{h} \sin(\omega t + \theta) \right) (\sin(\omega t) - U_{surf}) dt \quad (3.61)$$

We find that the nondimensional temperature of the surface with infinite  $C$  is  $U_{surf} = -0.1667$  (noting that  $U_{surf} = \overline{U_{surf}}$  in this case). The difference in  $U_{surf}$  that would be measured with the experimental model and the value that would be measured on an ideal model with infinite  $C$  is  $\Delta U_{surf} = 0.0085$ . In a location where the adiabatic effectiveness oscillates between  $0 < \eta < 0.5$ , or  $\eta_{fluc} = 0.25$ , this corresponds to an error in the measured value of  $\gamma$  of  $\varepsilon_\gamma = 0.002$ , significantly below other sources of experimental uncertainty (described in Section 4.6.4). The analysis with constant  $h$  is therefore vindicated as very conservative.

### 3.4.2. Nonzero Applied Heat Flux

The assumptions of damped surface temperature fluctuations are also required for the experiment involving heat flux at the surface to measure  $\overline{h_f}$ . It stands to reason that if the surface temperature fluctuations are sufficiently damped for the experiment without the heat flux plate, the surface temperature would also be damped for experiments involving the heat flux plate. In this section we will examine the surface temperature fluctuations with an applied surface heat flux.

Equation (3.35) provides the means for determining  $\overline{h_f}$  on a model with perfectly damped surface temperature oscillations ( $T_s' = 0$ ). In order to minimize uncertainty in the measured value of  $\overline{h_f}$  due to uncertainty in the measurement of  $\gamma$ , the coolant temperature may be set equal to the freestream temperature. For this case, but without the assumption that  $T_s' = 0$  used to arrive at Eq. (3.35), Eq. (3.34) instead becomes

$$\overline{h_f} = \frac{-\overline{q_f''}}{\overline{T_s} - T_\infty} - \frac{\overline{h_f' T_s'}}{\overline{T_s} - T_\infty} \quad (3.62)$$

We desire the second term on the right hand side of Eq. (3.62) to be negligible relative to  $\overline{h_f}$  in which limit Eq. (3.62) reduces to Eq. (3.35) with the special case of  $T_c = T_\infty$ . As a consequence of  $T_c = T_\infty$ , Eq. (3.62) has no dependence on  $\gamma$ ; however, limitations on the experimentalist's ability to maintain the coolant and freestream temperatures precisely equal will manifest themselves as experimental error. It is therefore recommended to use an equation for  $\overline{h_f}$  that incorporates  $\gamma$  such as Eq. (3.34) but with the smallest practical difference in the coolant and freestream temperatures to minimize the impact of the compounding uncertainties. Nevertheless, we shall continue our analysis of the influence of impact of surface temperature fluctuations with the  $T_c = T_\infty$  case without loss of generality for small differences in those temperatures.

We wish to understand the impact of neglecting the second term on the right hand side of Eq. (3.62) since we cannot directly measure that term with a time averaging method. The relative error in the measurement of  $\overline{h_f}$  that would occur by neglecting that term would be

$$\frac{\varepsilon_{\overline{h_f}}}{\overline{h_f}} = \frac{\overline{h_f}' T_s'}{\overline{h_f} (\overline{T_s} - T_\infty)} \quad (3.63)$$

Through comparison of Eq. (3.63) with Eq. (3.62), we can also write

$$\frac{\varepsilon_{\overline{h_f}}}{\overline{h_f}} = \frac{-\overline{q_f}''}{\overline{h_f} (\overline{T_s} - T_\infty)} - 1 \quad (3.64)$$

Because the adiabatic wall temperature is constant and equal to  $T_\infty$ , only the variable heat transfer coefficient could cause the surface temperature to fluctuate. For the purposes of our analysis, we shall let the heat transfer coefficient vary sinusoidally in time.

$$h(t) = \overline{h} + h_{fluc} \sin(\omega t + \theta) \quad (3.65)$$

Since we apply a known heat flux,  $-\overline{q_f}''$ , with a heat flux plate<sup>h</sup>, the boundary condition used in the previous analysis, Eq. (3.38), becomes

$$-\overline{q_f}'' + h(t)(T_{aw} - T_s(t)) = -k \left. \frac{\partial T}{\partial x} \right|_{x=0} \quad (3.66)$$

Otherwise, the differential equation, Eq. (3.36), remains unchanged. However, the nondimensionalized version of the differential equation necessarily differs. In Eq. (3.40) the temperature scale used previously was  $T_{fluc}$ , which has no physical meaning in the current case since  $T_{aw}$  is constant, a consequence of  $T_c = T_\infty$ . Instead, we shall nondimensionalize surface temperature using:

$$W = \frac{\overline{h}(T - T_{aw})}{-\overline{q_f}''} \quad (3.67)$$

The scales for nondimensionalizing time and distance remain unchanged from Eqs. (3.41) and (3.42), repeated here:

$$\tau = \omega t \quad (3.41)$$

$$X = \frac{x}{(\alpha / \omega)^{1/2}} \quad (3.42)$$

The differential equation in the nondimensional variables is then written,

$$\frac{\partial W}{\partial \tau} - \frac{\partial^2 W}{\partial X^2} = 0 \quad (3.68)$$

$$W(X, \tau = 0) = 0 \quad (3.69)$$

$$W(X \rightarrow \infty, \tau) = 0 \quad (3.70)$$

---

<sup>h</sup> A heat flux plate provides a constant electrical heat flux, all of which is transferred via conduction, convection, and radiation. Although thermal radiation can be significant in the energy balance, for the purpose of studying the damping effect of conduction on surface temperature fluctuations (which is desirable since we wish for  $T_s'$  to be small), thermal radiation will have the tendency provide additional damping. Neglecting thermal radiation therefore causes the analysis to be conservative. Since we neglect thermal radiation here, we can say that the heat flux out of the electrical heat flux plate is  $-\overline{q_f}''$  since the average conduction is zero once periodic steady state is reached.

$$W(X=0, \tau) = \frac{1}{\frac{h_{fluc}}{\bar{h}} \sin \tau + 1} + \left( \frac{C}{\frac{h_{fluc}}{\bar{h}} \sin \tau + 1} \right) \frac{\partial W}{\partial X} \Big|_{X=0} \quad (3.71)$$

where again,

$$C = \frac{k}{\bar{h} \sqrt{\alpha/\omega}} \quad (3.47)$$

The differential equation, (3.68) was solved numerically with the appropriate boundary conditions and the constants  $C = 5.85$  and  $h_{fluc} / \bar{h} = 0.333$  as before. The time response at the surface for the first ten cycles is plotted in Fig. 3.4.

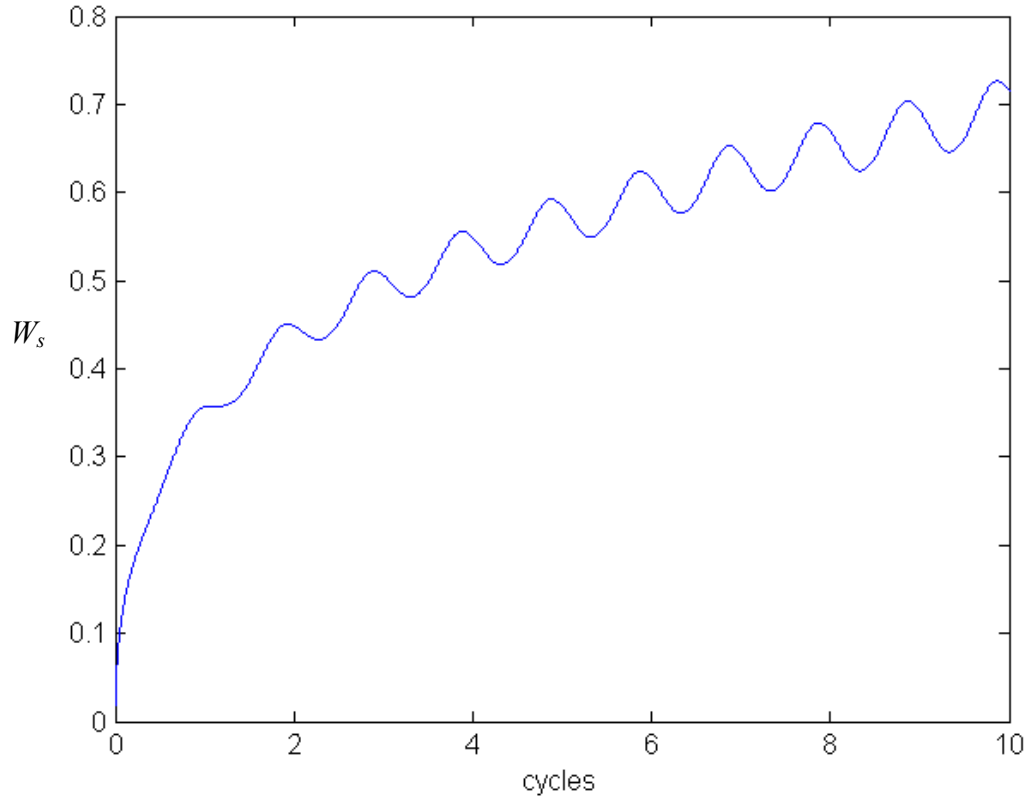


**Fig. 3.4** Temperature response at surface with nonzero applied heat flux for  $C = 5.85$ ,  $h_{fluc} / \bar{h} = 0.333$

Again, the computational model was run for a total of 300 cycles at which point the temperature response had reached periodic steady state. The final average

nondimensional surface temperature is  $\overline{W}_s = 1.007622$  with  $\max|W_s'| = 0.051406$ . Through comparison of Eq. (3.67) and (3.64), we can write

$$\frac{\overline{\varepsilon_{h_f}}}{\overline{h_f}} = \frac{1}{\overline{W}_s} - 1 = -0.0076 \quad (3.72)$$

Thus, the error in the heat transfer coefficient due to the assumption that the surface temperature is constant with the model used in the current experiments is less than 0.8%. Note that the apparent negative uncertainty in Eq. (3.72) is due to the fact that  $\overline{h_f}'T_s'$  is negative in Eq. (3.63) since when the heat transfer coefficient is elevated, the surface temperature tends to drop due to more efficient heat transfer taking place from the heat flux plate to the freestream.

It must be stressed that the experimental model analyzed here was designed such that  $C$  would be large without sacrificing small  $k$ . A model with different material characteristics or pulsing frequencies (or used with a different freestream velocity, thereby influencing the heat transfer coefficient) may not be suitable for this type of experiment.

### 3.5 The Physical Significance of the $h$ - $\eta$ Coupling Term

With a fairly exhaustive analysis of the heat transfer behavior at a surface with an oscillating convective boundary condition, we are now prepared to take another look at the net heat flux reduction equation and examine the physical significance of the coupling term found in Eq. (3.25), repeated here:

$$\overline{\Delta q_r} = 1 - \frac{\overline{h_f}}{h_0} \left( 1 - \frac{\overline{\eta}}{\phi} \right) + \frac{\overline{h_f}'\eta'}{h_0\phi} \quad (3.25)$$

In the development of (3.55), we assumed that the convective heat transfer coefficient was constant. The analytical model also assumes there is no bulk heat transfer through the material as is evident in Fig. 3.1 by the lack of thermal gradient regardless of time far into the solid (for large  $X$ ). Because there is no bulk heat transfer through the solid, the heat that is transferred into the solid during the time that the solid is cooler than the adiabatic wall temperature is offset exactly by the heat transfer out of the solid while the solid is warmer than the adiabatic wall temperature. In the limit as  $C \rightarrow \infty$ , the

surface temperature fluctuations approach zero. In the analytical model of Eq. (3.55), the constant heat transfer coefficient would cause that steady surface temperature to assume the average adiabatic wall temperature. However, in the more general case in which the heat transfer coefficient is unsteady, the surface would assume a temperature different from the average adiabatic wall temperature and this was examined in Section 3.4.1.1. This altered average surface temperature drives the conductive heat transfer into the component, thereby allowing this nondimensional temperature  $\gamma$  to be substituted directly into the original NHFR equation in place of  $\eta$  as shown in Eq. (3.31) without knowledge of  $\overline{h_f' \eta'}$ . Care must be taken to note that there is a difference between  $\gamma$  and  $\overline{\eta}$ . Unless designed such that  $T_s'$  is negligible, an experiment otherwise similar to that described here will yield neither  $\overline{\eta}$  nor  $\gamma$ . A computational simulation performed on a surface for which  $k = 0$  (implying  $C = 0$ ) can directly yield  $\overline{\eta}$ , which is of no value in determining  $\overline{\Delta q_r}$  without  $\overline{h_f' \eta'}$ .

### **3.6 Unsteady Film Cooling Behavior at Low Frequency**

Up until this point, we have examined the means by which one may measure the performance of unsteady film cooling through an experimental methodology. The complex nature of the Navier-Stokes equations generally precludes any attempt to accurately predict the performance of unsteady film cooling schemes through analytical means alone. However, this section presents a hypothesis that with existing performance data on steady film cooling, analytical predictions may be obtained for cases of low frequency unsteadiness.

With low frequency unsteadiness ( $F \ll 1$ ) and a continuous function for blowing rate as a function of time, the flow field changes slowly and is almost always at a quasi steady-state. If the blowing rate is a discontinuous function (such as a square wave), the dwell time in between step changes is much longer than the time during which the rapid transients occur. In either case, the flow transients are unimportant with  $F \ll 1$  and one must only consider the fractional time spent at each quasi-steady blowing rate. A mathematical approximation can be used to predict the performance of a low frequency

pulsed film cooling scheme using only performance data acquired with steady state film cooling. Let  $Z$  represent a parameter that is some measure of a film cooling scheme and is independent of unsteady fluctuation behavior. For example,  $Z$  may be an area averaged adiabatic effectiveness or the net heat flux reduction at a particular point of interest. If  $Z$  is known as a continuous function of steady mass flux ratio,  $M$ , for instance, the average performance with unsteady mass flux ratio,  $M(t)$ , may be obtained by averaging the performance over one cycle:

$$\bar{Z} \approx \frac{\omega}{2\pi} \int_0^{2\pi/\omega} Z(M(t)) dt \quad (3.73)$$

In the case of a discontinuous mass flux ratio, it is more convenient to use a probability density function,  $w(M)$ , that describes the fraction of time spent at each incremental mass flux ratio. The average of  $Z$  then becomes

$$\bar{Z} \approx \int_0^{\infty} w(M)Z(M)dM \quad (3.74)$$

For discontinuous blowing at  $n$  discrete blowing ratios,  $M_i$ , each with dwell time  $\Delta t_i$ ,

$$w(t) = \sum_{i=1}^n \frac{\Delta t_i}{2\pi/\omega} \delta(M - M_i) \quad (3.75)$$

where  $\delta(x)$  is the Dirac delta function,

$$\int_a^b \delta(x)dx = \begin{cases} 1, & \text{if } (a, b) \text{ contains the origin,} \\ 0, & \text{otherwise} \end{cases} \quad (3.76)$$

For the case of discrete blowing ratios, Eq. (3.74) becomes

$$\bar{Z} \approx \sum_{i=1}^n \frac{\Delta t_i}{2\pi/\omega} \delta(M - M_i)Z(M_i) \quad (3.77)$$

For the purposes of determining how much coolant is being used, the average blowing ratio is of importance:

$$\bar{M} = \frac{\omega}{2\pi} \int_0^{2\pi/\omega} M(t)dt \quad (3.78)$$

or

$$\bar{M} = \sum_{i=1}^n \frac{\Delta t_i}{2\pi/\omega} M_i \quad (3.79)$$

Neither Eq. (3.78) nor Eq. (3.79) depend on the low frequency assumption and are thus, exact equations.

An example is in order. If the film cooling is pulsed between two blowing ratios,  $M_1$  and  $M_2$  with the dwell time divided equally between the two blowing ratios, the average performance,  $\bar{Z}$ , in the  $F \rightarrow 0$  case may be calculated with Eq. (3.77).

$$\bar{Z} \approx \frac{1}{2}Z(M_1) + \frac{1}{2}Z(M_2) \quad (3.80)$$

The average blowing ratio may be calculated with (3.79).

$$\bar{M} = \frac{1}{2}M_1 + \frac{1}{2}M_2 \quad (3.81)$$

Naturally, we would like to know how  $\bar{Z}$  from Eq. (3.80) compares with the value of  $Z$  that would be obtained with steady blowing at  $\bar{M}$  from Eq. (3.81). Regardless of the relative dwell times,  $\Delta t_i$ , for the two blowing ratios  $M_1$  and  $M_2$ , the average performance,  $Z$ , would lie on a straight line segment connecting  $Z(M_1)$  and  $Z(M_2)$  as shown in Fig. 3.5. In the above example where  $\Delta t_1 = \Delta t_2 = 1/2$ , the average performance would lie in the middle of the line segment. The performance relative to the steady film cooling scheme with a blowing ratio equal to the average blowing ratio of the pulsed film cooling scheme depends on the shape of the  $Z(M)$  curve. Figure 3.5 shows two hypothetical  $Z(M)$  curves for a pair of points used in a hypothetical low frequency pulsing scheme. At  $M = \bar{M}$ , film cooling scheme *A* outperforms the pulsed scheme, but film cooling scheme *B* underperforms the pulsed scheme. It is evident that if  $Z''(M) > 0$  on  $(M_1, M_2)$ , then the pulsed scheme is superior to steady film cooling, but if  $Z''(M) < 0$  on  $(M_1, M_2)$ , then steady film cooling is superior to the pulsed film cooling scheme.

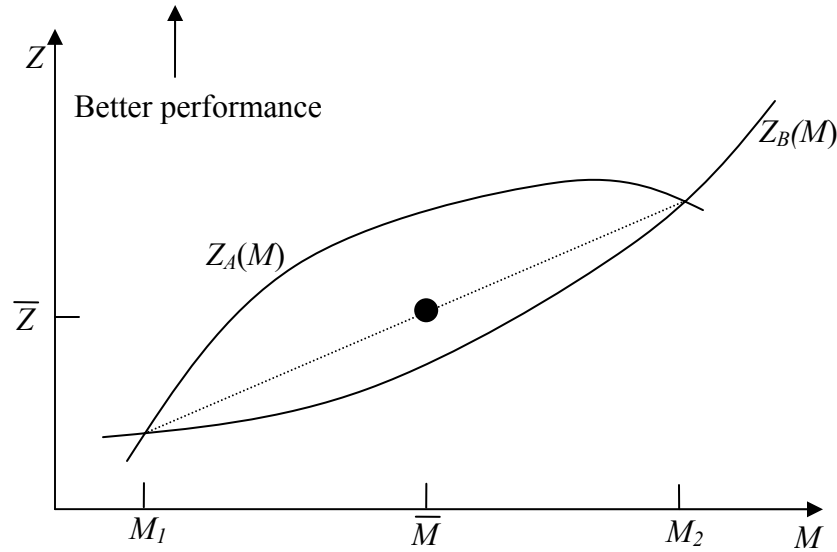


**Fig. 3.5 Two hypothetical  $Z(M)$  curves sharing a common pair of points used in a hypothetical pulsing scheme**

If the average mass flux ratio is selected to be near the optimum mass flux ratio, that is, the value of  $M$  that gives maximum  $Z$ , the  $Z(M)$  curve is likely to be concave-down ( $Z''(M) < 0$ ) due to the presence of a local maximum. Low frequency pulsed film cooling would thus be expected to yield performance inferior to steady film cooling. However, film cooling at a blowing ratio that is far from an optimum steady blowing ratio may well have  $Z''(M) > 0$  for which pulsed film cooling between two nonzero values of  $M$  may be superior to steady film cooling.

The empirical hypothesis presented in this section is tested as part of this research. The results are presented using experimental data in Section 5.3 and through computational simulations in Section 9.2.2. Interestingly, the highest frequency studied by Ekkad et al. (2006) is 20 Hz, which corresponds to a very low nondimensional frequency of  $F = 0.141$  in their experiments. Ekkad et al. (2006) reported that their results seemed to be independent of pulsing frequency. If indeed,  $F = 0.14$  is small enough that the low frequency limit is nearly reached, we would expect the average behavior of the pulsed film cooling scheme to be independent of frequency based on the conclusions of this section.

As mentioned earlier, the lowest frequency studied in the present research at model scale similar to that of Ekkad et al. (2006) is limited to 20 Hz ( $F = 0.148$ ) in order to avoid surface temperature fluctuations. In addition to the expectation that performance should be fairly frequency independent in this low  $F$  regime, we can make the case that this frequency is lower than the natural wake passage frequency in an engine. An engine operating at 10000 RPM with 30 nozzle guide vanes has a blade passage frequency of 5 kHz. The lowest frequency case studied presently of  $F = 0.148$  corresponds to approximately 3.5 kHz at engine scales, no faster than the natural unsteadiness that would occur due to wake passage.

## 4. Experimental Methodology for Leading Edge Pulsed Film Cooling Net Heat Flux Reduction

This chapter describes the methodology by which the temporally averaged net heat flux reduction due to pulsed film cooling was determined. Two sets of experiments were run to determine  $h$  and  $\gamma$  according to the theory developed in Section 3.3.

### 4.1 Leading Edge Model

The leading edge model was selected to replicate the leading edge geometry used by Ekkad et al. (2006). This leading edge design was intended to simulate a typical film cooled turbine blade leading edge. The model consisted of a half cylinder with a flat afterbody extending  $2.8 D$  downstream of the point where the cylindrical curvature meets the afterbody. The dimensions were selected such that the Reynolds number would match operating conditions ( $Re_D \approx 60000$ ) in a low speed wind tunnel. The leading edge diameter was 8.89 cm and the span was 36.35 cm. The leading edge model was 1.92 cm thick. A single 4.76 mm diameter film coolant hole was drilled in the model ( $D/d = 18.67$ ). The film cooling hole was located  $21.5^\circ$  from the stagnation line, angled  $20^\circ$  to the surface and  $90^\circ$  from the streamwise direction. Therefore, the hole length to hole diameter ratio was  $L/d = 11.79$ . The blunt afterbody extended 24.9 cm downstream of the location where the cylindrical leading edge met the flat afterbody. Figure 4.1 depicts the leading edge geometry and a cross section along the hole centerline is shown in Fig. 4.2. The plenum used to feed the coolant hole and the coolant hole itself are visible in Fig. 4.2. The coordinate system is shown in Fig. 4.3. The origin of the coordinate system is at the exit of the coolant hole, on the hole centerline. The  $x$  direction is in the downstream direction curved along the surface. The  $z$  direction is normal to the surface and the  $y$  direction is in the spanwise direction such that the coordinate system is right handed.

The leading edge model was constructed of General Plastics Last-A-Foam FR-7106, selected for its low thermal conductivity (coupled with acceptable specific heat and density to yield a sufficiently large  $C$  value as defined by Eq. (3.47)) and durability. Much of the rest of the model was constructed of Plexiglas in order to provide structural

rigidity and extra durability to the model. Additionally, the transparent Plexiglas allows for visual inspection and verification of the internal workings of the model.

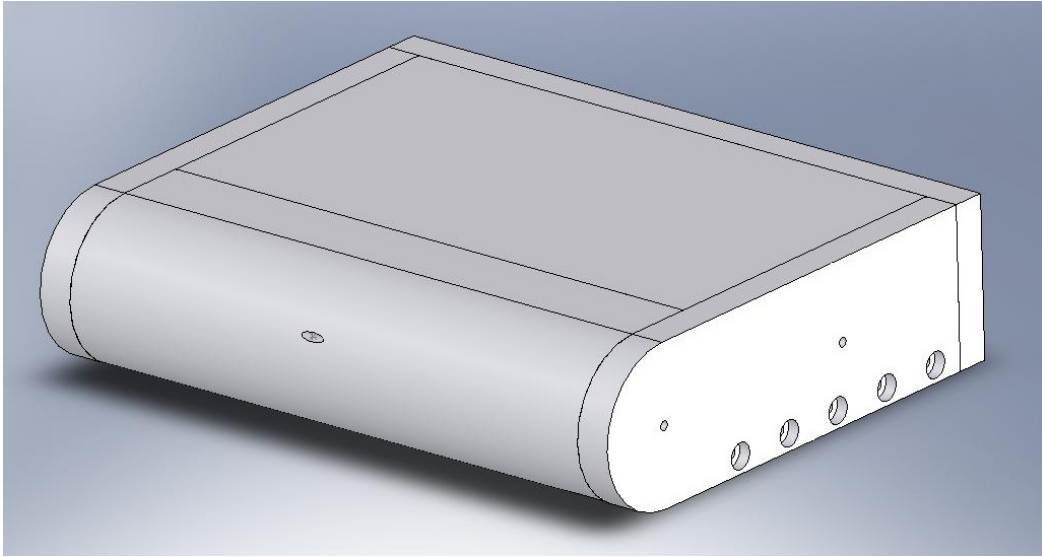


**Fig. 4.1 Leading edge model**

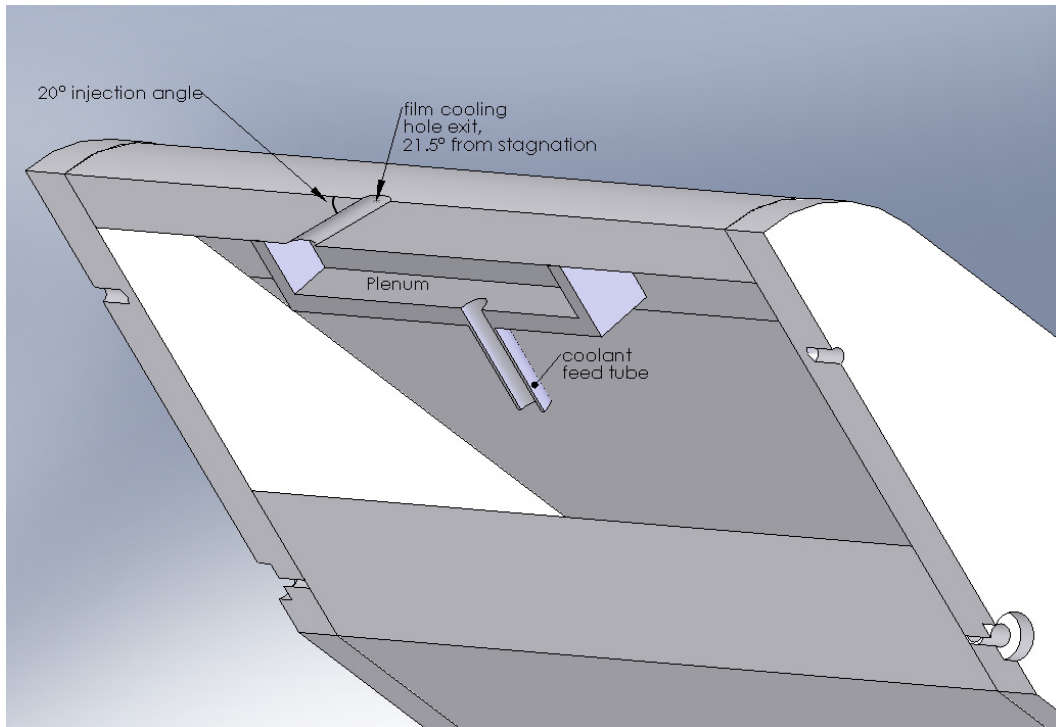


**Fig. 4.2 Leading edge model cross-section along plane oriented 21.5° from stagnation line and intersecting cylinder centerline**

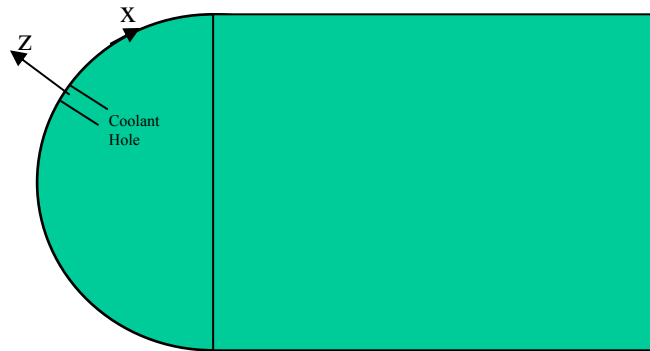


Fig. 4.3 Right handed coordinate system (y into page) (figure not to scale)

The RMS roughness of the unpainted foam was determined to be  $59 \mu\text{m}$  through the use of a Cobra Laser Profile Scanner. This is expected to yield a roughness Reynolds number of 4 in the vicinity of the hole (see Kays and Crawford (1980) for information on the roughness Reynolds number). This value is borderline between hydraulically smooth and transitionally rough, but turbulent transition is expected at approximately  $80^\circ$  from the leading edge (Incropera and DeWitt (1996)) and roughness is known to have little effect on the flow field where the boundary layer is laminar.

## 4.2 Wind Tunnel Facility

The open loop wind tunnel was powered by a single centrifugal blower, although a second blower in parallel with the first could be activated for additional flow. A butterfly valve immediately downstream of the blower was used to adjust the freestream velocity. The freestream temperature was controlled through a variable power heater immediately upstream of a cross flow heat exchanger through which chilled water may be run to provide further conditioning of the air temperature. The test section was 36.5 cm tall and 40 cm wide. The leading edge model was installed such that the spanwise direction was vertical in the tunnel. The freestream velocity at the entrance of the test section was verified with a pitot-static probe and was maintained such that the Reynolds number based on leading edge diameter was held within 2% of the desired value. At the baseline value of  $Re_D = 60000$ , the velocity was approximately 12 m/s, but depended on temperature. The rear of the model protruded approximately 2 cm from the

outlet of the wind tunnel. An open port in the test section adjacent to the model allowed IR access since the Plexiglas walls of the test section were opaque to IR wavelengths.

Four freestream conditions were used for the various experiments utilizing the wind tunnel. Freestream Reynolds numbers of  $Re_D = 60000$  and  $30000$  were used and attained by varying the freestream velocity. Two sets of turbulence characteristics were also used, termed “high” and “low.” The turbulence characteristics were varied by removing or replacing a grid made of 1.5 cm diameter rods located 1.2 m upstream of the leading edge model. The turbulence generator grid had bars spaced 6.9 cm in both the vertical and horizontal directions. The turbulence characteristics presented in Table 4.1 were measured using a hot film anemometer placed mid span 39 cm upstream of the leading edge model.

**Table 4.1 Wind Tunnel Freestream Conditions**

$Re_D$	Turbulence Condition	$Tu$ (%)	$\Lambda_f / d$
30000	Low	0.69	13
30000	High	4.7	7.7
60000	Low	0.67	24
60000	High	4.5	7.5

The film coolant was supplied to the model as shown in Fig. 4.4. The air was delivered by a compressed air system that was controlled manually through a pressure regulator upstream of an Omega FL-114 rotameter which, with knowledge of the temperature and pressure of the flow through the rotameter, provided the mass flow rate. Because the rotameter required steady flow in order to provide an accurate measurement of the flow rate, fluctuations from the pulsed solenoid valve were required to be isolated from the rotameter. For this, a sealed pressure vessel was installed between the rotameter and the solenoid valve. Although the flow out of the vessel was pulsed, the vessel had sufficient volume to attenuate pressure fluctuations within the vessel and allow essentially steady flow into the vessel. This requirement for a large volume was balanced with the requirement that the vessel be small enough that adjustments made at the pressure regulator resulted in steady state flow in a reasonable amount of time. A  $0.011 \text{ m}^3$  (3 gal) pressure vessel served as a simple pressure oscillation dampener. The volume of air within the pressure vessel was reduced further by filling the vessel with

water until approximately  $0.004 \text{ m}^3$  remained for air.<sup>i</sup> By assuming that the air acts as an ideal gas and the pressure is atmospheric in the vessel (a low, but conservative value for the purposes of this analysis), we can readily determine the amount of pressure fluctuations that would occur for a given pulsing scenario. For the worst case scenario of pulsing from a single hole at  $M = 2.0$ ,  $f = 20 \text{ Hz}$ ,  $DC = 50 \%$ ,  $Re_D = 60000$  the pressure fluctuations within the vessel would be approximately  $\pm 0.3\%$ . Since flow rate through a flow meter generally varies with the square root of the pressure difference across the flow meter, the flow rate into the vessel would vary by half of the pressure variation, or only  $\pm 0.15\%$ . The resulting nearly constant flow through the flow meter allowed for a conventional flow meter without rapid response (such as the rotameter) to be used to measure average coolant flow rate.

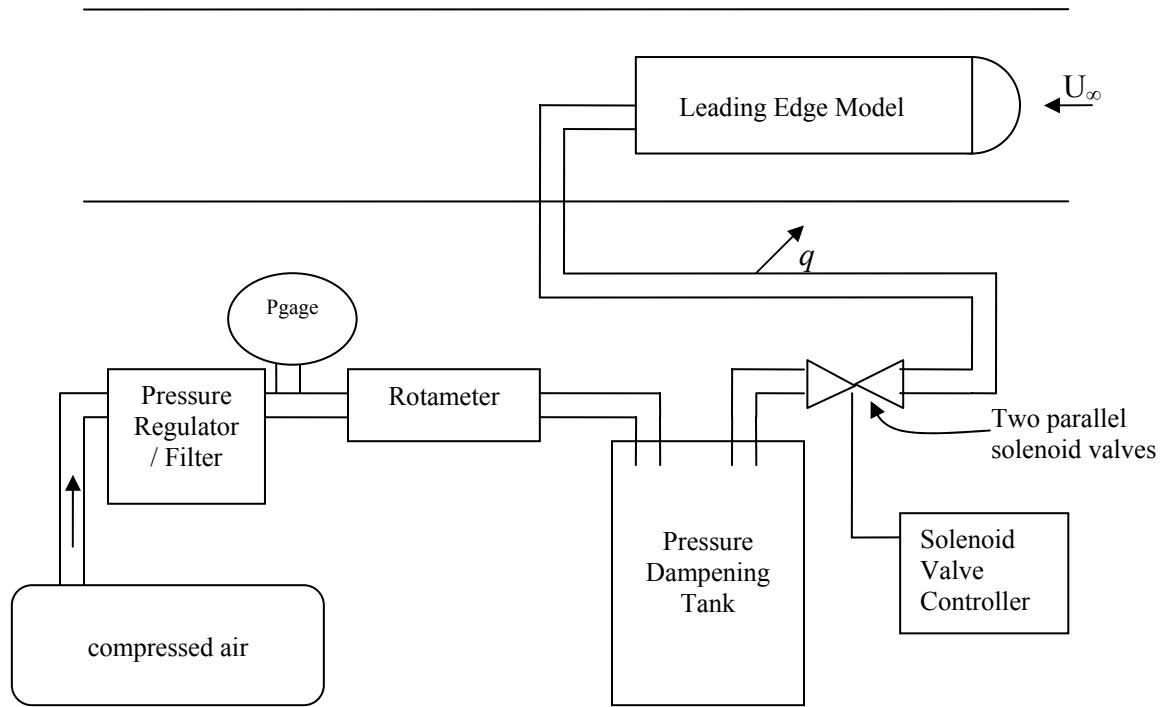


**Fig. 4.4 Schematic of Coolant Feed Line for Wind Tunnel Experiments**

Downstream of the pressure dampener, solenoid valves controlled by a Parker-Hannifin Iota One controller were used to control the pulsed coolant. The solenoid

<sup>i</sup> The water was encased in latex bladders to prevent humidification of the air as it passed through the vessel. Subsequent cooling of the air in the heat exchanger could otherwise result in frozen condensate blocking the heat exchanger.

valves were poppet valves produced by Parker-Hannifin and controlled in a binary fashion, that is, they were either “on” or “off.” Although the small size of the poppet valves allowed fast opening and closing times, the small flow area through the valves required a large pressure differential to drive the required flow through the valves. As a result, two valves were used in parallel to essentially double the flow rate for a given pressure differential.

The solenoid valves were not new when the present set of experiments began. Previous researchers including Ekkad et al. (2006) and Moore (2005) had used them for various purposes. Over time, grease and other foreign matter had accumulated inside the valves. As a result, it was evident during the experimentation that at least one of the two parallel valves was not closing completely. This behavior was confirmed during the waveform characterization (see Appendix A). Although the valve behavior was certainly off-design, this fortuitous situation actually allowed for expansion of the parameter space to include additional waveforms as it was a remarkably simple process to disassemble the valves, clean the parts, and replace the worn Teflon poppets, thereby restoring the valves to their as-new condition in which both valves closed completely. Following recharacterization of the waveforms of the flow from the reconfigured valves, additional experiments were conducted.

The coolant tubes downstream of the solenoid valves were mostly metal to minimize damping due to coolant line expansion and contraction. After passing through the pulsed solenoid valve, the coolant air was chilled or heated as necessary in a counter flow heat exchanger such that the coolant exiting the coolant hole was approximately 25 K cooler than the freestream for the unsteady coupled adiabatic effectiveness experiments, or within approximately 1 K of the freestream for the heat transfer experiments in order to mitigate uncertainty propagation of  $\gamma$  into  $\overline{h_f}$ . The second flow of the counter flow heat exchanger was pumped through a refrigerated chiller that has the option of heating the flow.

The flow entered the model through a fitting on the model’s back plate. From the back plate, the coolant was directed into a plenum that fed the coolant hole from inside the model as shown in Fig. 4.2.

### 4.3 Gamma Experiments

The gamma experiments were used to determine the spatial distributions of  $\gamma$ . The heat flux plate was not used in these experiments, but spatial temperature differences were achieved through the use of a coolant temperature that differed from the freestream temperature. Temperature differences of at least 20 K were sought to give sufficient accuracy in the infrared temperature measurements.

#### 4.3.1. Conduction Correction

Although the foam selected for the leading edge model had a thermal conductivity of only  $k=0.030$  W/(m-K), the effects of bulk conduction must be accounted since the material was not truly adiabatic. A conduction correction was employed to account for this heat transfer through the thickness of the leading edge. In the following development of the conduction correction, we first assume the coolant is steady and then consider unsteady cooling.

In the case of steady film cooling,  $\gamma = \eta$ . A one dimensional conduction correction is applied to the directly measured nondimensional wall temperature distribution,  $\gamma_{meas}$  defined as

$$\gamma_{meas} \equiv \frac{T_{\infty} - T_s}{T_{\infty} - T_c} \quad (4.1)$$

Recall that in the absence of bulk conduction,  $\gamma_{meas} = \gamma$  through comparison of Eq. (4.1) with (3.32), assuming the model was constructed with sufficiently large  $C$  and  $\overline{q_f}'' = 0$ . However, we wish to model this bulk conduction ( $\overline{q_f}''$ ) through the model.<sup>j</sup> The convective heat flux into the model balanced with the heat conducted to the inner wall of the model gives:

$$h(T_{aw} - T_s) = \frac{k}{b}(T_s - T_{wi}) \quad (4.2)$$

where  $b$  is the thickness of the foam. Solving for the adiabatic wall temperature and employing the definition of adiabatic effectiveness, Eq. (3.2), we can write:

---

<sup>j</sup> In the case of steady film cooling, bulk conduction through the solid equals the surface heat transfer since no cyclic heat transfer can occur.

$$\eta = \frac{T_{\infty} - T_s \left( \frac{k}{hb} + 1 \right) + \frac{k}{hb} T_{wi}}{T_{\infty} - T_c} \quad (4.3)$$

Define the similarly nondimensionalized internal wall temperature as

$$\theta \equiv \frac{T_{\infty} - T_{wi}}{T_{\infty} - T_c} \quad (4.4)$$

Appropriate substitution of  $\gamma_{meas}$  and  $\theta$  into Eq. (4.3) for  $T_w$  and  $T_{wi}$ , respectively yields:

$$\eta = \gamma_{meas} \frac{k}{hb} + \gamma_{meas} - \theta \frac{k}{hb} \quad (4.5)$$

Determination of the Biot number,  $\frac{hb}{k}$ , is done through the a measurement of the surface temperature with no film cooling present, but with characteristic conditions in the coolant plenum. The surface temperature on a perfectly adiabatic model would become  $T_{\infty}$  in the absence of external film cooling; however, conduction through a non-adiabatic model would result in a temperature differing from  $T_{\infty}$ . These measurements were performed each time an image was gathered by selecting a line of constant  $y$  far from the coolant hole such that this line is unaffected by film cooling. The nearly one-dimensional nature of the leading edge model allowed for this temperature distribution as a function of  $x$  to be extrapolated for all  $y$ . The one-dimensional assumption breaks down where the coolant hole is just below the surface. In this region ( $y/d > 1$ ), a temperature distribution as a function of both  $x$  and  $y$  was obtained by turning the coolant on at a blowing ratio of  $M \approx 2$  such that the coolant jet had no influence on the adiabatic effectiveness of the region  $y/d > 1$ . The temperature distribution of the surface unaffected by coolant blowing ( $T_{s0}$ ) was recorded and nondimensionalized in the usual fashion:

$$\gamma_0 \equiv \frac{T_{\infty} - T_{s0}}{T_{\infty} - T_c} \quad (4.6)$$

Without the influence of film cooling, the adiabatic wall temperature is  $T_{\infty}$  so the analog to the energy balance in Eq. (4.2) is

$$h(T_{\infty} - T_s) = \frac{k}{b}(T_s - T_{wi}) \quad (4.7)$$

Solving Eq. (4.7) for the Biot number and employing Eqs. (4.4) and (4.6) gives

$$\frac{hb}{k} = \frac{\theta - \gamma_0}{\gamma_0} \quad (4.8)$$

In Eq. (4.8) we assume that the heat transfer coefficient is influenced by a negligibly small amount by film cooling. Although we know that film cooling does change the heat transfer coefficient, the magnitude of this change is not large enough to have a significant effect on the conduction correction, particularly since the conduction correction is very small owing to the low thermal conductivity of the model material. Substitution of Eq. (4.8) into Eq. (4.5) yields:

$$\eta = \frac{\theta(\gamma_{meas} - \gamma_0)}{\theta - \gamma_0} \quad (4.9)$$

We observe that the conduction correction is linear with  $\gamma_{meas}$ , in agreement with the physics of the heat conduction. Since  $\theta$  represents the inner wall temperature, it is dependent on the internal convective heat transfer coefficient. In the limit as  $h_i \rightarrow \infty$  or  $q_{cond} \rightarrow 0$ , the internal wall temperature will assume the internal coolant temperature, thus  $\theta \rightarrow 1$ . The  $\theta = 1$  model is such that  $\eta = 1$  when  $\gamma_{meas} = 1$  since there is no conduction through the foam when the temperature is the same on both sides and  $\eta = 0$  when  $\gamma_{meas} = \gamma_0$  in accordance with the measurement of  $\gamma_0$ . A value of  $\theta < 1$  corrects the former of the two points involved in this model to account for the fact that if heat transfer through the model takes place, the temperature on the inner wall cannot be equal to the coolant temperature, thus it would be impossible for  $\gamma_{meas} = 1$ , even where  $\eta = 1$ . Measurements suggest that  $\theta \approx 0.9$  and  $\gamma_0 \approx 0.05$ . With these value, an assumption of  $\theta = 1$  would result in an error in computed adiabatic effectiveness of  $\Delta\eta \leq 0.0059$ , a small error suggesting that there is a great deal of tolerance for error in estimating  $\theta$ .

We shall now demonstrate that the preceding development of the conduction correction accounts for the third term on the right hand side of Eq. (3.27) for the general case of unsteady film cooling, repeated here:

$$\bar{\eta} = \frac{T_\infty - \bar{T}_s}{T_\infty - T_c} - \frac{\overline{h_f' \eta'}}{h_f} - \frac{\bar{q}''}{h_f(T_\infty - T_c)} - \frac{\overline{h_f' T_s'}}{h_f(T_\infty - T_c)} \quad (3.27)$$

Using

$$\bar{q}'' = \frac{k}{b}(\bar{T}_s - T_{wi}) \quad (4.10)$$

we can rewrite Eq. (3.27)

$$\bar{\eta} = \frac{T_\infty - \bar{T}_s}{T_\infty - T_c} - \frac{\overline{h_f' \eta'}}{h_f} - \frac{k(\bar{T}_s - T_{wi})}{h_f b(T_\infty - T_c)} - \frac{\overline{h_f' T_s'}}{h_f(T_\infty - T_c)} \quad (4.11)$$

or,

$$\bar{\eta} = \bar{\eta}_{meas} - \frac{\overline{h_f' \eta'}}{h_f} - \frac{\gamma_0}{\theta - \gamma_0} \cdot (\theta - \overline{\gamma_{meas}}) - \frac{\overline{h_f' T_s'}}{h_f(T_\infty - T_c)} \quad (4.12)$$

$$\bar{\eta} = \frac{\theta(\overline{\gamma_{meas}} - \gamma_0)}{\theta - \gamma_0} - \frac{\overline{h_f' \eta'}}{h_f} - \frac{\overline{h_f' T_s'}}{h_f(T_\infty - T_c)} \quad (4.13)$$

The first term on the right hand side of Eq. (4.13) is simply the temporal average of Eq. (4.9). The remaining terms account for the unsteady effects. The final term on the right hand side of Eq. (4.13) is neglected since the experiment was designed such that  $T_s'$  is negligible (which implies  $\overline{\gamma_{meas}} = \gamma_{meas}$ ). The resulting equation for  $\bar{\eta}$  is given by

$$\bar{\eta} = \frac{\theta(\gamma_{meas} - \eta_0)}{\theta - \eta_0} - \frac{\overline{h_f' \eta'}}{h_f} \quad (4.14)$$

From the definition of  $\gamma$  in Eq. (3.29), it is evident that,

$$\bar{\eta} = \gamma - \frac{\overline{h_f' \eta'}}{h_f} \quad (4.15)$$

Equations (4.14) and (4.15) are both satisfied if and only if

$$\gamma = \frac{\theta(\gamma_{meas} - \gamma_0)}{\theta - \gamma_0} \quad (4.16)$$

Therefore, the convenient technique by which conduction was accounted in Eq. (4.9) can be extended to the more general case of unsteady film cooling.

#### 4.4 Heat Transfer Experiments

The purpose of the heat transfer experiments was to determine the spatial time averaged heat transfer coefficient distribution. A known heat flux distribution was applied to the surface of the model and coolant temperature was maintained nearly equal to the freestream temperature. Measurement of the surface temperature yields the heat transfer coefficient through Eq. (3.35).

Application of a uniform heat flux distribution on a convectively cooled surface for determining the heat transfer coefficient distribution can be accomplished through the use of a electrical heat flux plate. Such a plate consists of an electrically resistive heating element with electrodes attached at two locations such that the heat flux distribution can be calculated. The heat flux plate used in this study consists of a 0.05 mm (0.002”) thick rectangular sheet of stainless steel (selected for its relatively high electrical resistivity) with copper buss bars (selected for their relatively low electrical resistivity) attached at opposing sides of the heat flux plate. An “unwrapped” drawing of the heat flux plate is shown in Fig. 4.5. The stainless steel sheet was attached to the half cylinder foam leading edge model with RTV (room temperature vulcanized) silicon. Copper buss bars were then bent to match the contour of the model and electrical connectors were soldered to the ends of the buss bars. Since the foam model was incompatible with the high temperatures required for soldering, the buss bars were not soldered to the stainless steel heat flux plate.<sup>k</sup> Instead, the bars were attached using a two component conductive epoxy filled with silver. This epoxy (product 40-3900 from “Epoxies, Etc...”) has a documented resistivity of  $1 \times 10^{-4} \Omega\text{-cm}$ , a tensile strength of  $6.52 \times 10^7 \text{ Pa}$ , and an operating temperature range of -50 to 170 °C. These properties make this epoxy an excellent substitute for solder for this application.

---

<sup>k</sup> An alternative is to solder the buss bars to the heat flux plate prior to bonding to the foam model; however, difficulties were encountered in accurately matching the contour of the foam, particularly since the assembly cannot be bent after soldering without wrinkling the heat flux plate. Furthermore, the harsh soldering operation itself can damage the heat flux plate.

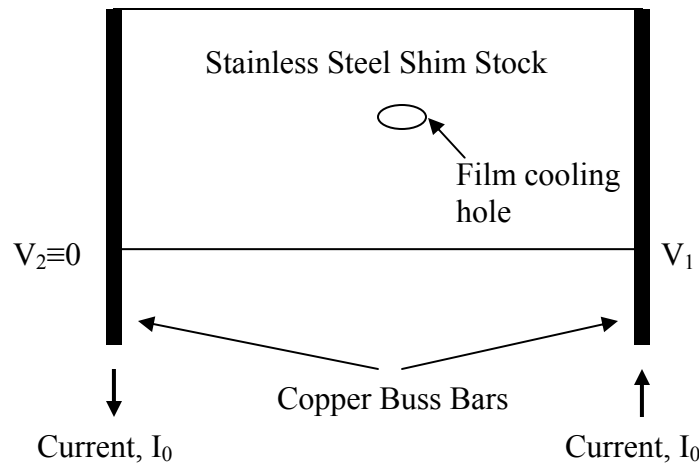


**Fig. 4.5 Heat flux plate schematic (not to scale)**

The low resistance copper buss bars with large cross section maintained a nearly uniform voltage across the stainless steel so that there was nearly uniform, one-dimensional current density within the stainless steel. A rigorous analysis of what is meant by “nearly uniform” in the preceding sentence is presented in Section 4.4.1. A measurement of the current through the heat flux plate along with knowledge of the behavior of the resistance of the heat flux plate with temperature allowed accurate determination of the power generated by the heat flux plate. Dividing that power by the surface area of the heat flux plate yielded the heat flux.

A necessary, but inconvenient, complication is the requirement of a film cooling hole through both the heat flux plate and the foam. The hole was burned through the assembly using a pulsed laser, selected in lieu of a drill for its ability to match cut the hole without damaging the heat flux plate adjacent to the hole. Section 4.4.2 discusses the complications that arise in calculation of the heat transfer coefficient due to the hole’s influence on the current density.

#### **4.4.1. Buss Bar Voltage Drop Analysis**

It is necessary to prove that the voltage drop along the length of each buss bar was negligible. The voltage drop along a buss bar can be expressed as:

$$\frac{\partial E}{\partial x} = \frac{I\mathfrak{R}_b}{A} \quad (4.17)$$

where  $\mathfrak{R}_b$  is the electrical resistivity of the buss bar material and  $A$  is the cross-sectional area of the buss bar. We begin the analysis by assuming that the current in the stainless steel is uniform, such that the axial current,  $I$ , through the buss bar decreases linearly to zero at the end of the buss bar ( $x = L$ ). The differential equation may then be expressed as:

$$\int_{E_1}^{E_2} dV = \int_0^L \frac{\mathfrak{R}_b}{A} \left( I_0 - \frac{I_0 x}{L} \right) dx \quad (4.18)$$

$$E_2 - E_1 = \frac{\mathfrak{R}_b I_0 L}{2A} \quad (4.19)$$

With a  $b = 0.05$  mm thick stainless steel heat flux plate that is 26.2 cm long and 14.0 cm wide, the voltage drop along a buss bar (of thickness 0.82 mm (1/16”) and width 12.7 mm (0.25”) would be 0.460% of the voltage drop across the heat flux plate using Eq. (4.19). The assumption that the current is uniform is actually a conservative one. The voltage variation along the buss bars would be symmetric and would result in the current density in the heat flux plate being greater in the vicinity of where the buss bars initially meet the heat flux plate than at the ends of the buss bars. This would result in less current through the buss bar than predicted in the preceding analysis with the linearly decreasing current along the length of the buss bar. This lower current would result in less voltage drop per Eq. (4.17). Indeed, an iterative analysis using the aforementioned technique could be used to refine the estimate of the voltage drop, assuming that the current flow is one-dimensional in the heat flux plate. Alternatively, a differential equation can be written to model this situation:

$$-\frac{A}{\mathfrak{R}_b} \frac{\partial^2 E}{\partial x^2} = \frac{(V_1 - 2E)b}{\mathfrak{R}_{HFP}L} \quad (4.20)$$

The solution to Eq. (4.20) is omitted here for brevity. Using the same parameters as used in Eq. (4.19) above, the voltage drop then becomes 0.457% of the average voltage drop across the heat flux plate. This is in excellent agreement with the assumption of uniform current—a consequence of nearly uniform current. Using the

0.457% figure, we can calculate that the difference in ohmic heating from one end of the heat flux plate to the other varies 1.8% using the one dimensional electrical conduction model. Due to two dimensional thermal conduction at the edges of the heat flux plate, 3 cm wide regions at each side of the heat flux plate are not used in the data analysis; a 14 cm wide heat flux plate as used in this analysis would have an 8 cm wide usable region in the center over which the ohmic heating would vary only 1.04%, again using the conservative one dimensional electrical conduction assumption. In our case, this region corresponds approximately to the surface of the quarter cylinder from the stagnation line to the interface of the cylindrical section with the flat afterbody. The ohmic heating would vary at most 0.52% from the mean value calculated assuming uniform voltage distribution along the buss bars. The ignored two dimensional electrical conduction effects provide even greater uniformity of the current density. Based on this analysis, we shall henceforth assume that voltage is constant along the buss bars.

#### **4.4.2. Nonuniform Current Density Considerations**

One of the arguments against the use of heat flux plates (thereby an argument for the use of transient heat transfer experiments or use of the mass transfer analogy) is the supposed difficulty of obtaining heat transfer coefficient data close to a hole. A heat flux plate with a hole cut out of it has a nonuniform heat flux distribution due to nonuniform current density in the vicinity of the hole. However, successful determination of the heat transfer coefficient does not depend on a uniform heat flux distribution, but rather a *known* heat flux distribution. In academic problems, we typically calculate heat transfer coefficients for two boundary conditions, the uniform temperature boundary condition and the uniform heat flux boundary condition. We recognize that the heat transfer coefficients obtained through those two boundary conditions differ due to the differing growth of the thermal boundary layers. On an actual turbine component, we expect neither boundary condition to be enforced. Thus, the experimentalist must select among imperfect boundary conditions that will still give meaningful results. A heat flux plate with a hole in it gives one such boundary condition, a nonuniform, but calculable, constant heat flux distribution. In Sections 4.4.2.1 and 4.4.2.2 we examine two

techniques that may be used to calculate an acceptable heat flux for the determination of the heat transfer coefficient in the vicinity of a hole cut in a heat flux plate.

#### 4.4.2.1 Local Current Density Calculation Method

Consider an “electrical region” defined as a mathematical surface that moves in such a way that no charge, or electrons, can cross the surface. The component of the surface’s velocity tangent to the surface is irrelevant, but for mathematical simplicity let us further define the surface’s velocity as equal to the velocity of the charge everywhere along the surface. Since electrons are neither created nor destroyed in our classical model, the charge in the electrical region must be constant. That is,

$$\frac{\partial}{\partial t} \int_{ER} q dV = 0 \quad (4.21)$$

where  $q$  is the charge density. Utilizing Leibnitz’s theorem, we can bring the time derivative inside the integral.

$$\int_{ER} \frac{\partial q}{\partial t} dV + \int_{ER} q w_i n_i dA = 0 \quad (4.22)$$

where  $w_i$  is the velocity of the surface defining the electrical region and  $n_i$  is the unit normal vector pointing outward from the surface. By the definition of the electrical region,  $w_i$  is also the velocity of the charge. The charge per unit volume,  $q$ , multiplied by the velocity of the charge,  $w_i$ , is the charge flux, also known as the current density,  $\hat{I}$ . The divergence theorem (Gauss’s theorem) allows us to convert the surface integral into a volume integral.

$$\int_{ER} \frac{\partial q}{\partial t} dV + \int_{ER} \frac{\partial \hat{I}_i}{\partial x_i} dV = 0 \quad (4.23)$$

$$\int_{ER} \left( \frac{\partial q}{\partial t} + \frac{\partial \hat{I}_i}{\partial x_i} \right) dV = 0 \quad (4.24)$$

Since the boundaries of the electrical region are selected arbitrarily, the only way for the above equation to be true is for the integrand to be zero:

$$\frac{\partial q}{\partial t} + \frac{\partial \hat{I}_i}{\partial x_i} = 0 \quad (4.25)$$

For a steady state situation as we have with a constant heat flux plate, the time derivative goes to zero and we are simply left with

$$\frac{\partial \hat{I}_i}{\partial x_i} = 0 \quad \text{or} \quad \nabla \cdot \hat{\mathbf{I}} = 0 \quad (4.26)$$

The relationship between voltage across a resistor and the current through the resistor is  $E = IR$ . This well-known equation is simply the one dimensionally integrated form of the more general equation,

$$-\frac{\partial E}{\partial x_i} = \hat{I}_i \mathfrak{R} \quad (4.27)$$

or

$$\hat{I}_i = -\frac{1}{\mathfrak{R}} \frac{\partial E}{\partial x_i} \quad (4.28)$$

where  $\mathfrak{R}$  is the electrical resistivity of the material. Above, we found that the divergence of the current density must be zero, thus for uniform electrical resistivity we can write

$$\frac{\partial}{\partial x_i} \frac{\partial}{\partial x_i} E = 0 \quad \text{or} \quad \nabla^2 E = 0 \quad (4.29)$$

Similar to the familiar equation for the power (heat) dissipated by a one dimensional resistor,  $q = I^2 R$ , the general equation for volumetric power density is

$$q''' = \hat{I}_i \hat{I}_i \mathfrak{R} \quad (4.30)$$

or

$$q''' = \frac{1}{\mathfrak{R}} \frac{\partial E}{\partial x_i} \frac{\partial E}{\partial x_i} \quad (4.31)$$

For the special case of two-dimensional heat flux plate, the heat flux becomes

$$q'' = \frac{b}{\mathfrak{R}} \frac{\partial E}{\partial x_i} \frac{\partial E}{\partial x_i} \quad (4.32)$$

where  $b$  is the thickness of the plate.

In summary, to determine the spatial heat flux distribution on a heat flux plate, one must solve the equation

$$\nabla^2 E = 0 \quad (4.33)$$

For the boundary conditions,  $E$  is known at either end of the heat flux plate (where the buss bars are located) and there is no current normal to the edges of the plate at the edges of the plate. That is,

$$n_i \hat{I}_i = 0 \quad (4.34)$$

By Eq. (4.28),

$$n_i \frac{\partial E}{\partial x_i} = 0 \quad (4.35)$$

Heat flux is then determined by

$$q_{elec}'' = \frac{b}{\mathfrak{R}} \frac{\partial E}{\partial x_i} \frac{\partial E}{\partial x_i} \quad (4.36)$$

$$q_{elec}'' = b \hat{I}_i \hat{I}_i \mathfrak{R} \quad (4.37)$$

$$q_{elec}'' = \frac{b}{\mathfrak{R}} \frac{\partial E}{\partial x_i} \frac{\partial E}{\partial x_i} \quad (4.38)$$

Not only are these equations simple to solve numerically, but the thermal engineer already has the code available to solve them. There is a direct analogy between these equations and the equations that describe steady state heat flow in a medium of constant, uniform, and isotropic thermal conductivity. Equation (4.28) is analogous to the thermal diffusion equation,

$$q_i'' = -k \frac{\partial T}{\partial x_i} \quad (4.39)$$

and Eq. (4.33) is analogous to the equation for the temperature distribution in a medium with steady state heat transfer with constant, uniform, and isotropic thermal conductivity.

$$\nabla^2 T = 0 \quad (4.40)$$

The current density is analogous to the thermal heat flux and temperature is analogous to voltage. Post-processing can be used to determine the  $q_{elec}''$  distribution.

Just as the equation used in the thermal analog equation assumes uniform (temperature independent) thermal conductivity, use of this method requires uniform (temperature independent) electrical resistivity. By Eq. (4.38), the electrical heat flux is

proportional to the square of the voltage gradient and inversely proportional to the local resistivity. Employing the one dimensional current flow assumption in which there are no lateral voltage gradients, a region of elevated electrical resistivity will have a depressed electrical heat flux directly proportional to the increase in electrical resistivity. The stainless steel producer, Allegheny Ludlum (1998) gives the electrical resistivity of type 301 stainless steel (like that used as the heat flux plate in the present study) as  $72 \times 10^{-6} \Omega\text{-cm}$  at  $20^\circ\text{C}$  and  $78 \times 10^{-6} \Omega\text{-cm}$  at  $100^\circ\text{C}$ . Additional resistivities given at higher temperatures suggest that in the range from  $20^\circ\text{C}$  to  $100^\circ\text{C}$ , the electrical resistivity varies nearly linearly, with only a slightly increasing rate with temperature. With temperatures typically ranging from 20 K across the heat flux plate, the electrical resistivity and therefore the electrical heat flux would thus be expected to vary  $\pm 1\%$ . If the current patterns were unaffected by this small nonuniformity in resistivity, the heat flux would thus vary  $\pm 1\%$ . However, regions of higher resistivity will generally have slightly lower current density than expected with the uniform resistivity model if a lower resistivity path is available. Due to the very small amount of nonuniformity in the resistivity and the competing effects of it on the heat flux, the resistance is assumed to be uniform for the purposes of this study.

The heat transfer / electrical current analogy was used to calculate the electrical heat flux distribution on the heat flux plate used in the present experimental regimen. COSMOS Works 2006 was used to numerically solve for the temperature distribution in the heat flux plate with the buss bars replaced by uniform and constant temperature boundary conditions. Through the analogy, the heat flux was converted to electrical current through the use of a Matlab script. This Matlab script further calculated the electrical heat flux distribution through knowledge of the current through the heat flux plate and the voltage drop across the heat flux plate. The ratio of the electrical heat flux to the average heat flux was then calculated.

The actual local electrical heat flux calculated with this technique was used in the steady form of Eq. (3.1) applied spatially to determine the true spatial  $h$  distribution. The relative heat fluxes at  $y/d$  locations of 0 and 2 are shown in Fig. 4.6. Along  $y/d = 0$ , the relative heat flux increases to 1.8 as the flow approaches the edge of the coolant hole.

This is a consequence of the convergence of the current streamlines as the current is forced to go around the coolant hole. At  $x/d = -0.5$ , the heat flux suddenly drops to zero due to the absence of electrical heat flux in the coolant hole. The symmetry of the current lines around the coolant holes causes the trend to reverse as the flow crosses over the coolant hole. At  $y/d = 2$ , just adjacent to the coolant hole, the heat flux reduces as the flow approaches  $x/d = 0$  and increases again for positive  $x/d$ . Exercising the analogy between the current flow and inviscid fluid flow, we may say that the drop in heat flux is a consequence of the proximity to a stagnation point.

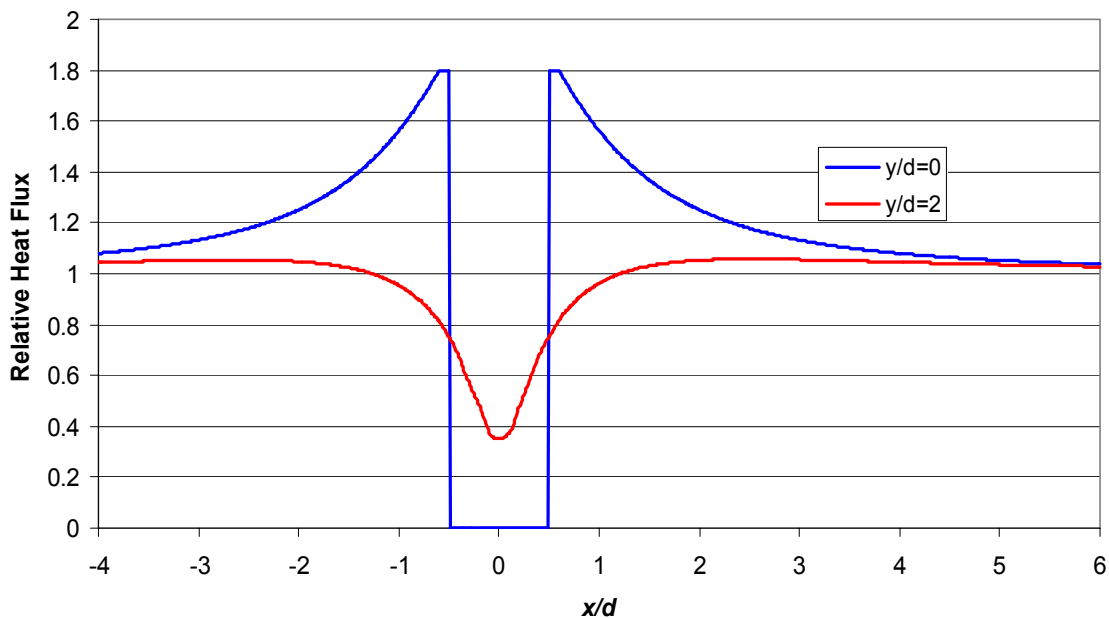


Fig. 4.6 Electrical heat flux relative to average heat flux at  $y/d = 0$  and 2

This local heat flux method was tested on the leading edge geometry described in Section 4.1, with the lone exception that the coolant hole was covered with Kapton tape. The covered hole eliminated the hydrodynamic influence of the hole on the heat transfer coefficient, thus if the heat flux were uniform, there would have been no spanwise variation in the measured heat transfer coefficient. Figure 4.7 demonstrates the spanwise nonuniformity in the Frössling number that develops as a result of the nonuniform heat flux in the vicinity of the coolant hole. At  $y/d = 0$ , the Frössling number increases as the flow approaches the coolant hole at  $x/d = -0.5$ . This is due to the rapid increase in heat flux (as shown in Fig. 4.6), but without a commensurate increase in surface temperature.

The lack of increase in the surface temperature is due to the thinner thermal boundary layer at this point than would have existed if the upstream region had a higher and uniform relative heat flux of 1.8. The surface temperature necessarily lags behind rapid changes in heat flux due to the time it takes to develop a thermal boundary layer consistent with the new heat flux. Likewise, at  $y/d = 2$ , the  $Fr$  number drops as the flow nears the coolant hole due to the lower heat flux in that vicinity (see Fig. 4.6) without a commensurate decrease in surface temperature. In this region, the thermal boundary layer is thicker than would exist if the heat flux had been lower and uniform upstream of this region ( $x/d = 0, y/d = 2$ ).

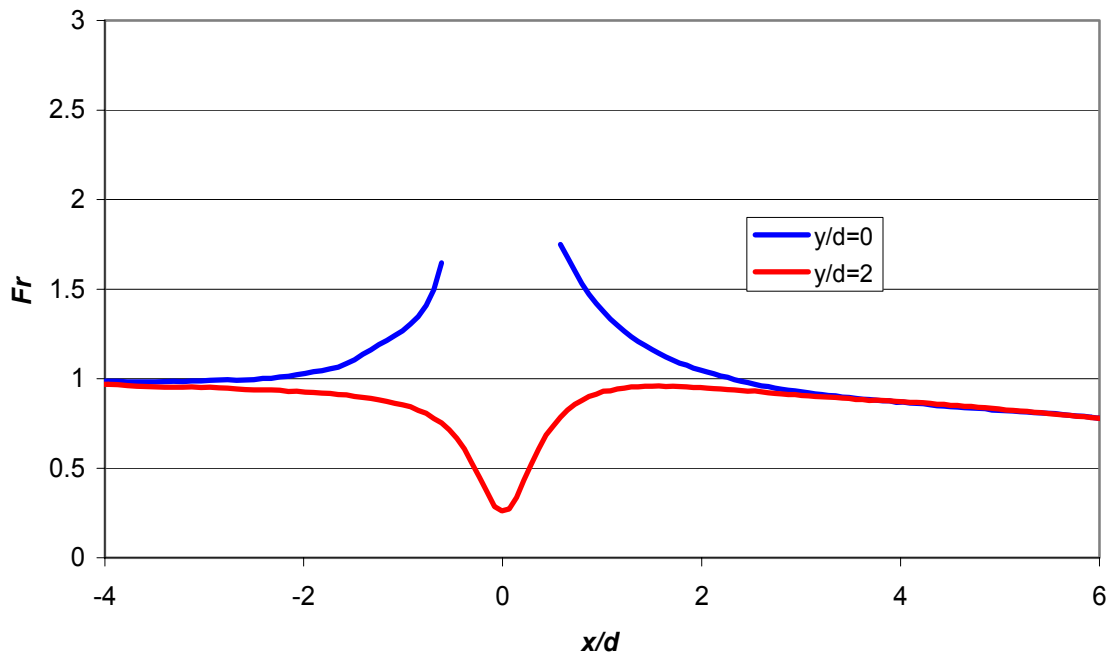


Fig. 4.7 Frössling number distributions attained using local heat flux method and hole covered; low turbulence,  $Re_D = 60k$

#### 4.4.2.2 The Uniform Heat Flux Correction Method

Although Fig. 4.7 does depict true Frössling number distributions, the local heat flux method has limited utility for determining the influence of film cooling because of the ambiguity of whether an effect on  $Fr$  is caused by hydrodynamic effects or the nonuniform heat flux. We thus seek an alternate technique that yields an effective heat

transfer coefficient uniform in the spanwise direction when hydrodynamic effects of the hole in the heat flux plate are not present.

Mick and Mayle (1988) measured heat transfer coefficients in the vicinity of coolant holes by using a heat flux plate with holes cut directly in it. The heat flux was determined using data from two non-film-cooled experiments prior to the actual experiment with film cooling. The first experiment measured the temperature distribution occurring on a model covered in a heat flux plate without holes. The second experiment repeated the first with the exception of holes in the heat flux plate, but no holes in the substrate. Temperature data from the first experiment was used to calculate the heat transfer coefficient distribution with the known applied heat flux through Eq. (3.1). The heat transfer coefficient distribution from the first experiment was assumed to apply to the second experiment since the geometry was unchanged. The temperature data from the second experiment along with the recently calculated heat transfer coefficient allowed the researchers to calculate the heat flux distribution on the heat flux plate with the holes, again through Eq. (3.1).

An adaptation of the technique of Mick and Mayle (1988) was ultimately used for the experimental results presented in this document. The data acquired for Fig. 4.7 (with the coolant hole covered with Kapton tape) was used to calculate a spatial distribution of factors that can be multiplied by the average electrical heat flux to yield the Frössling number as a function only of  $x$  acquired far from the coolant hole, where virtually no current nonuniformity was present. Essentially, a true Frössling number distribution was acquired along a line of constant  $y$  far from the coolant hole where the heat flux was uniform. At any other location (particularly those in the vicinity of the cooling hole), the spatial average of the heat flux was multiplied by a factor that such that the calculated Frössling number matches that at the same  $x/d$  location far from the coolant hole

#### **4.4.3. Data Reduction Procedure**

By measuring the electrical current through the heat flux plate, the total heat flux out of the plate was determined. The total heat flux was divided by the area to yield the average heat flux. The spatial heat flux factor distribution described in Section 4.4.2.2 was used to account for the nonuniform heat flux in the vicinity of the coolant hole. The

heat transfer out of the plate occurred by means of convection, conduction, and radiation. In order to determine the convection heat transfer coefficient,  $h$ , the amount of convection heat transfer was required. At steady state, conservation of energy dictates the following:

$$-q''_{convection} = -q''_{total} - q''_{conduction} - q''_{radiation} \quad (4.41)$$

This section describes how  $q''_{conduction}$  and  $q''_{radiation}$  were determined.

A one-dimensional cylindrical conduction model was used to calculate the loss of heat through the foam substrate. Lateral temperature gradients were negligible for conduction purposes except at the edges of the heat flux plate. Rutledge (2004) used a similar heat flux plate, but with higher thermal conductivity foam, and found that a one-dimensional conduction model was within 10% of a multi-dimensional model everywhere within 1.5 cm of the edges. In the present set of experiments, conductive heat loss was less than 2% of the applied electrical heat flux, so a 10% error in estimation of the conductive heat loss would only correspond to a 0.2% error in determination of the convective heat flux.

The one dimensional model used the 0.030 W / (m K) thermal conductivity of the General Plastics Last-A-Foam as reported by General Plastics along with the known outside surface temperature. Because high resolution internal surface temperature data was unavailable, this temperature was estimated through a heat conduction analysis. We can write the equations that govern the conduction heat transfer through the cylindrical foam model by balancing the conduction with the internal convection.

$$q''_{cond} = \frac{k}{r_o \ln \left( \frac{r_o}{r_i} \right)} (T_s - T_{si}) = h_i (T_{si} - T_c) \quad (4.42)$$

From this relation we can find an expression for the inner surface temperature.

$$T_{si} = \frac{\frac{k}{r_o \ln\left(\frac{r_o}{r_i}\right)} T_s + hT_c}{h_i + \frac{k}{r_o \ln\left(\frac{r_o}{r_i}\right)}} \quad (4.43)$$

Substitute this expression for the inner surface temperature into the conduction equation from Eq. (4.42).

$$q''_{cond} = \frac{k}{r_o \ln\left(\frac{r_o}{r_i}\right)} \left( T_s - \frac{\frac{k}{r_o \ln\left(\frac{r_o}{r_i}\right)} T_s + hT_c}{h_i + \frac{k}{r_o \ln\left(\frac{r_o}{r_i}\right)}} \right) \quad (4.44)$$

Algebraic manipulation gives the following:

$$q''_{cond} = \frac{k}{r_o \ln\left(\frac{r_o}{r_i}\right)} \left( \frac{h_i}{h_i + \frac{k}{r_o \ln\left(\frac{r_o}{r_i}\right)}} \right) (T_s - T_c) \quad (4.45)$$

Through comparison of Eq. (4.45) with Eq. (4.42), we can see that

$$\frac{h_i}{h_i + \frac{k}{r_o \ln\left(\frac{r_o}{r_i}\right)}} = \frac{(T_s - T_{si})}{(T_s - T_c)} \quad (4.46)$$

In order to determine this quantity, two thermocouples were placed on the internal surface in order to characterize the internal surface temperature during the experiments.

The quantity  $\frac{h_i}{h_i + \frac{k}{r_o \ln\left(\frac{r_o}{r_i}\right)}}$  was determined to be approximately 0.86 (for which

$$h_i \approx 7 \text{ W}/(\text{m}^2 \text{ K}).$$

The radiation correction employed the assumption that both the heat flux plate and the walls of the tunnel were diffuse gray surfaces. Conveniently, the Plexiglas walls had approximately the same emissivity as the flat black paint ( $\varepsilon \approx 0.95$ ) covering the heat flux plate. The walls of the tunnel were assumed to have a uniform temperature equal to that of the freestream. These assumptions were verified experimentally.

With the preceding assumptions, the local radiation heat transfer out of the heat flux plate may be written:

$$q''_{rad} = \varepsilon\sigma(T_s^4 - T_\infty^4) \quad (4.47)$$

where the  $T_s$  is the local surface temperature on the heat flux plate. The maximum heat loss due to radiation was approximately 10% of the electrical heat flux.

Having compensated the measured electrical heat flux for conduction and radiation, we know the actual convective heat flux through Eq. (4.41). The resulting surface temperature was measured and nondimensionalized to form  $\lambda$ , from which the convective heat transfer coefficient was calculated through Eq. (3.35), repeated here:

$$\overline{h}_f = \frac{-\overline{q}_f''}{(T_\infty - T_c)(\gamma - \lambda)} \quad (3.35)$$

As discussed in Section 3.3, the denominator does not approach zero as  $T_c \rightarrow T_\infty$ . Instead, it simply decreases the dependence of the calculated value of  $\overline{h}_f$  on the measured value of  $\gamma$ . In fact,  $T_c$  and  $T_\infty$  were maintained within 1 K of each other in the  $\overline{h}_f$  experiments to minimize uncertainty propagation.

#### **4.5 Spanwise and Area Averaging of the Net Heat Flux Reduction and Heat Transfer Coefficient Ratios**

Although measurements of  $\gamma$  and  $h$  are inherently spatial, the presentation of the data was often facilitated through the use of spanwise or area averaging. The area used for area averaging has a spanwise extent of  $-5.57 < y/d < 2.29$  (for a spanwise length of  $7.86d$ ) and a streamwise extent from  $0.5 < x/d < 9.5$ .<sup>1</sup> The spanwise extent of the

<sup>1</sup>The flat afterbody began at  $x/d \approx 10$  and this flat afterbody does not replicate actual turbine geometry.

region was selected to approximately match the spacing of the holes on a typical airfoil. Additionally, due to the occasionally high spanwise penetration of the jet in the negative  $y$  direction at high blowing ratios, the region was selected to be off-center from the hole in order to accurately capture the effects of the jet. The same spanwise extent was used for data that was spanwise averaged alone. The streamwise length extends from the downstream edge of the hole at  $x/d = 0.5$  to an  $x$  location that is near the end of the curvature of the half cylinder leading edge model.

Simple spanwise averaging of the net heat flux reduction data would yield an average of a fractional (or percent) change, which is not a useful parameter. As an illustration, consider the hypothetical film cooled and non-film cooled heat fluxes at two discrete points as shown in Table 4.2. Although film cooling influences the heat flux at each point, the average heat flux is the same with and without film cooling, that is, 3 units of heat flux. The average of the fractional changes, however, results in an average  $\Delta q_r = -0.25$ . The implication of this result reported without the raw data is that film cooling caused a 25% increase in the average heat transfer—clearly not so.

**Table 4.2 Illustration of Pitfall with Spanwise Averaged NHFR**

<i>Point</i>	$q_0$ "	$q_f$ "	$\Delta q_r$
A	2	4	-1
B	4	2	0.5
<b>Mean</b>	<b>3</b>	<b>3</b>	<b>-0.25</b>

A more useful parameter in lieu of an average of a percent change would be the percent change of an average. In the example of Table 4.2, the desired result would be zero, since the average heat flux was unchanged by film cooling. Since we frequently desire results that are indicative of performance at a particular streamwise position on a turbine component that averages the performance in the spanwise direction, we shall define the net spanwise heat flux reduction,  $\Delta q_{r,span}$  as

$$\Delta q_{r,span} = 1 - \frac{\int_{-\Delta y}^{\Delta y} q_f dy}{\int_{-\Delta y}^{\Delta y} q_0 dy} \quad (4.48)$$

With unsteady film cooling, Eq. (4.48) becomes,

$$\overline{\Delta q_{r,span}} = 1 - \frac{\int_{-\Delta y}^{\Delta y} (\overline{h_f}(\phi - \overline{\eta}) - \overline{h_f} \overline{\eta'}) dy}{\int_{-\Delta y}^{\Delta y} h_0 \phi dy} \quad (4.49)$$

Throughout this document, whenever we seek a spanwise averaged reporting of a spatial ratio, we use this technique of spanwise averaging the components of the ratio prior to taking the ratio. For example, in the case of spanwise averaged reporting of the heat transfer coefficient augmentation,  $h_f / h_0$ , we use the appropriate adaptation of Eq. (4.48):

$$\frac{h_f}{h_{0,span}} = 1 - \frac{\int_{-\Delta y}^{\Delta y} h_f dy}{\int_{-\Delta y}^{\Delta y} h_0 dy} \quad (4.50)$$

The same averaging principle is employed for area averaging. For area averaging, the integrals in Eq. (4.50) become simply become double integrals, integrating over the area of interest as in:

$$\Delta q_{r,area} = 1 - \frac{\int_{-\Delta x}^{\Delta x} \int_{-\Delta y}^{\Delta y} q_f dy dx}{\int_{-\Delta x}^{\Delta x} \int_{-\Delta y}^{\Delta y} q_0 dy dx} \quad (4.51)$$

## 4.6 Uncertainty Analysis

Each measurement conducted in order to calculate  $\gamma$ ,  $h$ , and ultimately the net heat flux reduction,  $\Delta q_r$ , was subject to some uncertainty. These uncertainties propagate, thereby causing some uncertainty in the calculated parameters. An analysis of these uncertainties is presented in this section.

Uncertainty propagation was performed using the method of Kline and McClintock (1953). With this technique, a parameter  $Z$  that is a function of parameters,  $X_1, X_2, \dots$ , each with uncertainty  $\varepsilon_{X_1}, \varepsilon_{X_2}, \dots$ , has an uncertainty computed by:

$$\varepsilon_z = \sqrt{\left(\frac{\partial Z}{\partial X_1} \varepsilon_{X_1}\right)^2 + \left(\frac{\partial Z}{\partial X_2} \varepsilon_{X_2}\right)^2 + \dots} \quad (4.52)$$

Complex numerical algorithms used to calculate certain parameters may not lend themselves well to calculating some partial derivatives. In these cases, the quantity  $\frac{\partial Z}{\partial X_i} \varepsilon_{X_i}$  was substituted with the sensitivity of the parameter  $Z$  to the parameter  $X_i$ , obtained simply by recomputing  $Z$  with a value of  $X_i$  adjusted by its uncertainty.

#### 4.6.1. Freestream Reynolds Number

The freestream Reynolds number is a function of the freestream velocity, diameter of the leading edge, and the kinematic viscosity of the freestream air at the temperature of the air. The Sutherland equation was used to determine the kinematic viscosity and the diameter of the leading edge was machined to tight tolerances and verified. The dominant source of uncertainty in  $Re_D$  was caused by the measurement of the freestream velocity.

The freestream velocity was calculated using the Bernoulli equation with the pressure across a pitot-static probe positioned such that it was hanging approximately 7 cm from the top of the wind tunnel in mid span. The height was selected such that the pitot-static measurement was not influenced by the boundary layer on the wall of the wind tunnel, but also not so far into the flow that any wake shed off of the probe would interfere with measurements on the leading edge model. The density of the fluid was obtained through the ideal gas law using the temperature of the freestream, a relatively negligible source of error for this purpose.

The pitot-static pressure could be read to within 1.3 Pa, corresponding to an uncertainty in recorded velocity, and thereby the recorded Reynolds number, of approximately 1%. Additionally, this Reynolds number was held within 2% of the target value (either  $Re_D = 30000$  or  $60000$ ) so the actual Reynolds number may have differed by up to 3% from the target value. When calculating Frössling number, the recorded Reynolds number with 1% uncertainty was used instead of the target Reynolds number.

Similarly, when calculating blowing ratio, the computed freestream velocity was used instead of the target freestream velocity corresponding the target Reynolds number.

Since the freestream Reynolds number was held within 2% of the target value and since freestream temperature variations caused the target velocity to vary somewhat, the freestream velocity,  $U_\infty$ , was not fixed. This resulted in some variation in nondimensional pulsing frequency ( $F = fD/U_\infty$ ) since the dimensional pulsing frequency,  $f$ , was held fixed. The variation in nondimensional frequency was within approximately 3% of the mean value.

#### 4.6.2. Blowing Ratio

During the course of an experiment, the coolant blowing ratio,  $M$ , (computed through Eq. (2.1)) was set to a variety of desired values. Although the computed blowing ratio was a function of the freestream velocity (see Section 4.6.1), a great source of error stemmed from the flow rate measurement from the rotameter. The rotameter had a claimed accuracy of 1% or one-half of the scale divisions, whichever is greater. At the lowest coolant flow rates used (corresponding to  $M = 0.25$  at  $Re_D = 30000$ ), this translates to an uncertainty of 10%. At higher blowing ratios without the solenoid valve connected, this translates to an uncertainty of 2%. However, when the solenoid valve was connected, the higher fluid pressure in the rotameter at the high blowing rates caused the flow rate differences between divisions to be greater, resulting in uncertainties of approximately 3%. The overall uncertainties in blowing ratio thus range from 10% at the very low blowing rates to 4% at the highest blowing rate of  $M = 2.0$ .

The LabVIEW data acquisition software calculated the necessary rotameter float position to obtain the various target blowing ratios. This calculation occurred in real time and was a function of freestream velocity, freestream temperature, coolant temperature, and coolant temperature at the rotameter. The required rotameter position was rounded to the nearest graduation and the flow rate was set accordingly. Rounding to the nearest rotameter graduation caused the actual  $M$  (as measured by the rotameter) to differ from the target  $M$  by  $\Delta M < 0.025$ . The blowing ratio is generally reported as the target

blowing ratio; however, the most precise measurement is provided in some figures, including all figures reporting area-averaged data.

### 4.6.3. Temperature Measurements

Spatially resolved surface temperature measurements were obtained via infrared thermometry. The infrared camera yielded temperature measurements that were a function not only of the thermal radiation detected by the camera, but also of the surface emissivity, distance to the object, and relative humidity. Although approximate values of emissivity, distance, and humidity were used in the camera settings, uncertainty in those measurements as well as the camera's algorithm were bypassed somewhat by calibrating the temperature output by the camera to two Type J thermocouples placed on the model surface. Uncertainty in the calibration was determined via the standard deviation given by Bevington and Robinson (2003):

$$\sigma = \sqrt{\frac{\sum_{i=1}^N (T_{Measured} - T_{Calculated})_i^2}{N - (m + 1)}} \quad (4.53)$$

where  $N$  is the total number of data points and  $m$  is the order of the curve fit. The standard deviation multiplied by 1.96 gives the uncertainty with 95% confidence.

Since every thermocouple used in the experiments was welded from the same batch of thermocouple wire, bias error between the thermocouples was virtually eliminated, particularly useful since calculations of  $\gamma$  and  $h$  rely only on temperature differences. Nevertheless, the data acquisition unit was found to introduce some uncertainty into the thermocouple measurements such that the resulting uncertainty in the thermocouple temperature was found to be approximately  $\pm 0.3$  K. Considering all of these factors, the uncertainty of the IR camera calibration was within  $\pm 0.5$  K.

The precision uncertainty of the thermocouples was determined through an ice bath test to be approximately  $\pm 0.01$  K. Because many measurements involve the difference between two temperatures, the precision uncertainty and thus the repeatability of experiments is better than the stated uncertainties since the same thermocouples were used for all experiments of a given type ( $\gamma$  and  $h$ ).

#### 4.6.4. Gamma

The surface temperatures were substituted into Eqs. (4.1) and (4.16) to determine the unsteady coupled adiabatic effectiveness,  $\gamma$ . Equation (3.32) gives  $\gamma$  if there were no conduction. The surface temperature measurements as well as coolant and freestream temperature measurements described in Section 4.6.3 cause an uncertainty of 0.02 in the accuracy of this value of gamma uncorrected for conduction. Although the one-dimensional conduction correction introduces additional uncertainty, it is bound by physics at both extremes of possible temperatures and is customized with the actual conduction measured and is thus negligible by comparison.

Although the accuracy in the measurements of  $\gamma$  was 0.02, the precision of the measurements was only approximately 0.01 since the dominant source of precision error was in the IR camera calibration. However, even that error was not completely random. Although the IR calibration should have random oscillations around the true calibration, the calibration is fixed, thus measurements in a particular regime of the calibration will tend to have similar bias error. In order to gauge the measurement precision, we shall examine the spanwise averaged adiabatic effectiveness measured through several repetitions of the same case ( $M = 0.75$ ; low  $Tu$ ;  $Re_D = 60k$ ) in Fig. 4.8. The five samples of the same condition were acquired over a time period of 1.12 hours. The maximum difference between any of these five samples was  $\Delta\eta = 0.0041$ , which occurred immediately downstream of the coolant hole at  $x/d = 0.68$  where there is a large gradient in  $\eta$ . From Fig. 4.8, we can see that it is relatively inconsequential which data point within a particular experiment was used for data reporting, but generally the data acquired after the greatest amount of time at steady state or with the actual blowing ratio nearest the target blowing ratio was selected. A sixth trial (2A) is shown in Fig. 4.8 depicting the spanwise averaged  $\eta$  obtained during a test 17 days later. The results of the second trial were within  $\eta \approx 0.008$  of the results obtained during the previous test. Although this would generally be considered excellent repeatability for an adiabatic effectiveness experiment, much of the difference in  $\eta$  can actually be attributed to the small difference in blowing ratio. Although the target blowing ratio was  $M = 0.75$  in all

cases, the actual blowing ratios differed by  $\Delta M = 0.03$ . Figure 4.9 shows the area averaged adiabatic effectiveness (see Section 4.5 for the specific area that was used) data for the range of blowing ratios for both Trial 1 and Trial 2. Although the difference in  $M$  is small, we can see in Fig. 4.9 that  $\eta$  is very sensitive (relative to the precision uncertainty) to  $M$  in this regime. The discrepancy in  $M$  between the two trials at  $M \approx 0.75$  is evident in Fig. 4.9, but a very smooth line could be drawn through the entire data set. This result suggests that the dominant source of variance between multiple measurements of a repeated condition lies in the variation of the blowing ratio about the target blowing ratio. From an analysis of the repeated measurements performed in Trial 1, the precision uncertainty in the area averaged adiabatic effectiveness is estimated to be  $\Delta\eta < 0.002$ .

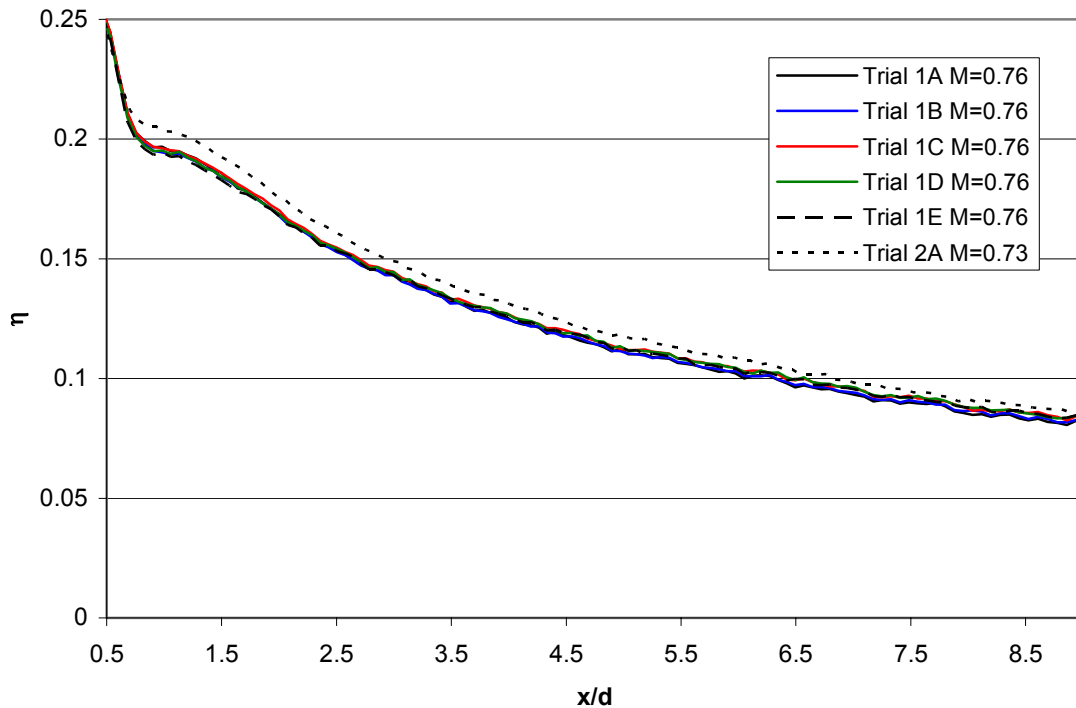


**Fig. 4.8** Repeatability of  $\eta$  within a test and between tests;  $M = 0.75$  (steady); low  $Tu$ ;  $Re_D = 60k$ . Trial 2 was conducted 17 days after Trial 1.

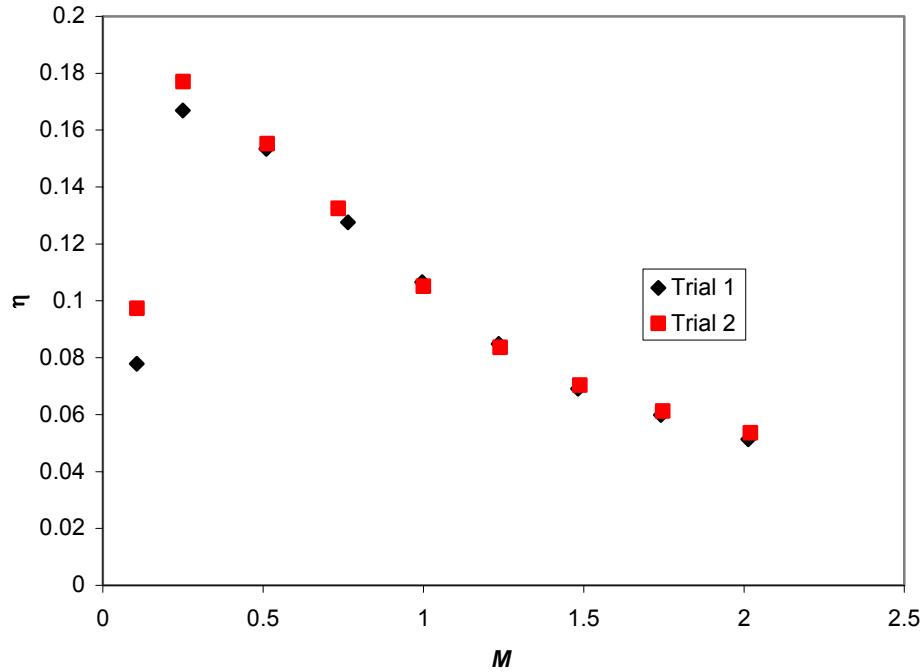


Fig. 4.9 Area averaged  $\gamma$ , low  $Tu$ ,  $Re_D = 60k$ , steady. Trial 2 was conducted 17 days after Trial 1.

#### 4.6.5. Heat Transfer Coefficient

The heat transfer coefficient distributions were calculated using Eq. (3.35), repeated here:

$$\bar{h}_f = \frac{\overline{-q_f''}}{(T_\infty - T_c)(\gamma - \lambda)} \quad (3.35)$$

In order to reduce the influence of the uncertainty in  $\gamma$  on the uncertainty in  $\bar{h}_f$ , the coolant temperature was maintained as close as possible to the freestream temperature. As discussed in Section 3.3, bringing  $T_\infty - T_c$  to zero does not cause the calculated  $\bar{h}_f$  to increase without bounds. Instead, it causes the adiabatic wall temperature to become  $T_\infty$ , independent of  $\gamma$ . In this case, Eq. (3.35) becomes

$$\bar{h}_f = \frac{\overline{-q_f''}}{T_s - T_\infty} \quad (4.54)$$

The uncertainty in  $\overline{q_f}$  results from the uncertainty in the voltage measurement across the shunt resistor, the 1% uncertainty in the shunt resistance, uncertainty in the resistance of the heat flux plate, and uncertainty in the measurement of the heat flux plate area. The uncertainties of the heat flux plate resistance, shunt resistance, and the heat flux plate area all manifest themselves as bias errors. In a typical case for which  $\overline{q_f} = -1230 \text{ W/m}^2$ , the uncertainty in the heat flux would be  $25 \text{ W/m}^2$ , or 2%. The resulting uncertainty in  $\overline{h_f}$  if Eq. (4.54) applies is then dependent not only on the uncertainty in the temperature measurements (see Section 4.6.3), but also the quantity  $T_s - T_\infty$  in the denominator of Eq. (4.54). In regions where this quantity is small,  $\overline{h_f}$  is large and even small errors in the temperature measurements can lead to enormous percentage errors in  $\overline{h_f}$ . In the small localized regions of the highest heat transfer coefficient,  $T_s - T_\infty \approx 5 \text{ K}$ , leading to an uncertainty in  $\overline{h_f}$  of 12%. Over the greater region of the heat flux plate, the temperature difference would be more typically  $T_s - T_\infty \approx 15 \text{ K}$ , yielding uncertainties of 5%. Although this is a respectable uncertainty for measurements of heat transfer coefficient, the precision uncertainty, useful for determining the effects of the parameters investigated in the present study, is much less.

If Eq. (3.35) were used instead in order to account for  $T_c \neq T_\infty$ , the uncertainty in  $\gamma$  would manifest itself as an additional uncertainty in the  $T_s - T_\infty$  temperature difference. Since  $|T_\infty - T_c| < 1 \text{ K}$  for all cases, a 0.02 uncertainty in  $\gamma$  would lead to an additional uncertainty of at most 0.02 K for that temperature difference. This is insignificant relative to the uncertainties of 0.3 K in  $T_\infty$  and 0.5 K in  $T_s$ .

A useful nondimensional presentation of the heat transfer coefficient is through the use of the Frössling number, defined as

$$Fr = \frac{Nu}{\sqrt{Re_D}} = \frac{hD}{k\sqrt{Re_D}} \quad (4.55)$$

Although the Frössling number is dependent on the freestream Reynolds number, the relatively small uncertainty of  $Re_D$  (which has only a power of  $\frac{1}{2}$  in Eq. (4.55)) implies

that the uncertainty in the Frössling number is essentially the same as the uncertainty in the heat transfer coefficient itself.

It is also useful to express the ratio of the heat transfer coefficient with film cooling to the heat transfer coefficient without film cooling,  $\overline{h}_f / h_0$ . Although the uncertainties of both  $\overline{h}_f$  and  $h_0$  do play a role, we often use the same value of  $h_0$  when comparing cases, so it becomes bias error only and the precision uncertainty is the same as with  $\overline{h}_f$ . Nevertheless, we are sometimes forced to compare  $\overline{h}_f / h_0$  values where the denominators do differ. In these cases, the uncertainty is approximately 10% where  $\overline{h}_f / h_0 \approx 1.4$ .

Similar to the situation with our computation of  $\gamma$  discussed in Section 4.6.4, many of the measurements that go into the computation of  $\overline{h}_f / h_0$  had bias errors that did not change during the course of the experiments presented in this document. For example, the same thermocouples were used for all measurements, and the use of the same heat flux plate and shunt resistor cause much of the uncertainty in the heat flux to influence only the accuracy of the results, not the precision. Naturally, we desire high precision in order to compare  $\overline{h}_f / h_0$  with differing blowing or freestream conditions. In order to demonstrate the precision of the measurements, Fig. 4.10 shows four calculations of the spanwise averaged  $\overline{h}_f / h_0$ , the data of which was gathered over two separate tests; Trial 2 took place 16 days after Trial 1. Not only were the  $h_f$  measurements repeated in each trial, but so too were the  $h_0$  measurements. Past  $x/d = 0.7$ , the largest difference in the results is at  $x/d \approx 8.5$ , where the average of Trial 1 differed from the average of Trial 2 by 2%. The largest difference within a particular test was 1.5%. The area averaged results for a variety of blowing ratios are shown in Fig. 4.11 where the  $M = 1$  cases differ by 0.1%. The greatest difference was with the  $M = 0.75$  cases which differ by 1.3%; however, it is evident that this difference is primarily a result of blowing ratio mismatch, that is Trial 1 was conducted with  $M = 0.737$  and Trial 2 was conducted at  $M = 0.757$ .

Aside from the precision of the experiments, improved repeatability through averaging data is due to the effect of averaging the many data points that each contribute to the area or spanwise averaged results. The process of averaging  $N$  independent data points corresponding to  $N$  pixels from the IR camera data would result in reducing the uncertainty by a factor of  $\sqrt{N}$ .<sup>m</sup> However, much of the error at each data point is not random; for example, an error in the coolant temperature is the same for each pixel in a single image so that error does not decrease with averaging. The excellent repeatability is indicative of a consistent experimental methodology and therefore excellent precision. In fact, repeated measurements suggest that the precision in area-averaged measurements of  $h_f / h_0$  performed on the same day is within 1%.

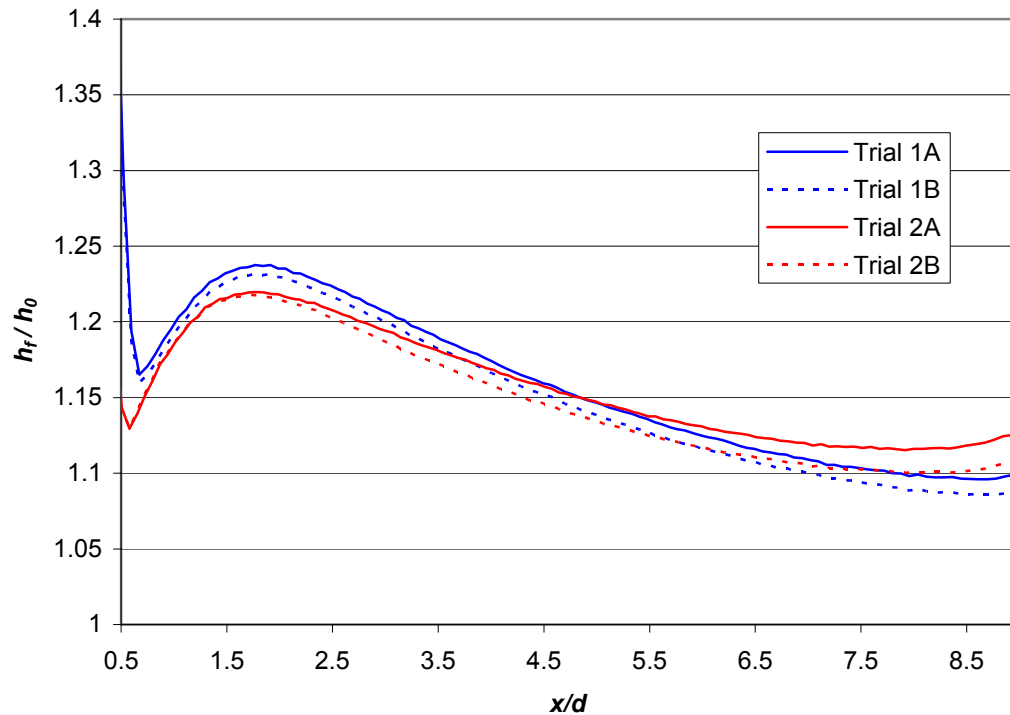


**Fig. 4.10** Repeatability of  $h_f / h_0$  within a test and between tests;  $M = 1.0$  (steady); high  $Tu$ ;  $Re_D = 60k$ . Trial 2 was conducted 16 days after Trial 1.

<sup>m</sup> On a curved surface, each pixel from the IR camera corresponds to a slightly different areas on the surface, thus the pixels carry different weights when the data is area-averaged. The factor of  $\sqrt{N}$  would technically apply only to a surface for which the surface normal at each pixel is angled equally with respect to the camera.

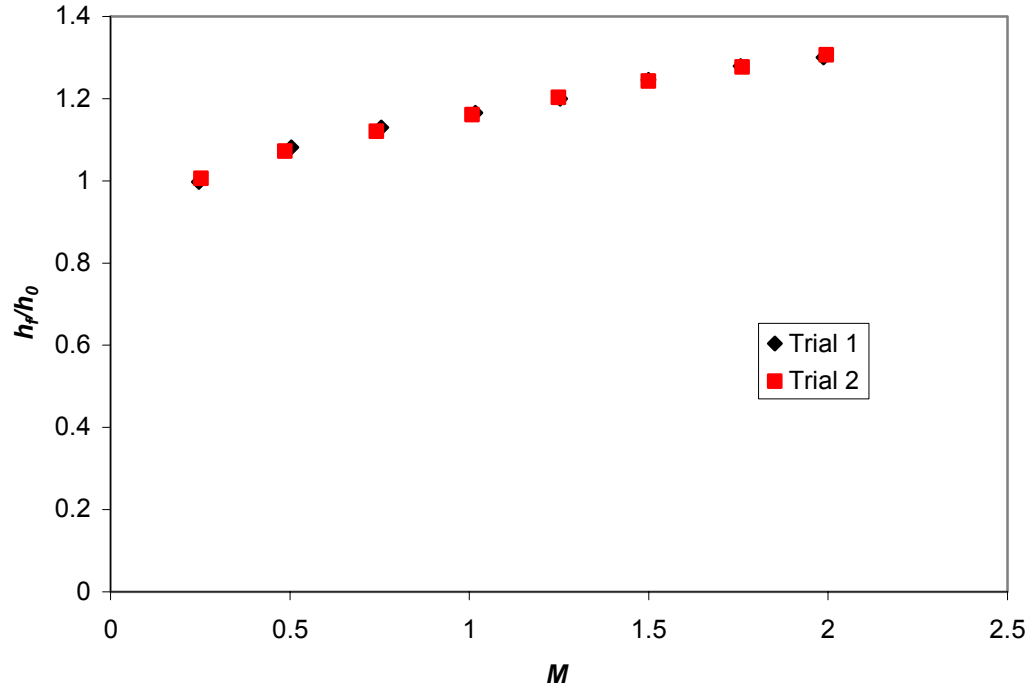


Fig. 4.11 Area averaged  $h_f / h_0$ , high  $Tu$ ,  $Re_D = 60k$ , steady. Trial 2 was conducted 16 days after Trial 1.

#### 4.6.6. Net Heat Flux Reduction

The heat transfer coefficient augmentation,  $\overline{h_f} / h_0$ , along with the unsteady coupled adiabatic effectiveness,  $\gamma$ , allowed for the calculation of the net heat flux reduction due to film cooling according to Eq. (3.31), repeated here:

$$\overline{\Delta q_r} = 1 - \frac{\overline{h_f}}{h_0} \left( 1 - \frac{\gamma}{\phi} \right) \quad (3.31)$$

It is worthwhile resisting the temptation to consider the uncertainty in  $\overline{\Delta q_r}$  as a percentage. Due to the “1-” that appears in Eq. (3.31), the formulation may cause a large heat flux ratio (the second term on the right hand side of Eq. (3.31)) to become small in terms of  $\overline{\Delta q_r}$ , and a small ratio to become large in terms of  $\overline{\Delta q_r}$ . In a hypothetical location in a typical coolant plume where  $\overline{h_f} / h_0 = 1.4$  and  $\gamma = 0.45$ , the net heat flux reduction would be  $\overline{\Delta q_r} = 0.650 \pm 0.025$ , or a 7% uncertainty in the heat flux ratio ( $0.025 / (1 - 0.65) = 0.07$ ). However, if the blade unfortunately had the same

$\bar{h}_f/h_0 = 1.4$ , but with  $\gamma = 0.05$ , then  $\overline{\Delta q_r} = -0.283 \pm 0.091$ , which is still a 7% uncertainty in the heat flux ratio. For a case in which there is a stronger influence of the coolant jet such that  $\bar{h}_f/h_0 = 2.0$  and  $\gamma = 0.7$ , the net heat flux reduction would be  $\overline{\Delta q_r} = 1.333 \pm 0.037$ . This would then be an 11% uncertainty in the heat flux ratio, a result of greater uncertainty with the higher heat transfer coefficients. In a third case, we consider a region with no influence of film cooling, that is  $\bar{h}_f/h_0 = 1.0$  and  $\gamma = 0$  from which we would compute  $\overline{\Delta q_r} = 0 \pm 0.071$ .

Figure 4.12 shows  $\Delta q_{r,span}$  from four repetitions of the same conditions. The  $\eta$  and  $h_f/h_0$  data that went into calculating  $\Delta q_r$  for the two trials were acquired 17 and 16 days after the previous data sets, respectively. The maximum difference in  $\Delta q_r$  between the average results of the two trials downstream of  $x/d = 0.7$  is 0.02, or a 2% difference in the net heat flux. The area averaged results for a variety of blowing ratios are shown in Fig. 4.13. Area averaging reduces that difference in the two trials to only 0.006; however, at  $M = 1.25$  the difference in area averaged  $\Delta q_r$  is 0.012.

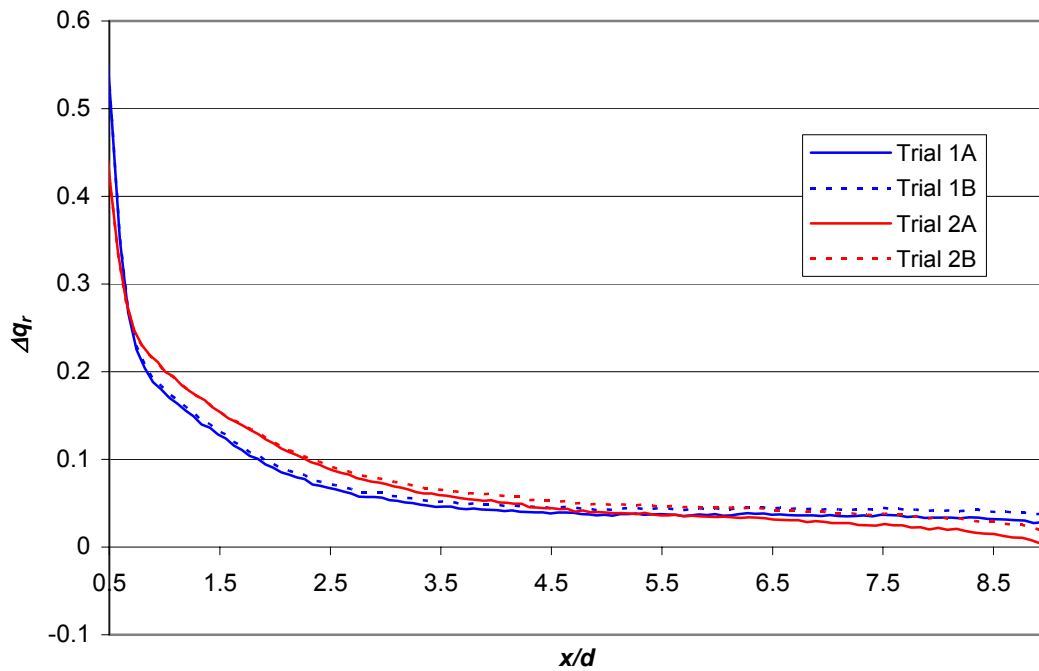


Fig. 4.12 Repeatability of  $\Delta q_r$  with a test and between tests;  $M = 1.0$  (steady); high  $Tu$ ;  $Re_D = 60k$ .

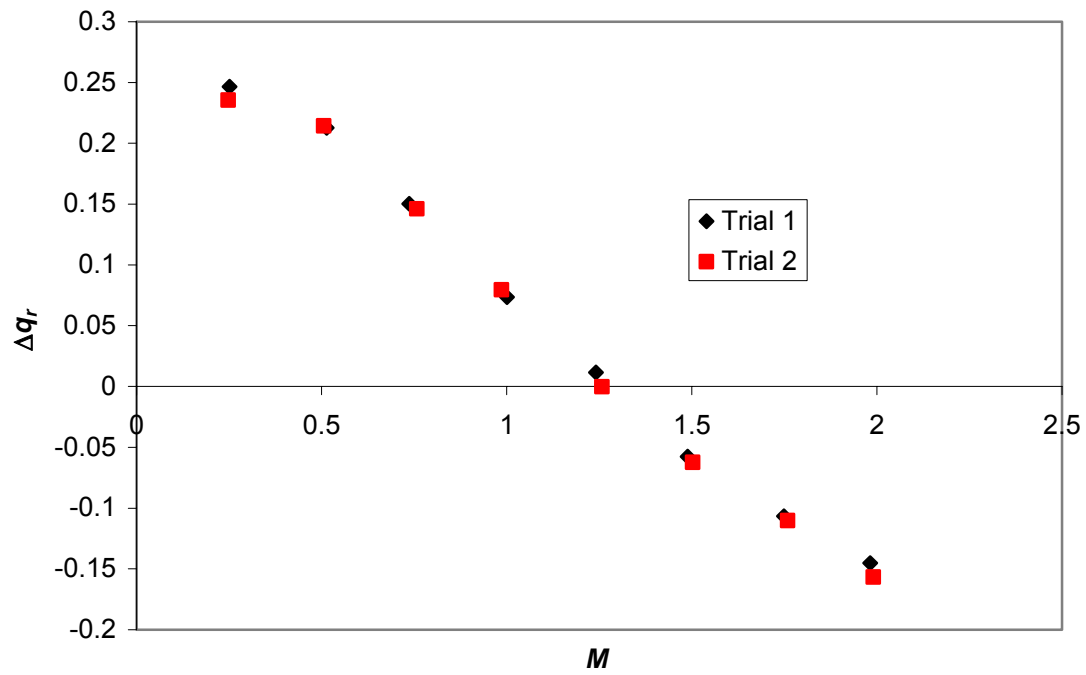


Fig. 4.13 Area averaged  $\Delta q_r$ , high  $Tu$ ,  $Re_D = 60k$ , steady.

## 5. Net Heat Flux Reduction Results

Experiments to determine the net heat flux reduction were performed using the experimental theory developed in Section 3.3. The experimental results presented in this chapter consist of two sets of  $\overline{\Delta q_r}$  data. During each set, pulsed and steady film cooling were characterized. The pulsed solenoid valves were used as supplied for the first set of data and then the poppets were replaced prior to the second data set. For the first set of data, the valves closed only partially; for the second set the valves closed completely. Each set consisted of two days of experimentation—one to acquire the unsteady coupled adiabatic effectiveness data and another to acquire the heat transfer coefficient data. These four days of experimentation followed seven initial non-contiguous days of experiments used to verify and improve the methodology. The “partial valve closure” gamma data were acquired on 19 Sept 2008 followed by the heat transfer data on 22 Sept 2008. The “complete valve closure” gamma and heat transfer data were acquired on 6 Oct 2008 and 8 Oct 2008, respectively.

Steady film cooling results are presented in Section 5.1, followed by the pulsed jet results in Section 5.2. Appendix A contains the characterization of the pulsed jet waveforms used in Section 5.2. Additionally, the low frequency prediction technique described in Section 3.6 is tested in Section 5.3.

### 5.1 Steady Jet Results

In order to fully understand the influence of pulsing a coolant jet, we must first understand the behavior of the steady coolant jet. This section examines the steady jet behavior. Net heat flux reduction data were acquired in the range  $0 \leq M \leq 2.0$  with a resolution of  $\Delta M = 0.25$ . Some additional data were acquired for the baseline case of low freestream turbulence and  $Re_D = 60k$ . We begin with an overview of the steady film cooling results at the baseline condition. Sections 5.1.1 through 5.1.3 will provide more detailed data as well as describe the impact of freestream turbulence and  $Re_D$ .

Spanwise averaged plots of the film cooling parameters are shown for a variety of blowing ratios in Figs. 5.1 through 5.4. Although some spatial information about the distributions is inherently lost through the spanwise averaging process, it provides a

convenient technique for comparing cases. For a description of the averaging process for the heat transfer coefficient augmentation and the net heat flux reduction, see Section 4.5.

In Fig. 5.1, we observe that  $M = 0.25$  clearly has the highest spanwise averaged adiabatic effectiveness ( $\gamma = \eta$  for steady film cooling). The peak is  $\eta = 0.26$  immediately downstream of the coolant hole and dropping to  $\eta = 0.11$  at  $x/d = 9$ . Poorer adiabatic effectiveness occurs as the blowing ratio is increased in increments of  $\Delta M = 0.25$  up to  $M = 2.0$ . Also note that the blowing ratio,  $M = 0.1$  has a spanwise averaged adiabatic effectiveness profile that falls between the  $M = 1.25$  and  $M = 1.5$  cases.

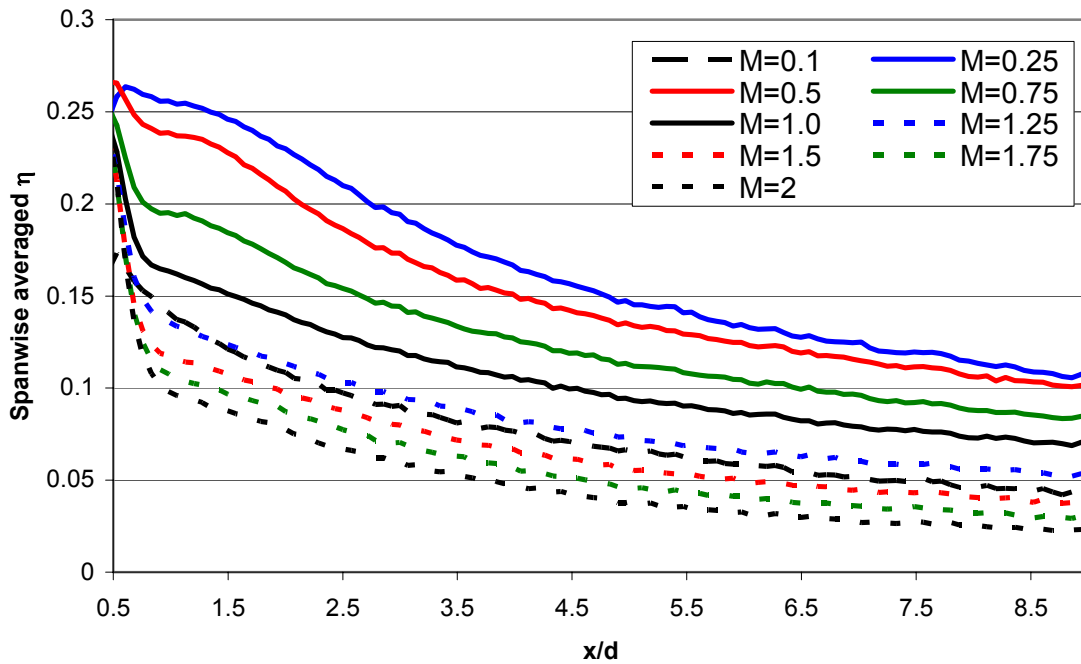


Fig. 5.1 Spanwise averaged adiabatic effectiveness for steady film cooling, low  $Tu$ ,  $Re_D = 60k$

Spanwise averaged heat transfer coefficient augmentation,  $h_f / h_0$  results are shown in Fig. 5.2. In this case, we have monotonically increasing  $h_f / h_0$  with increasing  $M$ . Interestingly, it appears that the heat transfer coefficient is actually lower at  $M = 0.1$  than it is at  $M = 0$ . Although certainly possible, the minimum spanwise  $h_f / h_0$  in this case is 0.97, within the experimental uncertainty of 1. From  $M = 0.25$  up to  $M = 2.0$  in

increments of  $\Delta M = 0.25$ , spanwise  $h_f/h_0$  increases to a maximum peak of 1.53, indicating a 53% increase in spanwise heat transfer coefficient at  $M = 2.0$  over the no-blowing case. An interesting feature in Fig. 5.2 is that the peak spanwise  $h_f/h_0$  is at  $x/d = 1.8$  at  $M = 0.25$ , but shifts downstream to  $x/d = 2.0$  at  $M = 2.0$ . In all of the cases  $h_f/h_0$  increases with  $x$  for  $x/d > 8$ . As evident in Fig. 5.3, this increase in  $h_f/h_0$  is not due to an increase in the heat transfer coefficient. In fact,  $Fr$  drops with a steeper slope in the region  $x/d > 8$  ( $>70.5^\circ$  from stagnation), possibly due to the approaching transition from the curved portion of the leading edge to the flat afterbody. The slopes of the spanwise averaged  $Fr$  are approximately equal in this region for all  $M$ , thus the relative size of  $Fr_f$  increases relative to  $Fr_0$ .

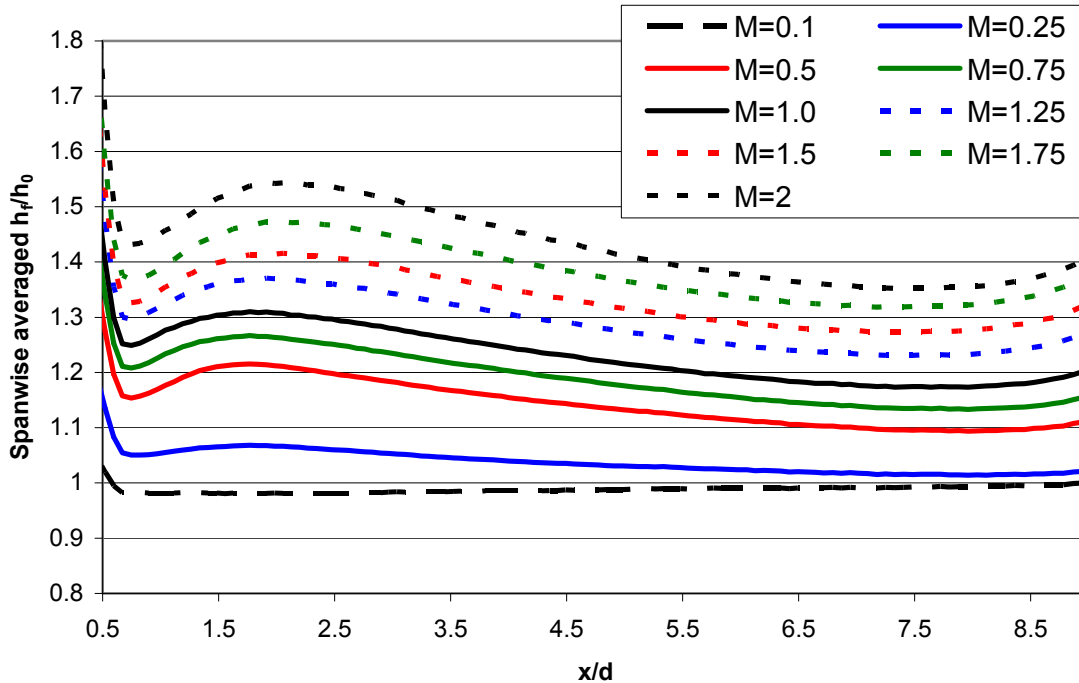


Fig. 5.2 Spanwise averaged heat transfer coefficient augmentation for steady film cooling, low  $Tu$ ,  $Re_D = 60k$

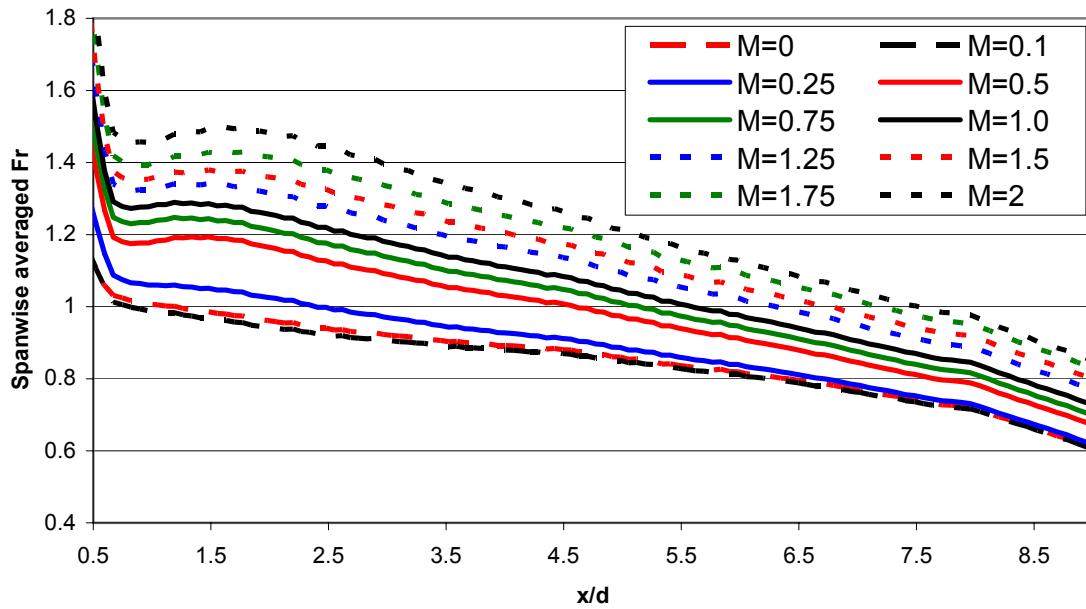


Fig. 5.3 Spanwise averaged Frössling number for steady film cooling, low  $Tu$ ,  $Re_D = 60k$

Spanwise net heat flux reduction plots are shown in Fig. 5.4. The  $M = 0.25$  case had the best  $\Delta q_r$  performance, with a 50% decrease in heat load immediately downstream of the hole tapering to 18% at  $x/d = 9$ . The use of any more coolant causes a decrease in  $\Delta q_r$ . In fact, even  $M = 0.1$  is superior to  $M = 0.75$  for  $x/d > 1.8$ . For  $M \geq 1.25$  the spanwise net heat flux reduction is almost uniformly negative, indicating a net heat flux increase. This is due to the very high heat transfer coefficient augmentation due to film cooling, without a commensurate decrease in adiabatic wall temperature.

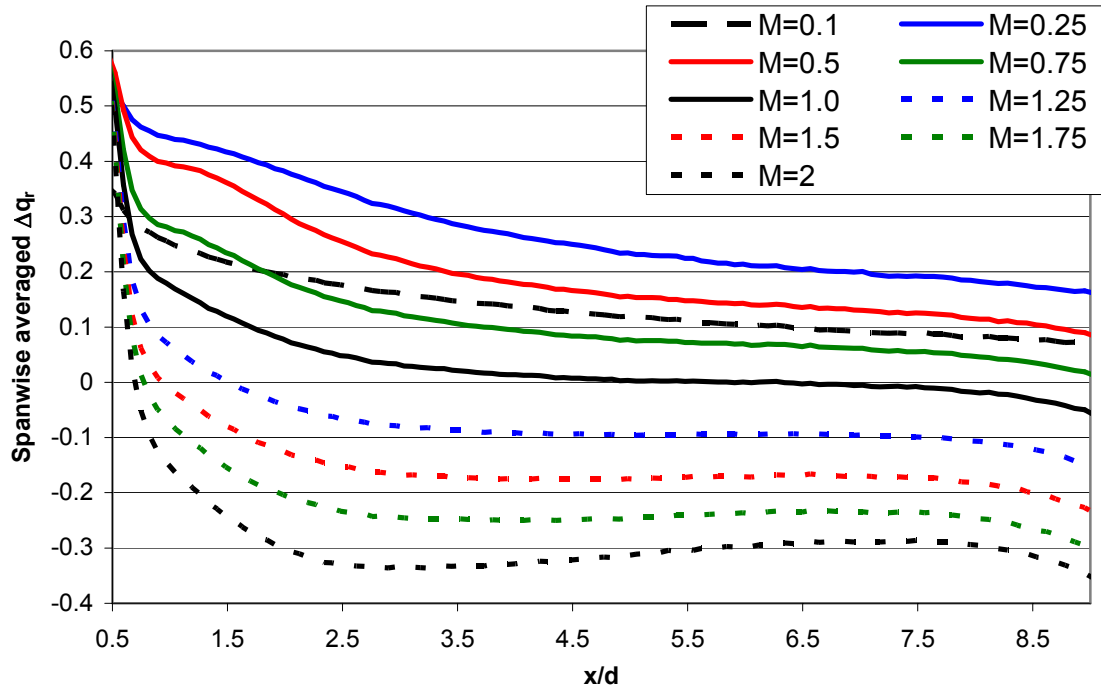


Fig. 5.4 Spanwise averaged net heat flux reduction for steady film cooling, low  $Tu$ ,  $Re_D = 60k$

### 5.1.1. Influence of Freestream Turbulence and Reynolds Number on Adiabatic Effectiveness

The area averaged adiabatic effectiveness results for a variety of blowing ratios and all four freestream conditions are summarized in Fig. 5.5. The highest resolution data was acquired for the baseline condition of low freestream turbulence,  $Re_D = 60k$ . For both the  $Re_D = 60k$  and  $30k$  cases, increasing the freestream turbulence intensity tends to reduce  $\gamma$ . This phenomenon is probably a result of the higher turbulence causing the coolant to mix more with the freestream. All four freestream conditions perform similarly for the higher blowing ratios,  $M > 1$ ; however, at lower blowing ratios the performance is more greatly affected by freestream condition with the low freestream turbulence,  $Re_D = 60k$  performing best. From Fig. 5.5 it is also evident that the freestream Reynolds number variations have as much of an effect as the turbulence intensity variations. A more detailed analysis employing the spatial contours of the adiabatic effectiveness data follows.

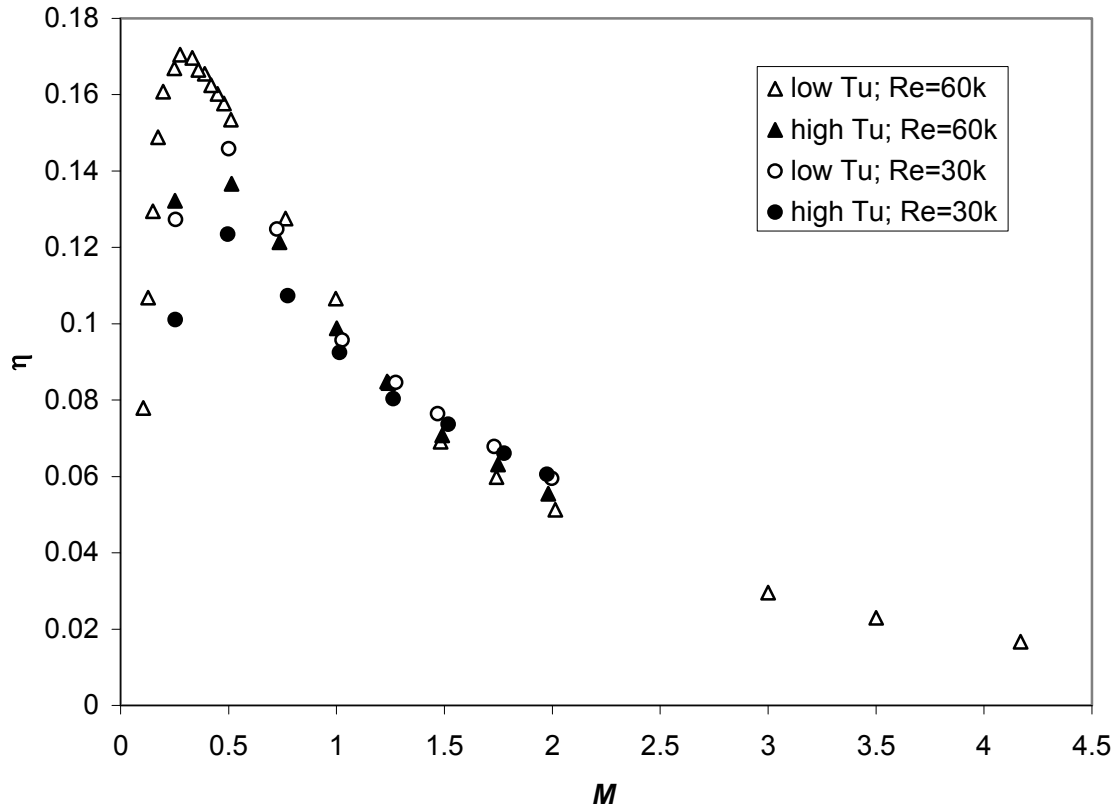
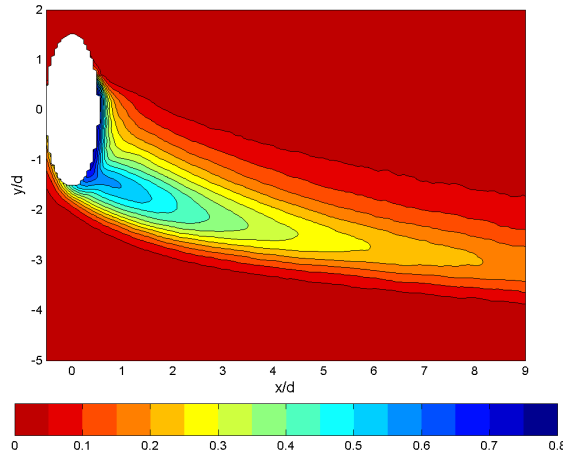
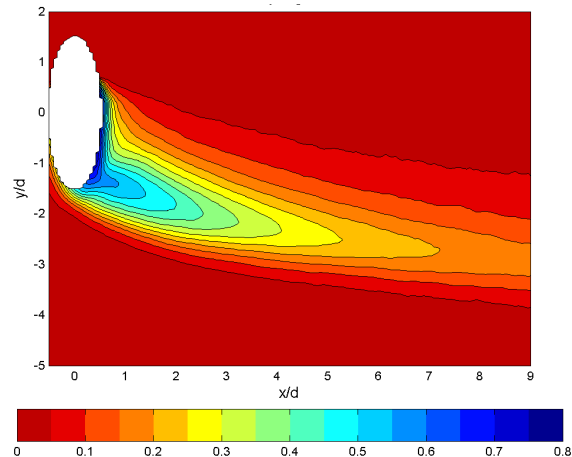


Fig. 5.5 Area averaged  $\eta$  for steady film cooling

Figure 5.6 shows the adiabatic effectiveness ( $\eta = \gamma$  for steady film cooling) contours at a blowing ratio of  $M = 1.5$  for the baseline condition of low freestream turbulence and  $Re_D = 60k$ . The freestream flow is in the positive  $x$  direction and the coolant travels through the coolant hole with velocity components in the negative  $y$  and positive  $z$  (out of the page) directions. The coolant exits the coolant hole and turns in the direction of the freestream but retains some of its velocity in the negative  $y$  direction as evident in Fig. 5.6. As the coolant travels downstream, mixing takes place between the coolant and the freestream, reducing the adiabatic effectiveness in the downstream direction. The adiabatic effectiveness contours for the remaining three freestream conditions are shown in Figs. 5.7 through 5.9, but we shall delay discussion of these conditions for the moment.



**Fig. 5.6** Adiabatic effectiveness contours for steady film cooling,  $\gamma = \eta$ ,  $M = 1.5$ , low  $Tu$ ,  $Re_D = 60k$



**Fig. 5.7** Adiabatic effectiveness contours for steady film cooling,  $\gamma = \eta$ ,  $M = 1.5$ , high  $Tu$ ,  $Re_D = 60k$

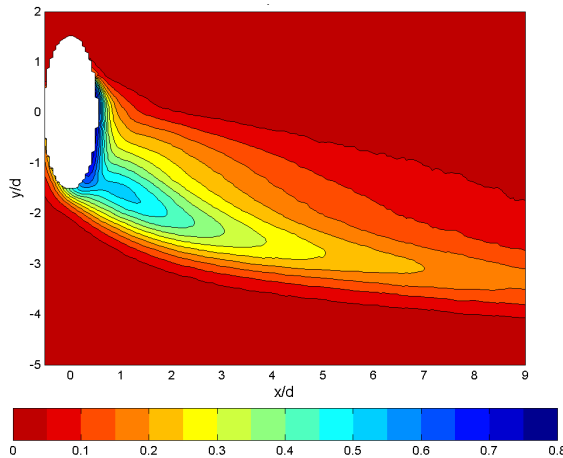


**Fig. 5.8** Adiabatic effectiveness contours for steady film cooling,  $\gamma = \eta$ ,  $M = 1.5$ , low  $Tu$ ,  $Re_D = 30k$

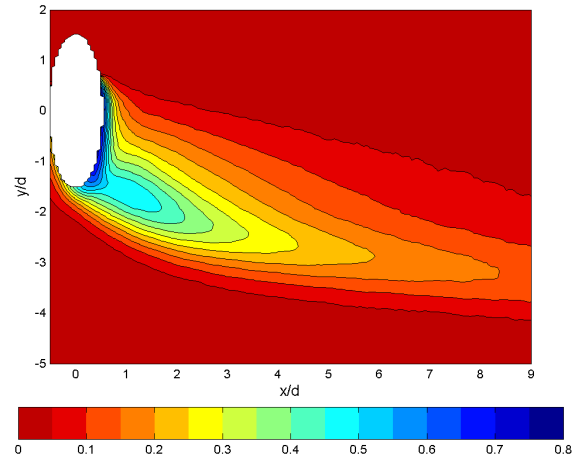


**Fig. 5.9** Adiabatic effectiveness contours for steady film cooling,  $\gamma = \eta$ ,  $M = 1.5$ , high  $Tu$ ,  $Re_D = 30k$

Figures 5.10 through 5.13 show the adiabatic effectiveness contours for a jet with blowing ratio  $M = 0.5$  for the four freestream conditions. The lower momentum of the jet relative to the freestream causes it to turn in the direction of the freestream much faster than the  $M = 1.5$  jet in Figs. 5.6 through 5.9. In these cases, the lower  $M$  jet also has a much higher adiabatic effectiveness than the higher  $M$  jet. For example, the peak adiabatic effectiveness at  $x/d = 3$  is approximately 0.2 higher at  $M = 0.5$  than at  $M = 1.5$  for the low turbulence,  $Re_D = 60k$  case. This is especially nice considering that the

$M = 0.5$  jet uses only a third of the coolant relative to the  $M = 1.5$  jet. The rationale for this better performance at lower  $M$  is that the higher momentum jet penetrates into the freestream (+ $z$  direction) more than the lower momentum jet, thus the coolant is lifted off of the surface it is intended to protect. This is confirmed in the flow visualization in Chapter 7.

Figures 5.10 and 5.11 show the adiabatic effectiveness contours ( $\gamma = \eta$  for steady film cooling) for low and high turbulence respectively at  $Re_D = 60k$  with  $M = 0.5$ . The corresponding contours for  $Re_D = 30k$  are shown in Fig. 5.12 and Fig. 5.13. At  $x/d = 3$ , the peak  $\gamma$  is reduced by  $\Delta\gamma \approx 0.05$  when switching from low to high turbulence for both freestream Reynolds numbers. Even more degradation is evident closer to the hole. The  $\gamma$  contours at low turbulence extend farther downstream than the contours at high turbulence; however, the coolant plume is wider at high turbulence. A comparison of the area averaged  $\gamma$  data in Fig. 5.5 reveals that the low turbulence case is superior to the high turbulence case by  $\Delta\gamma = 0.022$  and  $\Delta\gamma = 0.017$  in the area averaged sense at  $M = 0.50$  for the low and high Reynolds number cases, respectively.

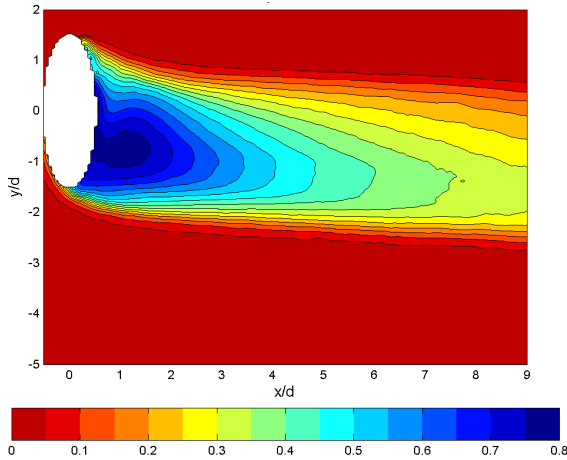


**Fig. 5.10** Adiabatic effectiveness contours for steady film cooling,  $\gamma = \eta$ ,  $M = 0.5$ , low  $Tu$ ,  $Re_D = 60k$

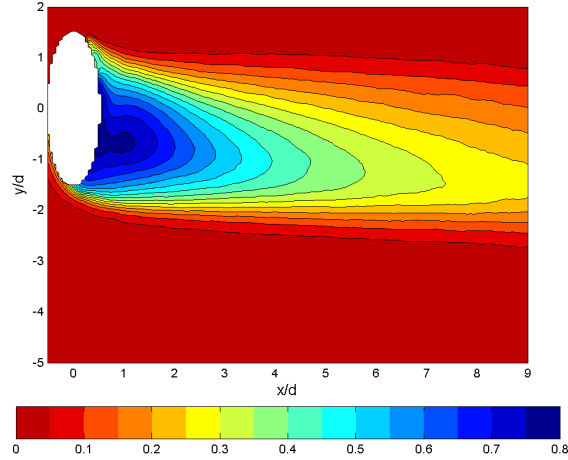


**Fig. 5.11** Adiabatic effectiveness contours for steady film cooling,  $\gamma = \eta$ ,  $M = 0.5$ , high  $Tu$ ,  $Re_D = 60k$

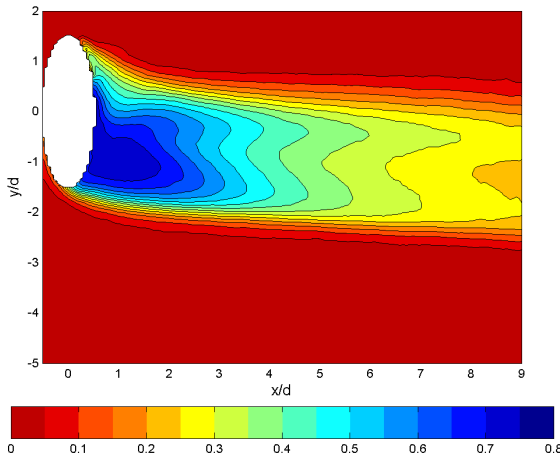


**Fig. 5.12** Adiabatic effectiveness contours for steady film cooling,  $\gamma = \eta$ ,  $M = 0.5$ , low  $Tu$ ,  $Re_D = 30k$

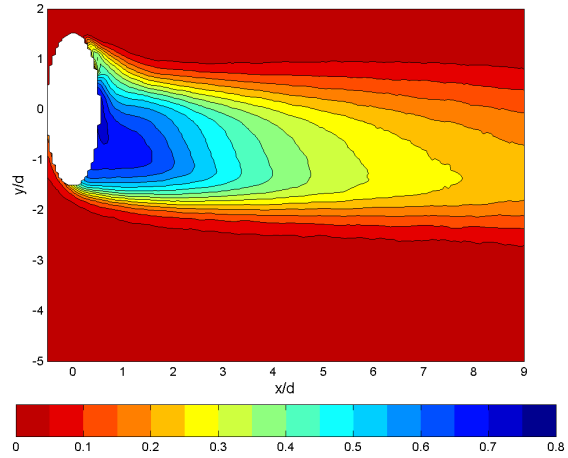


**Fig. 5.13** Adiabatic effectiveness contours for steady film cooling,  $\gamma = \eta$ ,  $M = 0.5$ , high  $Tu$ ,  $Re_D = 30k$

If we make a direct comparison between Figs. 5.10 and 5.12, we can determine the influence of freestream Reynolds number on adiabatic effectiveness at  $M = 0.5$  at low freestream turbulence. The peak adiabatic effectiveness at each  $x/d$  location is  $\Delta\eta \approx 0.05$  higher at  $Re_D = 60k$  than at  $Re_D = 30k$ . By comparing Figs. 5.6 and 5.8 we can evaluate the influence of  $Re_D$  at  $M = 1.5$ , again at low freestream turbulence. Again, the peak effectiveness at each  $x/d$  location is higher at  $Re_D = 60k$  than at  $Re_D = 30k$ ; however, the coolant plume at  $Re_D = 30k$  is 30% wider at  $x/d = 4$  than at  $Re_D = 60k$  when measured by

the spanwise extent of the  $\eta = 0.05$  contour. This additional width of the coolant plume more than offsets the reduction in peak  $\eta$  at low  $Re_D$  as evident through comparison of the area averaged data in Fig. 5.5. As  $M$  is increased even higher, the lower freestream Reynolds number outperforms the higher freestream Reynolds number, opposite the case at lower blowing ratios.

As mentioned above, the coolant plume for the low turbulence,  $Re_D = 30k$  case in Fig. 5.8 is unique in that it is wider than the corresponding  $Re_D = 60k$  case in Fig. 5.6 if one measures width with the  $\eta = 0.05$  contour. If instead, one measures width with the  $\eta = 0.15$  contour, there is a strong contraction in the adiabatic effectiveness plume width on the interval  $3 \leq x/d \leq 5$ . The contraction appears unusual because it takes place predominantly on the upper (larger  $y/d$ ) part of the coolant plume and the contour deviates a great deal from the perceived streamlines in that locale. One explanation for this could be that the coolant convects off of the surface rapidly in this region; however, we will revisit this phenomenon when we consider the flow visualization results in Section 7.1. The phenomenon is even more evident at  $M = 1.0$  as shown in Fig. 5.14. This plot of  $\eta$  at  $M = 1.0$  also contains further evidence suggesting a significant  $z$  component of the flow direction downstream of the hole. There is a contour interval  $0.60 \leq \eta \leq 0.65$  located at approximately  $x/d = 1.1$ ,  $y/d = -1.2$  that is an island, not connected with the coolant hole. This suggests that coolant dropped down onto the surface at this location.

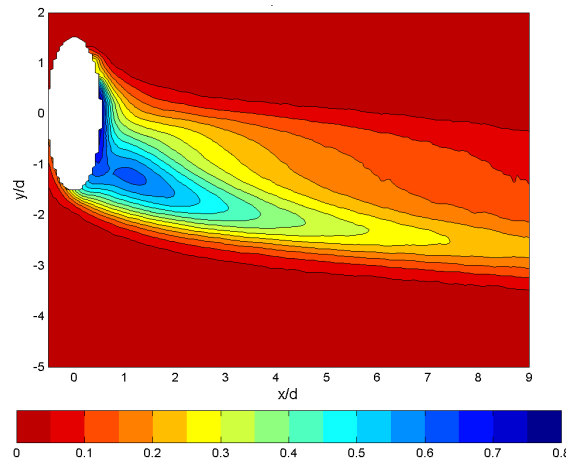


Fig. 5.14 Adiabatic effectiveness contours for steady film cooling,  $\gamma = \eta$ ,  $M = 1.0$ , low  $Tu$ ,  $Re_D = 30k$

By comparing Figs. 5.11 and 5.13, we can determine the influence of  $Re_D$  on adiabatic effectiveness at  $M = 0.5$ , high turbulence. Again, the  $Re_D = 60k$  case is clearly superior to the  $Re_D = 30k$  case, with an adiabatic effectiveness difference of  $\Delta\eta \approx 0.05$  along the entire streamwise line of peak adiabatic effectiveness. The analogous influence of  $Re_D$  on adiabatic effectiveness at  $M = 1.5$  can be determined through a comparison of Figs. 5.7 and 5.9. Again, the contours extend farther downstream in the  $Re_D = 60k$  case, although the difference is  $\Delta\eta < 0.05$  and the coolant plume is significantly narrower than the plume at  $Re_D = 30k$ . At  $x/d = 4$  for instance, the coolant plume for the  $Re_D = 30k$  case is approximately 20% wider than at  $Re_D = 60k$  when measured by the width of the  $\eta = 0.05$  contour. By studying the area averaged plots in Fig. 5.5, we find that the  $Re_D = 30k$  case performs similarly to the  $Re_D = 60k$  case at  $M = 1.5$ , but there is clearly a trend that suggests that  $Re_D = 30k$  is preferable at low  $M$ . For  $M > 1.5$ , the higher Reynolds number is preferable. This is similar to the observation at low freestream turbulence.

A less pronounced area averaged effect of turbulence is evident at high blowing ratios than at the closer to optimum blowing ratio,  $M = 0.5$ . In fact, the area-averaged data in Fig. 5.5 show increasing the turbulence intensity causes virtually no change at  $M = 1.5$  and a slight increase in area-averaged  $\gamma$  at  $M = 2.0$  for  $Re_D = 60k$ . Figures 5.6 and 5.7 show the contour plots of  $\gamma$  at low and high turbulence, respectively, for  $M = 1.5$  and  $Re_D = 60k$ . Although the peak  $\gamma$  is lower at high turbulence than at low turbulence, the jet plume is slightly wider. The increased turbulent mixing not only causes increased mixing normal to the wall, but it also causes increased mixing in the spanwise ( $y$ ) direction as well. The same conclusion on the effect of freestream turbulence at  $M = 1.5$ , but at  $Re_D = 30k$  can be reached through a comparison of Figs. 5.8 and 5.9 and for the low and high turbulence cases, respectively.

A striking phenomenon is evident with the  $M = 0.50$ , low turbulence,  $Re_D = 30k$  case in Fig. 5.12 compared to the other freestream conditions at that blowing ratio. The coolant divides into two distinct fingers that extend downstream. The fingering phenomenon is not present for the high turbulence case in Fig. 5.13, nor is it present at  $Re_D = 60k$  in Fig. 5.10; however, it is present at lower blowing ratios. Figures 5.15

through 5.18 show the  $M = 0.25$  adiabatic effectiveness contours for the four freestream conditions. The trend of a smaller retained velocity component in the negative  $y$  direction continues at this even lower blowing ratio and the fingering phenomenon is still present with the low turbulence  $Re_D = 30k$  condition, but it is now present also at low turbulence  $Re_D = 60k$ . The coolant divides into multiple distinct fingers that extend downstream. At  $M = 0.25$ , the coolant just seeps out of the coolant hole; in fact the momentum ratio is only  $I = 0.058$ . In contrast, the  $M = 0.50$  jet in Fig. 5.10 has a momentum ratio of  $I = 0.24$ . Evidently, the flow physics changes somewhat at very low coolant flow rates. Although it may be tempting to blame this unusual contour pattern on a defective model, no defects were evident aside from the  $59 \mu m$  surface roughness described in Section 4.1. Furthermore, three other leading edge models were tested, all of which exhibited this phenomenon. Since  $Re_D$  was adjusted by varying the freestream velocity and  $M$  was adjusted by varying the coolant mass flow rate, the coolant flow rate at  $M = 0.25$  with  $Re_D = 60k$  was approximately equal to the coolant flow rate at  $M = 0.5$  with  $Re_D = 30k$ . This suggests that the fingering phenomenon may be related to the coolant Reynolds number, which is approximately equal in both of these cases. The phenomenon continues to occur at even lower blowing ratios as shown in Fig. 5.19, which depicts the adiabatic effectiveness contours at  $M = 0.1$  at low freestream turbulence,  $Re_D = 60k$ . Although not shown, the fingering phenomenon still does not occur for the high turbulence condition, even at  $M = 0.1$ . Section 7.1 will provide additional insight with flow visualization and Section 9.1 discusses some observations of this phenomenon with computational simulations.

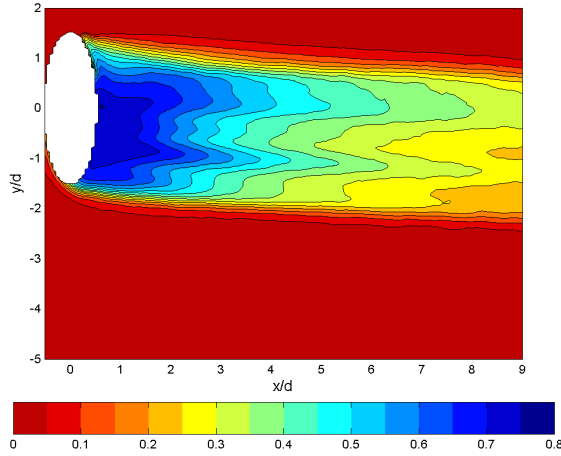


**Fig. 5.15** Adiabatic effectiveness contours for steady film cooling,  $\gamma = \eta$ ,  $M = 0.25$ , low  $Tu$ ,  $Re_D = 60k$

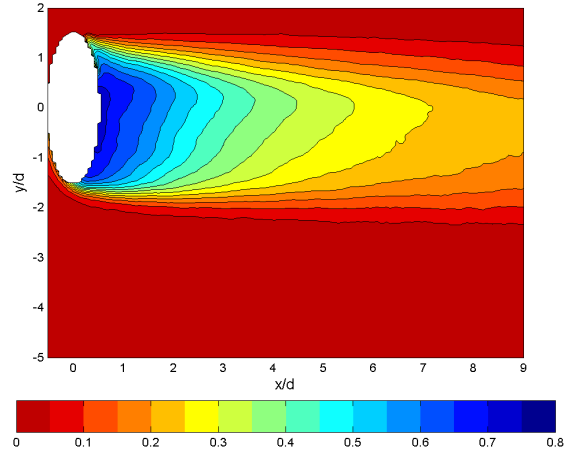


**Fig. 5.16** Adiabatic effectiveness contours for steady film cooling,  $\gamma = \eta$ ,  $M = 0.25$ , high  $Tu$ ,  $Re_D = 60k$

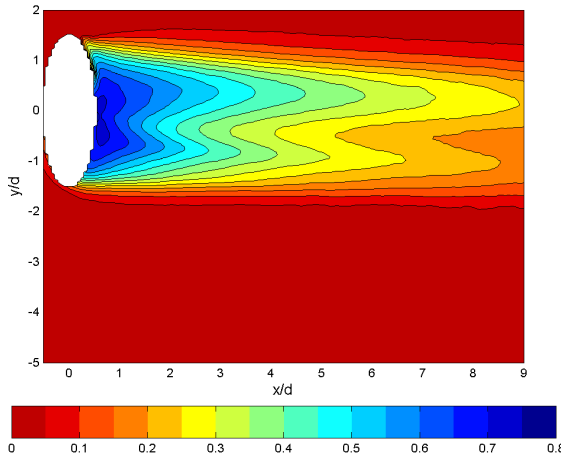


**Fig. 5.17** Adiabatic effectiveness contours for steady film cooling,  $\gamma = \eta$ ,  $M = 0.25$ , low  $Tu$ ,  $Re_D = 30k$

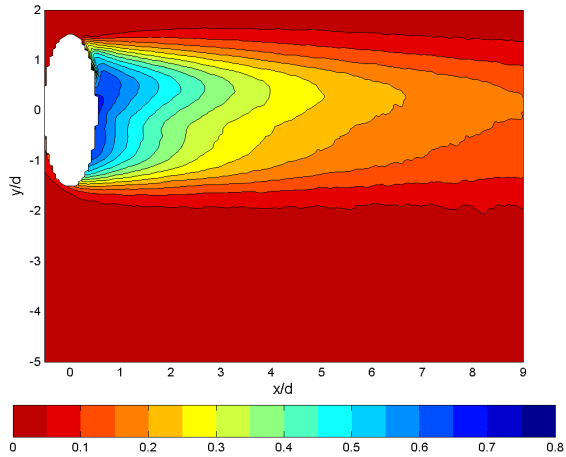


**Fig. 5.18** Adiabatic effectiveness contours for steady film cooling,  $\gamma = \eta$ ,  $M = 0.25$ , high  $Tu$ ,  $Re_D = 30k$

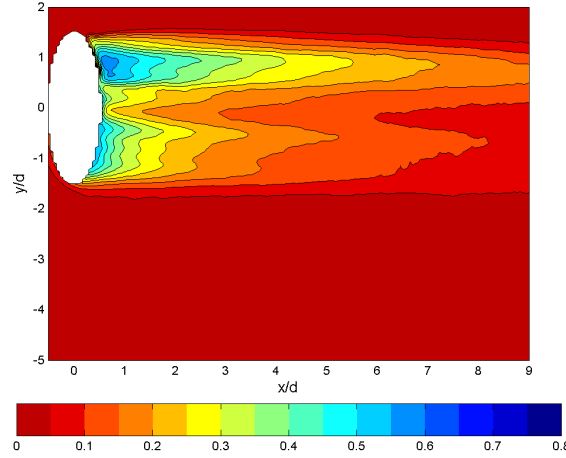


Fig. 5.19 Adiabatic effectiveness contours for steady film cooling,  $\gamma = \eta$ ,  $M = 0.1$ , low  $Tu$ ,  $Re_D = 60k$

### 5.1.2. Influence of Freestream Turbulence and Reynolds Number on Frössling Number

Heat transfer coefficients were nondimensionalized in the form of the Frössling number,  $Fr \equiv Nu_D / \sqrt{Re_D}$ . Kays and Crawford (1980) demonstrate through a boundary layer analysis that the stagnation Frössling number on a circular cylinder in cross flow may be written,

$$Fr = 1.15Pr^{0.4} \quad (5.1)$$

In the case of air for which  $Pr = 0.705$ , we find that the stagnation Frössling number is conveniently  $Fr = 1.00$ . On a circular cylinder,  $Fr$  decreases downstream of the stagnation line at the leading edge. From Giedt (1949), we find that at  $40^\circ$  from the stagnation line,  $Fr$  is approximately 0.9 at  $Re_D = 71k$ . There is some Reynolds number dependence off the stagnation line due in part to turbulent transition and separation.

In order to validate the experimental technique used to measure heat transfer coefficient, Fig. 5.20 shows the Frössling number as a function of angular distance downstream from the stagnation along a line at approximately  $y/d = 5.5$ , sufficiently far from the coolant hole that its influence on  $h$  is negligible, verified by the absence of significant spanwise gradients in  $h$  at that location. Since the Frössling solution given by Eq. (5.1) was developed for the ideal case of no freestream turbulence, only the low turbulence cases match the theoretical stagnation value ( $Fr = 1.00$ ) well. At  $Re_D = 60k$ ,

the measured stagnation Frössling number was  $Fr = 1.01$  and at  $Re_D = 30k$ , the measured stagnation Frössling number was  $Fr = 1.03$ . At  $40^\circ$  from the stagnation line, the measured values were 0.91 and 0.92 for  $Re_D = 60k$  and  $30k$ , respectively. The results compare well with the results of the circular cylinder experiments of Giedt (1949) out to  $60^\circ$  from the stagnation line, at which point the results begin to differ. Giedt's heat transfer coefficient drops more rapidly at that point than the results of the present study and Giedt observed an apparent turbulent transition at approximately  $77^\circ$ . Differences between Giedt's circular cylinder and the half cylinder with a flat afterbody may be responsible for these differences in  $Fr$  in the region approaching the  $90^\circ$  point. Mick and Mayle (1988) used a geometry identical to that used presently, but the Reynolds number was markedly higher ( $Re_D = 100k$ ). The results of Mick and Mayle agree well with the present study within  $30^\circ$  from the stagnation line; however Mick and Mayle observed a more gradual decrease in  $Fr$  than either Giedt or the present study. At the  $66^\circ$  location, Mick and Mayle report a Frössling number 15% higher than the present study. Differences cannot be attributed due to differences in the freestream turbulence intensity; Mick and Mayle used  $Tu = 0.4\%$ , similar to the low turbulence condition in the present study. In order to determine if the differences may be due to the higher  $Re_D$  used by Mick and Mayle, Giedt's circular cylinder results at  $Re_D = 101k$  are presented. Giedt reported a slight increase in  $Fr$  with the higher  $Re_D$ , but not one large enough to account for the differences. At any rate, we shall be satisfied with the excellent agreement of the present results with those of Giedt. High turbulence cases from the present study are also shown in Fig. 5.20 to demonstrate the dependence of  $Fr$  on freestream turbulence intensity.

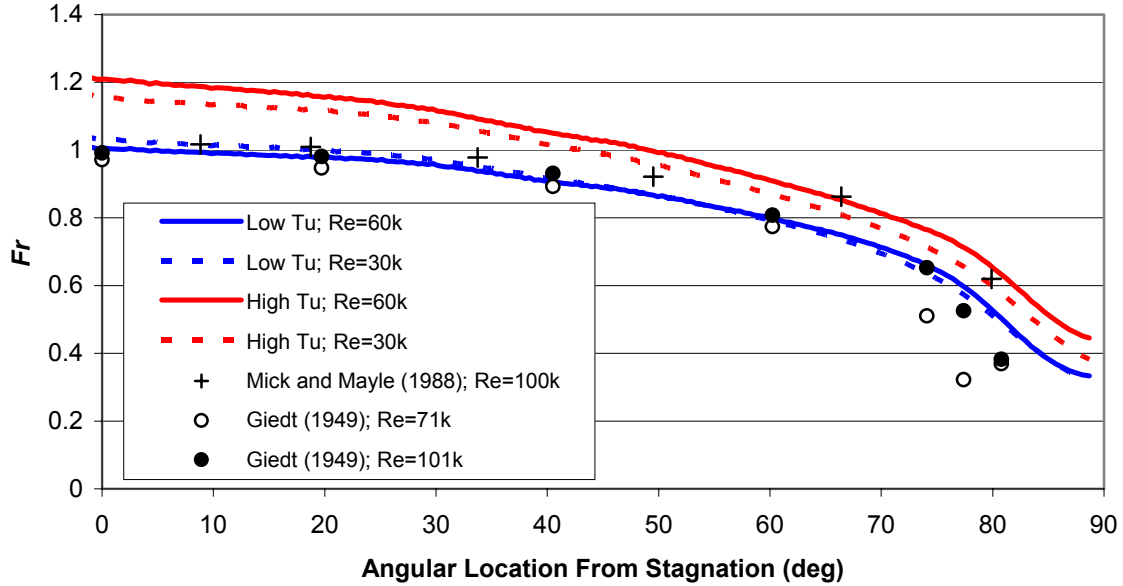


**Fig. 5.20 Frössling number distribution with no film cooling and no influence of film cooling hole**

In Fig. 5.20 the non-film-cooled surface Frössling number was virtually unaffected ( $\sim 3\%$  effect) by changing  $Re_D$  at the low turbulence condition. Note that only with zero freestream turbulence should there be no influence of  $Re_D$  on stagnation  $Fr$ . There was a weak influence of  $Re_D$  at high turbulence, with the higher Reynolds number yielding approximately 5% higher  $Fr$  than the lower Reynolds number at the stagnation line. The influence of freestream turbulence is much more pronounced, with the high freestream turbulence yielding stagnation Frössling numbers 21% and 12% higher than low turbulence for the high and low Reynolds numbers, respectively. At the location where the film cooling hole would be ( $21.5^\circ$  from the leading edge), the high turbulence case yields a Frössling number 18% higher than at low turbulence for the  $Re_D = 60k$  case and 12% higher with the  $Re_D = 30k$  case, exemplifying that turbulence intensity has a greater influence on  $Fr$  at the higher Reynolds number.

In order to understand the influence of the film cooling jet on heat transfer coefficient, spatial Frössling number distributions with film cooling were compared to those with the film cooling jet turned off at the same freestream conditions. The  $Fr_f / Fr_0$  results are shown in Figs. 5.21 through 5.32. As in Section 5.1.1, the figures

for each of the four freestream conditions are grouped according to blowing ratio. Clearly, the higher blowing ratios cause higher elevations in the heat transfer coefficient. At  $M = 1.5$  (see Fig. 5.21), the film cooling is responsible for a localized increase of 110% ( $Fr_f / Fr_0 = 2.1$ ) at low turbulence,  $Re_D = 60k$ . On the other hand, the analogous  $M = 0.25$  jet in Fig. 5.29 causes a localized increase of only 20%, with most of the area virtually unaffected by the jet. In all of these cases, the location of maximum  $Fr$  augmentation is at  $y/d > 0$ , even though Figs. 5.6 through 5.18 show that the peak adiabatic effectiveness is generally at  $y/d < 0$ . In Fig. 5.29, two distinct regions of peak  $Fr$  occur downstream of the coolant hole. This is a classic “fork tine” pattern of heat transfer coefficient that is well documented for many film cooling jets. Similar fork-tine patterns appear for  $M = 0.5$ ,  $Re_D = 30k$  in Figs. 5.27 and 5.28.

The influence of the film cooling jet itself is generally less at high freestream turbulence than at low freestream turbulence due to greater relative mixing of the jet at low turbulence compared to mixing resulting from freestream turbulence. This observation is evident with lower  $Fr_f / Fr_0$  values at high freestream turbulence than at low freestream turbulence.<sup>n</sup> For example, comparing Figs. 5.21 and 5.22 reveals that switching from low turbulence to high turbulence decreases the peak  $Fr_f / Fr_0$  from approximately 2.1 to 1.8 at  $M = 1.5$ ,  $Re_D = 60k$ .

Reducing the freestream Reynolds number from  $Re_D = 60k$  to  $Re_D = 30k$  tends to reduce  $Fr_f / Fr_0$  in the figures shown here. Although the influence is very small at  $M = 1.5$ , the influence of Reynolds number on  $Fr_f / Fr_0$  becomes stronger at lower blowing ratios. For example, comparing Figs. 5.25 and 5.27 reveals that the peak value of  $Fr_f / Fr_0$  is reduced from approximately 1.8 to 1.2 by reducing  $Re_D$  from 60k to 30k at  $M = 0.5$ , low freestream turbulence. This effect is due to an actual reduction in  $Fr_f$  when  $Re_D$  is reduced as opposed to an increase in  $Fr_0$ .

<sup>n</sup> Recall that for the purposes of determining net heat flux reduction due to film cooling, both  $Fr$  and  $Fr_0$  in the ratio  $Fr / Fr_0$  are acquired at the same freestream condition.

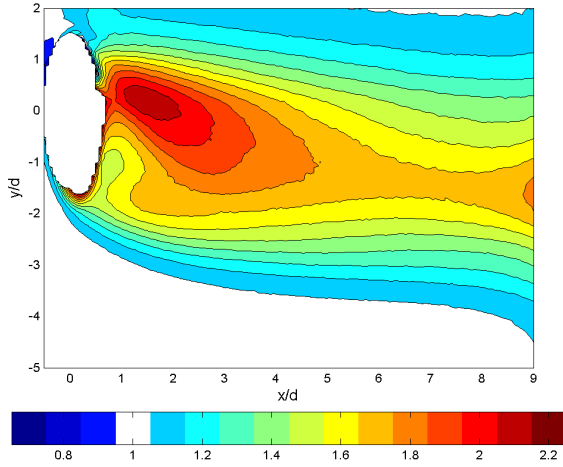


**Fig. 5.21**  $Fr_f / Fr_0$  contours for steady film cooling,  $M = 1.5$ , low  $Tu$ ,  $Re_D = 60k$

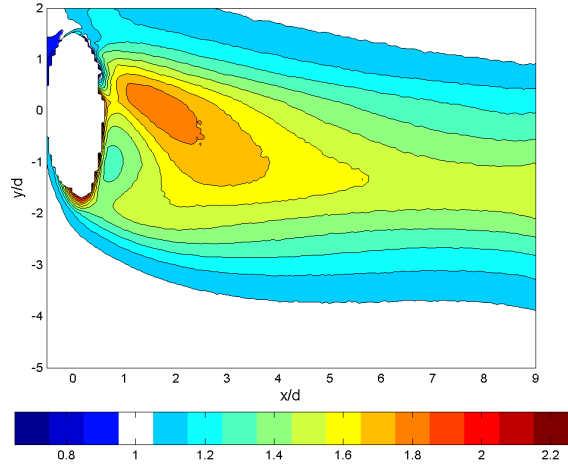


**Fig. 5.22**  $Fr_f / Fr_0$  contours for steady film cooling,  $M = 1.5$ , high  $Tu$ ,  $Re_D = 60k$

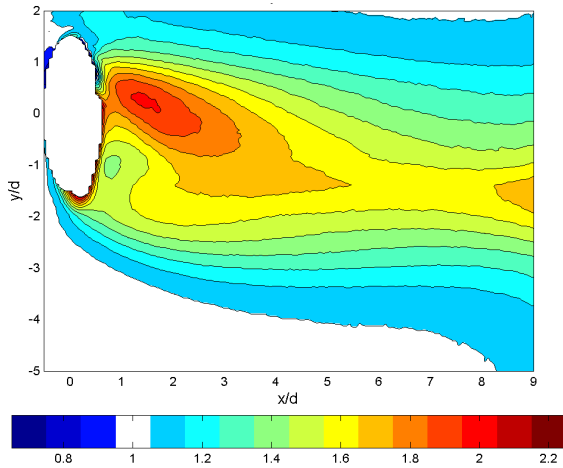


**Fig. 5.23**  $Fr_f / Fr_0$  contours for steady film cooling,  $M = 1.5$ , low  $Tu$ ,  $Re_D = 30k$

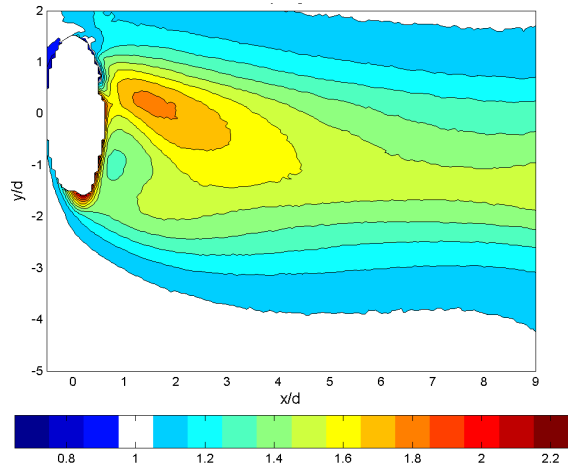


**Fig. 5.24**  $Fr_f / Fr_0$  contours for steady film cooling,  $M = 1.5$ , high  $Tu$ ,  $Re_D = 30k$

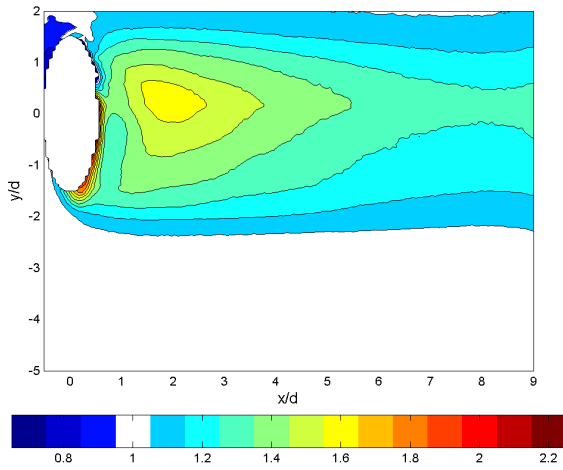


**Fig. 5.25**  $Fr_f / Fr_0$  contours for steady film cooling,  $M = 0.5$ , low  $Tu$ ,  $Re_D = 60k$

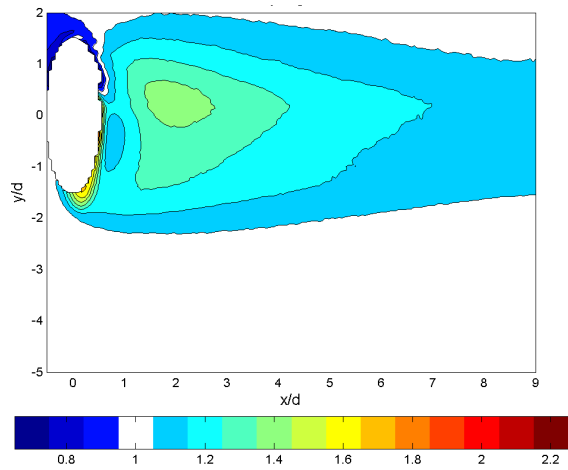


**Fig. 5.26**  $Fr_f / Fr_0$  contours for steady film cooling,  $M = 0.5$ , high  $Tu$ ,  $Re_D = 60k$

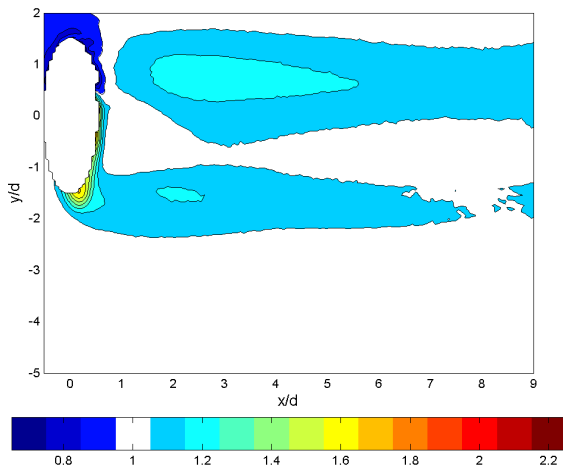


**Fig. 5.27**  $Fr_f / Fr_0$  contours for steady film cooling,  $M = 0.5$ , low  $Tu$ ,  $Re_D = 30k$

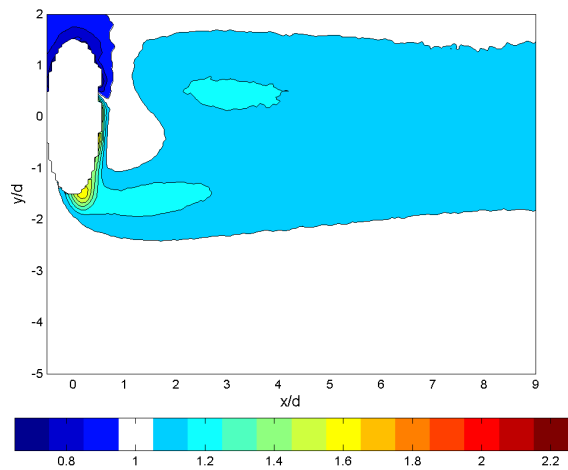


**Fig. 5.28**  $Fr_f / Fr_0$  contours for steady film cooling,  $M = 0.5$ , high  $Tu$ ,  $Re_D = 30k$

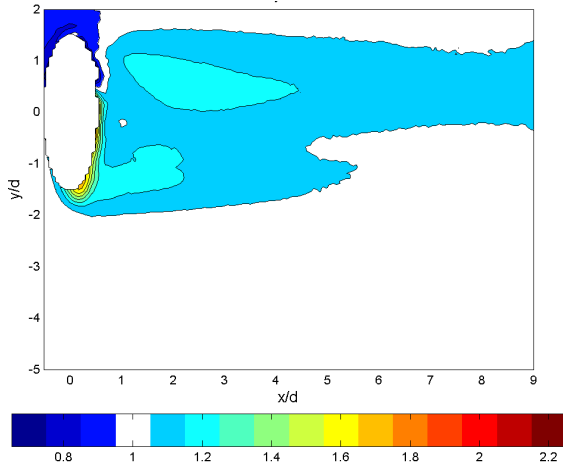


**Fig. 5.29**  $Fr_f / Fr_0$  contours for steady film cooling,  $M = 0.25$ , low  $Tu$ ,  $Re_D = 60k$

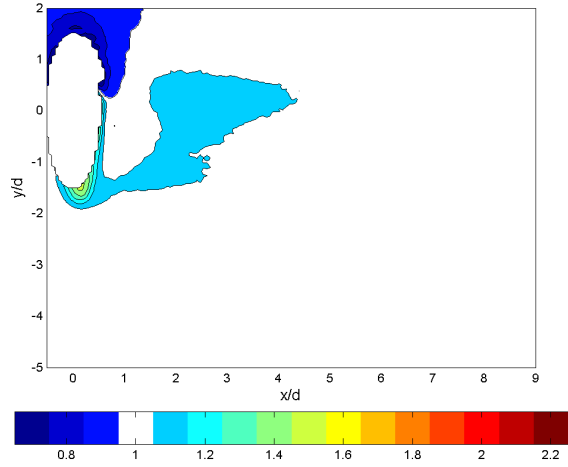


**Fig. 5.30**  $Fr_f / Fr_0$  contours for steady film cooling,  $M = 0.25$ , high  $Tu$ ,  $Re_D = 60k$

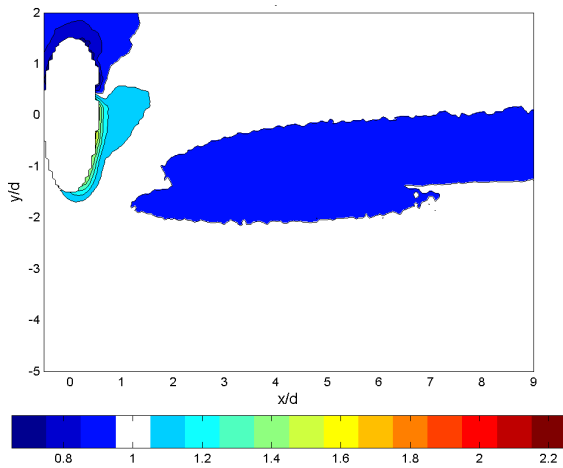


**Fig. 5.31**  $Fr_f / Fr_0$  contours for steady film cooling,  $M = 0.25$ , low  $Tu$ ,  $Re_D = 30k$

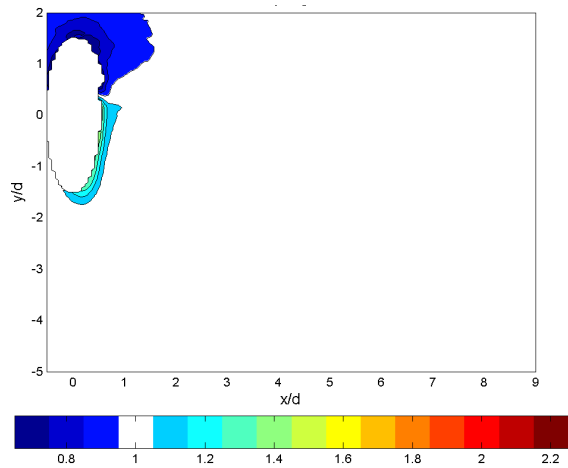


**Fig. 5.32**  $Fr_f / Fr_0$  contours for steady film cooling,  $M = 0.25$ , high  $Tu$ ,  $Re_D = 30k$

Frössling number ratios are summarized in the area-averaged sense in Fig. 5.33 for a range of blowing ratios. The trend of higher  $Fr_f / Fr_0$  at low freestream turbulence is very evident and is always the case for  $M > 0.5$ . At low freestream turbulence, the earlier noted trend that  $Fr_f / Fr_0$  is higher at  $Re_D = 60k$  than at  $Re_D = 30k$  rings true; however, at high freestream turbulence the effect of Reynolds number appears to be the opposite. The exceptions of this effect tend to be exemplified by the figures shown earlier, particularly at  $M = 0.25$  and  $1.5$ .

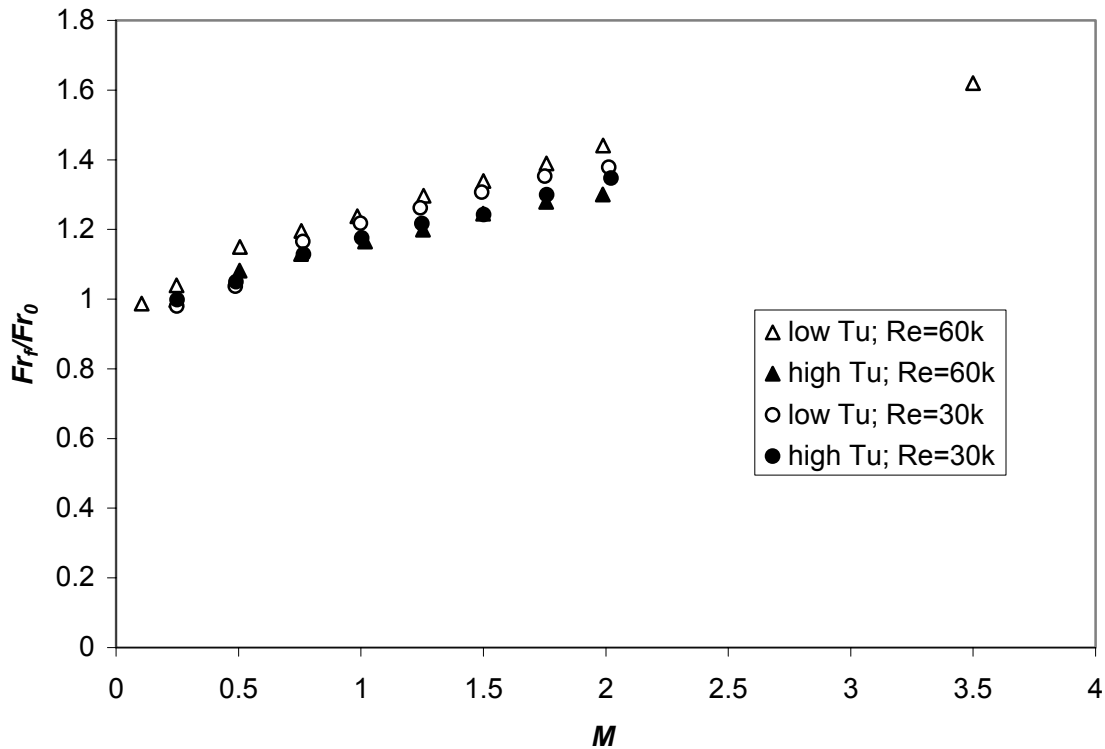


Fig. 5.33 Area averaged  $Fr_f / Fr_0$  for steady film cooling

### 5.1.3. Influence of Freestream Turbulence and Reynolds Number on Net Heat Flux Reduction

The net heat flux reduction was calculated using the heat transfer coefficient ratios (Figs. 5.21 through 5.32) along with the adiabatic effectiveness results (Figs. 5.6 through 5.18) with Eq. (3.31), noting that  $\eta = \gamma$  with steady film cooling and the Frössling number ratio,  $Fr_f / Fr_0$  is equivalent to  $h_f / h_0$ . An overall effectiveness of  $\phi = 0.6$  was used for the calculations. The net heat flux reduction contours for  $M = 1.5$ , 0.5, and 0.25 are shown in Figs. 5.34 through 5.45. The  $M = 1.5$  case performs so miserably that a large swath of Fig. 5.34 is out of range of the contours, selected to show better resolution where  $\Delta q_r > 0$ . This is a result of enormous heat transfer coefficient augmentation as shown in Fig. 5.21 in a location with very low adiabatic effectiveness as shown in Fig. 5.6. The  $M = 0.5$  case performs significantly better, although there is still a region of  $\Delta q_r < 0$  where there was significant heat transfer coefficient augmentation, but little

protection from the coolant. For example, Fig. 5.38 shows a region of  $\Delta q_r < 0$  downstream of the top portion of the coolant hole. The adiabatic effectiveness contour plot in Fig. 5.11 shows that this upper region is not protected as well as the lower region; however in the  $Fr_f / Fr_0$  plot in Fig. 5.25, the increase in heat transfer coefficient due to the film cooling jet is actually biased toward the upper part of the coolant hole. The  $M = 0.25$  cases in Figs. 5.42 through 5.45 have  $\Delta q_r \geq 0$  everywhere due to excellent film coverage and very little heat transfer coefficient augmentation (see Figs. 5.29 through 5.32), resulting in  $\Delta q_r$  contours that closely resemble the shapes of the  $\eta$  contours (see Figs. 5.29 through 5.32).

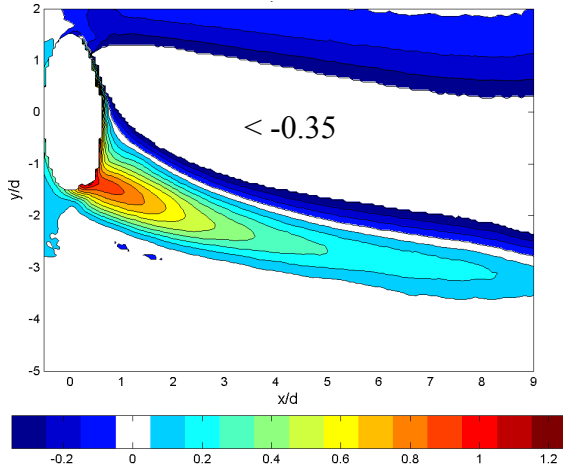


Fig. 5.34 Net heat flux reduction,  $\Delta q_r$ , contours for steady film cooling,  $M = 1.5$ , low  $Tu$ ,  $Re_D = 60k$

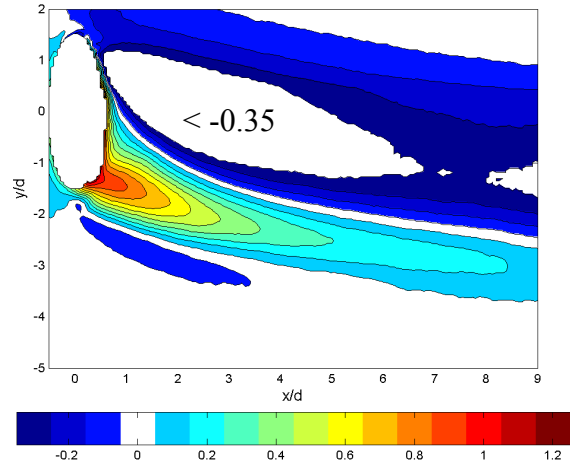


Fig. 5.35 Net heat flux reduction,  $\Delta q_r$ , contours for steady film cooling,  $M = 1.5$ , high  $Tu$ ,  $Re_D = 60k$

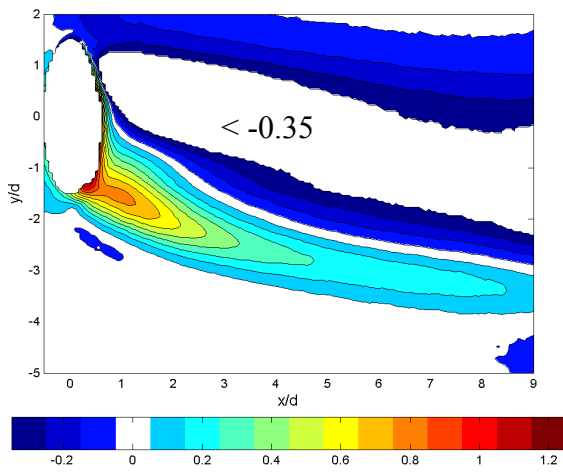


Fig. 5.36 Net heat flux reduction,  $\Delta q_r$ , contours for steady film cooling,  $M = 1.5$ , low  $Tu$ ,  $Re_D = 30k$

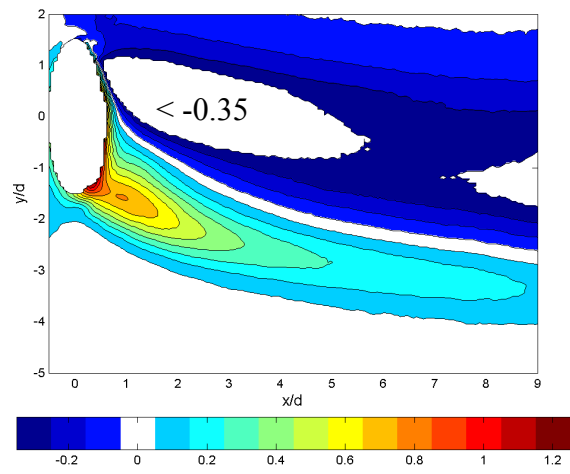


Fig. 5.37 Net heat flux reduction,  $\Delta q_r$ , contours for steady film cooling,  $M = 1.5$ , high  $Tu$ ,  $Re_D = 30k$

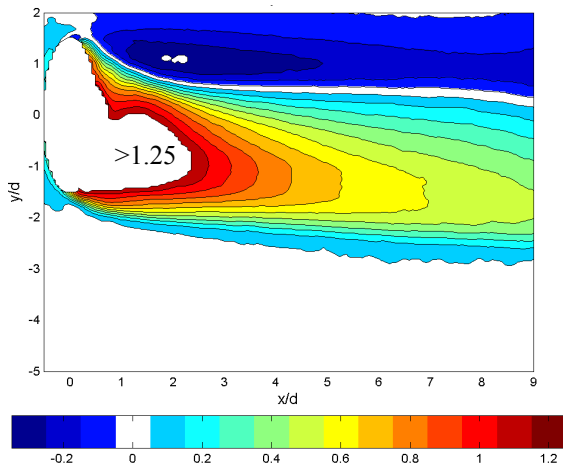


Fig. 5.38 Net heat flux reduction,  $\Delta q_r$ , contours for steady film cooling,  $M = 0.5$ , low  $Tu$ ,  $Re_D = 60k$

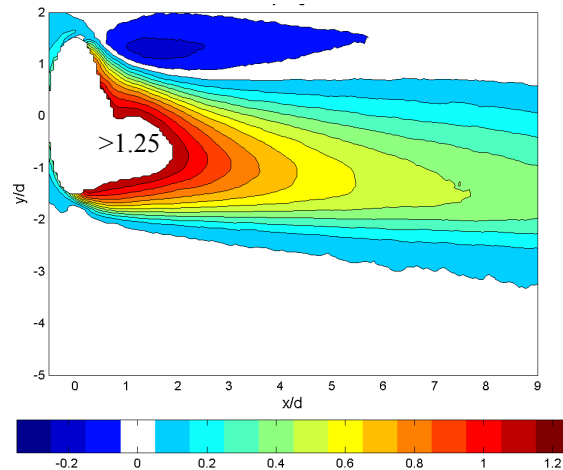


Fig. 5.39 Net heat flux reduction,  $\Delta q_r$ , contours for steady film cooling,  $M = 0.5$ , high  $Tu$ ,  $Re_D = 60k$

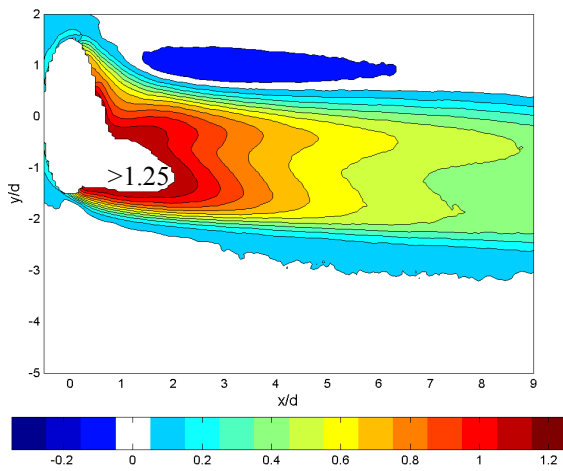


Fig. 5.40 Net heat flux reduction,  $\Delta q_r$ , contours for steady film cooling,  $M = 0.5$ , low  $Tu$ ,  $Re_D = 30k$

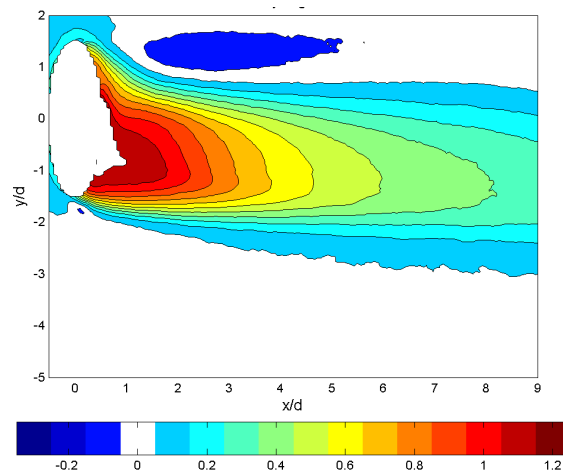
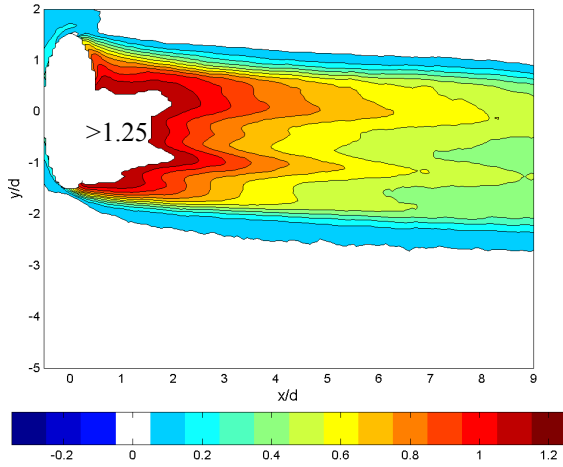
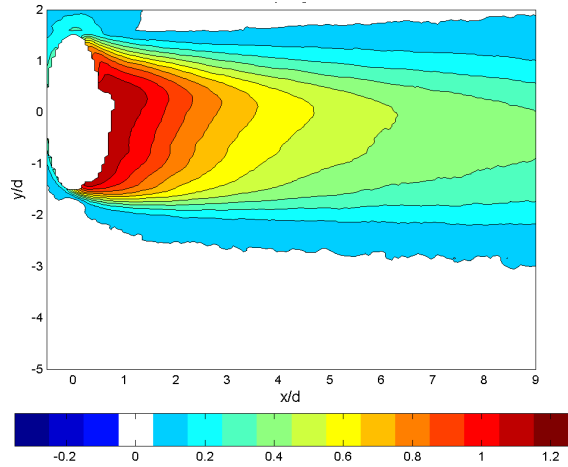


Fig. 5.41 Net heat flux reduction,  $\Delta q_r$ , contours for steady film cooling,  $M = 0.5$ , high  $Tu$ ,  $Re_D = 30k$



**Fig. 5.42** Net heat flux reduction,  $\Delta q_r$ , contours for steady film cooling,  $M = 0.25$ , low  $Tu$ ,  $Re_D = 60k$



**Fig. 5.43** Net heat flux reduction,  $\Delta q_r$ , contours for steady film cooling,  $M = 0.25$ , high  $Tu$ ,  $Re_D = 60k$

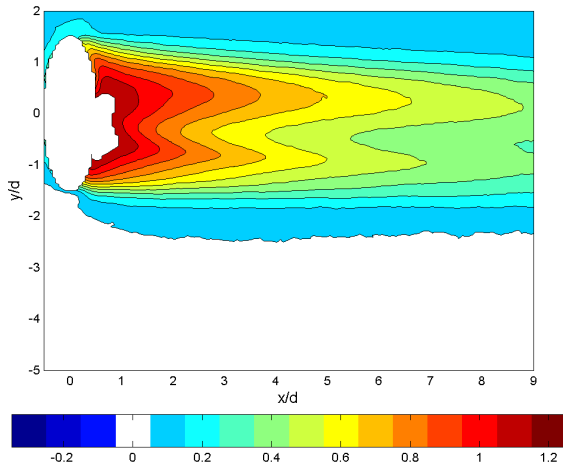


**Fig. 5.44** Net heat flux reduction,  $\Delta q_r$ , contours for steady film cooling,  $M = 0.25$ , low  $Tu$ ,  $Re_D = 30k$

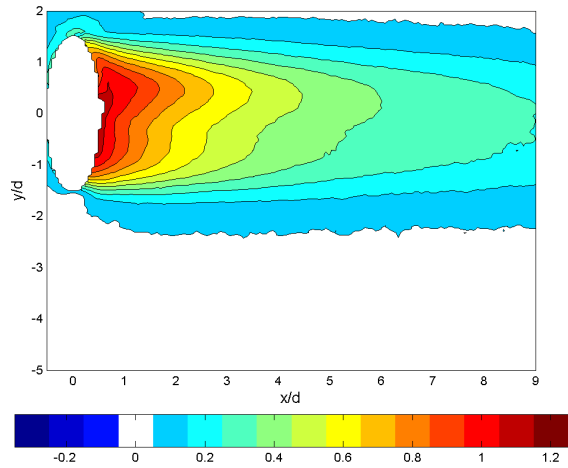


**Fig. 5.45** Net heat flux reduction,  $\Delta q_r$ , contours for steady film cooling,  $M = 0.25$ , high  $Tu$ ,  $Re_D = 30k$

The net heat flux reduction is summarized in the area-averaged sense in Fig. 5.46. The net heat flux reduction is a strong function of the blowing ratio, with peak performance at  $M < 0.75$  for all freestream conditions. At  $M > 1.25$ , the net heat flux to the leading edge is increased by film cooling. For this particular leading edge film cooling hole, it would be very easy to waste thermodynamically expensive coolant while negating the very purpose of the coolant.

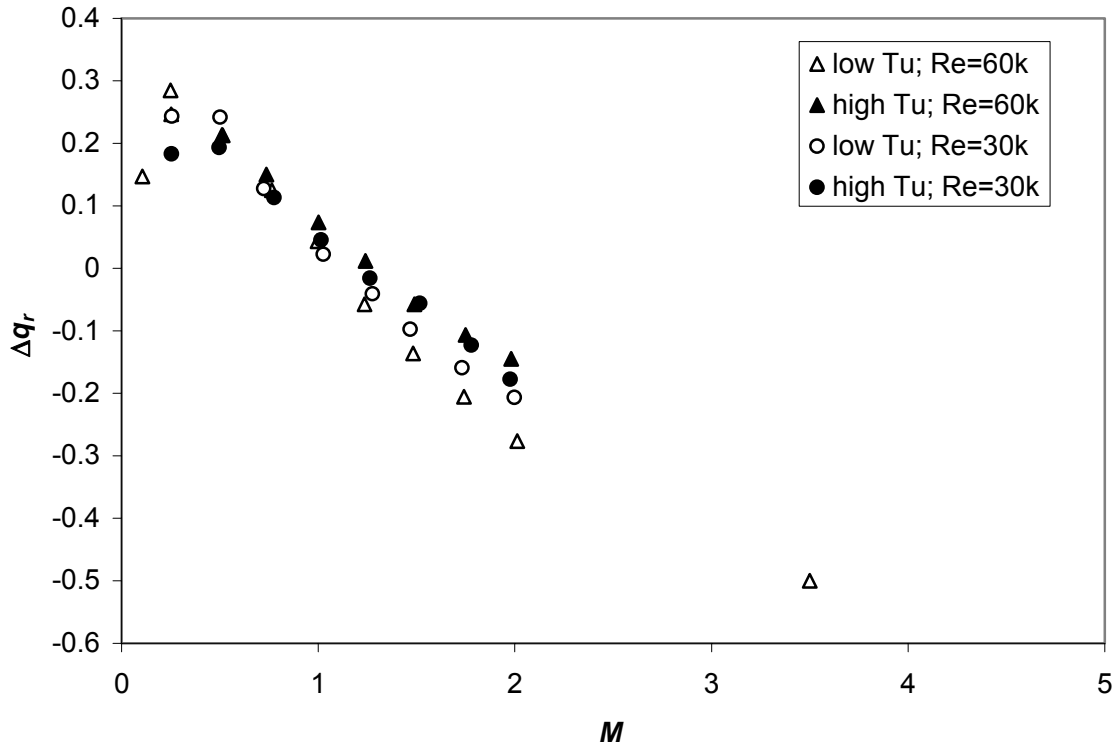


Fig. 5.46 Area averaged  $\Delta q_r$  for steady film cooling

## 5.2 Pulsed Jet Results

In this section, we present the experimental measurements of  $\gamma$ , the unsteady coupled adiabatic effectiveness with pulsed film cooling and the influence of pulsed film cooling on Frössling number.  $\gamma$  is defined in Eq. (3.29) and repeated here:

$$\gamma \equiv \overline{\eta} + \frac{\overline{h_f' \eta'}}{\overline{h_f}} \quad (3.29)$$

Although  $\gamma = \eta$  for the special case of steady film cooling (as in Section 5.1), it is worth emphasizing that for the general pulsed film cooling conditions presented here,  $\gamma \neq \eta$ . The importance of  $\gamma$  lies in the fact that it can be used to determine the net heat flux reduction in a fashion analogous to  $\eta$  with steady film cooling. The net heat flux reduction was determined using Eq. (3.31), repeated here:

$$\overline{\Delta q_r} = 1 - \frac{\overline{h_f}}{h_0} \left( 1 - \frac{\gamma}{\phi} \right) \quad (3.31)$$

For convenience, the Frössling number ratio,  $\overline{Fr_f} / Fr_0$  may be substituted for  $\overline{h_f} / h_0$ .

Since an objective of this study is to determine the influence of pulsing an otherwise steady jet at the same average coolant flow rate on the heat flux, we also find use for a parameter that describes the net heat flux reduction due to pulsing. This is in contrast to Eq. (3.31), in that Eq. (3.31) merely gives the net heat flux reduction due to film cooling relative to a non-film-cooled surface. Instead we desire the following formulation:

$$\overline{\Delta q_{r,pulsed}} \equiv 1 - \frac{\overline{q_f''}}{q_{f''}^{steady}} \quad (5.2)$$

From the definition of  $\Delta q_r$  in Eq. (3.13), we can rewrite this in terms of the net heat flux reduction calculated from Eq. (3.31).

$$\overline{\Delta q_{r,pulsed}} = 1 - \frac{\overline{\Delta q_r} - 1}{\Delta q_{r,steady} - 1} \quad (5.3)$$

Due to the meaningful definition of area averaged net heat flux reduction in Eq. (4.51), area averaged quantities may be substituted in the right hand side of Eq. (5.3) to yield the area averaged  $\overline{\Delta q_{r,pulsed}}$ .

The experimental methodology is presented in detail in Section 4.3. The parameter space includes two freestream Reynolds numbers ( $Re_D = 60k$  and  $30k$ ), average blowing ratios,  $\overline{M}$ , in the range  $0 \leq \overline{M} \leq 2.0$  with resolution of  $\Delta \overline{M} = 0.25$  (although it was not possible to perform some experiments in the entire range due to the high pressures required to force the coolant through the solenoid valves), duty cycles  $DC = 25\%$ ,  $50\%$ , and  $75\%$  (again when possible), pulsing frequencies of 20 Hz, 40 Hz, and 80 Hz, and two freestream turbulence intensities.<sup>o</sup> Additionally, two waveform shapes were attained through either partial or complete closure of the solenoid valves. The waveforms are described in Appendix A. The two freestream turbulence intensities are simply referred as “high” or “low.” More detailed information on the freestream turbulence characteristics is presented in Table 4.1 on page 47. The nondimensional frequencies ( $F$ ) corresponding to the dimensional frequencies ( $f$ ) of the solenoid valve

<sup>o</sup> At engine conditions, the 20 Hz case would scale to approximately 3.5 kHz.

controller are presented in Table 5.1. The nondimensional frequencies varied as indicated in Table 5.1 due to small differences in the freestream velocity necessary to maintain the appropriate freestream Reynolds number despite changes in the freestream temperature. The nondimensional frequencies were held to within approximately 3% of the average. Note that the  $F \approx 0.294$  and  $F \approx 0.594$  cases were run for both freestream Reynolds numbers (see arrows in Table 5.1); however, the different dimensional frequencies result in different waveforms as described in Appendix A. The 80 Hz pulsing frequency was used only in the complete valve closure configuration and the 40 Hz pulsing frequency was used only in the partial valve closure configuration.

**Table 5.1 Dimensional Frequencies and Corresponding Nondimensional Frequencies Used in Net Heat Flux Reduction Experiments**

<b>Dimensional Pulsing Frequency</b>	<b>Nondimensional Frequency with <math>Re_D = 30000</math></b>	<b>Nondimensional Frequency with <math>Re_D = 60000</math></b>
20 Hz	0.294±0.010	0.148±0.004
40 Hz	0.590±0.019	0.295±0.009
80 Hz	1.195±0.025	0.598±0.019

We shall begin by considering how the pulsed jet compares with a steady jet at the baseline condition of low freestream turbulence and  $Re_D = 60k$ . This is followed by an examination of how variations in the freestream Reynolds number and turbulence intensity influence the pulsed jet performance.

### **5.2.1. The Baseline Condition: Low Freestream Turbulence, $Re_D = 60k$**

We begin by examining the pulsed jet results at the baseline condition of low freestream turbulence and  $Re_D = 60k$ . Figures 5.47 through 5.50 show contours of  $\gamma$  for several pulsing scenarios, all at  $\bar{M} = 0.25$  and  $F = 0.148$ . A great deal of dependence on the  $M(t)$  waveform shape is evident. An examination of the waveforms in Appendix A reveals the pattern that the more time the jet spends near the steady optimum blowing ratio of  $M = 0.25$  (see Fig. 5.5 on page 87), the higher the resulting  $\gamma$  contours. This is merely a qualitative hint at the validity of the low frequency approximation in Section

3.6. In fact, it is impossible to determine  $\gamma$  from the low frequency approximation with steady  $\eta$  data alone since  $\gamma$  contains  $\overline{h_f' \eta'}$  (see Eq. (3.29)); however, the dominant term in  $\gamma$  is  $\overline{\eta}$ . From Fig. 5.5, we can see that the curve of  $\eta(M)$  is very peaked and concave-down in the vicinity of  $M = 0.25$ . Thus any deviation from the mean value of  $\overline{M} = 0.25$  would result in a deterioration of performance in terms of  $\overline{\eta}$ . The complete valve closure (complete VC) configuration had larger amplitude fluctuations in  $M(t)$  than the partial VC configuration due to more effective closing of the valves. The blowing ratio actually becomes negative during the complete VC configuration at this frequency. Clearly,  $\eta = 0$  during this short time that  $M < 0$ , but even when the jet turns back on, we would expect  $\eta$  to continue to be zero until the hot fluid that was ingested into the coolant hole is completely expelled. The 75% duty cycle had lower amplitude fluctuations in  $M(t)$  than the 50% duty cycle cases resulting from the same  $\overline{M}$  but with longer “on” times, thus more closely resembling a steady jet.

It is also worth noting a contrast between  $\gamma$  with the pulsed film cooling and  $\gamma$  with steady film cooling (see Fig. 5.15 on page 94). The steady case clearly yields higher values of  $\gamma$  than any of the pulsed cases. The coolant fingers extending downstream of the cooling hole are also much more pronounced with steady film cooling, although they are barely discernable in Figs. 5.47 and 5.48. The various blowing ratios that are achieved during the course of a cycle with pulsed coolant (each blowing ratio has its own unique  $\gamma$  positions of the coolant fingers, with none evident at  $M = 0.5$ ) causes a smearing of the fingers when the time average of the adiabatic effectiveness is taken.

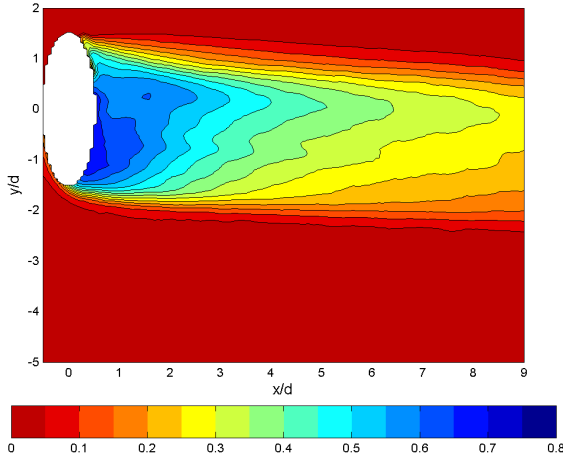


**Fig. 5.47**  $\gamma$  contours for  $\overline{M} = 0.25$ , low  $Tu$ ,  $Re_D = 60k$ ,  $F = 0.148$ ,  $DC = 50\%$ , partial VC

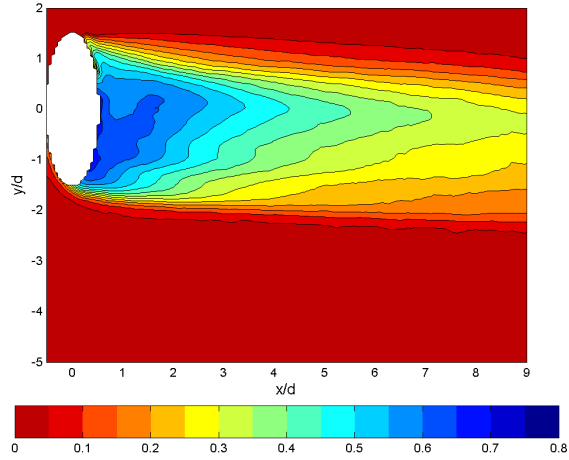


**Fig. 5.48**  $\gamma$  contours for  $\overline{M} = 0.25$ , low  $Tu$ ,  $Re_D = 60k$ ,  $F = 0.148$ ,  $DC = 75\%$ , partial VC

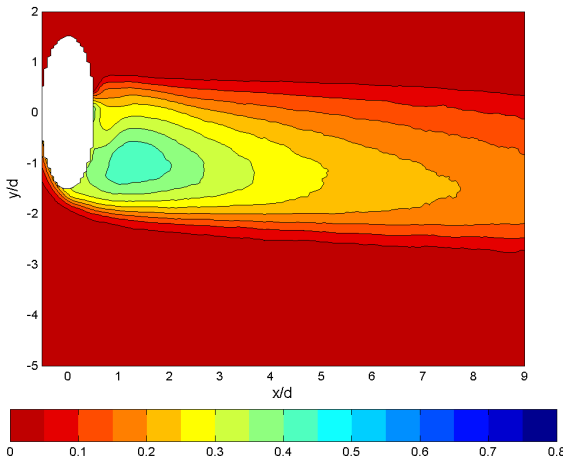


**Fig. 5.49**  $\gamma$  contours for  $\overline{M} = 0.25$ , low  $Tu$ ,  $Re_D = 60k$ ,  $F = 0.148$ ,  $DC = 50\%$ , complete VC

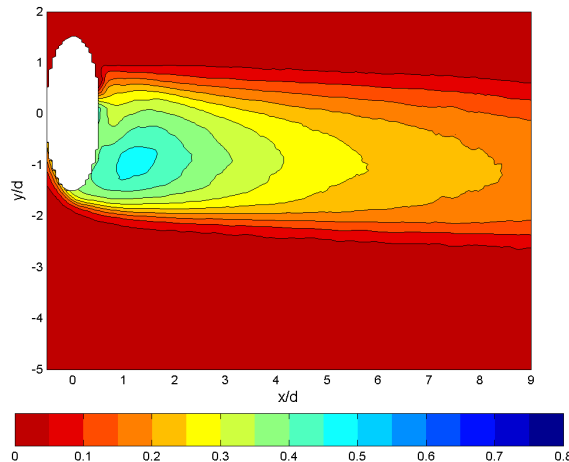


**Fig. 5.50**  $\gamma$  contours for  $\overline{M} = 0.25$ , low  $Tu$ ,  $Re_D = 60k$ ,  $F = 0.148$ ,  $DC = 75\%$ , complete VC

The nearly linear nature of the  $Fr_f / Fr_0$  curve as a function of steady blowing ratio (see Fig. 5.33) might lead one to expect that pulsing  $\gamma$  would have very little influence on  $\overline{Fr_f} / Fr_0$  relative to steady film cooling according to the low frequency approximation. Similarly, we might not expect much difference between low amplitude pulsing and high amplitude pulsing as we have with the partial VC and complete VC configurations. In fact, we might even expect the high amplitude (complete VC) configuration to occasionally give lower  $Fr_f / Fr_0$  due to a slight concave-down

curvature to the curve in Fig. 5.33 at extreme high and low  $M$ . Recall that unlike  $\eta$  or  $\gamma$ , we desire  $Fr_f / Fr_0$  to be low. As shown in Figs. 5.51 through 5.54, a beneficial influence of higher amplitude pulsing is not evident for  $\overline{M} = 0.25$ . In fact, the reverse is true; however, this is not inconsistent with the low frequency prediction technique and is addressed in Section 5.3.2. Although the differences between the 50% and 75% duty cycles are negligible, the partial VC configuration with generally lower amplitude pulsing had lower  $\overline{Fr}_f / Fr_0$  than the complete VC configuration.

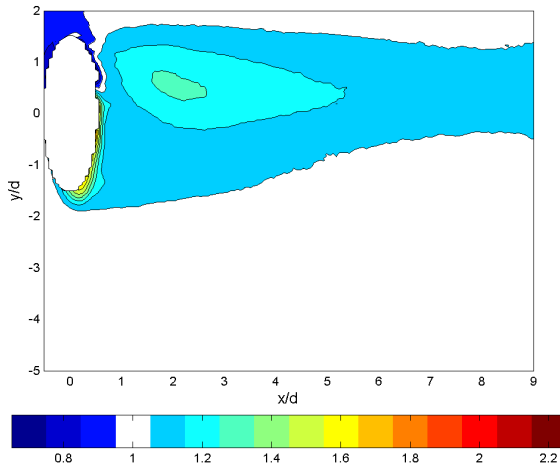


**Fig. 5.51**  $\overline{Fr}_f / Fr_0$  contours for  $\overline{M} = 0.25$ , low  $Tu$ ,  $Re_D = 60k$ ,  $F = 0.148$ ,  $DC = 50\%$ , partial VC

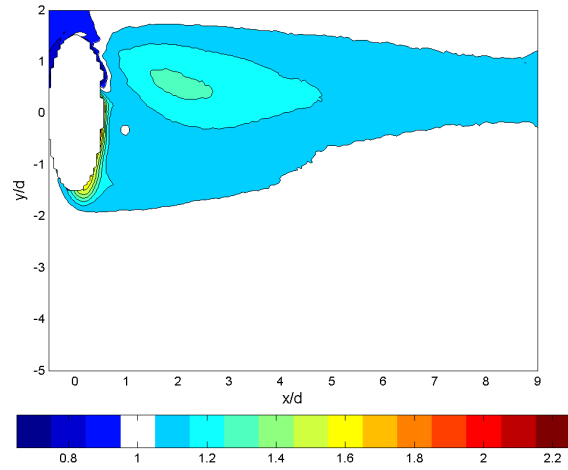


**Fig. 5.52**  $\overline{Fr}_f / Fr_0$  contours for  $\overline{M} = 0.25$ , low  $Tu$ ,  $Re_D = 60k$ ,  $F = 0.148$ ,  $DC = 75\%$ , partial VC

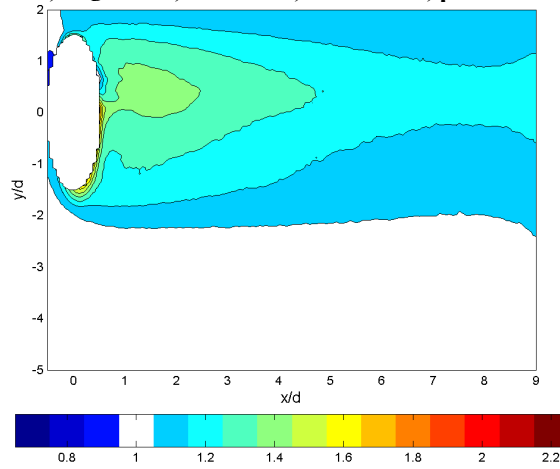


**Fig. 5.53**  $\overline{Fr}_f / Fr_0$  contours for  $\overline{M} = 0.25$ , low  $Tu$ ,  $Re_D = 60k$ ,  $F = 0.148$ ,  $DC = 50\%$ , complete VC

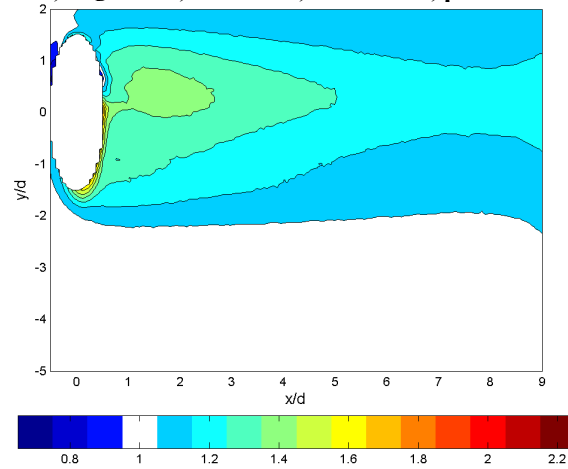


**Fig. 5.54**  $\overline{Fr}_f / Fr_0$  contours for  $\overline{M} = 0.25$ , low  $Tu$ ,  $Re_D = 60k$ ,  $F = 0.148$ ,  $DC = 75\%$ , complete VC

With both  $\gamma$  and  $\overline{Fr_f} / Fr_0$ , we observed more desirable performance from the lower amplitude pulsations than with higher amplitude pulsations. Thus, we should expect no different with  $\overline{\Delta q_r}$ , which is simply a combination of the influence of both of those parameters. The analogous  $\overline{\Delta q_r}$  plots for the  $\overline{M} = 0.25$  cases are shown in Figs. 5.55 through 5.58. The influence of the waveform shape on the net heat flux reduction is remarkable. The peak  $\overline{\Delta q_r}$  for both of the partial VC configuration cases was  $\overline{\Delta q_r} \approx 1.2$ , but was only  $\overline{\Delta q_r} \approx 0.7$  for the complete VC configuration. Again, this trend makes sense from the low frequency approximation by considering the concave-down nature of the steady  $\Delta q_r(M)$  curve in Fig. 5.46 in the vicinity of  $M = 0.25$ .

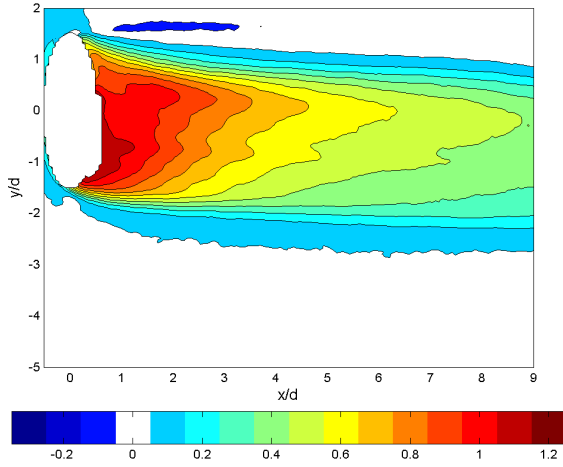


**Fig. 5.55**  $\overline{\Delta q_r}$  contours for  $\overline{M} = 0.25$ , low  $Tu$ ,  $Re_D = 60k$ ,  $F = 0.148$ ,  $DC = 50\%$ , partial VC

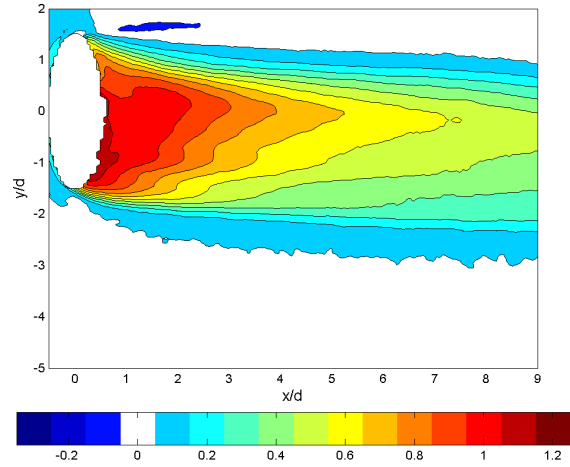


**Fig. 5.56**  $\overline{\Delta q_r}$  contours for  $\overline{M} = 0.25$ , low  $Tu$ ,  $Re_D = 60k$ ,  $F = 0.148$ ,  $DC = 75\%$ , partial VC

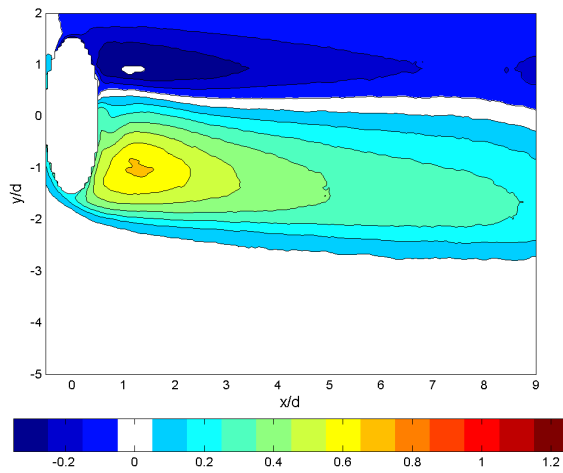


**Fig. 5.57**  $\overline{\Delta q_r}$  contours for  $\overline{M} = 0.25$ , low  $Tu$ ,  $Re_D = 60k$ ,  $F = 0.148$ ,  $DC = 50\%$ , complete VC

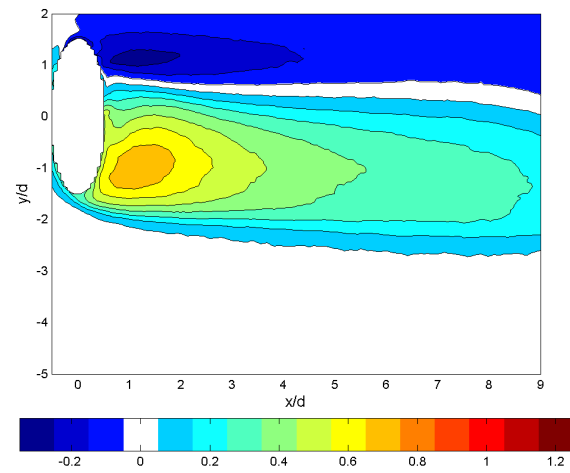


**Fig. 5.58**  $\overline{\Delta q_r}$  contours for  $\overline{M} = 0.25$ , low  $Tu$ ,  $Re_D = 60k$ ,  $F = 0.148$ ,  $DC = 75\%$ , complete VC

At higher blowing ratios, the shape of the performance curves as functions of steady blowing ratio changes significantly. The  $\eta(M)$  curve in Fig. 5.5 becomes concave-up at high  $M$ .  $\gamma$  contours for the partial VC and complete VC configurations are shown in Figs. 5.60 and 5.61 along with the corresponding steady results in Fig. 5.59. In neither pulsed case are the  $\gamma$  contours as high as in the steady case; however, the pulsed footprints are wider. In the context of the low frequency approximation, this could be described as a consequence of spending time at various blowing ratios, each

with its own unique degree of spanwise jet penetration. In fact, the  $\gamma$  contours for the complete VC configuration in Fig. 5.61 reveal two distinct tines, most evident along the  $\gamma = 0.05$  contour. This is probably a consequence of dwelling at two different blowing ratios, without spending much time at other blowing ratios in between.

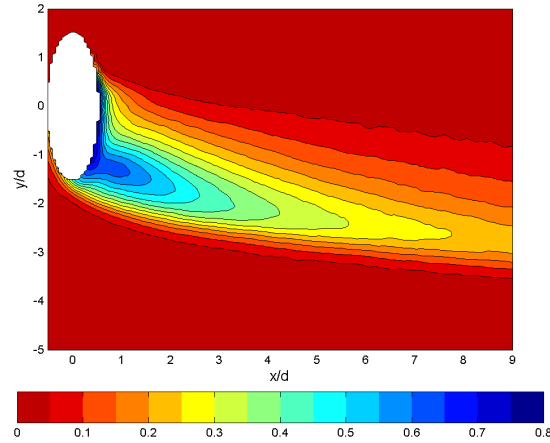


**Fig. 5.59**  $\gamma$  contours for  $M = 1.25$ , low  $Tu$ ,  $Re_D = 60k$ , steady

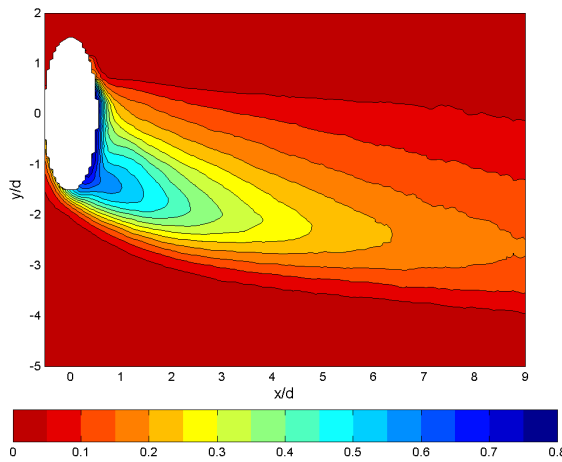


**Fig. 5.60**  $\gamma$  contours for  $\bar{M} = 1.25$ , low  $Tu$ ,  $Re_D = 60k$ ,  $F = 0.148$ ,  $DC = 50\%$ , partial VC

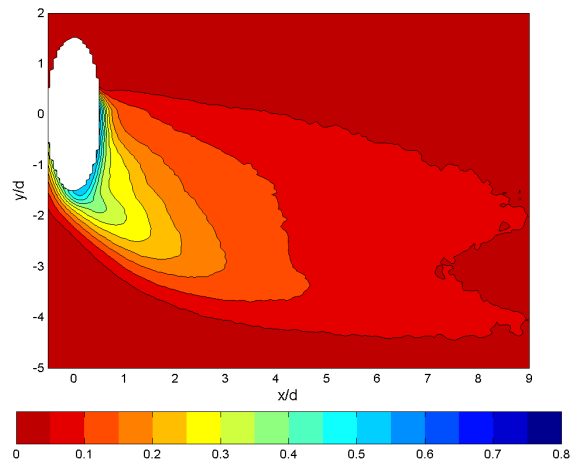


**Fig. 5.61**  $\gamma$  contours for  $\bar{M} = 1.25$ , low  $Tu$ ,  $Re_D = 60k$ ,  $F = 0.148$ ,  $DC = 50\%$ , complete VC

We shall now examine a case for which pulsing yielded a higher net heat flux reduction than steady film cooling. Figures 5.62 and 5.63 show the  $\gamma$  contours for the steady and  $F = 0.148$ ,  $DC = 50\%$ , partial VC pulsed cases at  $\bar{M} = 2.0$ , respectively. The pulsed case exhibits a wider  $\gamma$  footprint at the expense of  $\gamma$  contours that do not extend

as far downstream as in the steady film cooling case. The area-averaged  $\gamma$  from the pulsed case was measured to be 0.007 higher than the steady case. Heat transfer coefficient augmentation contours for the same steady and pulsed cases are shown in Figs. 5.64 and 5.65. Better performance (lower  $\overline{Fr_f} / Fr_0$ ) is obvious with the pulsed case than the steady case, with area averaged  $\overline{Fr_f}$  1.4% lower than the steady case. The result is an area averaged  $\overline{\Delta q_{r,pulsed}}$  of 2.9%, indicating that the pulsed case has 2.9% lower net heat flux than the steady case. The  $\overline{\Delta q_r}$  contours for the steady and pulsed cases are shown in Figs. 5.66 and 5.67. Note that the scales in Figs. 5.66 and 5.67 are inverted relative to prior NHFR contour plots to better represent negative  $\overline{\Delta q_r}$  values. The minimum  $\overline{\Delta q_r}$  is in the -1 contour interval in the pulsed case, but is in the -1.2 contour interval for the steady case.

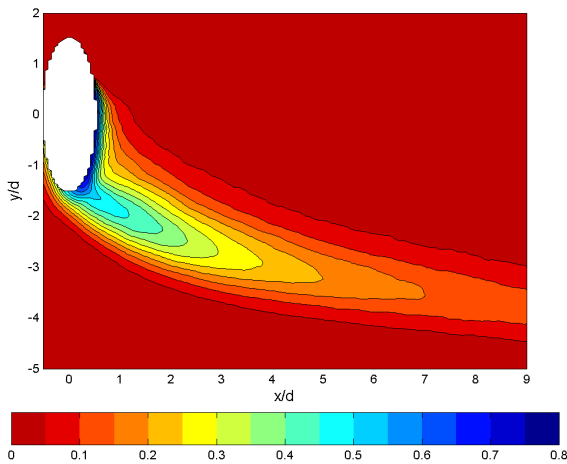


**Fig. 5.62**  $\gamma$  contours for  $\overline{M} = 2.0$ , low  $Tu$ ,  $Re_D = 60k$ , steady

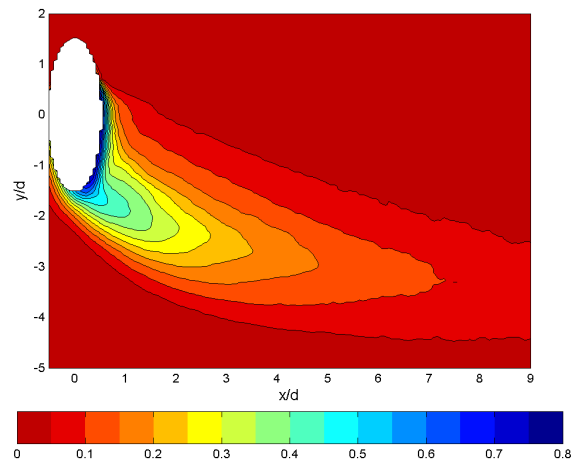


**Fig. 5.63**  $\gamma$  contours for  $\overline{M} = 2.0$ , low  $Tu$ ,  $Re_D = 60k$ ,  $F = 0.148$ ,  $DC = 50\%$ , partial VC

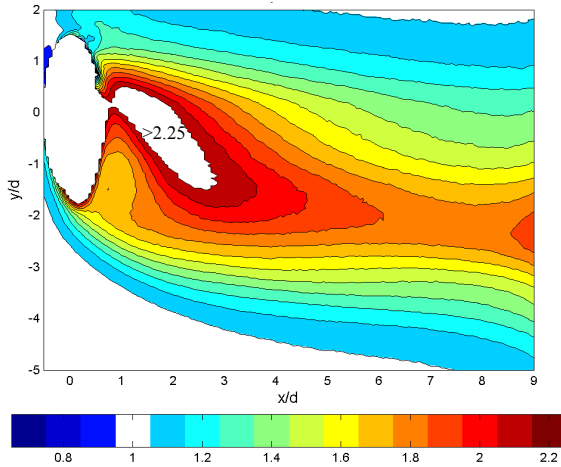


**Fig. 5.64**  $Fr_f / Fr_0$  contours for  $\bar{M} = 2.0$ , low  $Tu$ ,  $Re_D = 60k$ , steady

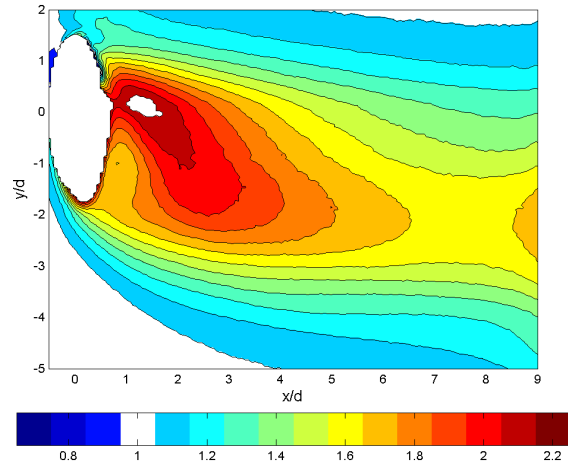


**Fig. 5.65**  $Fr_f / Fr_0$  contours for  $\bar{M} = 2.0$ , low  $Tu$ ,  $Re_D = 60k$ ,  $F = 0.148$ ,  $DC = 50\%$ , partial VC

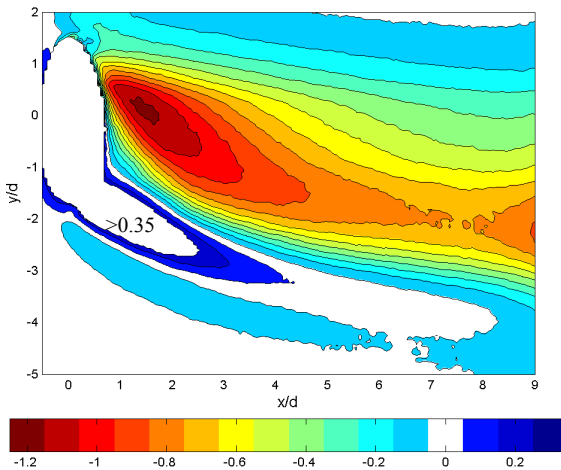


**Fig. 5.66**  $\Delta q_r$  contours for  $M = 2.0$ , low  $Tu$ ,  $Re_D = 60k$ , steady

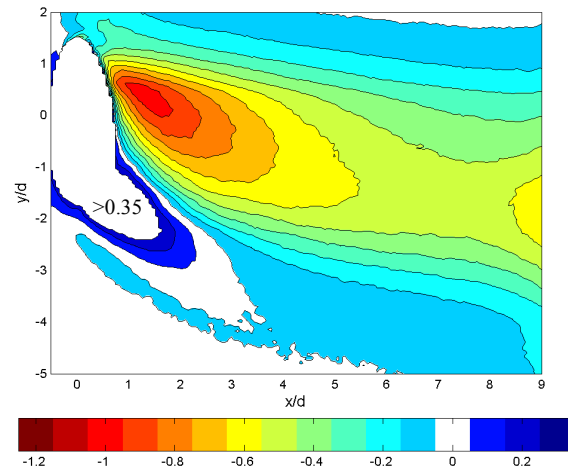


**Fig. 5.67**  $\Delta q_r$  contours for  $\bar{M} = 2.0$ , low  $Tu$ ,  $Re_D = 60k$ ,  $F = 0.148$ ,  $DC = 50\%$ , partial VC

A summary of how the area-averaged  $\gamma$  results for pulsed film cooling compare with  $\gamma$  attainable with steady film cooling is presented in Fig. 5.68. At the lower blowing ratios, there is a severe performance degradation due to pulsing; however, at the higher blowing ratios, pulsing can yield an improvement in  $\gamma$  relative to the steady case. Due to the strong waveform dependence and the tendency for pulsed cases to perform better with lower amplitude pulsing, the complete VC configuration performed much worse than the partial VC configuration at all blowing ratios tested.

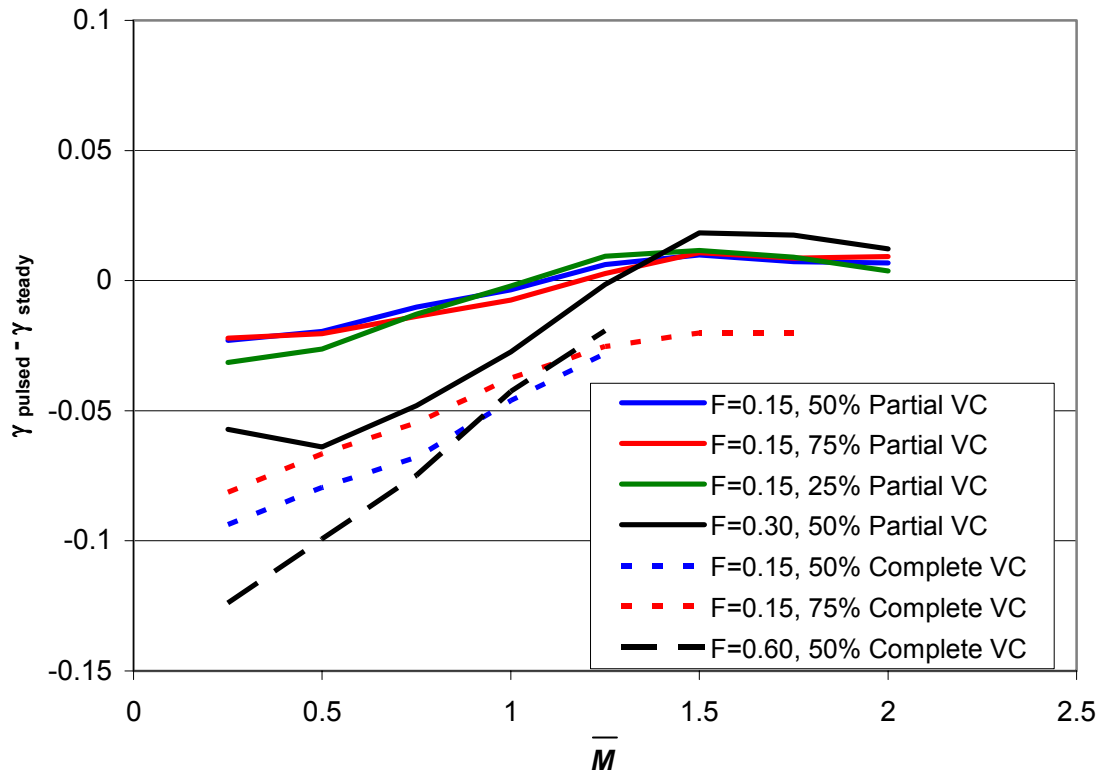


Fig. 5.68 Difference in  $\gamma$  between pulsed and steady cases as a function of  $\bar{M}$ ; low  $Tu$ ;  $Re_D = 60k$

An analogous summary for Frössling number ratio is presented in Fig. 5.69. Again, the complete VC configuration tends to perform poorer than the partial VC configuration. In fact, for the  $F = 0.598$  complete VC case, there is a 9% increase in area averaged  $Fr$  over the steady case at  $\bar{M} = 0.25$ . The degradation drops rapidly with increasing  $\bar{M}$ , but the partial VC case still tends to perform better, with several cases yielding slightly lower values of  $Fr$  than the steady case at certain values of  $\bar{M}$ .

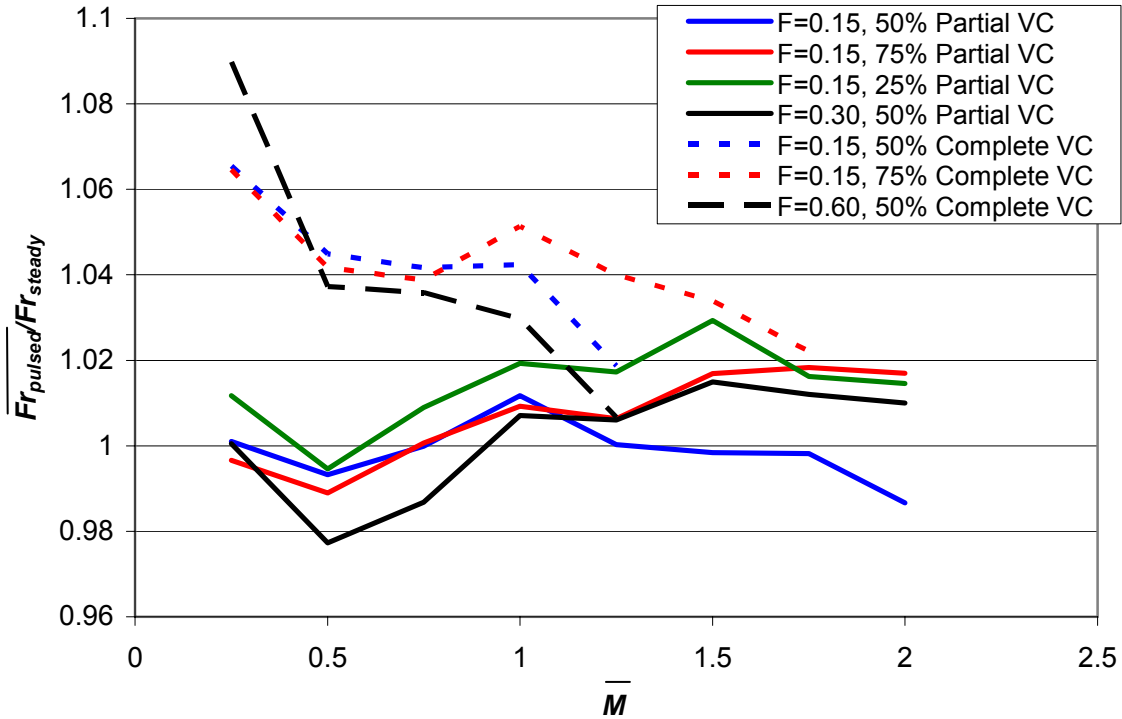


Fig. 5.69 Ratio of  $\overline{Fr}$  between pulsed and steady cases as a function of  $\bar{M}$ ; low  $Tu$ ;  $Re_D = 60k$

A summary of the  $\overline{\Delta q_{r,pulsed}}$  results are shown in Fig. 5.70. Recall that  $\overline{\Delta q_{r,pulsed}}$  describes the reduction in net heat flux due to pulsing an otherwise steady jet at matched  $\bar{M}$  as defined by Eq. (5.2) on page 108. The  $F = 0.148$ ,  $DC = 50\%$  pulsing case performs better than the steady case for  $\bar{M} \geq 1.25$  as do the other partial VC pulsing cases with the exception of the  $F = 0.148$ ,  $DC = 25\%$  case, which has a net heat flux reduction nearly equal to the steady jet at those higher values of  $\bar{M}$ . The complete VC configuration performed much worse than the partial VC configuration, a result of higher amplitude pulsations. The  $F = 0.598$  complete VC case has a very large  $\frac{d}{dM} \overline{\Delta q_{r,pulsed}}$  relative to the other pulsed cases, indicating that it might perform well compared to a steady jet at higher values of  $\bar{M}$ . The effective closing of the valves in the complete VC state made it impractical to force coolant through them at  $\bar{M} > 1.25$  (with  $DC = 50\%$ ) with the available equipment.

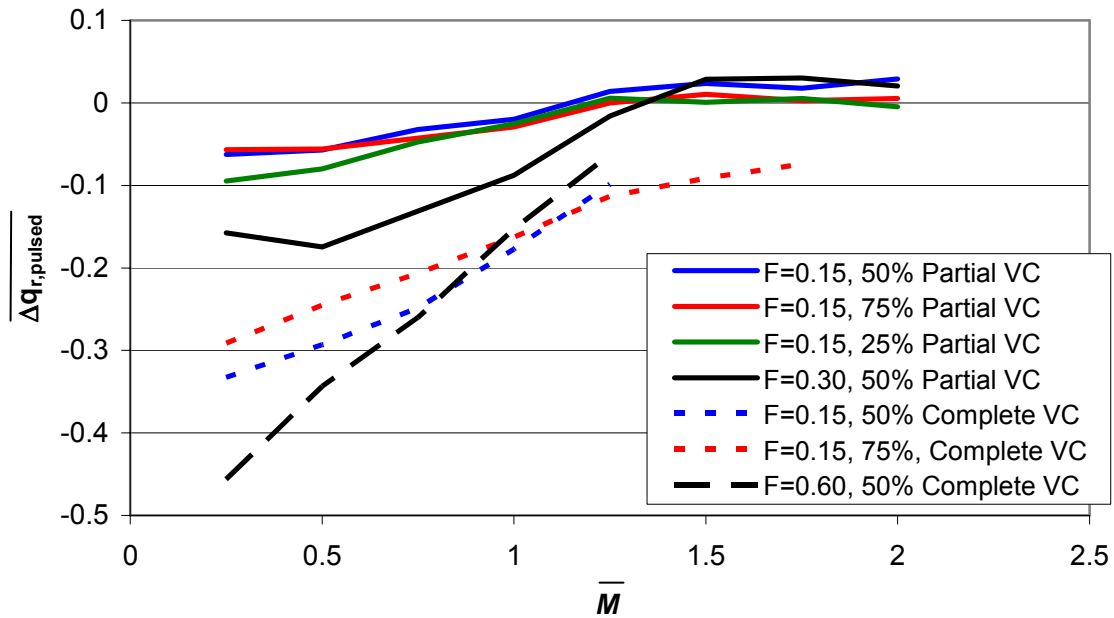


Fig. 5.70 Net heat flux reduction due to pulsing as a function of  $\bar{M}$  ; low  $Tu$ ;  $Re_D = 60k$

### 5.2.2. The Influence of Freestream Turbulence and Reynolds Number on Pulsed Film Cooling

The four freestream conditions allow us to determine the influence of freestream turbulence and Reynolds number on the performance of pulsed film cooling schemes. A summary of the unsteady coupled adiabatic effectiveness,  $\gamma$ , results for the low frequency,  $DC = 50\%$  cases is shown in Fig. 5.71. The  $Re_D = 30k$ ,  $F = 0.29$  partial VC cases at each turbulence condition are presented with two sets of  $Re_D = 60k$  data for comparison. In order to maintain a constant nondimensional pulsing frequency,  $F$ , with a change in freestream Reynolds number, the dimensional pulsing frequency was changed (see Table 5.1 on page 109). Because the waveform shape changed with a change in frequency (see Appendix A), it was impossible to maintain all conditions constant with the exception of a change in Reynolds number. For that reason, both matched waveform shape and matched nondimensional frequency are given in Fig. 5.71 for a comparison with the  $Re_D = 30k$  cases. Although it may at first seem unobvious why we would want to compare results at different nondimensional frequencies but with the same waveform shape, we must remember that Section 3.6 describes that at low frequency (for which

$F \leq 0.30$  almost certainly qualifies) the performance of a pulsed film cooling scheme is expected to depend only on waveform shape and not frequency. When we compare the four cases with matched waveform shape (the  $F = 0.15$ ,  $Re_D = 60k$  data with the  $F = 0.29$ ,  $Re_D = 30k$  data), the trends observed near optimum blowing ratios in the vicinity of  $\overline{M} = 0.25$  are similar to the trends we saw with steady film cooling in Fig. 5.5. That is, the low turbulence cases performed better than the high turbulence cases and the high freestream Reynolds number outperformed the low Reynolds number. When we compare the data for the two Reynolds numbers at matched nondimensional frequency ( $F \approx 0.30$ ), the high Reynolds number performed poorer than the low Reynolds number. These results at  $Re_D = 60k$ ,  $F = 0.30$  are unusual, not only because they are among the few results such that  $\gamma$  at  $Re_D = 60k$  was lower than at  $Re_D = 30k$ , but also because  $\gamma$  increases on the interval  $1.0 < M < 1.25$ .<sup>p</sup> As usual, the low turbulence case has  $\gamma$  similar to or better than the high turbulence cases. Interestingly, all of the  $\gamma$  data collapses for  $M \geq 1.25$  in Fig. 5.71.

---

<sup>p</sup> This unusual behavior of  $\gamma$  as a function of  $\overline{M}$  was repeated during preliminary experimentation.

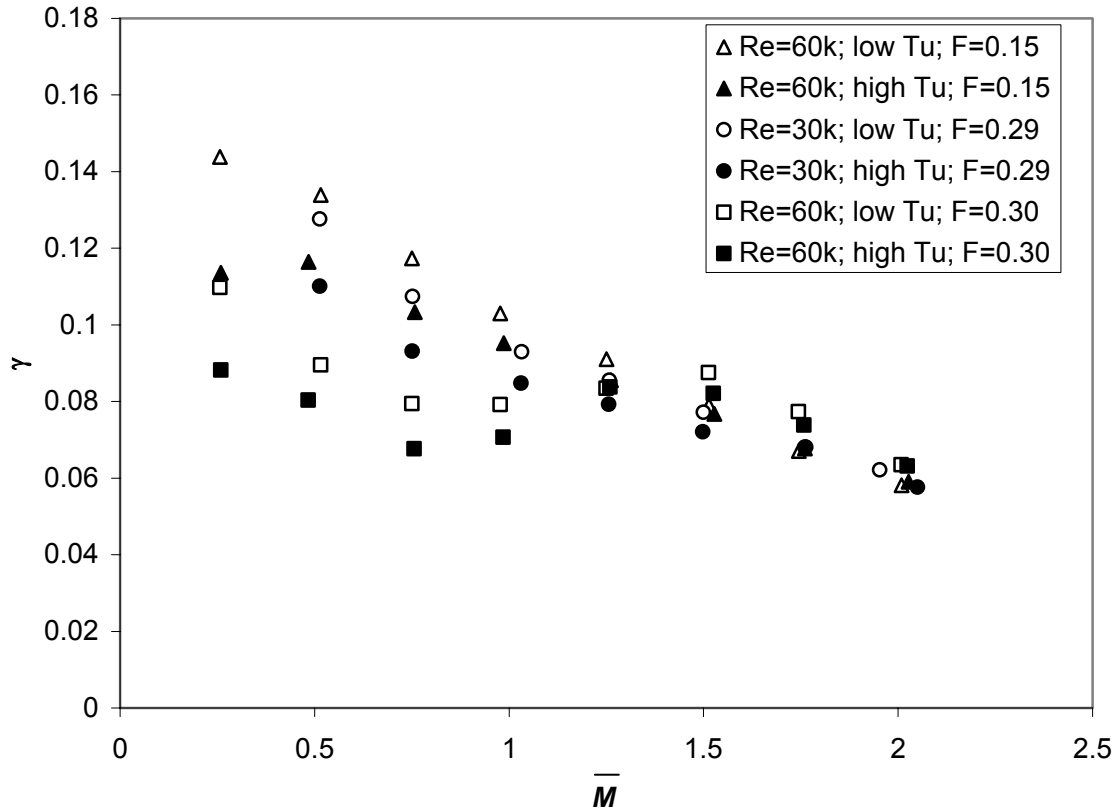


Fig. 5.71 Area averaged  $\gamma$  for pulsed film cooling;  $F \approx 0.15$  and  $0.30$ ,  $DC = 50\%$ , partial VC

Figure 5.72 gives the analogous results for area-averaged  $Fr / Fr_0$ . The influence of freestream turbulence intensity and Reynolds number on  $Fr / Fr_0$  for the low frequency pulsed cases was similar to the steady results shown in Fig. 5.33. The three high turbulence cases performed virtually identically in terms of area averaged  $Fr / Fr_0$ . At low turbulence,  $Fr / Fr_0$  was approximately 3% higher at  $\bar{M} = 1.0$  for  $Re_D = 30k$  and 7% higher for  $Re_D = 60k$  than their respective high turbulence conditions. As with the steady results, freestream Reynolds number had virtually no effect at high freestream turbulence. Also notable is the lack of the influence of pulsing frequency and waveform shape at high turbulence.

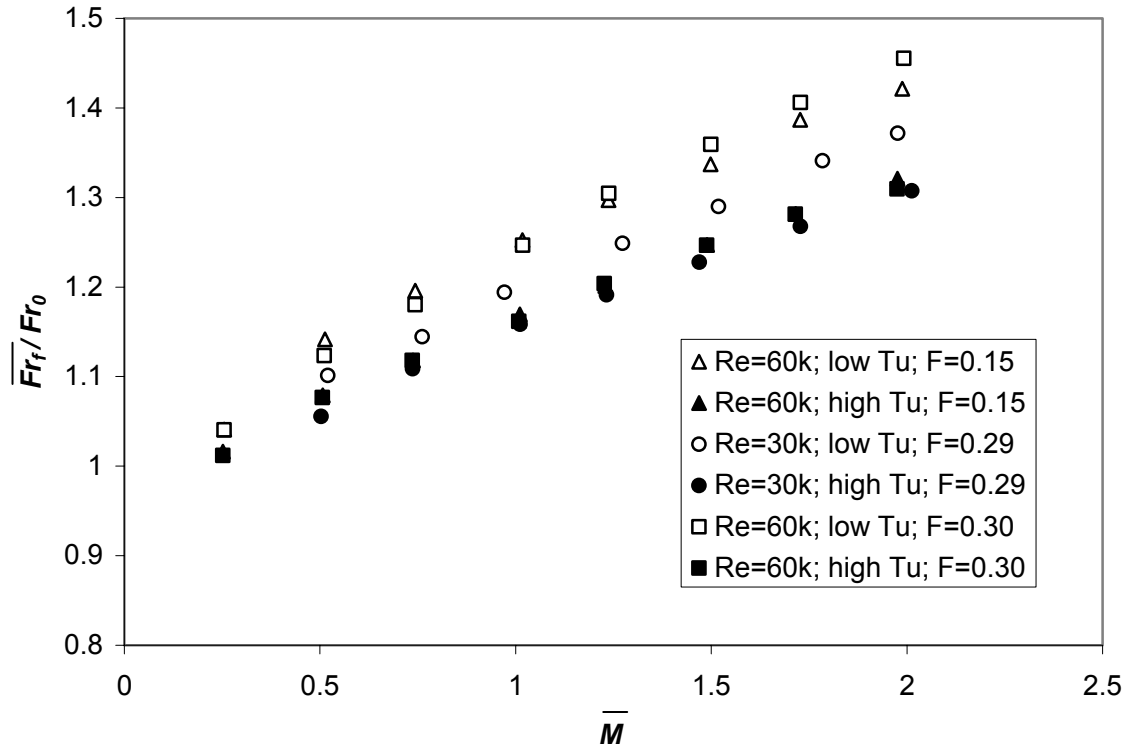


Fig. 5.72 Area averaged  $\overline{Fr_f} / Fr_0$  for pulsed film cooling;  $F \approx 0.15$  and  $0.30$ ,  $DC = 50\%$ , partial VC

The area-averaged net heat flux reduction data for the low frequency pulsed cases are shown in Fig. 5.73. The influences of Reynolds number and turbulence are quite similar to those with steady film cooling depicted in Fig. 5.46. Film cooling tends to be most beneficial at high freestream turbulence,  $Re_D = 60k$  for  $\bar{M} > 0.5$ . At high  $\bar{M}$ , all high turbulence conditions perform similarly; however for  $\bar{M} < 1.25$ , the  $Re_D = 60k$ ,  $F = 0.3$  cases performs significantly poorer than the others. This is particularly interesting since Fig. 5.46 shows very little influence of either Reynolds number or freestream turbulence in the range  $0.5 \leq \bar{M} \leq 1.0$  with steady film cooling. This lack of influence in that regime remains true for the four cases that all had the same waveform. Only the  $Re_D = 60k$ ,  $F = 0.3$  cases had different waveforms. This suggests that the waveform shapes are very important, perhaps more than nondimensional frequency, at least at this low frequency regime as we would expect from the hypothesis in Section 3.6.

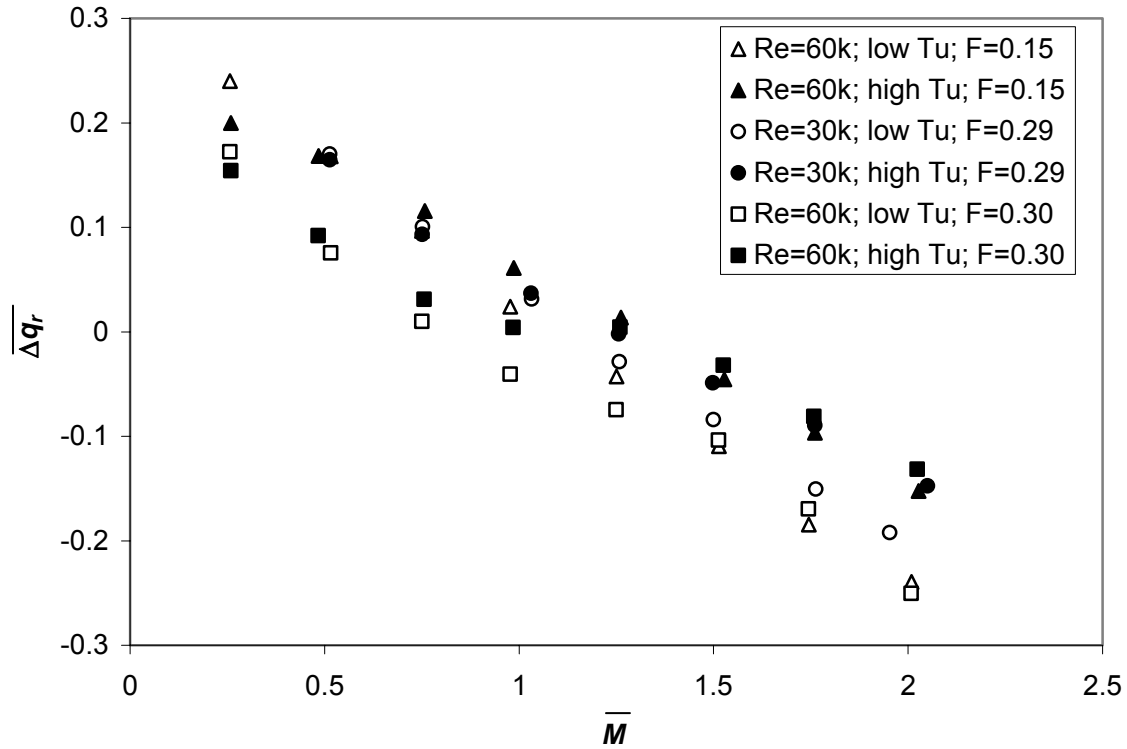


Fig. 5.73 Area-averaged  $\overline{\Delta q_r}$  for pulsed film cooling;  $F \approx 0.15$  and  $0.30$ ,  $DC = 50\%$ , partial VC

Having examined the influence of freestream turbulence and Reynolds number at low pulsing frequencies, we now turn our attention to the highest frequencies examined in this experimental regimen. Figure 5.74 shows the area averaged  $\gamma$  results for pulsed film cooling at  $Re_D = 60k$ ,  $F = 0.6$  in the complete VC configuration with two sets of  $Re_D = 30k$  data for comparison. The first set, at  $F = 1.20$  has matched waveform shape, the other at  $F = 0.59$  has matched frequency. A comparison between the two waveforms in Appendix A reveals that the matched frequency cases have remarkably similar waveforms, even though the latter set was acquired prior to reconfiguring the valves.

Figure 5.74 reveals just how important the decision to compare constant  $F$  or constant waveform shape can be. For example, at  $\overline{M} = 1.0$ , the low turbulence  $Re_D = 60k$  case has area-averaged  $\gamma = 0.062$ . Changing the Reynolds number to  $Re_D = 30k$  increases  $\gamma$  to 0.091 if  $F$  remains constant, but decreases it to 0.032 if the waveform shape and dimensional frequency,  $f$ , remain constant.

Remarkably, the  $Re_D = 30k$ ,  $F = 1.20$  area-averaged  $\gamma$  results were insensitive to turbulence intensity; however, cutting the nondimensional frequency in half to  $F = 0.59$  resulted in a very strong influence of freestream turbulence. This suggests that the  $F = 1.20$  frequency was high enough that dynamics due to the unsteady film cooling dominate over effects from the freestream.<sup>9</sup>

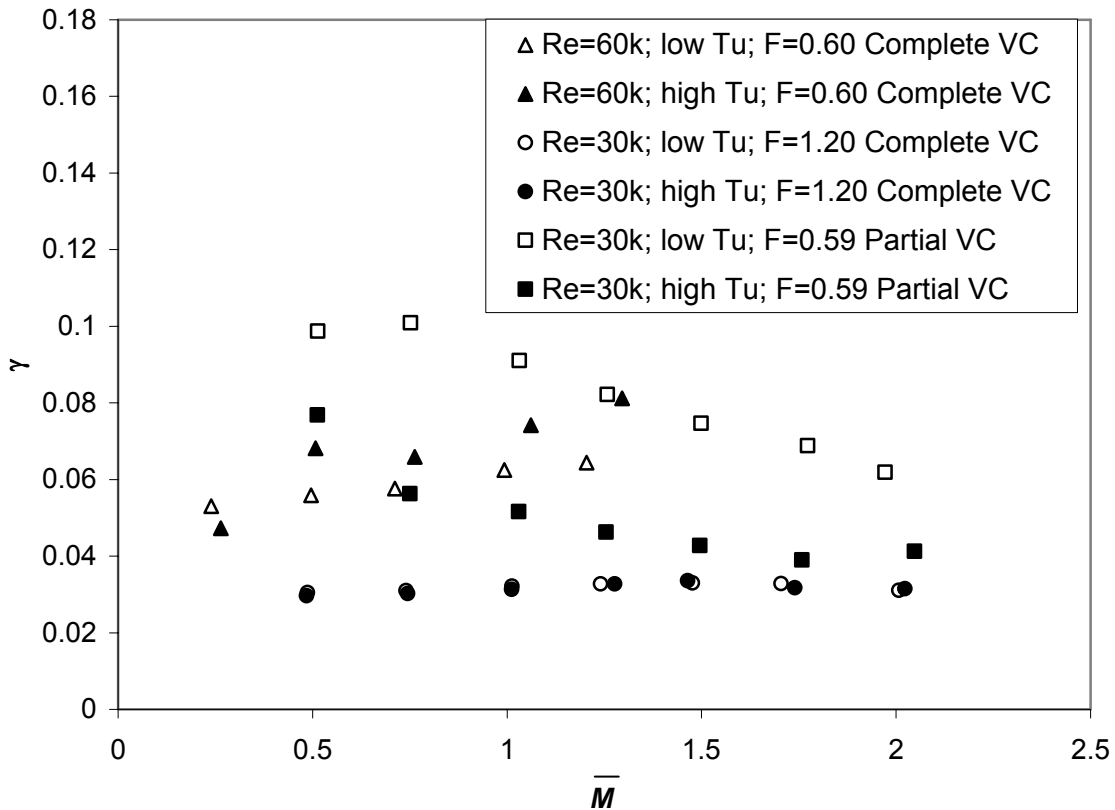


Fig. 5.74 Area averaged  $\gamma$  for pulsed film cooling;  $F \approx 0.60$  and  $1.20$ ,  $DC = 50\%$

The  $\overline{Fr_f} / Fr_0$  results for the same cases as above are shown in Fig. 5.74. As usual, the low freestream turbulence cases tended to have higher  $\overline{Fr_f} / Fr_0$  than their corresponding high freestream turbulence cases. There is very little frequency dependence, but strong Reynolds number dependence at low freestream turbulence, exemplified by the high  $\overline{Fr_f} / Fr_0$  values at low freestream turbulence,  $Re_D = 60k$ .

<sup>9</sup> Flow visualization for  $Re_D = 30k$ ,  $F = 1.2$  is examined in Section 7.2.

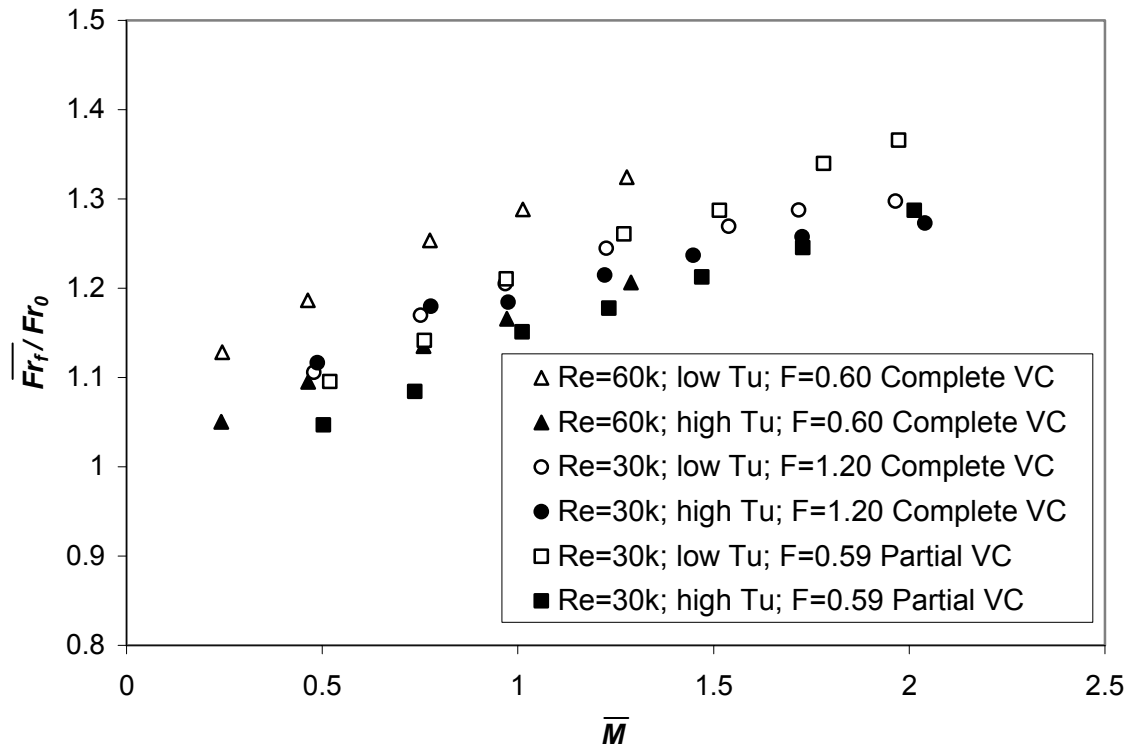


Fig. 5.75 Area averaged  $\bar{Fr}_f / Fr_0$  for pulsed film cooling;  $F \approx 0.60$  and  $1.20$ ,  $DC = 50\%$

Figure 5.76 gives the area-averaged  $\bar{\Delta q}_r$  results. Despite the great similarities between the two waveform shapes, there are tremendous differences in the results for the  $F = 1.20$  and  $F = 0.59$  results at constant  $Re_D = 30k$ . With matched waveform shape (as opposed to nondimensional frequency), the low turbulence cases performed similarly at the two Reynolds numbers. The low frequency theory developed in Section 3.6 suggests that the results should be dependent only on waveform shape as long as the frequency is “low.” If this remained true for the present set of frequencies, we should see both sets of  $Re_D = 30k$  data match well, since even the two waveforms are very similar. Apparently, this frequency regime is high enough that there is strong frequency dependence on the jets, even with very similar waveform shapes.

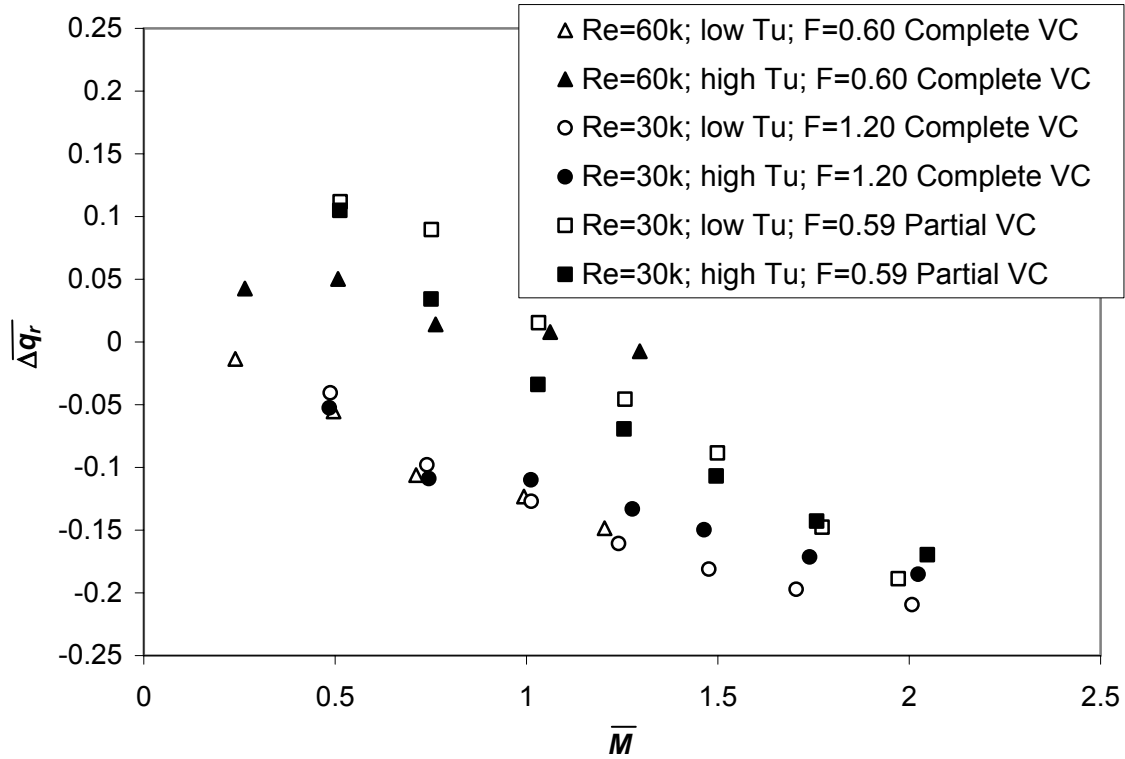


Fig. 5.76 Area-averaged  $\overline{\Delta q_r}$  for pulsed film cooling;  $F \approx 0.60$  and  $1.20$ ,  $DC = 50\%$

Ultimately, we wish to understand the performance of pulsed film cooling as it compares to steady film cooling. Figure 5.70 on page 120 presented the net heat flux reduction due to pulsing for the baseline condition,  $Re_D = 60k$ , low turbulence. The analogous results for the remaining three freestream conditions are shown in Figs. 5.77 through 5.79. The valves in the complete VC state perform worse than in the partial VC state at low  $\overline{M}$ , although there is rapid improvement with increasing  $\overline{M}$ . This was particularly so with the  $Re_D = 30k$ , low turbulence case in which the  $F = 1.20$  complete VC configuration had positive  $\overline{\Delta q_{r,pulsed}}$  at  $\overline{M} = 2.0$ . The case in which pulsing was most beneficial over the steady scheme was at  $Re_D = 30k$ , high turbulence, pulsing at  $F = 0.29$ ,  $DC = 25\%$  in the partial VC configuration at  $\overline{M} = 2.0$ . In that case, pulsing resulted in 4.1% lower heat flux than the steady film cooling scheme at matched blowing ratio.

Since waveform shape was a strong function of dimensional pulsing frequency (see Appendix A), it is difficult to gauge the influence of a change in frequency alone on

the film cooling performance. We are afforded one such opportunity by comparing the 40 Hz partial VC configuration with the 80 Hz complete VC configuration. As mentioned earlier, both of these conditions had very similar waveform shapes. In Fig. 5.70 on page 120 and Figs. 5.77 through 5.79, we can compare these two cases for a variety of average blowing ratios. At  $Re_D = 60k$ , we are comparing  $F = 0.30$  and  $0.60$ ; at  $Re_D = 30k$ , we are comparing  $F = 0.59$  and  $1.20$ . At none of the tested average blowing ratios did the higher frequency case outperform the lower frequency; however, the improvement in relative performance with  $\bar{M}$  was greater at the high frequency. At  $Re_D = 60k$ , high turbulence in Fig. 5.77, both jets performed comparably at  $\bar{M} = 1.25$ , but higher  $\bar{M}$  data was not available for the higher frequency jet. In general, the low frequency performance prediction technique (from Section 3.6) is not applicable at these frequencies since there is obvious frequency dependence on the results. The experimental flow visualization in Section 7.2 affords some insight into the reasons we see this frequency dependence.

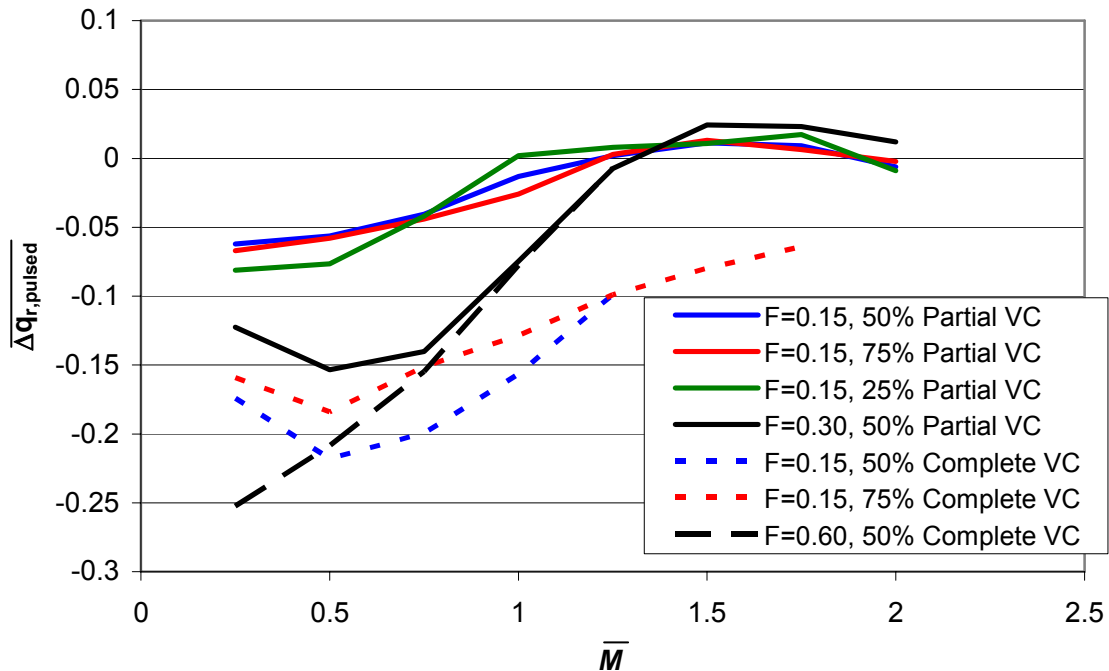


Fig. 5.77 Net Heat flux reduction due to pulsing as a function of  $\bar{M}$ , high  $Tu$ ,  $Re_D = 60k$

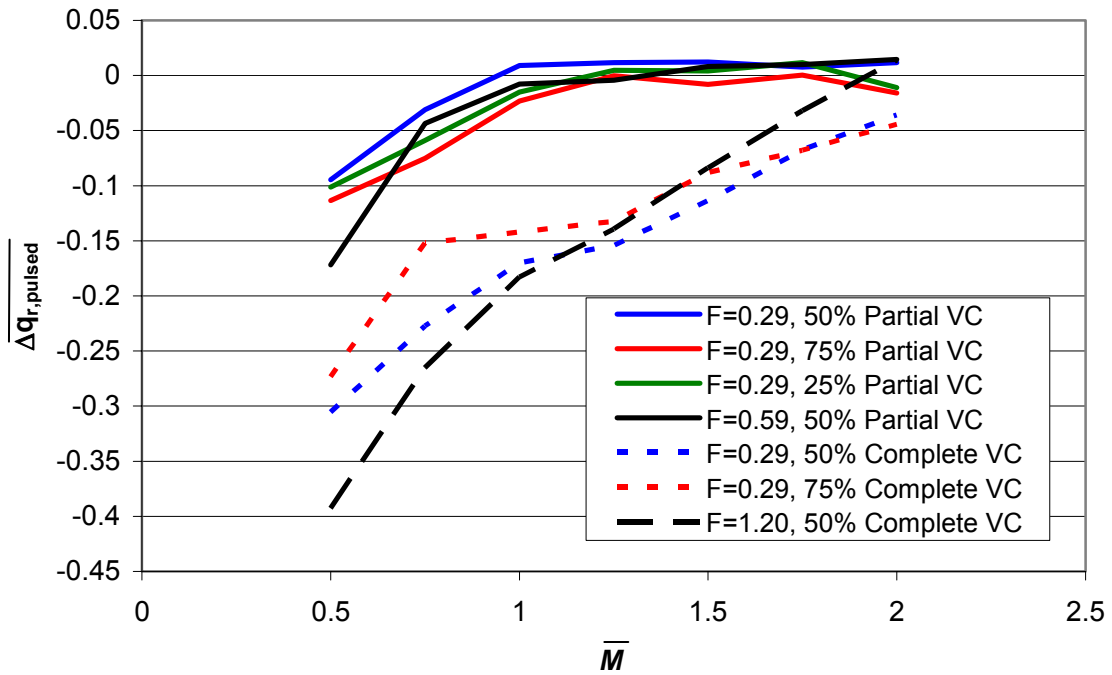


Fig. 5.78 Net Heat flux reduction due to pulsing as a function of  $\bar{M}$ , low  $Tu$ ,  $Re_D = 30k$

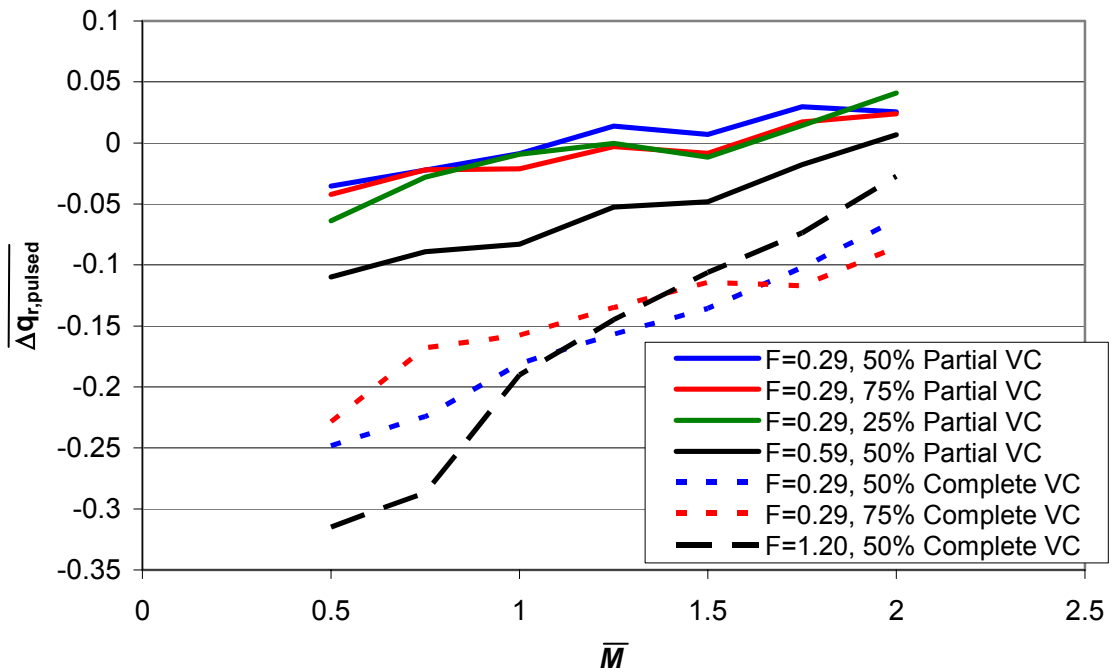


Fig. 5.79 Net Heat flux reduction due to pulsing as a function of  $\bar{M}$ , high  $Tu$ ,  $Re_D = 30k$

### 5.3 Validity of the Low Frequency Prediction Technique

In Section 3.6, a hypothesis regarding the behavior of pulsed film cooling in the limit of low pulsing frequencies was presented. Specifically, as pulsing frequencies are decreased, transient effects of the pulsing scheme are expected to have decreasing importance. At sufficiently low frequencies, the transient effects may be insignificant, suggesting that the net heat flux reduction may be computed through Eq. (3.73) adapted for net heat flux reduction:

$$\overline{\Delta q_r} \approx \frac{\omega}{2\pi} \int_0^{2\pi} \Delta q_r(M(t)) dt \quad (5.4)$$

#### 5.3.1. Net Heat Flux Reduction Performance Prediction

The  $M(t)$  curves in Appendix A along with the steady area-averaged  $\Delta q_r(M)$  data in Fig. 5.46 on page 107 were used to predict the area-averaged  $\overline{\Delta q_r}$  for pulsed jets at the baseline condition of low turbulence,  $Re_D = 60k$ . The net heat flux reduction data of Fig. 5.46 were fitted with a linear interpolation for the purposes of evaluating Eq. (5.4). The prediction was performed for 28 separate  $M(t)$  curves for the lowest frequency ( $F = 0.148$ ) tested. The results transformed into  $\overline{\Delta q_{r,pulsed}}$  (to show the net heat flux reduction due to pulsing) are summarized in Fig. 5.80 along with the actual data acquired with the pulsed experiments. The prediction technique with the 50% and 75% duty cycles with the partial VC condition performed quite well, yielding  $\overline{\Delta q_{r,pulsed}}$  within 3% of the actual measurements with the pulsed jets.

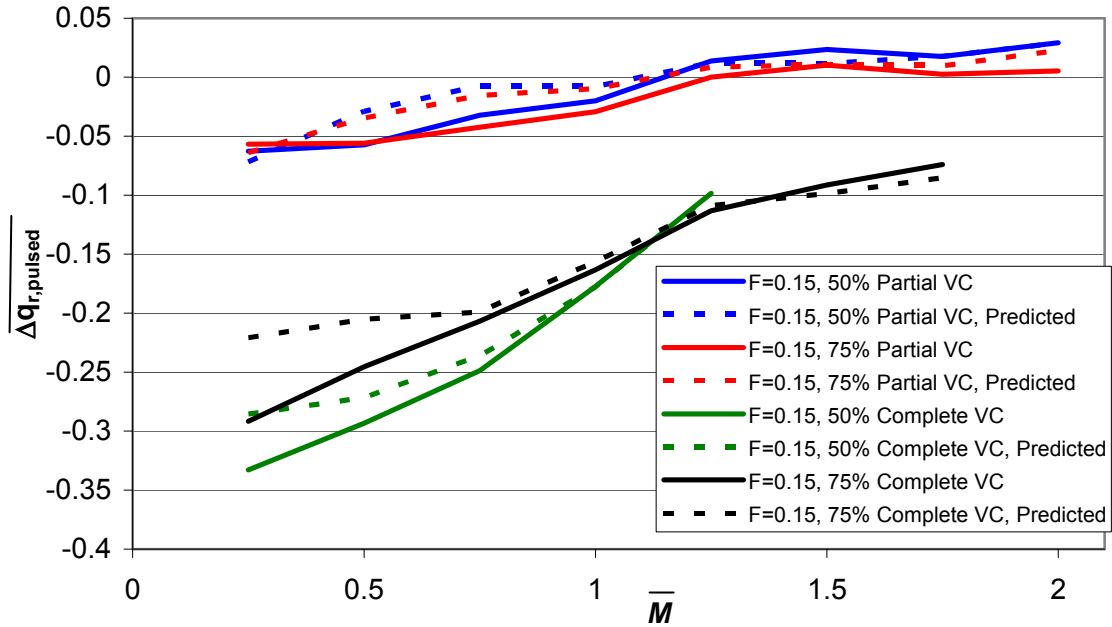


Fig. 5.80 Net heat flux reduction due to pulsing as a function of  $\bar{M}$ ; low  $Tu$ ;  $Re_D = 60k$ ; low frequency prediction vs. actual results

The performance predictions with the complete VC configuration were not as straightforward as with the partial VC configuration due to the negative blowing ratio observed with the complete VC configuration (see Appendix A). During the time that  $M(t) < 0$ , it was assumed that  $\Delta q_r = 0$ . Although not strictly true, even in the quasi-steady sense used to arrive at Eq. (5.4), this is a good assumption. Obviously,  $\eta = 0$  while  $M(t) < 0$ , but the influence of suction on  $h$  is more subtle, with  $h_f$  probably greater than  $h_0$ , a result of thinning of the boundary layer due to the suction. The result would thus probably be  $\Delta q_r < 0$  during this time, but it would not be expected to be of a large magnitude relative to the values of  $\Delta q_r$  obtained during the remaining majority of the cycle time. Although no heat transfer experiments with steady negative blowing ratios were conducted as part of this experimental regimen, they could be performed, in theory, to provide a more complete picture of the influence of suction on  $h_f$ . We must also consider what is ingested during the time that  $M(t) < 0$ . Because there is no upstream film cooling on the geometry of the current experiment, the ingested fluid has a

nondimensional temperature of  $\theta = 0$  during a  $\gamma$  experiment. Thus, the coolant hole is at least partially filled with “coolant” at a nondimensional temperature of  $\theta = 0$  instead of the normal  $\theta = 1$ . When this hot fluid is discharged from the coolant hole, the quasi-steady adiabatic effectiveness remains at  $\eta = 0$  due to the absence of cool coolant at  $\theta = 1$ . Despite the zero adiabatic effectiveness during this time, the jet influences the heat transfer coefficient which in turn influences the net heat flux reduction. For the case of  $\eta = 0$ , the net heat flux equation (Eq. (3.11)) becomes

$$\Delta q_r = 1 - \frac{h_f}{h_0} \quad (5.5)$$

which is readily available from the set of steady heat transfer coefficient data that was acquired and reported in Fig. 5.33 (noting that  $h_f / h_0$  is equivalent to  $Fr_f / Fr_0$ ). The  $Fr_f / Fr_0$  curve as a function of steady blowing ratio in Fig. 5.33 was used along with Eq. (5.5) to compute the quasi-steady net heat flux reduction until the hot fluid in the coolant hole was expelled. The amount of fluid ingested by the coolant hole was calculated by integrating the  $M(t)$  curve over the time that  $M(t) < 0$ . Once  $M(t) > 0$ , integration began again to determine when the ingested fluid was completely expelled.

The prediction technique does not perform as well with the complete VC configuration at the lower average blowing ratios, with a maximum error of 5% for the 50% duty cycle case and a maximum error of 7% for the 75% duty cycle case, evident in Fig. 5.80. The trends are still predicted well with better accuracy toward higher average blowing ratios. At low average blowing ratios, the  $M(t)$  curves oscillate in the vicinity of the peak of the performance curve where there are sharp gradients in the steady  $\Delta q_r(M)$  curve. Uncertainties in either curve would have propagated severely into the overall performance from the prediction technique. Furthermore, the assumption that  $h = h_0$  during the time that  $M(t) < 0$  would tend to cause an overprediction in  $\overline{\Delta q_r}$ . Naturally, since the heat transfer coefficients are lower at lower values of  $M$ , a small error caused by this assumption would have a greater relative effect compared to the larger  $\overline{M}$  cases where  $\overline{Fr_f} / Fr_0$  is much larger. Because the  $M(t)$  curves for the complete VC

configuration tended to have sharper gradients in  $M$ , partially due to higher amplitude, the transient events associated with valve turn-on and turn-off were probably of greater importance compared to the lower amplitude and gentler fluctuations in  $M$  obtained with the valves in their partial VC state.

### 5.3.2. Frössling Number Augmentation Performance Prediction

We turn our attention to the unusual behavior of pulsed jet  $\overline{Fr_f} / Fr_0$  we saw in Figs. 5.51 through 5.54 on page 112. In those figures we observed that high amplitude pulsing resulted in higher  $\overline{Fr_f} / Fr_0$  than the low amplitude pulsing despite an apparent expectation from Fig. 5.33 (showing an almost linear  $Fr_f / Fr_0$  curve as a function of steady  $M$ , with a slight downward concavity at extreme  $M$ ) that the higher amplitude should perform similarly to the lower amplitude, with possibly lower  $\overline{Fr_f} / Fr_0$ .

The techniques applied above to predict average net heat flux reduction were applied to the steady  $Fr_f / Fr_0$  data to predict the performance with pulsed film cooling. The results are shown in Fig. 5.81. Indeed, the performance prediction technique does indicate a slightly higher  $\overline{Fr_f} / Fr_0$  with the higher amplitude (complete VC) configuration than the lower amplitude configuration. This is due to local regions of slightly concave-up portions of the curve in Fig. 5.33. Although the prediction worked very well for the partial VC (low amplitude) waveform, it underpredicted  $\overline{Fr_f} / Fr_0$  with the high-amplitude waveform. The simplest explanation for this underprediction stems from the negative blowing ratio attained during the course of the complete VC waveform. As discussed in Section 5.3.1, we have assumed that when  $M < 0$ , steady  $Fr_f / Fr_0 = 1$ . This value was hypothesized to be lower than it should be due to boundary layer thinning at  $M < 0$ , but without steady data at  $M < 0$ , this assumption is reasonable. The assumption that  $Fr_f / Fr_0 = 1$  when  $M < 0$ , would tend to underpredict  $\overline{Fr_f} / Fr_0$  for the pulsed scheme. Thus the partial VC configuration for which  $M > 0$  at all times was accurately predicted by the low frequency prediction technique, but the complete VC

configuration with its occasional  $M < 0$ , was underpredicted by as much as 3.6%. Note that this underprediction would cause the predicted value of  $\overline{\Delta q_r}$  to be high by this amount. Indeed, this could account for some of the overprediction of  $\overline{\Delta q_r}$  for the complete VC configuration in Fig. 5.80, particularly at low  $\overline{M}$ .

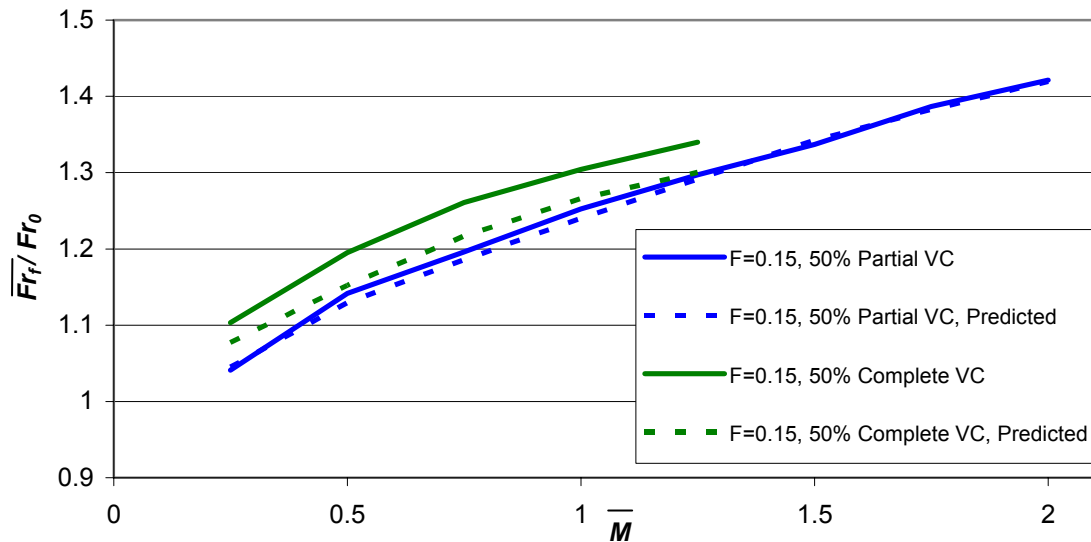
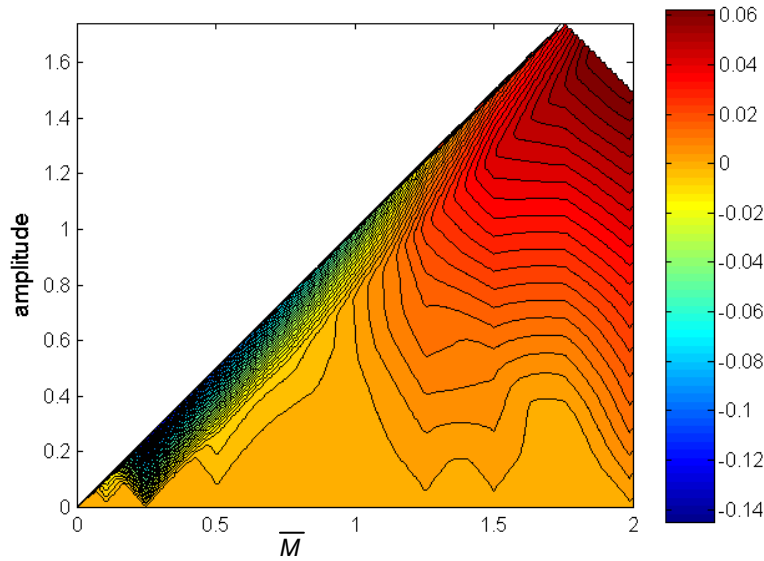


Fig. 5.81 Frössling number augmentation due to pulsing as a function of  $\overline{M}$ ; low  $Tu$ ;  $Re_D = 60k$ ; low frequency prediction vs. actual results

### 5.3.3. Performance Prediction with Hypothetical Waveforms

Having demonstrated that the low frequency prediction technique is an excellent method of predicting performance for pulsing frequencies as high as  $F = 0.148$ , we may predict the performance of additional hypothetical waveforms. Four different hypothetical waveforms were selected—sine, sawtooth, square, and triangle. Because steady net heat flux reduction data was acquired at a maximum blowing ratio of  $M = 3.5$ , the range of blowing ratios attained during any of the proposed cycles was limited to  $M(t) \leq 3.5$ . The cycles were also limited such that  $M(t) \geq 0$ . All permissible combinations of  $\overline{M}$  and amplitude in increments of  $\Delta M = 0.01$  were used to make candidate waveforms of the four types mentioned above. The candidate waveforms were tested with Eq. (5.4). Figures 5.82 through 5.85 display the predicted area-averaged

$\overline{\Delta q_{r,pulsed}}$  results for the sine, sawtooth, square, and triangle waveforms, respectively for the low turbulence,  $Re_D = 60k$  data set. In no case was a true optimum combination of  $\overline{M}$  and amplitude found because the best performing combinations were always limited by the maximum blowing ratio of  $M = 3.5$ . Large  $\overline{M}$  and large amplitude tended to perform the best. The highest value of  $\overline{\Delta q_{r,pulsed}}$  obtained during the course of these simulations was  $\overline{\Delta q_{r,pulsed}} = 10.9\%$  with a square wave with average blowing ratio  $\overline{M} = 1.88$  fluctuating with an amplitude of 1.62. In contrast, the best performing waveform (relative to the corresponding steady blowing case) during the course of the pulsed film cooling experiments at low freestream turbulence and  $Re_D = 60k$  had  $\overline{\Delta q_{r,pulsed}} = 2.9\%$ . Incidentally, the prediction technique correctly predicted a maximum of  $\overline{\Delta q_{r,pulsed}} = 2.9\%$  with the  $F = 0.148$ ,  $DC = 50\%$ , partial VC configuration as shown in Fig. 5.80.



**Fig. 5.82** Area averaged  $\overline{\Delta q_{r,pulsed}}$  performance prediction for sinusoidal  $M(t)$  waveforms of various average blowing ratio and amplitude. Max  $\overline{\Delta q_{r,pulsed}} = 6.6\%$  at  $\overline{M} = 1.88$ , amplitude = 1.62

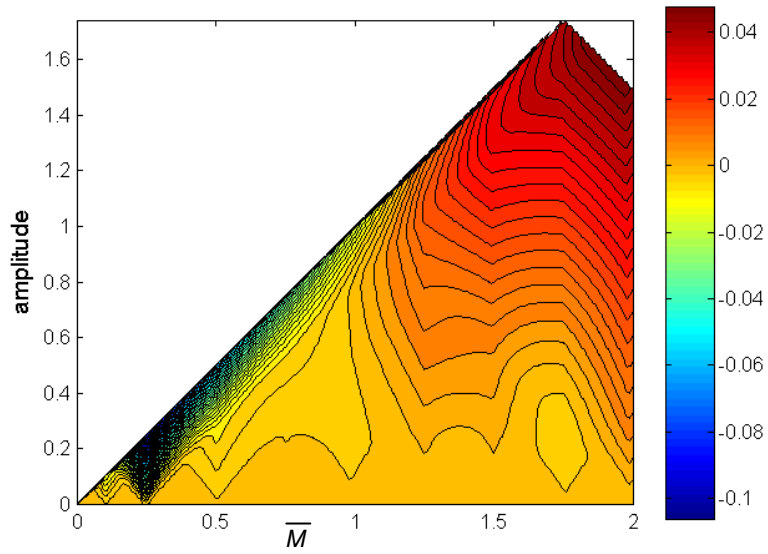


**Fig. 5.83** Area averaged  $\overline{\Delta q_{r,pulsed}}$  performance prediction for sawtooth  $M(t)$  waveforms of various average blowing ratio and amplitude.  $\overline{M}$  ramps up linearly and drops instantly. Max  $\overline{\Delta q_{r,pulsed}} = 5.0\%$  at  $\overline{M} = 1.96$ , amplitude = 1.54

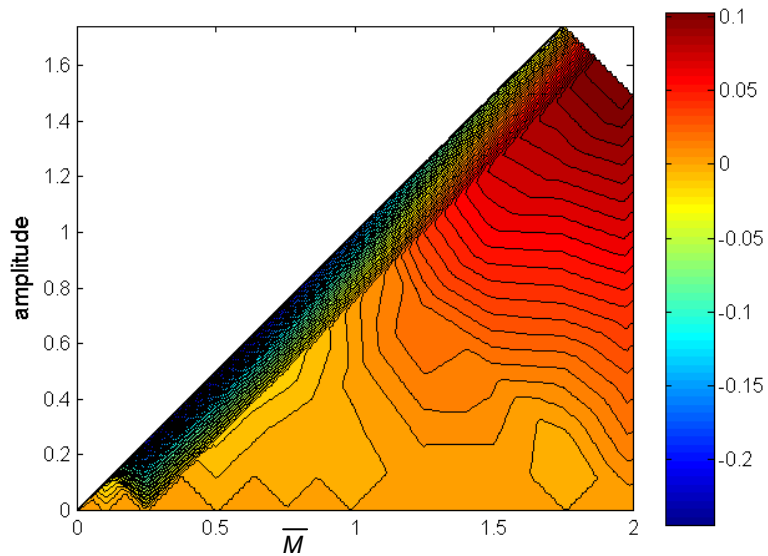


**Fig. 5.84** Area averaged  $\overline{\Delta q_{r,pulsed}}$  performance prediction for square wave  $M(t)$  waveforms of various average blowing ratio and amplitude. Max  $\overline{\Delta q_{r,pulsed}} = 10.9\%$  at  $\overline{M} = 1.88$ , amplitude = 1.62

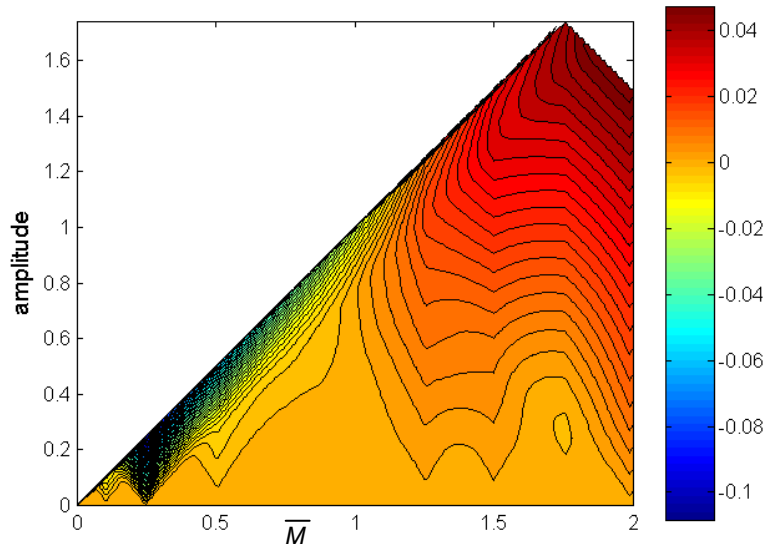


**Fig. 5.85 Area averaged  $\overline{\Delta q_{r,pulsed}}$  performance prediction for triangle wave  $M(t)$  waveforms of various average blowing ratio and amplitude.  $M$  ramps up and down linearly. Max  $\overline{\Delta q_{r,pulsed}} = 5.0\%$  at  $\bar{M} = 1.98$ , amplitude = 1.52**

## 6. Experimental Methodology for Flow Visualization

Having established the thermal influence of a pulsed film cooling jet on the leading edge region of a turbine blade, we now turn our attention to the coolant flow field itself, responsible for the thermal effects. Experiments employing a water channel were conducted to visualize the coolant flow field. A water channel was desirable in that it allowed the fluid velocities to be slowed a great deal without increasing the physical size of the model while continuing to match the Reynolds number. Slowing the velocity has the benefit of providing greater temporal resolution in the flow field measurements, which is particularly useful for visualizing unsteady film cooling.

### 6.1 Water Channel Facility

A model with the same geometry and dimensions as that described in Section 4.1 was used for this set of experiments. In fact, one of the Plexiglas frames used for the net heat flux reduction experiments was reused for the flow visualization experiments. The foam half-cylinder leading edge was replaced with a model made of type 316 stainless steel with identical exterior and hole dimensions. Type 316 stainless steel was selected for its dimensional stability, resistance to oxidation, and compatibility with a variety of paints that may be useful for future research. The stainless steel leading edge was fabricated in three sections, each cut using wire electrical discharge machining (EDM). The three sections were pinned together to form the final shape. The middle section had a region with the appropriate inner diameter to achieve the desired hole length to diameter ratio of  $L/d = 11.79$ . The remaining two pieces had much thinner walls in order to avoid unnecessary weight. The model was substantively identical to the wind tunnel model depicted in Figs. 4.1 and 4.2 on page 45.

The free surface water channel maintained by the Air Force Research Laboratory Air Vehicles Directorate was used for the flow visualization. This recirculating water channel had a test section 60 cm wide, 46 cm deep, and 2.7 m long. A freestream turbulence intensity of  $Tu = 0.1\%$  was reported by Kaplan et al. (2007). The leading edge model was placed vertically in the test section, resting on the bottom with the leading edge approximately 1.5 m downstream of the upstream end of the test section. The water

channel's test section had a maximum approach velocity of 45 cm/s. This was not fast enough to achieve a Reynolds number of  $Re_D = 60000$  with the model described above;<sup>†</sup> however, it was fast enough to obtain  $Re_D = 30000$  at a velocity of  $U_\infty \approx 0.3$  m/s. This is a factor of 20 slower than the velocity used in the wind tunnel to achieve the same Reynolds number. Thus the matched nondimensional pulsing frequencies involved dimensional frequencies of only approximately  $1/20^{\text{th}}$  the dimensional frequencies used with the wind tunnel. The slow velocities and slow pulsing frequencies were conducive to visualization of the unsteady film cooling.

The measured freestream Reynolds number of  $Re_D = 30,000$  was held within 2% of the target Reynolds number through adjustments in the freestream velocity. Two honeycomb screens and three wire mesh screens created uniform flow into the test section. A secondary loop supplied film coolant for the model. Average coolant flow rate was obtained using a rotameter upstream of the same two parallel solenoid valves used with the wind tunnel experiments. Since a rotameter is only accurate for constant (un-pulsed) flow, a tank containing a large air bubble that dampened flow rate unsteadiness was placed between the rotameter and the solenoid valve as shown in Fig. 6.1. Although the flow out of the vessel was pulsed, the vessel had a sufficient volume of (compressible) air that pressure fluctuations within the vessel were sufficiently small and the flow into the vessel was essentially steady.

---

<sup>†</sup> A larger model was not used in order to avoid free surface effects due to the model's flow blockage.

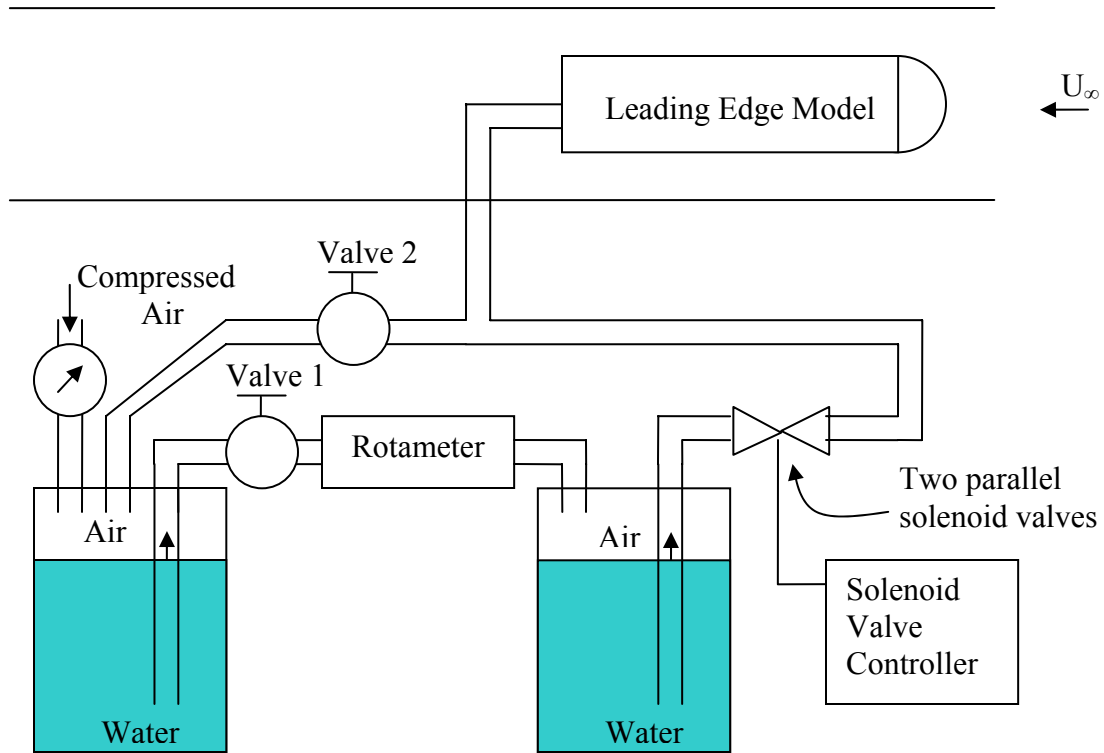


Fig. 6.1 Schematic of Coolant Feed Line for Water Channel Experiments

## 6.2 Parameter Space

The parameter space was limited to a freestream Reynolds number of  $Re_D = 30000$  and a pulsed film cooling duty cycle of 50%. Blowing ratios were varied between  $M = 0.1$  and 2 for steady film cooling, but ranged from  $\bar{M} = 0.1$  to 1.0 for the pulsed cases, limited by the high pressures required to force water through the solenoid valves. The nondimensional pulsing frequencies were  $F = 0.148, 0.294, 0.590,$  and 1.195 to match those from the wind tunnel experiments described in Table 5.1. For brevity, only the most interesting, relevant, or unique results are shown.

## 6.3 Pulsed Jet Waveforms

The relatively low frequency of the valves (as compared with the wind tunnel experiments) and the virtually incompressible nature of the water would ideally lead to nearly square wave pulsations of the coolant. Although the water itself is nearly compressible, the fast opening and closing of the solenoid valve could result in non-

instantaneous changes in the exit velocity of the coolant due to the flexible tubing acting as a spring-dashpot system. A rough characterization of the pulsed jet waveforms was conducted by photographing bubbles traveling through a tube in the model. Small bubbles were introduced into the coolant stream through Valve 2 in Fig. 6.1. The model was laid on its side for this procedure so that a loop in the coolant line within the model would be nearly horizontal in order to prevent the buoyancy of the bubbles from influencing the measurements. Photographs were acquired at 30 frames per second and bubble positions were recorded. Central differencing was used to approximate the instantaneous velocity of the bubbles.

For all pulsed cases, there was a small amount of suction ( $M < 0$ ) that would occur following valve closure. The water had a great deal of momentum as it traveled through the tubing between the solenoid valves and the hole exit. When the solenoid valves shut off, the water continued to move forward, decelerating as some combination of the flexible tubing and cavitation acted as a spring. Once the coolant flow stopped, the tubing released its strain energy, returning to its original shape as it pulled water in from the coolant hole. The negative blowing ratio could be confirmed even without observing the bubbles in the tubing simply by placing a finger against the coolant hole. At the lowest frequency tested, the “off” time of the valves was sufficiently long for the mass-spring-dashpot system to cycle twice before the valve turned back on.

Figures 6.2 and 6.3 present the approximate blowing ratio waveforms acquired by observing the motion of bubbles through the hoses. With the exception of the negative blowing ratio immediately after solenoid valve turn-off, the waveforms were indeed similar to square waves, with peak blowing ratios approximately double the average blowing ratios.

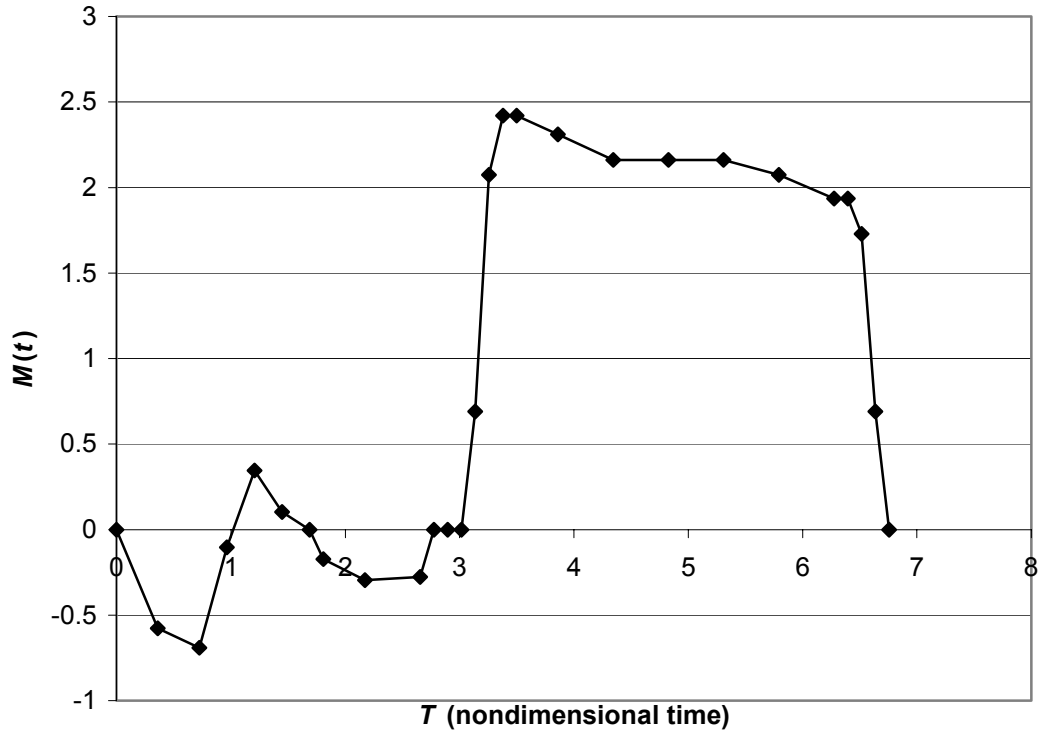


Fig. 6.2 Approximate  $M(t)$  for  $\bar{M} = 1.0, F = 0.148, DC = 50\%$

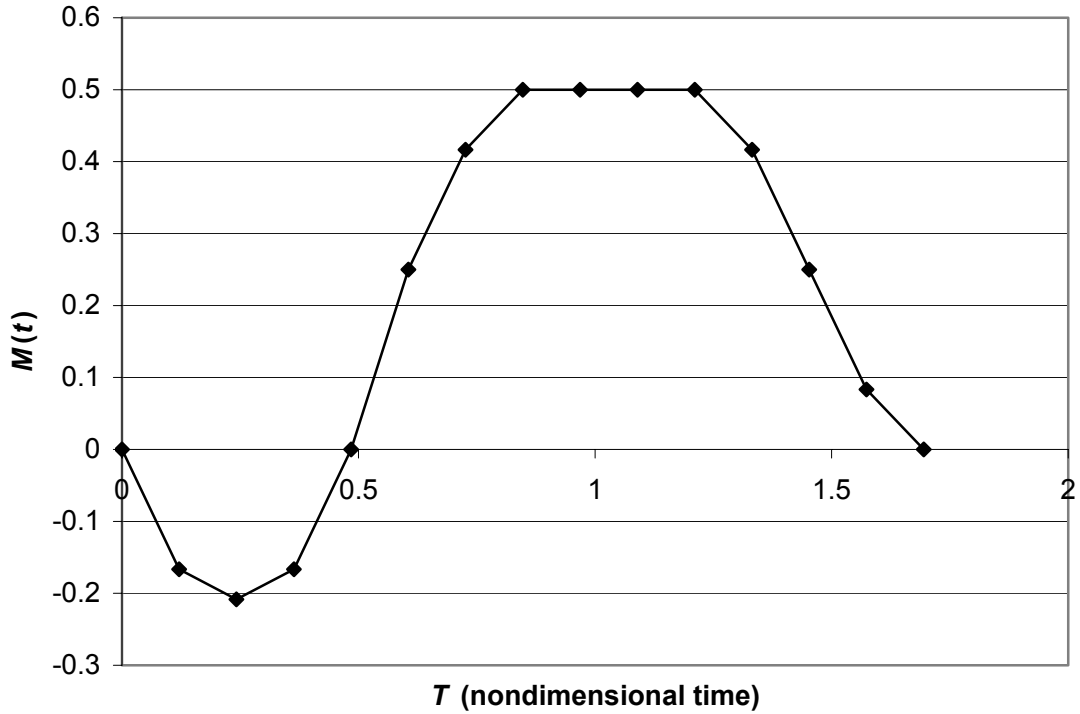


Fig. 6.3 Approximate  $M(t)$  for  $\bar{M} = 0.25, F = 0.590, DC = 50\%$

## 6.4 Flow Visualization Technique

Since the purpose of this experimental regimen was to determine the coolant propagation under various unsteady blowing rates, the coolant water supply was colored while the freestream was left relatively colorless. Blue food coloring, soluble in water and very safe, was used to color the coolant supply in a proportion of approximately 1:1900. Although the primary ingredient of the food coloring was water, the second most abundant ingredient was propylene glycol. Even if we assume that the food coloring was pure propylene glycol, the food coloring would increase the viscosity of the water by a negligible amount, approximately 0.1% as determined through the Refutas equation. As the testing progressed, the recirculating freestream would take on a bluish hue, countered by adding a small amount of bleach to the freestream. Alterations in viscosity remained insignificant.

Grayscale photography was performed at 30 frames per second from two primary camera angles. One angle was from the side to show the  $x$  and  $y$  extents of the film cooling coverage (Camera Angle 1 in Fig. 6.4). The second was from underneath the water channel to show the  $z$  dimension (Camera Angle 2 in Fig. 6.4). Color photographs were also obtained from the third camera angle in Fig. 6.4 such that the  $z$  and  $y$  extents of the film cooling jet were apparent in the region from  $x/d \approx 0.5$  to  $x/d \approx 2$ .

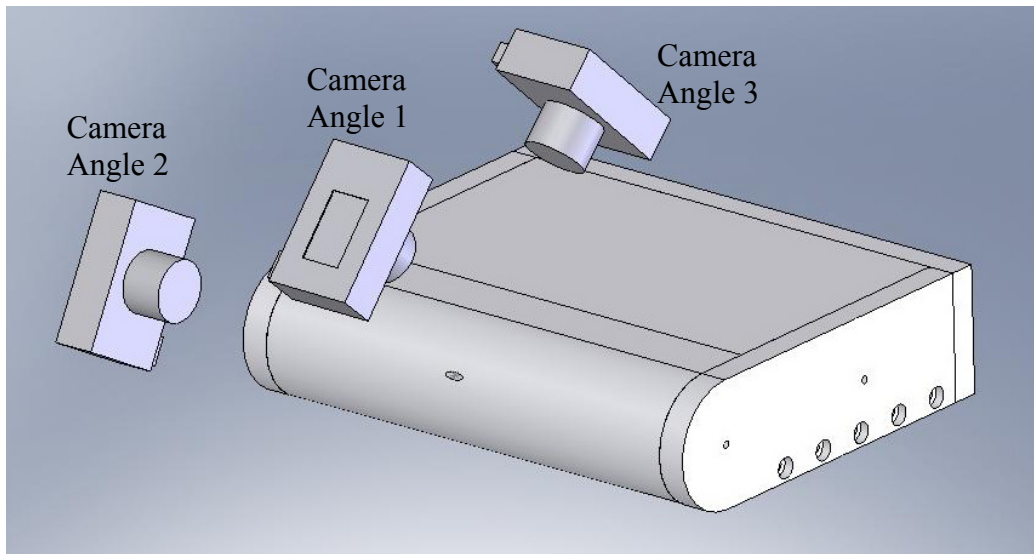


Fig. 6.4 Leading edge model and camera positions

The exterior curved surface of the leading edge model was painted white to achieve good contrast with the blue dye. Red marks that provide a visual reference for images were placed on the leading edge at increments of  $1 d$  in the  $x$  direction along the line  $y/d = -5.7$ , spaced at increments of  $2 d$  in the  $x$  direction along the line  $y/d = 2$ , and spaced at  $1 d$  in the  $y$  direction along the line  $x/d = 0$ .

## **6.5 Uncertainty Analysis**

The flow visualization measurements were qualitative and thus were not subject to measurement uncertainty. However, the flow conditions were subject to uncertainty. These include the freestream Reynolds number and the blowing ratio.

### **6.5.1. Freestream Reynolds Number**

As with the wind tunnel experiments, the measured Reynolds number was allowed a  $\pm 2\%$  range about the target Reynolds number (in this case  $Re_D = 30k$ ). Because the viscosity of water is a strong function of temperature, the velocity required to attain a particular Reynolds number could vary considerably from one experiment to the next. For example, at  $24^\circ\text{C}$ , the  $\pm 2\%$  acceptable freestream velocity range was from  $0.306 \text{ m/s}$  to  $0.318 \text{ m/s}$  whereas at  $23^\circ\text{C}$  (only one degree cooler), the  $\pm 2\%$  acceptable freestream velocity range was from  $0.314 \text{ m/s}$  to  $0.326 \text{ m/s}$ . Data acquisition infrastructure was unavailable to make continuous freestream temperature measurements. In practice, the freestream temperature was measured occasionally, resulting in freestream temperature uncertainties of approximately  $0.5^\circ\text{C}$  when we factor in thermocouple uncertainty. This temperature uncertainty alone is responsible for  $1.3\%$  uncertainty in the freestream Reynolds number.

The velocity was determined by measuring the time it took a float to pass between two marks placed on the water channel glass. The velocity of the float on the surface and the velocity near the mid-depth of the water channel was confirmed to be approximately equal by injecting dye near the mid-depth of the channel and observing that the dye moved at the same rate as the float. The marks were  $1.42 \text{ m}$  apart and the float was given enough time to accelerate to the freestream velocity prior to passing the first mark. Timings were conducted using a stopwatch in order to establish the velocity. The water

channel impeller speed was adjusted based on the measured velocity until the resulting velocity was within the 2% range described above. The final velocity prior to flow visualization was established by determining the average from five timings. From repeated measurements, the uncertainty in the velocity due to timing errors was approximately 5%.

The resulting overall uncertainty in the measured freestream Reynolds number was approximately 6%. Since this measured value was held within 2% of the target Reynolds number, the total deviation of freestream Reynolds number could be approximately  $\pm 8\%$  of  $Re_D = 30k$ , or  $\pm 2400$ .

### 6.5.2. Blowing Ratio

The blowing ratio was calculated with Eq. (2.1). Although density was taken as a function of temperature, water density is a very weak function of temperature so that uncertainty was dominated by uncertainty in the freestream and coolant velocities. As discussed in Section 6.5.1, the measured freestream velocity had a 6% uncertainty. The rotameter uncertainty was 1% or one-half of the scale divisions; however, in practice, the rotameter was generally able to be held to within 1 scale division of the target value. At a blowing ratio of  $M = 0.25$ , this corresponds to a coolant flow rate uncertainty of 12%. At  $M = 1$ , the flow rate uncertainty was 3%. Using the method of Kline and McClintock (1953), we find that the overall uncertainty in  $M$  is 13% at  $M = 0.25$  and 7% at  $M = 1.0$ .

### 6.5.3. Timing

All imagery was acquired at 30 frames per second so that an image was acquired every 0.033 seconds. The uncertainty of the time of a given image is half of that time. This corresponds to an uncertainty in the stated nondimensional time of  $\pm 0.05$ .

## 7. Flow Visualization Results

This chapter presents the results of the flow visualization experiments performed according to the methodology in Chapter 6. Individual images are labeled in terms of nondimensional time,  $T = tU_{\infty} / D$  so that in one unit of nondimensional time, the freestream travels one leading edge diameter.

### 7.1 Steady Jet Results

Figure 7.1 shows the flow issued by a jet at a steady blowing ratio of  $M = 0.25$  from Camera Angle 1 (see Fig. 6.4 on page 143 for the camera angles). The geometry is oriented the same way in these figures as the contour plots in Chapter 5; however, surface curvature is present in these photographs. Vertical dots on the left hand side of the photos are spaced at increments of  $1 d$ . The top row of horizontal dots are spaced at increments of  $2 d$  and the bottom row are spaced at  $1 d$ . The coolant exited the coolant hole with very little momentum and turned in the direction of the freestream. By comparing the six frames in Fig. 7.1, each acquired at different times, it is evident that there is local unsteadiness in the flow despite the steady blowing ratio. The unsteadiness is of a sufficiently small magnitude that it is clear that resulting values of  $\eta'$  and  $h_f'$  are negligible for this steady film cooling case. The coolant flow field can be characterized as laminar, but unsteady, with time scales too long to be characterized as turbulence. Smooth streaks of coolant attest to the laminar nature of the coolant. The coolant streaks evident at  $M = 0.25$  are probably related to the fingers of elevated adiabatic effectiveness observed at low  $M$  and low freestream turbulence. The analogous adiabatic effectiveness plot is Fig. 5.17 on page 94. Only two streaks are seen in the adiabatic effectiveness plot; however, the averaging process used to obtain Fig. 5.17 results in spanwise smearing of the streaks.

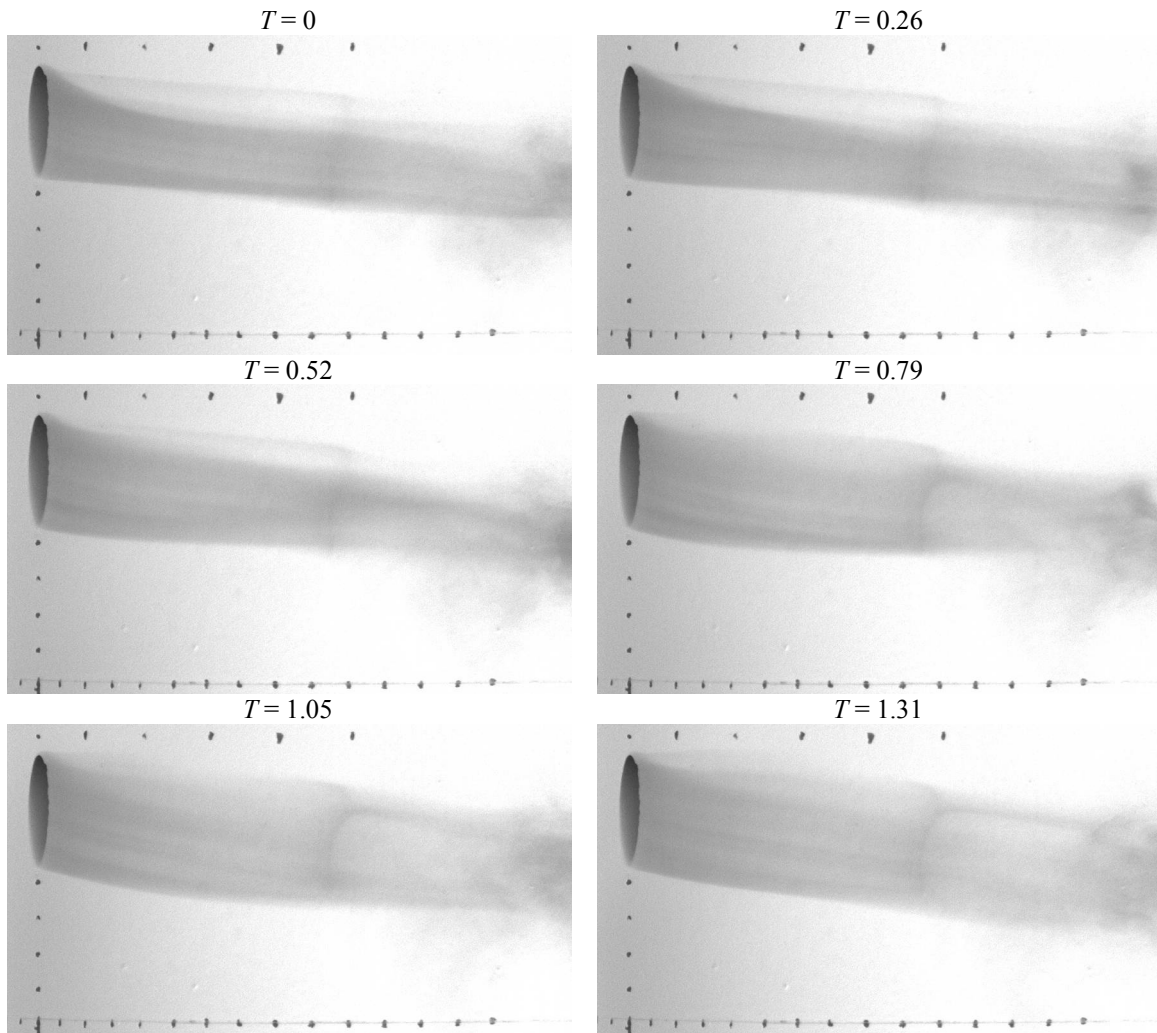


Fig. 7.1 Near surface normal view of coolant at several points in time, steady  $M = 0.25$ . (Camera Angle 1)

Although Fig. 7.1 shows the  $x$  and  $y$  extent of the film cooling jet, we cannot determine how far off the surface in the  $z$  direction the coolant penetrates from Camera Angle 1. Camera Angle 2 does yield that information in Figure 7.2 which shows the coolant from a view nearly parallel to the surface. The camera view is in the negative  $y$  direction. A photograph with no film cooling present is shown in Fig. 7.3 for comparison. The penetration of the jet off of the surface in the  $x$  direction is minimal. The laminar nature of the coolant plume remains clear in Fig. 7.2. The maintenance of the coolant plume close to the surface is responsible for high film cooling effectiveness at  $M = 0.25$ .

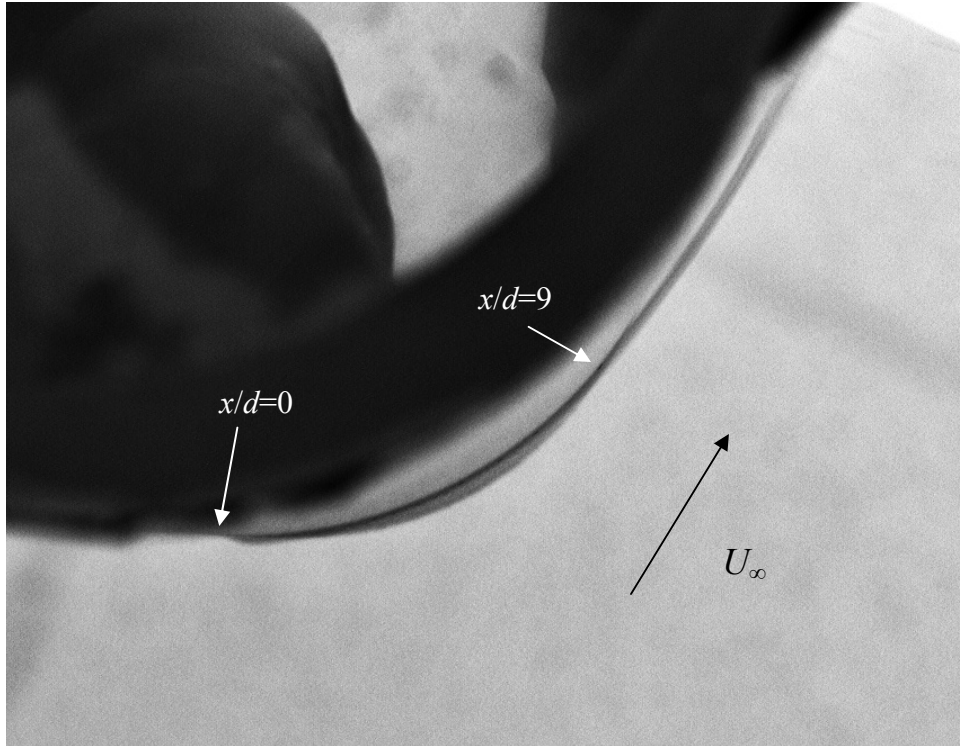


Fig. 7.2 Near parallel to surface view of coolant, steady  $M = 0.25$ . (Camera Angle 2)

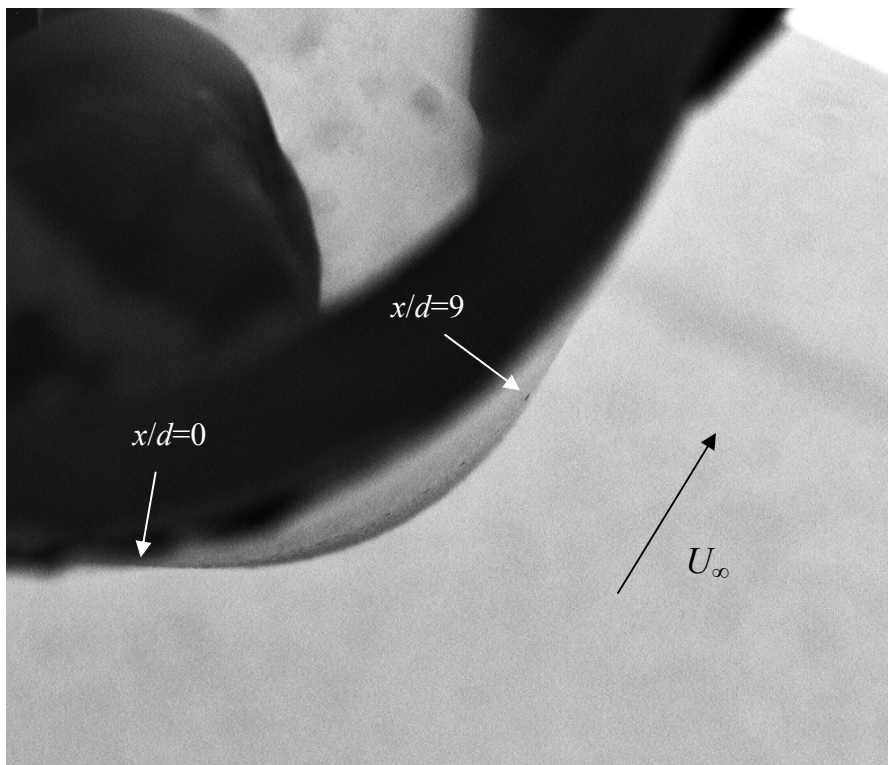
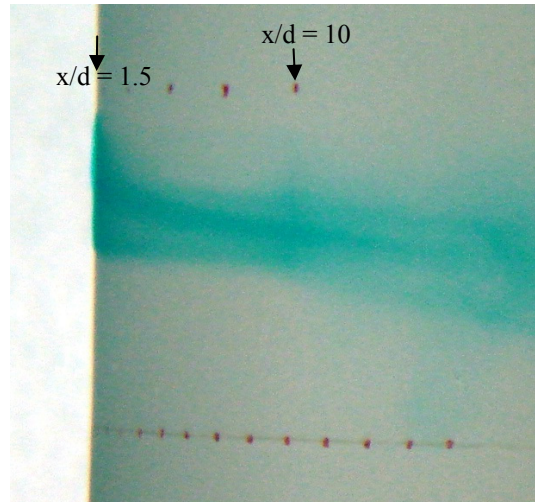


Fig. 7.3 Near parallel to surface view, steady  $M = 0$ . (Camera Angle 2)

Coolant at a steady blowing ratio of  $M = 0.25$  from Camera Angle 3 is shown in Fig. 7.4. This figure is similar to Fig. 7.1; however, the camera was moved to the right so that the thickness of the coolant plume in the  $z$  and  $y$  dimensions is evident. The left edge of the model is at  $x/d = 1.5$  so we can determine how far the coolant penetrates just downstream of the coolant hole. At  $M = 0.25$ , the coolant penetrates very little, remaining attached to the surface of the model.



**Fig. 7.4 Off-surface view of coolant at  $M = 0.25$ . Left edge of model is at  $x/d = 1.5$ . (Camera Angle 3)**

An interesting flow feature is the flow separation that occurs at  $x/d \approx 13$ . Since this region is on the flat afterbody, it is outside our region of interest for practical turbine blade leading edge region film cooling. There is also a small separation line at  $x/d = 9.5$ , visible in both Fig. 7.4 and Fig. 7.1. In addition to recirculating coolant in the separation regions, some coolant tends to travel in the spanwise direction within the spanwise oriented vortices. This phenomenon was also evident in the IR photography acquired during both the adiabatic effectiveness and heat transfer experiments. The separation was characterized by very low heat transfer coefficients, or high temperatures on the heat flux plate.

The Camera Angle 1 view of coolant at  $M = 0.5$  is shown in Fig. 7.5. The coolant is laminar, owing to the smoothness of the streaks of coolant (evident in the adiabatic effectiveness plot in Fig. 5.12); however, the unsteadiness in the coolant jet occurs with

shorter length scales. The smooth streaks of coolant are obvious in Fig. 7.5 and are believed to be responsible for the fingers of elevated adiabatic effectiveness evident in Fig. 5.13. Note that only for the  $Re_D = 30k$ , low turbulence case, were these coolant fingers detected in Chapter 5 at  $M = 0.5$ . The near parallel view (from the Camera Angle 2) of the  $M = 0.50$  jet is shown in Fig. 7.6, where it is clear that the coolant plume is thicker than in the  $M = 0.25$  case pictured in Fig. 7.2. Figure 7.7 shows the coolant penetration at  $x / d = 1.5$  for  $M = 0.5$  from Camera Angle 3. The local unsteadiness in the coolant jet propagation was very obvious from this angle, so two photographs acquired at two random times are shown in Fig. 7.7. The behavior of the coolant as it turns in the freestream direction is clearly complex and unsteady, with what appears to be an unsteady vortex that forms at the lower part of the hole.

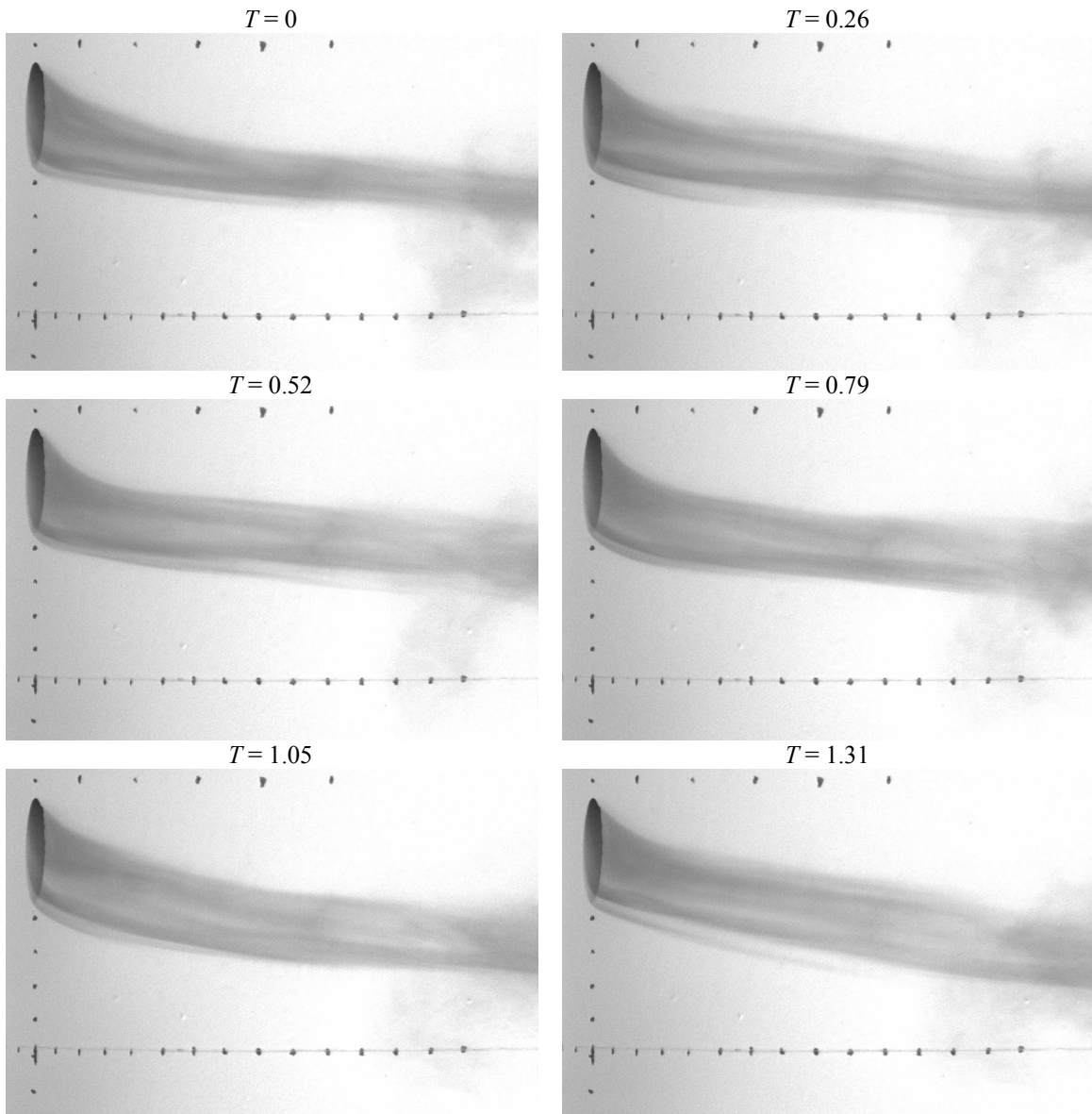


**Fig. 7.5** Near surface normal view of coolant at several points in time, steady  $M = 0.50$ . (Camera Angle 1)

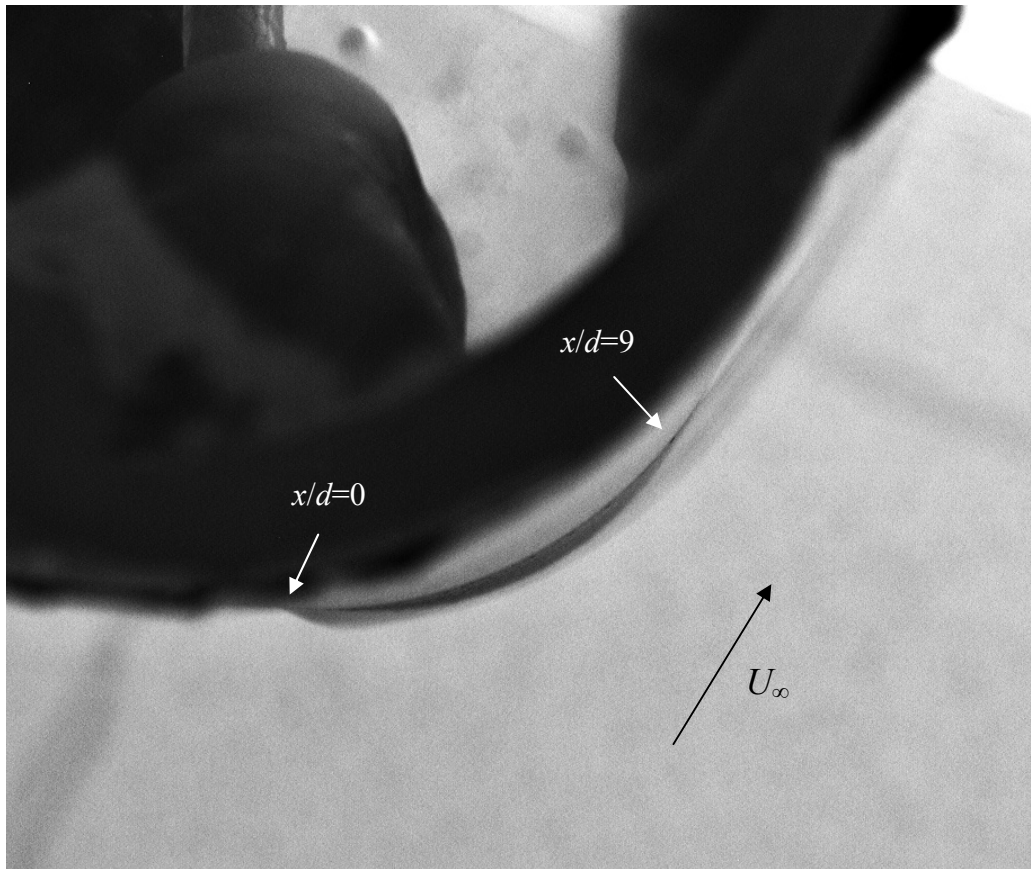


Fig. 7.6 Near parallel to surface view of coolant, steady  $M = 0.50$ . (Camera Angle 2)

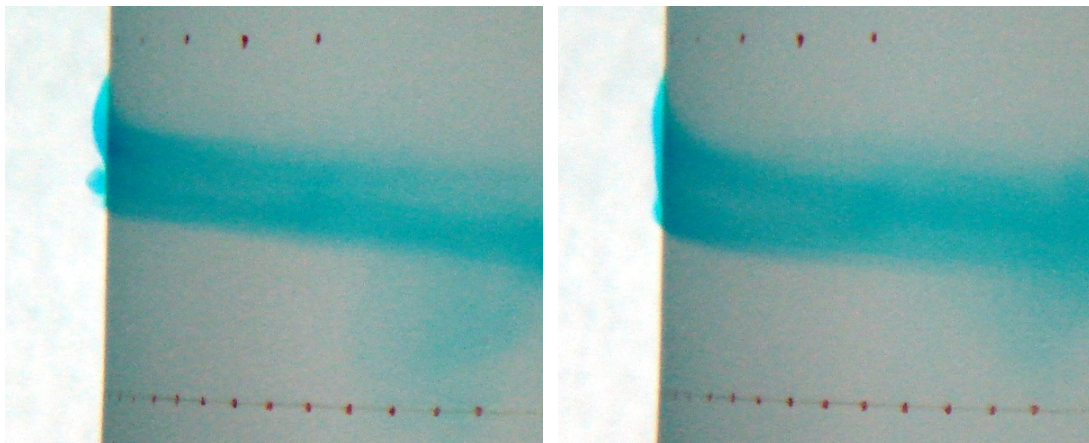
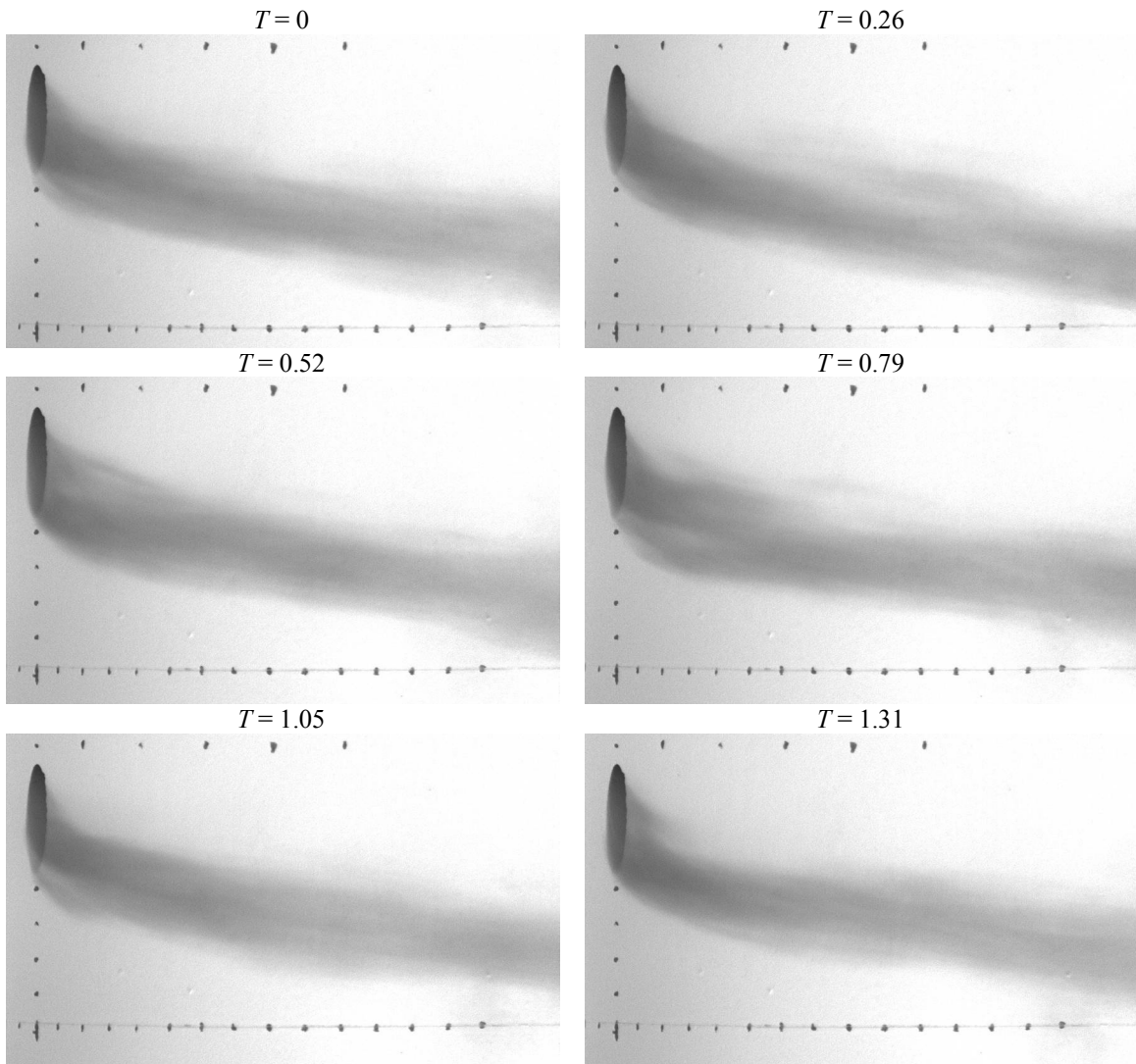


Fig. 7.7 Off-surface view of coolant at  $M = 0.5$ . Two images taken at two random times. Left edge of model is at  $x/d = 1.5$ . (Camera Angle 3)

Figures 7.8 and 7.9 show the surface normal and parallel view photos, respectively, acquired with steady blowing at  $M = 1.0$ . At  $M = 1.0$ , the coolant flow may be characterized as fully turbulent. There were no smooth streaks of coolant, and turbulent structures were visible to the naked eye, although these structures were smeared slightly in the photographs due to nonzero exposure time. In Fig. 7.9, the coolant penetrates several hole diameters into the freestream by the time the coolant reaches  $x/d = 9$ . This coolant that is detached from the surface does little to improve adiabatic effectiveness. Instead, the great deal of  $z$  momentum of the jet results in very little coolant remaining attached to the surface. Detachment is evident in Fig. 7.9 immediately downstream of the coolant hole; the lack of perspective in this view indicates that the detachment in this region is for all  $y$  and is not just a partial detachment. Some coolant reattaches at  $x/d \approx 1$  and that is the coolant on which we depend for the bulk of the elevated adiabatic effectiveness. Recall that the adiabatic effectiveness plot for the low turbulence,  $Re_D = 30k$  case is shown in Fig. 5.14 on page 91. In Fig. 5.14 we noted that there is an island of elevated adiabatic effectiveness immediately downstream of the coolant hole that suggests coolant lift-off and reattachment. Fig. 7.9 supports that hypothesis. In addition to the poor adiabatic effectiveness due to the thick turbulent coolant plume, the additional turbulence created by the jet increases the heat transfer coefficient far higher than it would be with a lower blowing ratio jet.

In Fig. 5.14 we also noted a contraction in the adiabatic effectiveness plume width on the interval  $3 \leq x/d \leq 5$ . A corresponding contraction in jet width is not obvious by looking at any one frame in Fig. 7.8; however, when taken as a slideshow, turbulent structures of coolant can be seen propagating occasionally downstream along the upper part of the main coolant plume. These structures may have the tendency of increasing the average adiabatic effectiveness for  $x/d < 5$ , but may detach from the surface in the interval  $3 \leq x/d \leq 5$ . Indeed, turbulent structures are seen detaching from the surface in the near-parallel view when viewed as a slideshow. The lack of depth perspective in this view cannot absolutely confirm that these structures are responsible for the adiabatic effectiveness plume contraction seen in Fig. 5.14, but offer a possible explanation.



**Fig. 7.8** Near surface normal view of coolant at several points in time, steady  $M = 1.0$ .  
(Camera Angle 1)

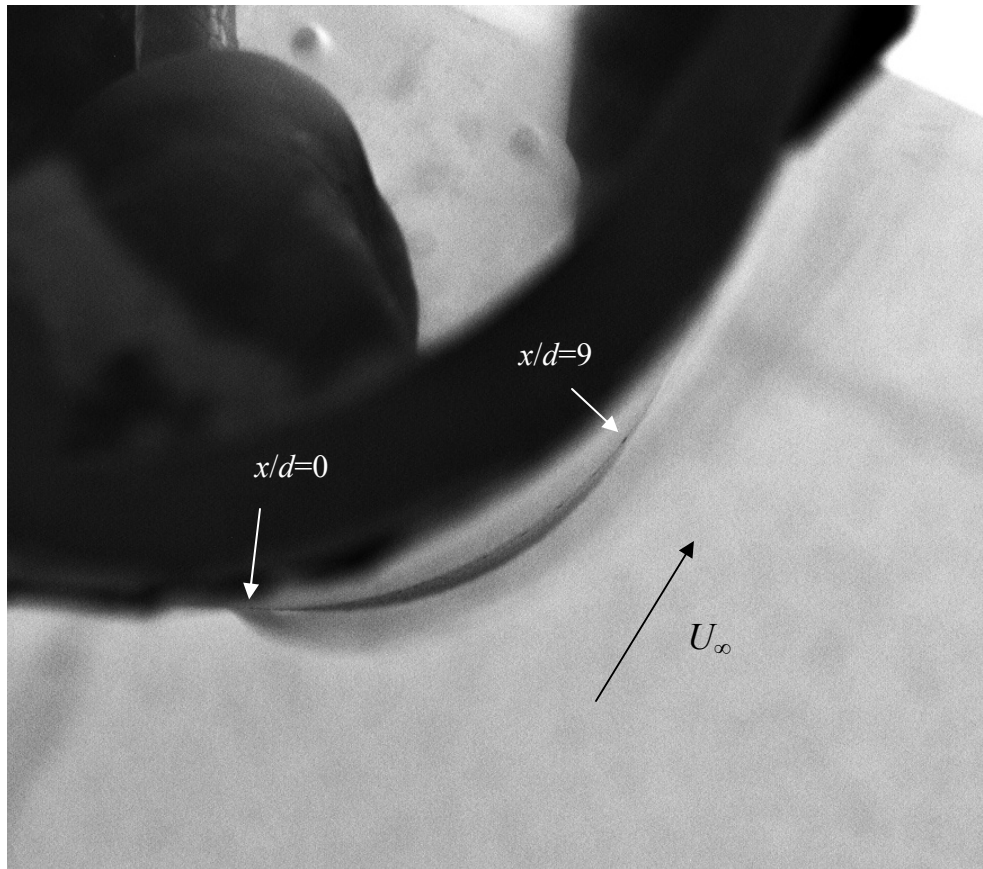


**Fig. 7.9 Near parallel to surface view of coolant, steady  $M = 1.0$ . (Camera Angle 2)**

The poor qualities of the  $M = 1.0$  jet that we observed above are only exacerbated at higher blowing ratios, as demonstrated with the  $M = 2.0$  jet as shown in Figs. 7.10 through 7.12. The greater amount of jet momentum causes more coolant to flow off of the surface it is intended to protect. In Fig. 7.12, the coolant plume is approximately  $1.5 d$  thick at its thickest point.

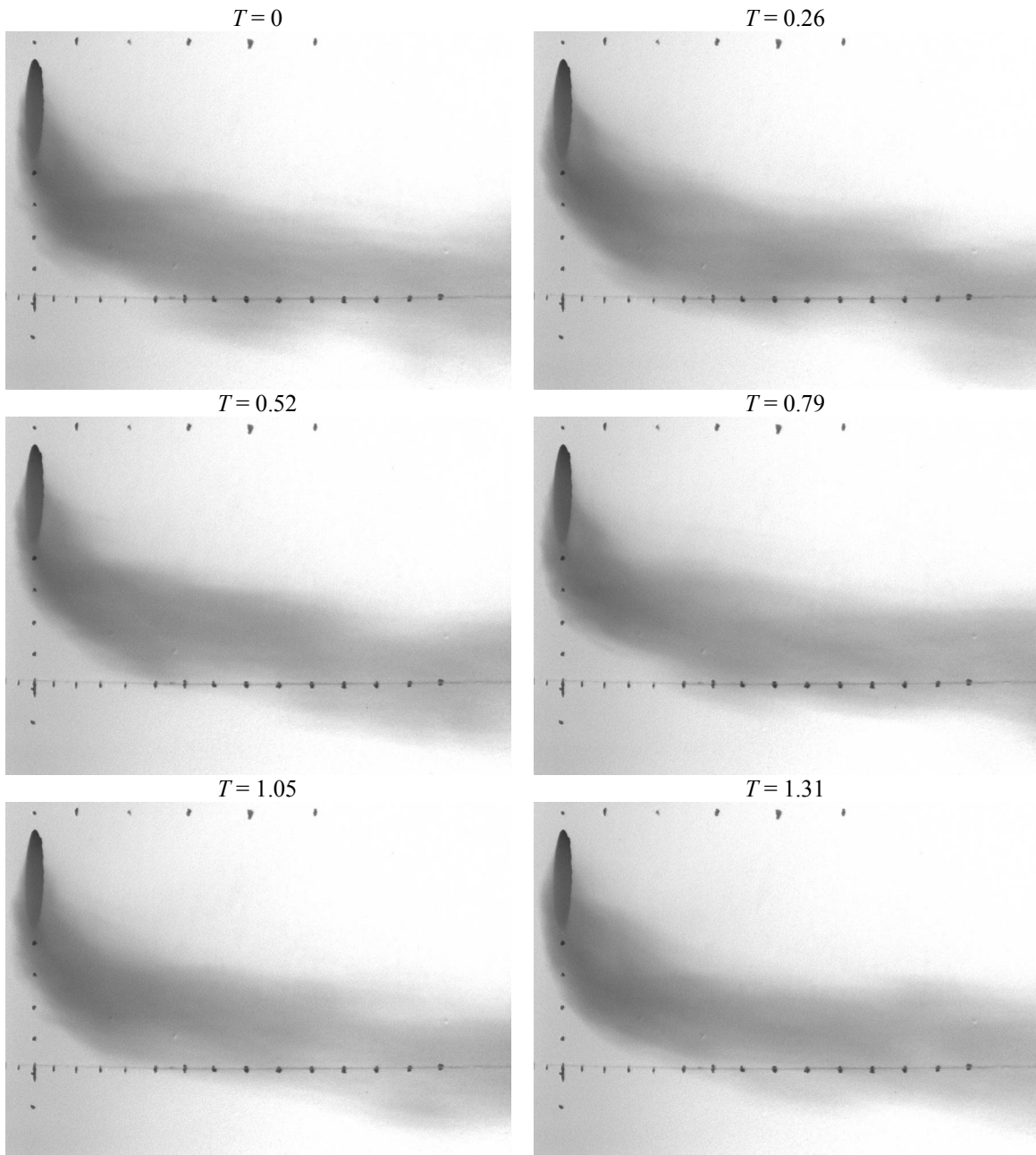


**Fig. 7.10** Near surface normal view of coolant at several points in time, steady  $M = 2.0$ . (Camera Angle 1)

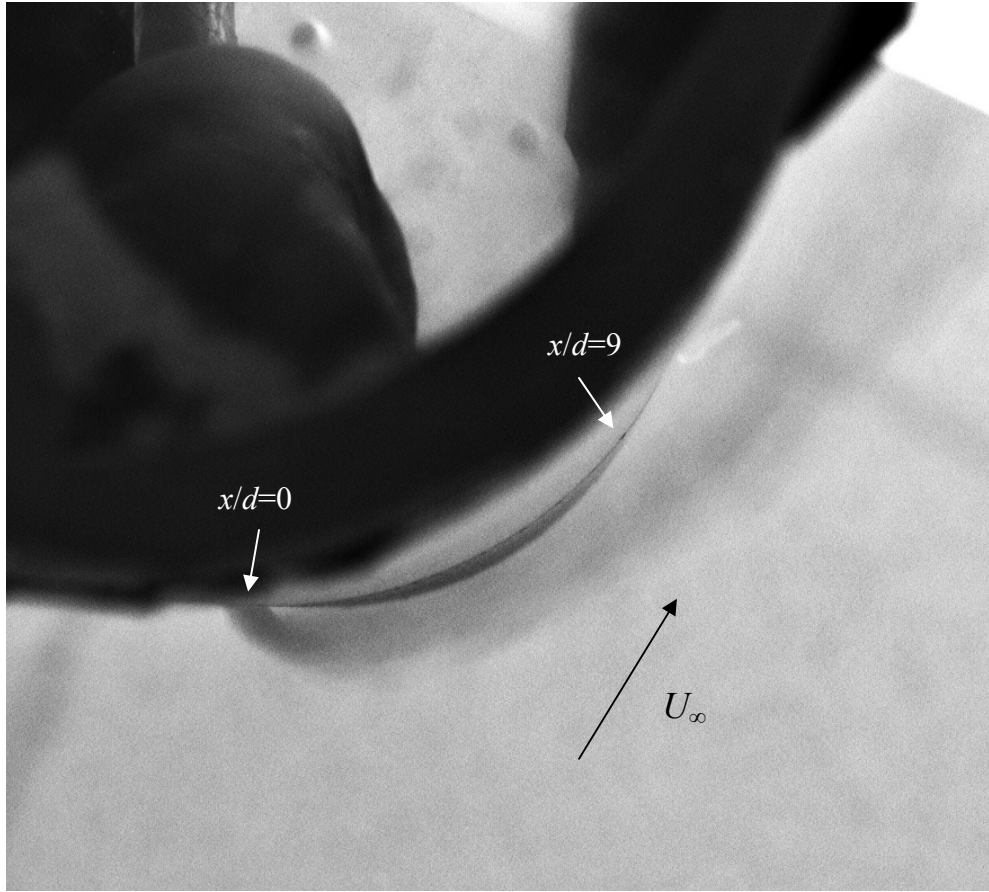


Fig. 7.11 Near parallel to surface view of coolant, steady  $M = 2.0$ . (Camera Angle 2)

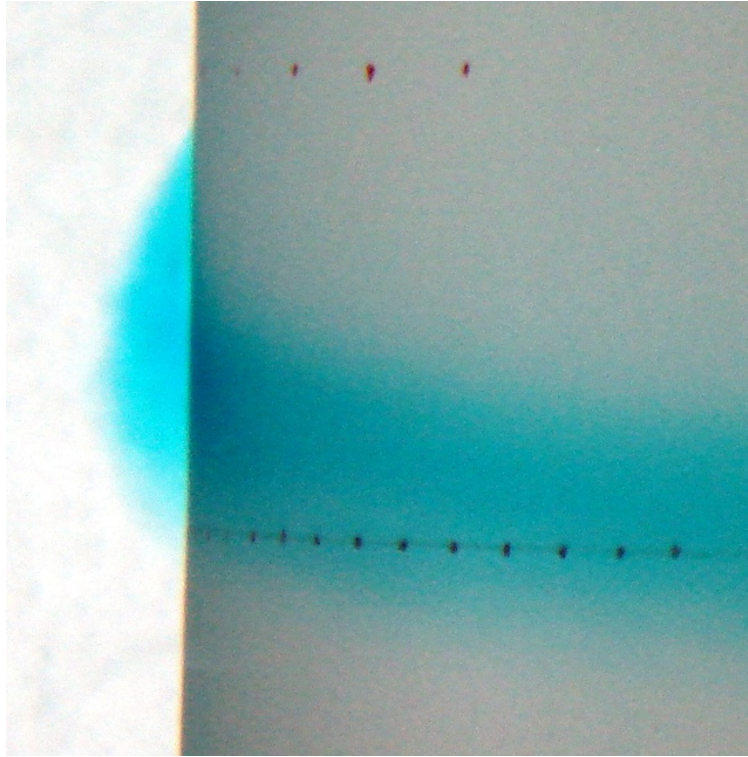


Fig. 7.12 Off-surface view of coolant at  $M = 2.0$ . Left edge of model is at  $x/d = 1.5$ . (Camera Angle 3)

## 7.2 Pulsed Jet Results

Figure 7.13 shows the coolant startup event for film cooling pulsed at a nondimensional frequency of  $F = 0.148$  (approximately 3.5 kHz at engine scale) with an average blowing ratio of  $\bar{M} = 0.25$ . At this frequency, the total cycle time is  $1/F = 6.76$ .  $T = 0$  is defined as the time the jet turns on. At  $T = 0.52$ , the jet reaches  $x/d = 9$ , near the location that the curved portion of the half cylinder leading edge meets the flat afterbody. Indeed, in  $\Delta T = 0.5$  the freestream travels one-half of the leading edge diameter, so such behavior would be expected. By  $T = 1.31$ , the coolant behavior has essentially reached steady state. Since the pulsed jet waveform is nearly square, the blowing ratio at this time is  $M \approx 0.5$ . Comparing the  $T = 1.84$  frame of Fig. 7.13 with the steady  $M = 0.5$  jet pictured in Fig. 7.5 confirms that the pulsed jet reaches a steady state condition very similar to the steady  $M = 0.5$  jet. This steady state behavior continues until the jet turns off at  $T = 3.38$ . This shutdown event is shown in Fig. 7.14. As discussed in Section 6.3, the blowing ratio becomes negative for a short time after turn-off. This is not obvious in

Fig. 7.14 because there is no dye to observe the freestream that gets drawn into the coolant hole. At this low frequency, the blowing ratio becomes positive again briefly even though the solenoid valve remains off for reasons discussed in Section 6.3. This is evident in the  $T = 3.93$  frame in Fig. 7.14, in which a small amount of dyed coolant has exited the coolant hole. This mass of coolant propagates downstream before the surface reaches a steady state “off” condition until  $T = 6.76$  (equivalent to  $T = 0$ ) when the cycle repeats. The startup and shutdown events account for only a short percentage of the total cycle time—approximately 30% when we consider steady state as having been obtained when the coolant is essentially steady in the region  $0.5 \leq x/d \leq 10$ . If we consider discrete points on the surface, the transient events account for a far smaller percentage of the time. For example, consider a point on the surface immediately downstream of the coolant hole in Fig. 7.13. The point reaches a condition in which the coolant immediately over it is unchanged after  $T = 0.52$ . Similarly, a point farther away from the coolant hole (at say,  $x/d = 10$ ) experiences an extended “off” period lasting until  $T \approx 0.52$ , but has an extended “on” period in Fig. 7.14 until  $T \approx 3.93$  even though the jet turns off at  $T = 3.38$ . At both  $T = 0.52$  and  $T = 3.93$ , the transient events for the point last at most  $\Delta T \approx 0.3$ , in which case the transient events account for only approximately 9% of the cycle time. This relative importance of the steady state conditions to the transient conditions that is obvious with the flow visualization helps explain the success of the low-frequency prediction technique at  $F = 0.148$  in Section 5.3. It also helps explain why this pulsed case has performance inferior to the steady  $M = 0.25$  case. Although Fig. 5.46 shows that the steady  $M = 0.25$  and  $M = 0.50$  cases (at low turbulence,  $Re_D = 30k$ ) performed similarly in terms of net heat flux reduction, the pulsed jet of Fig. 7.13 and Fig. 7.14 spends half of its time at  $M = 0$ , which has  $\Delta q_r = 0$ .

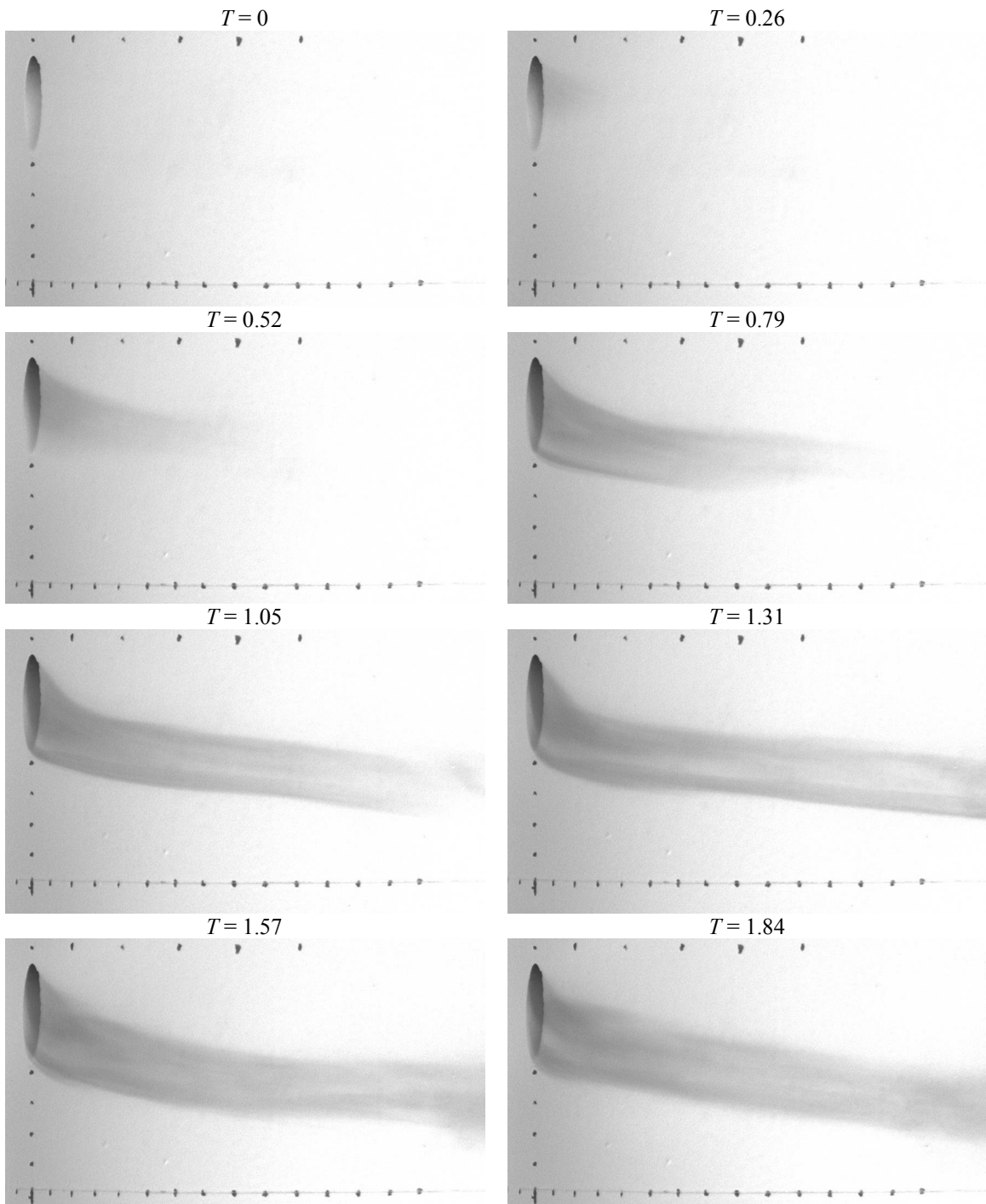
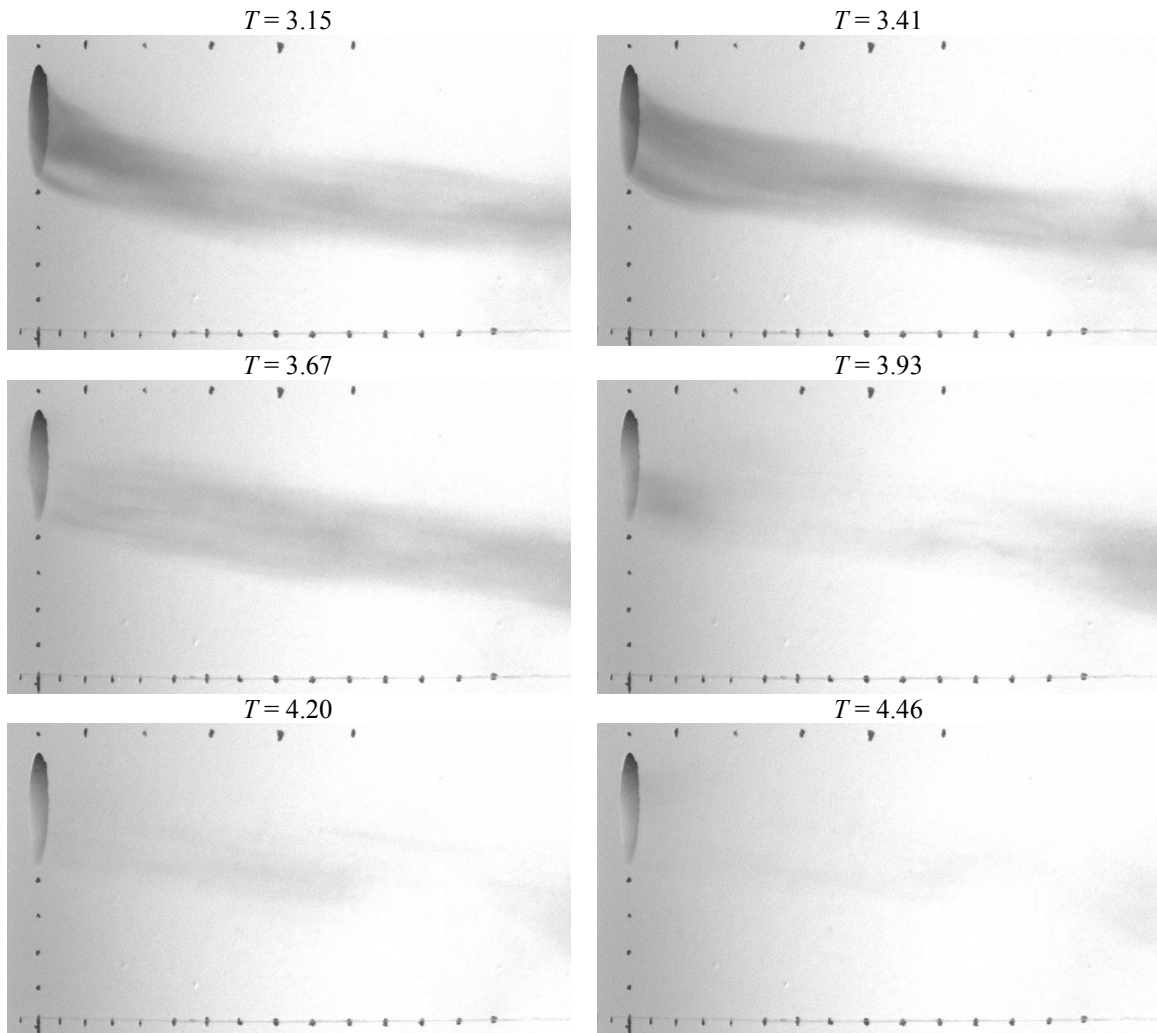


Fig. 7.13 Near surface normal view of coolant startup event,  $\overline{M} = 0.25$ ,  $F = 0.148$ . (Camera Angle 1)



**Fig. 7.14 Near surface normal view of coolant shutdown event,  $\bar{M} = 0.25$ ,  $F = 0.148$ . (Camera Angle 1)**

Analogous photographs for the  $\bar{M} = 1.0$ ,  $F = 0.148$  case are shown in Figs. 7.15 and 7.16. As with the  $\bar{M} = 0.25$  case above, the jet reaches steady-state rapidly relative to the total cycle time of  $\Delta T = 6.76$ . The jet turns on at  $T = 0$  in Figs. 7.15 and 7.16, and is visible in the  $T \approx 0.25$  frames. In Fig. 7.15, the jet rapidly resembles the steady  $M = 2.0$  jet shown in Fig. 7.10, as we would expect since the jet spends half of its time at  $M \approx 2.0$ . The view in the spanwise direction afforded by Fig. 7.16 reveals an interesting departure from the simple alternation between  $M = 0$  and  $M = 2.0$ . A distinct mass of coolant indicated by the oval in the  $T = 0.48$  frame has penetrated farther into the freestream than the remainder of the coolant to exit the coolant hole. We shall see this phenomenon again and reserve discussion.

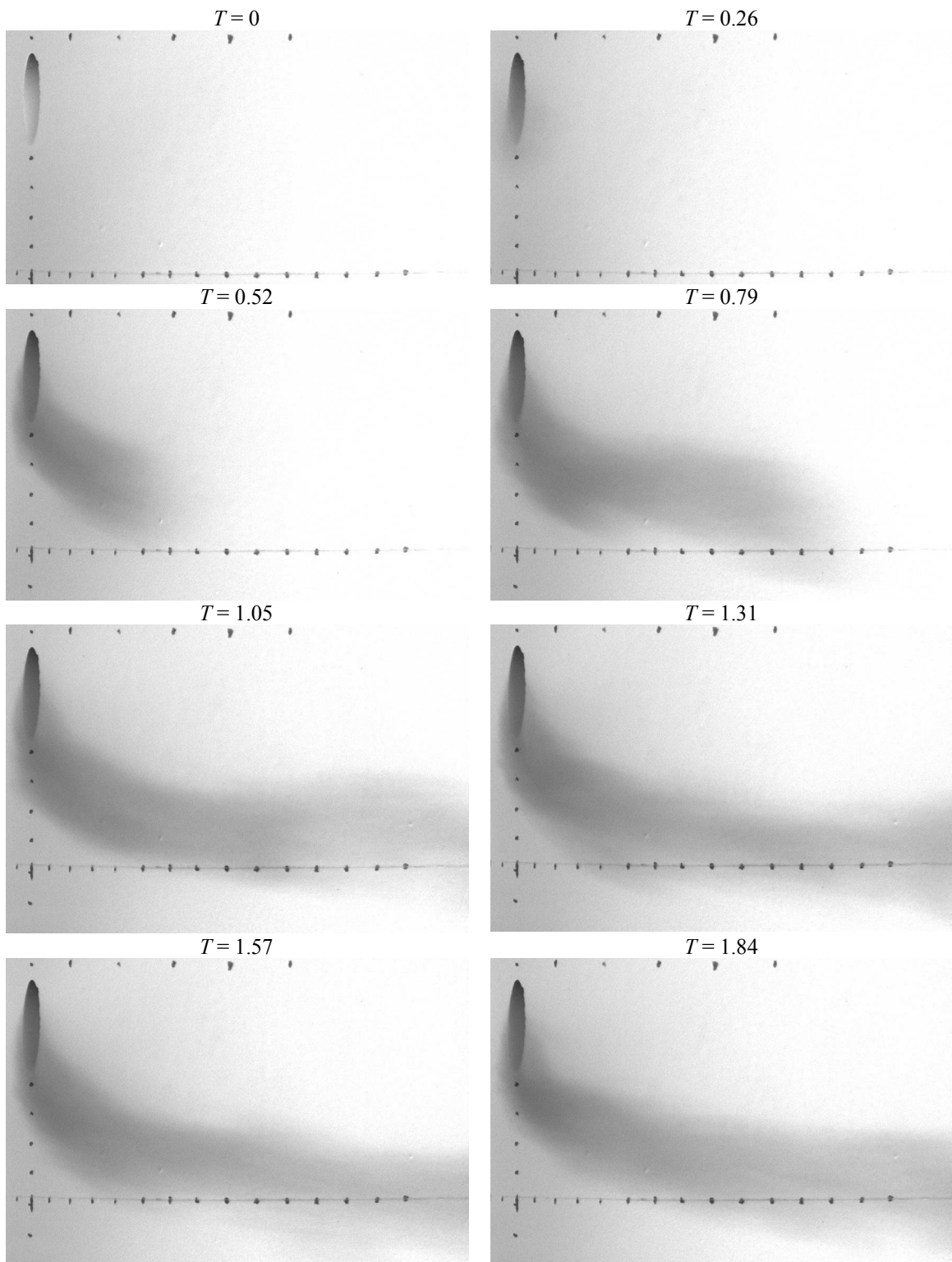


Fig. 7.15 Near surface normal view of coolant startup event,  $\overline{M} = 1.0$ ,  $F = 0.148$ . (Camera Angle 1)

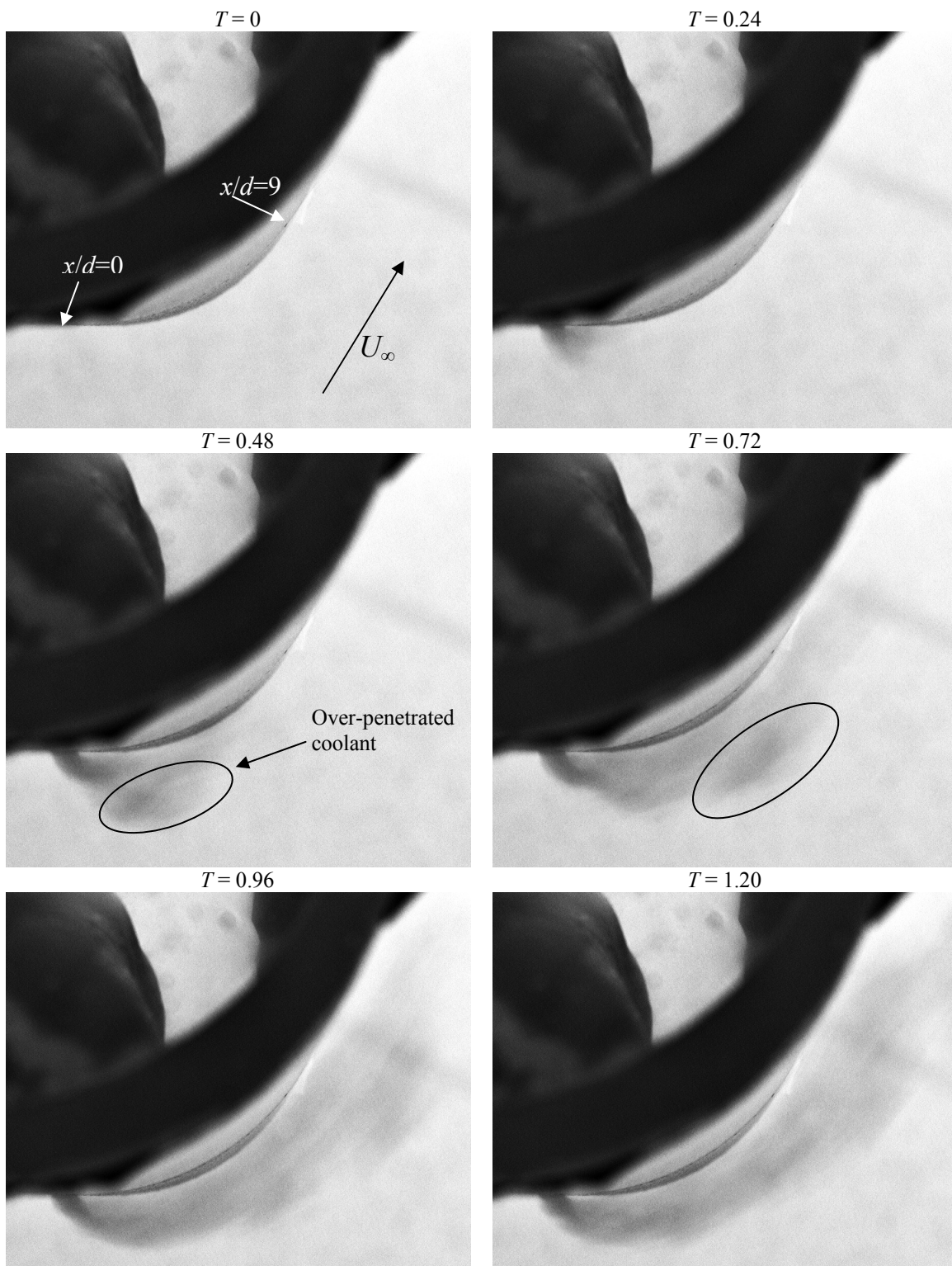


Fig. 7.16 Near parallel to surface view of coolant startup event,  $\bar{M} = 1.0$ ,  $F = 0.148$ . (Camera Angle 2)

The  $F = 0.294$  jets are not remarkably different from the  $F = 0.148$  jets. As we saw with the  $F = 0.148$  jets, the cycle time is long enough for the jets to reach steady state “on” and “off” conditions. Such is also the case with the  $F = 0.294$  jets; the cycle time is only half as long, affecting only the time at the quasi-steady conditions. As such, the startup and shutdown events are almost identical to those of the  $F = 0.148$  jets shown above, thus the  $F = 0.294$  jets are not shown.

We shall proceed to the next higher frequency,  $F = 0.590$ , the  $\overline{M} = 0.25$  jet of which is pictured in Figs. 7.17 and 7.18. For this jet, the cycle time is  $1/F = 1.694$ . The jet turns on at  $T = 0$  and is visible in the  $T \approx 0.25$  frames in Figs. 7.17 and 7.18. A comparison of the  $T = 0.24$  frame in Fig. 7.18 with the steady  $M = 0.5$  jet in Fig. 7.6 shows that the pulsed jet penetrates into the freestream more at  $T = 0.24$  than the steady  $M = 0.5$  jet even though the pulsed jet has an instantaneous blowing ratio of  $M \approx 0.5$  at this time. In the next frame ( $T = 0.48$ ) in Fig. 7.18, this initial amount of film coolant with the extra penetration is distinct from the coolant that resembles the steady  $M = 0.5$  jet in Fig. 7.6. That over-penetrated coolant (indicated by the oval) propagates downstream far from the wall as shown in the  $T = 0.72$  frame in Fig. 7.18. The coolant jet turns off at  $T = 0.85$ , as is evident in the  $T = 0.96$  and 1.20 frames.

The over-penetration of the coolant during the startup event is very obvious in the  $F = 0.590$  jet in Fig. 7.18, but was also pointed out with the  $F = 0.148$  jet in Fig. 7.16, particularly in the  $T = 0.48$  frame. It is almost always present to varying degrees. The magnitude of this over-penetration during jet startup is probably dependent on the rate at which the startup occurs, with the most extreme over-penetration occurring with a perfect step increase in blowing ratio. Although the solenoid valves pulse in a nearly square wave fashion, the actual jet startup is not instantaneous due to flexibility in the coolant tubing. The overpenetration of the first coolant to exit the coolant hole during startup resembles a phenomenon observed by M'Closkey et al. (2002) with an actively controlled normal jet in cross flow.

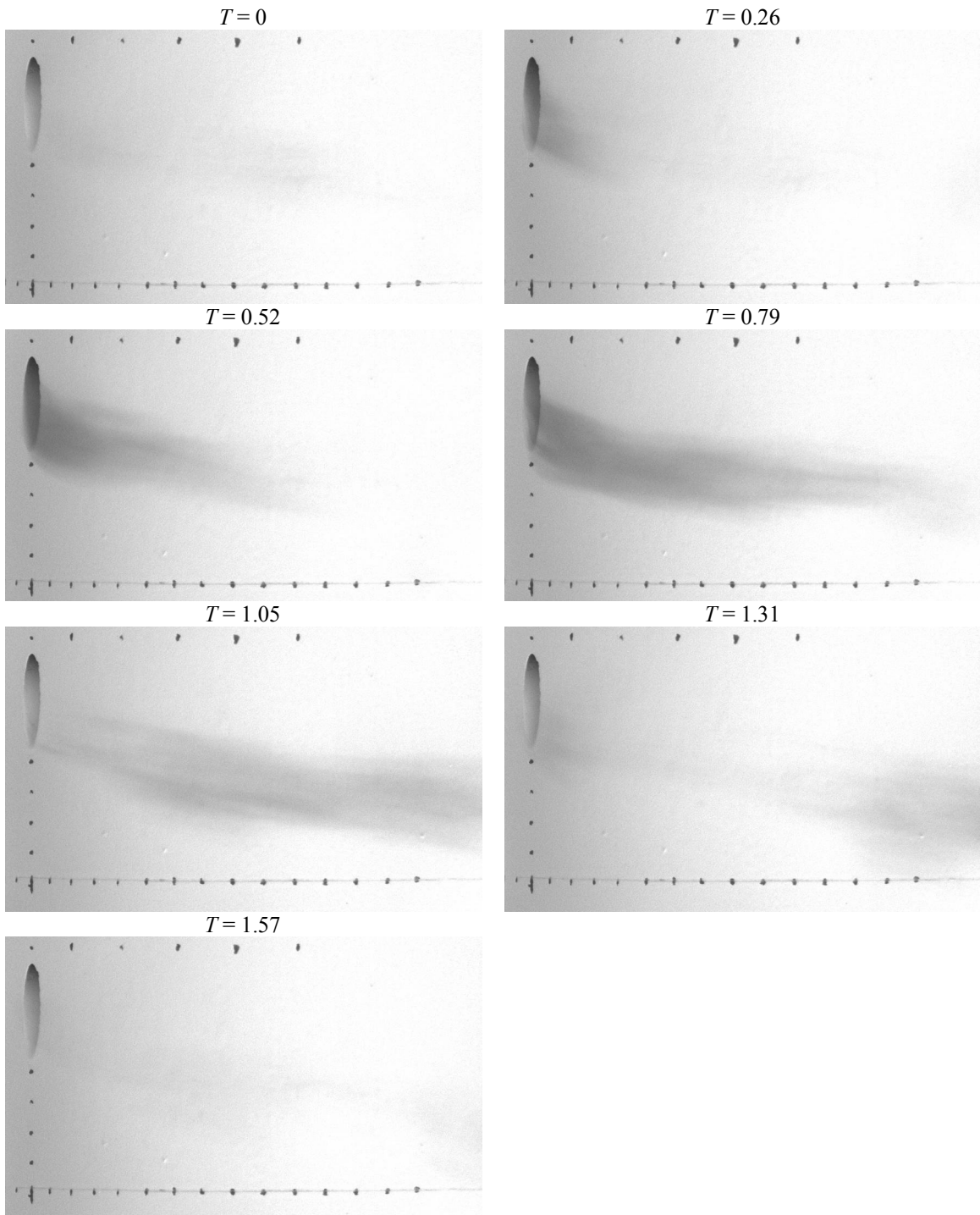


Fig. 7.17 Near surface normal view of coolant cycle,  $\overline{M} = 0.25$ ,  $F = 0.590$ . (Camera Angle 1)

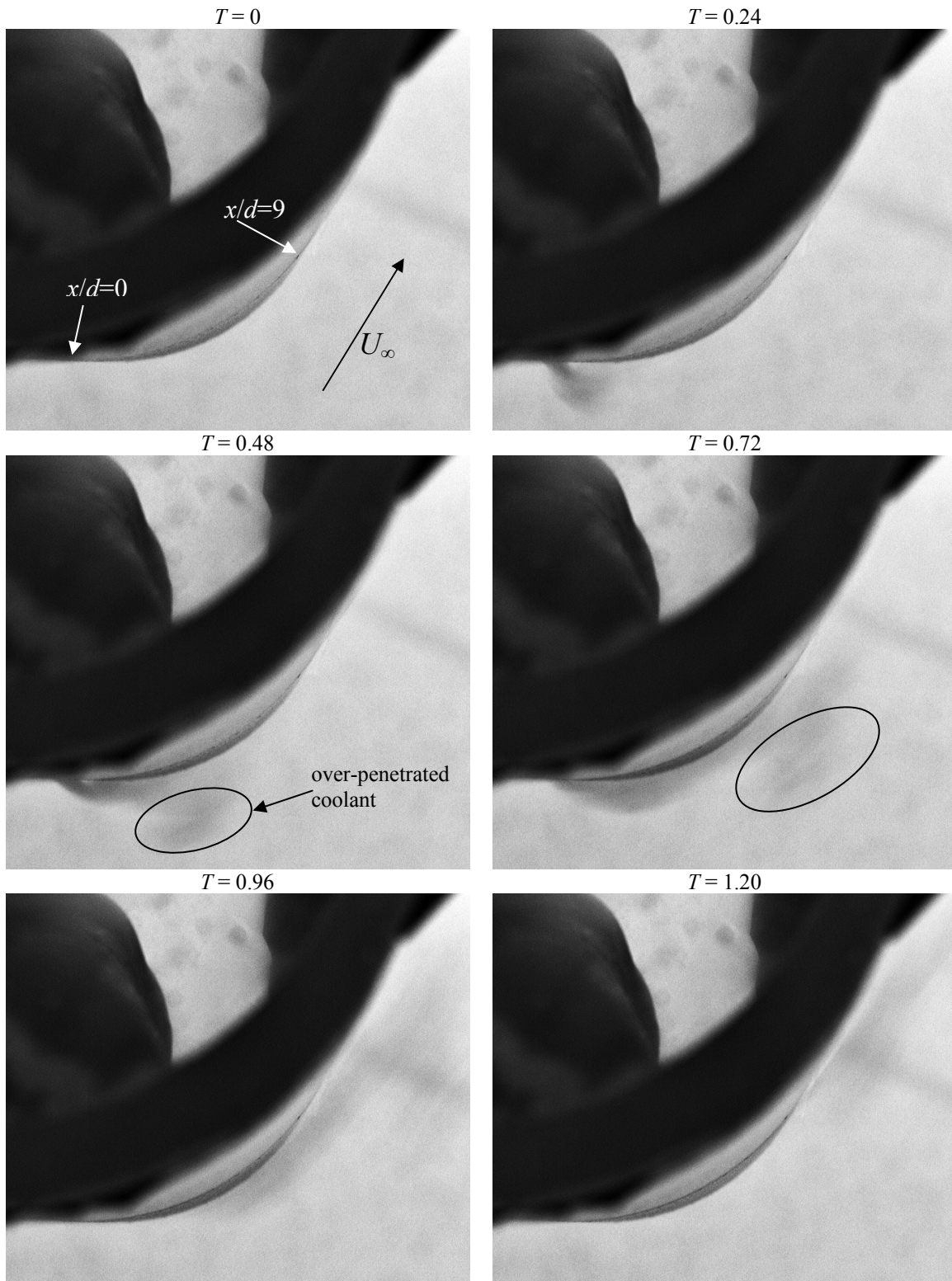


Fig. 7.18 Near parallel to surface view of coolant startup event,  $\overline{M} = 0.25$ ,  $F = 0.590$ .  
(Camera Angle 2)

The  $\bar{M} = 0.25$  at  $F = 1.195$  results are shown in Figs. 7.19 and 7.20. Here we combine the laminar nature of the steady  $M = 0.5$  jet (switched off for half the time to yield  $\bar{M} = 0.25$ ) with the violent unsteadiness of relatively high frequency pulsations. As we noted with the same average blowing ratio at  $F = 0.590$ , the coolant again has a distinct over-penetrating mass at jet turn-on; however, the cycle time is too short for the remainder of the coolant to reach a quasi-steady state. In fact, it appears that the majority of the coolant remains in the over-penetrating mass. After the over-penetration, the following coolant exiting the hole remains attached to the surface and maintains the smooth flowing lines characteristic of laminar coolant flow. The over-penetrating turbulent mass is most pronounced in the near-parallel view in Fig. 7.20 for  $T \geq 0.36$ . The laminar attached coolant is more pronounced in Fig. 7.19 due to the streamwise stretching of the coolant. The turbulent mass diffuses in all directions more than the attached laminar coolant. The diffusion of the over-penetrated coolant is evident in Fig. 7.20, as larger ellipses are required to encompass the mass as it propagates downstream.

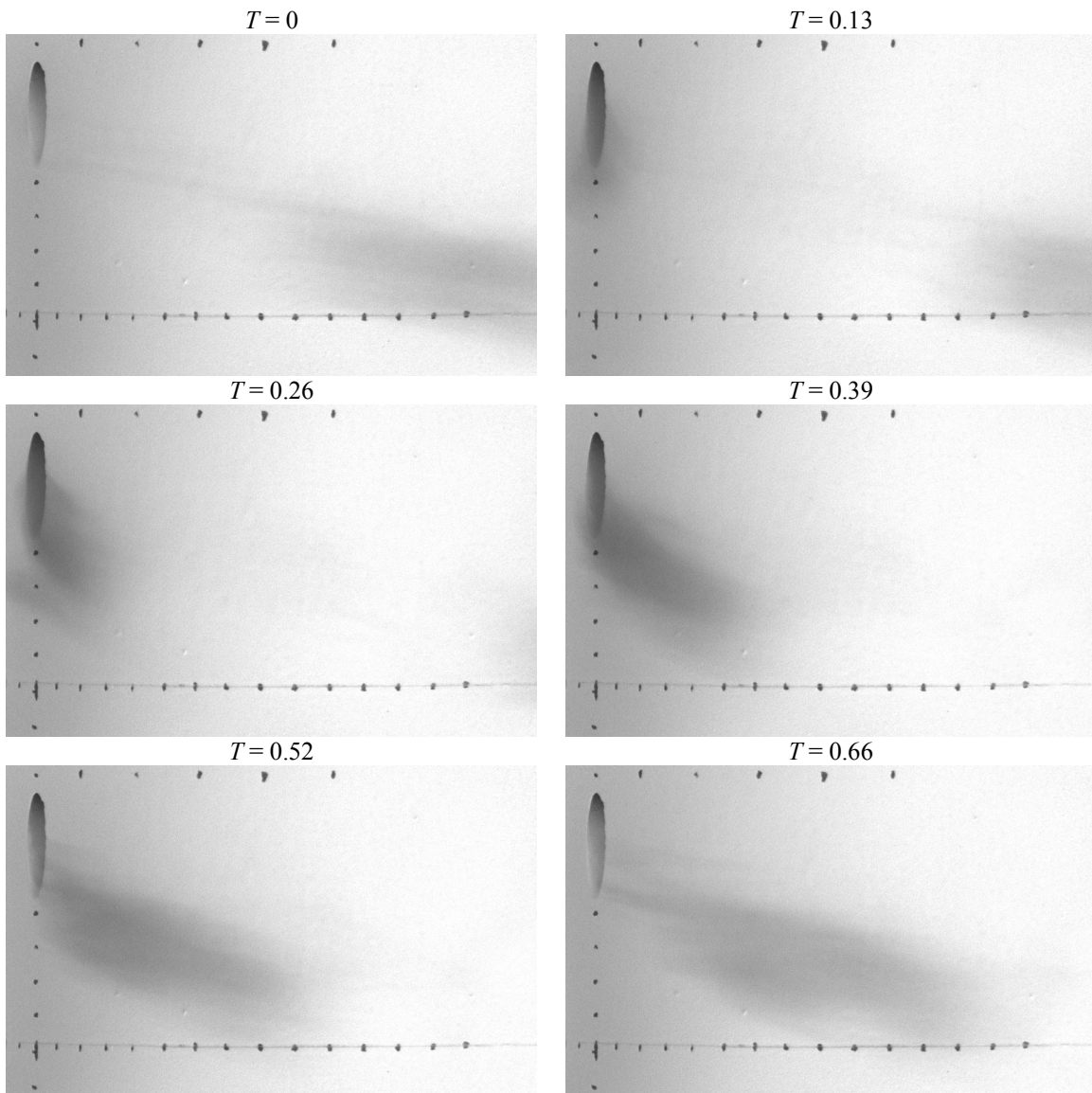


Fig. 7.19 Near surface normal view of coolant cycle,  $\overline{M} = 0.25$ ,  $F = 1.195$ . (Camera Angle 1)

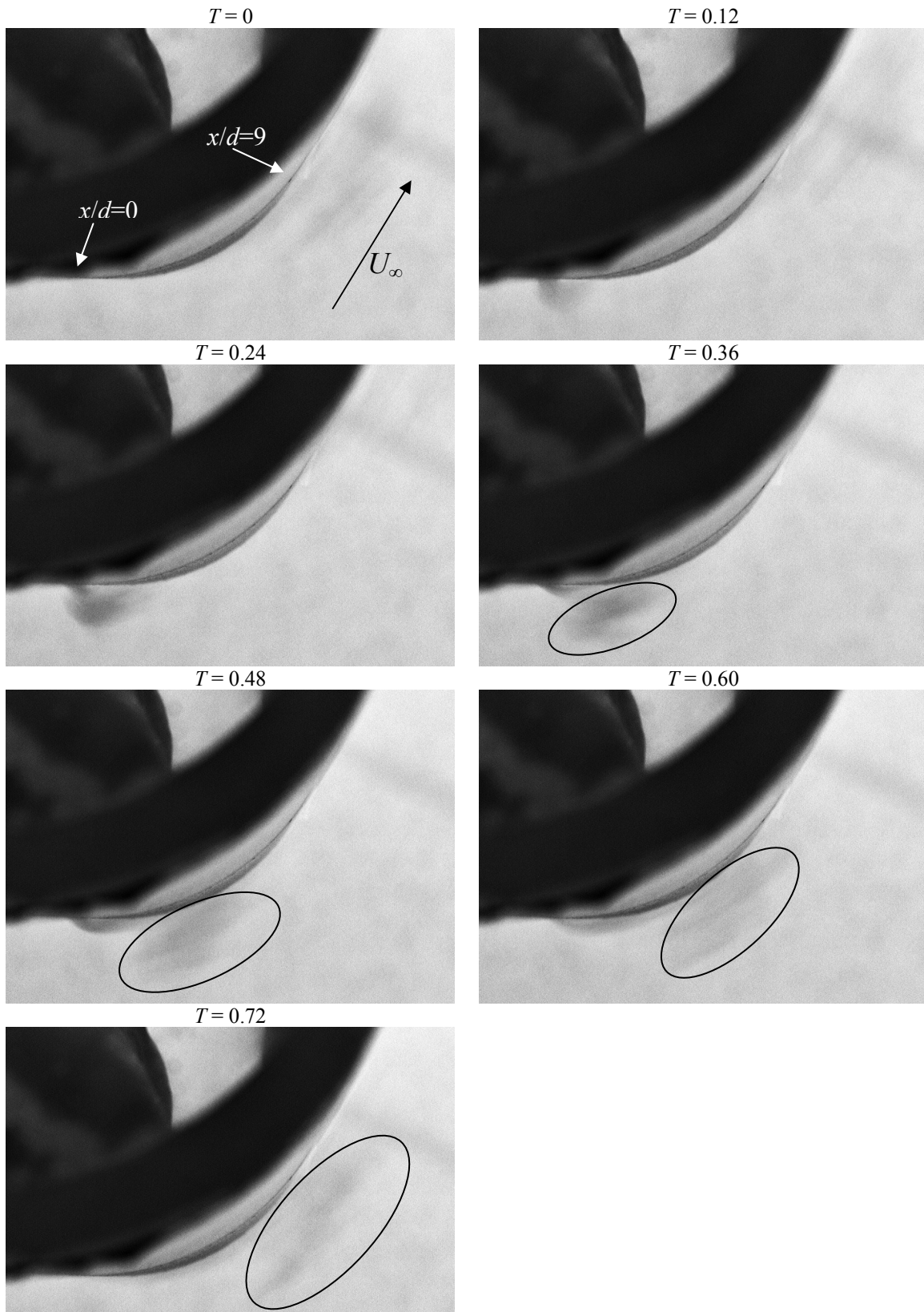


Fig. 7.20 Near parallel to surface view of coolant cycle,  $\overline{M} = 0.25$ ,  $F = 1.195$ . (Camera Angle 2)

A look at the  $\overline{M} = 0.75$  jet at  $F = 1.195$  affords a better view of the some of the high frequency pulsed film cooling dynamics because of the greater amount of coolant. The Camera Angle 1 view in Fig. 7.21 shows how fast this pulsing really occurs. The entire physical length of the coolant pulse is approximately only  $10 d$ . During each pulse, a very small amount of coolant gets trapped in the boundary layer and is visible as the smooth lines of laminar coolant. As clearly visible from Camera Angle 2 in Fig. 7.22, the vast majority of the coolant is turbulent and far from the surface it is intended to protect. The very short pulses do not give the coolant sufficient time to reach a quasi-steady state during either the “on” or “off” periods. Slower moving coolant in the boundary layer remains behind as the bulk of the coolant is swept downstream farther from the surface it is intended to protect. The fact that the vast majority of the coolant penetrates far into the freestream at  $F = 1.195$  is a possible reason for the lack of degradation due to high freestream turbulence noticed at  $Re_D = 30k$  for this pulsing frequency in the  $\gamma$  results presented in Fig. 5.74.

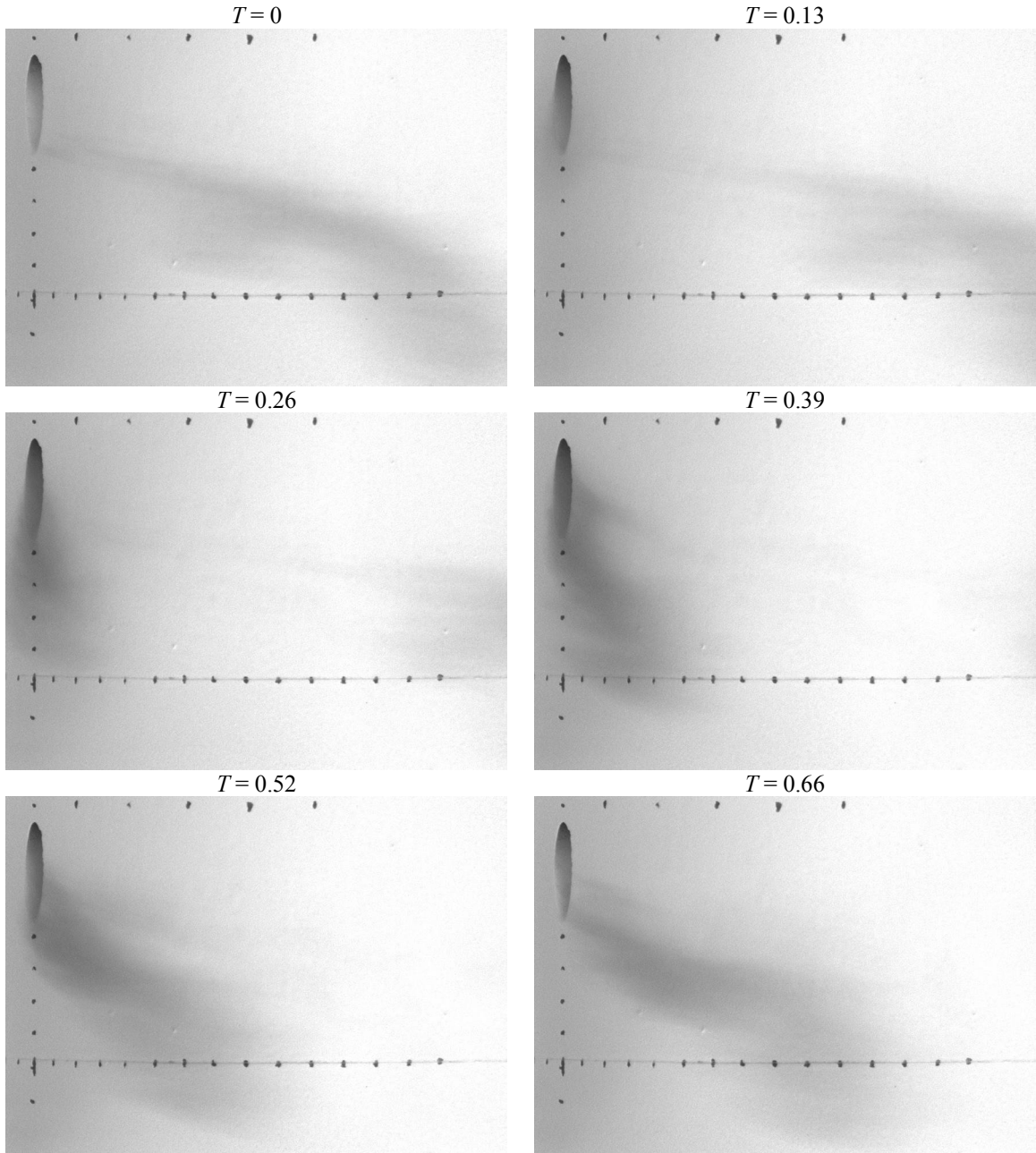


Fig. 7.21 Near surface normal view of coolant cycle,  $\bar{M} = 0.75$ ,  $F = 1.195$ . (Camera Angle 1)

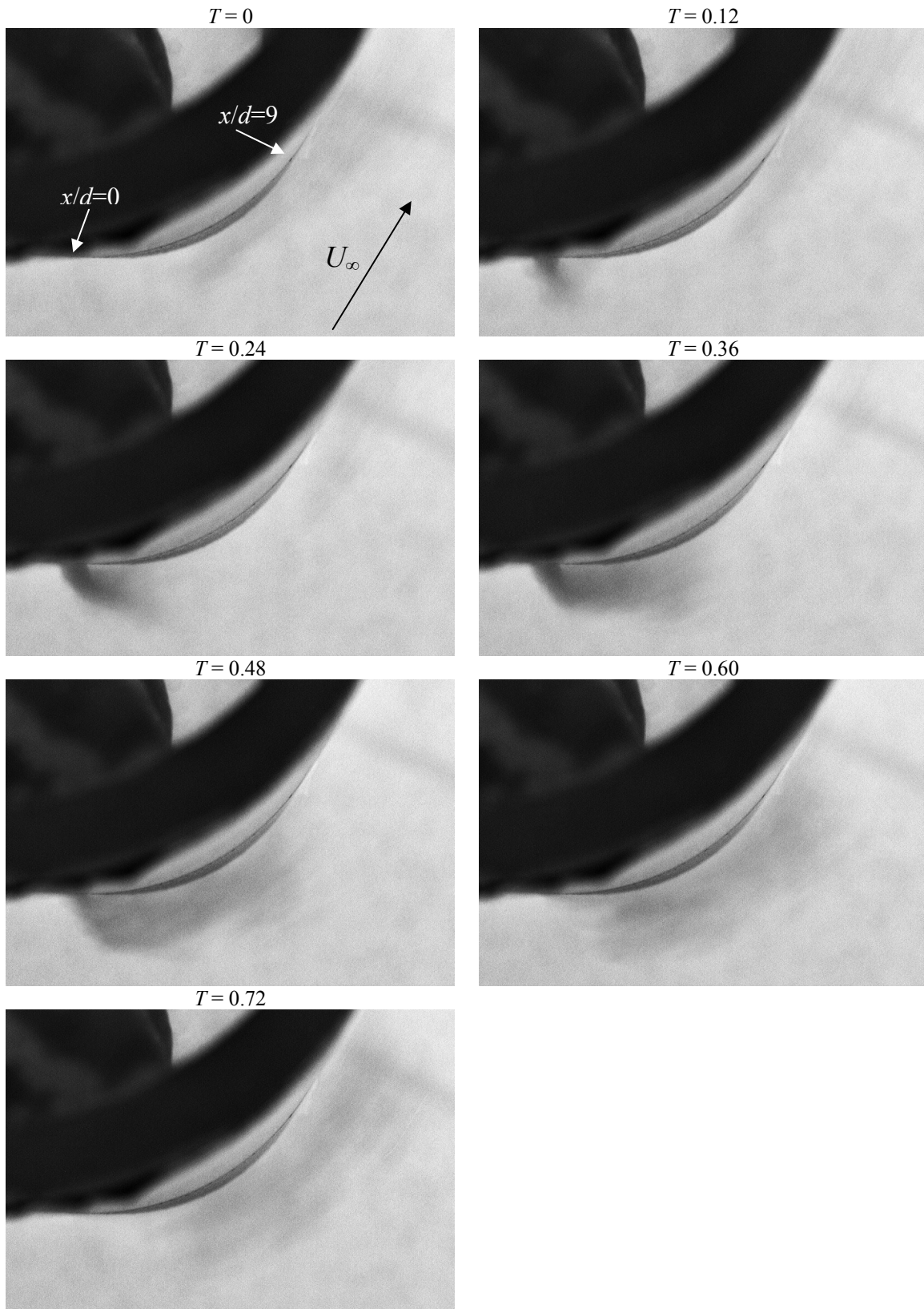
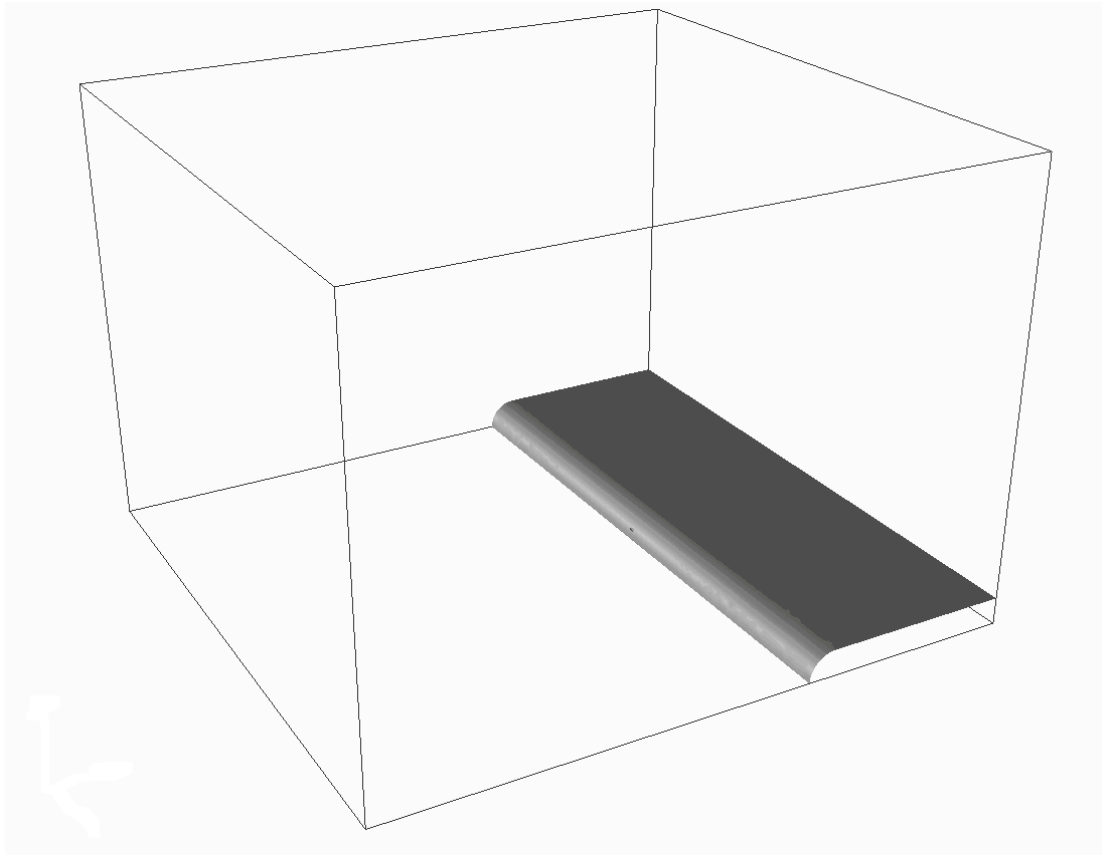


Fig. 7.22 Near parallel to surface view of coolant cycle,  $\overline{M} = 0.75$ ,  $F = 1.195$ . (Camera Angle 2)

## 8. Computational Fluid Dynamics Methodology

The experiments performed in the wind tunnel were designed to give temporally averaged data relevant to the calculation of the net heat flux reduction. Temporally resolved surface and flow field data were obtained through a computational study. This section presents the methodology by which a computational analog to the experiments described in Chapters 4 and 5 was performed. In addition to this computational simulation of the single hole geometry, an additional study of a row of coolant holes spaced 7.86 hole diameters apart was carried out using the same techniques as described in this section, the only notable difference being the use of periodic boundary conditions on either side of the hole to model an infinitely long row of holes.

The grid geometry shown in Fig. 8.1 uses a one meter span leading edge with a symmetry plane corresponding to the locus of streamlines intersecting the stagnation line on the leading edge. Otherwise, the geometry and coordinate system matches that in Figs. 4.1 and 4.3. A single coolant hole of 0.476 cm diameter in the middle of the leading edge has a length to diameter ratio of  $L/d = 11.79$  such that the dimensions matched the dimensions of the physical model described in Chapter 4. The span of the leading edge was  $209 d$ . The computational domain extended  $146 d$  upstream of the leading edge and  $146 d$  above the flat afterbody. The coolant hole inlet boundary condition was set at plane normal to the axis of the hole with mass flow in the direction of the hole axis distributed uniformly across the surface area of the inlet. The plenum was not modeled due to the high  $L/d$  of the coolant hole. Although Leylek and Zerkle (1994) conclude there is an influence of the plenum on the coolant hole exit velocity profile, they used a maximum  $L/d$  of 3.5, which is only 30% of that used in the present study so the plenum is not expected to have as great an influence in the current study.



**Fig. 8.1 Computational domain**

An unstructured mesh was generated on the computational surfaces using GridGen’s implementation of Delaunay triangulation. In order to control the volume grid growth rate away from wall grids, additional “transparent” surface grids (surface grids through which fluid flow is unimpeded in any way) were placed offset from the leading edge and the afterbody a distance of approximately the leading edge radius. The unstructured volume grid was generated using SolidMesh, which uses the Advancing-Front/Local-Reconnection grid generation routine (Marcum, 1998). Prismatic cells were used in the vicinity of the wall surfaces in a fashion intended to resolve turbulent boundary layers with the nearest cell spaced with  $z^+$  of order one.<sup>s</sup>

The intent of the computational study is to model the physical experiment rather than actual engine operating conditions. The physical experiment that was modeled was

---

<sup>s</sup> In popular literature, this is usually referred to as the “wall  $y^+$ ,” referring to the distance of the first grid point from the wall, nondimensionalized according to the inner law. Since  $z$  is the coordinate direction perpendicular to the wall in our present coordinate system, we use the term  $z^+$  instead of  $y^+$ .

a low speed flow (Mach  $< 0.04$  freestream) and the temperature range in the physical experiment was such that the coolant to freestream density ratio was  $DR \approx 1$  so the computational model assumed constant density flow. Fluent's three dimensional node-based segregated solver was used for all computations. All discretization schemes were second order.

The direct numerical simulation by Muldoon and Acharya (2007) found an absence of large scale turbulent structures near the hole exit where a starting vortex was found to cause differences between the pulsed and unpulsed cases. Since the computationally expensive direct simulation of turbulence unlikely provided any benefit over a simpler turbulence model, a turbulence model was used in the current study. Additionally, the coolant hole was modeled and therefore expected to give more accurate results in the near-hole region than a direct simulation assuming a laminar flow boundary condition at the exit of the hole incapable of interacting with the oncoming flow as used by Muldoon and Acharya (2007). In the current study turbulence was modeled using the realizable  $k$ - $\epsilon$  model with enhanced wall treatment, which uses a two layer model such that the domain is divided into fully turbulent and viscosity-affected regions (Fluent Inc., 2005). The realizable  $k$ - $\epsilon$  model has been proven to be superior to the standard  $k$ - $\epsilon$  model with jets and mixing layers (Fluent Inc., 2005) and has been used with at least some success with film cooling flows (see, for example, Harrison and Bogard, 2007 and Kartuzova et al., 2008). For the purposes of the convergence study, the turbulence at the inlet and outlet of the computational wind tunnel was modeled to have an intensity of  $Tu = 1\%$  and a length scale of  $\Lambda_f = 2.1 d$ . The coolant hole inlet was modeled to have a turbulence intensity of  $Tu = 1\%$  and a length scale of  $\Lambda_f = 0.42 d$ .

### **8.1 Grid Convergence**

Grid convergence was established using a slightly higher Reynolds number flow than was used in following uses of the grid. The Reynolds number used to establish grid convergence was  $Re_D = 77000$ . Fluent's steady solver was used and convergence was assumed when the largest scaled residual (usually on  $\epsilon$ ) was of order  $10^{-5}$ . When feasible, largest residuals of order  $10^{-7}$  were attained. In order to develop a sufficiently fine grid that the results would be grid independent, different sized grids were tested at a steady

blowing ratio of  $M = 1$  and the results for several of these grids are compared in Figs. 8.2 through 8.4. Recall that  $x$  is the distance along the surface in the streamwise direction and  $y$  is the distance in the spanwise direction and the hole is angled in the negative  $y$  direction. It is evident from Figs. 8.2 through 8.4 that the 9.2 million cell grid was sufficient for grid independence. When spanwise averaged across the bulk of the jet ( $-2.5 < y/d < 1.5$ ), the adiabatic effectiveness determined with the 9.2 million cell grid was within 0.5% of the measured value with the 8.9 million cell grid and within 1.5% of the measured value with the 7.6 million cell grid.

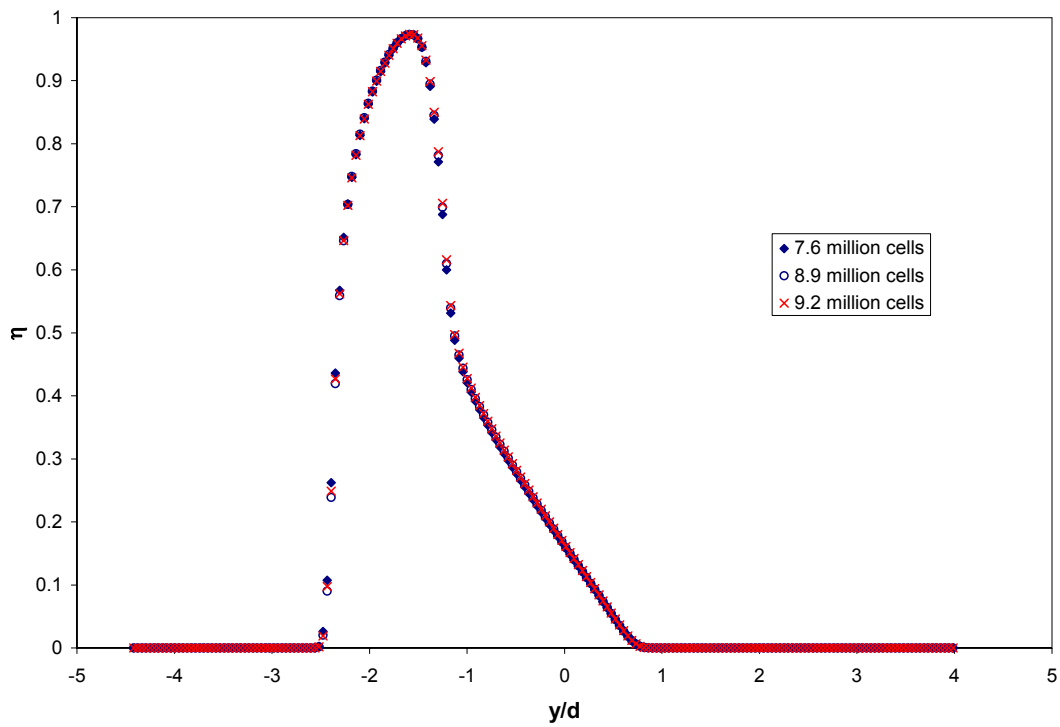


Fig. 8.2 Adiabatic effectiveness plots for several grids at  $x/d = 1$

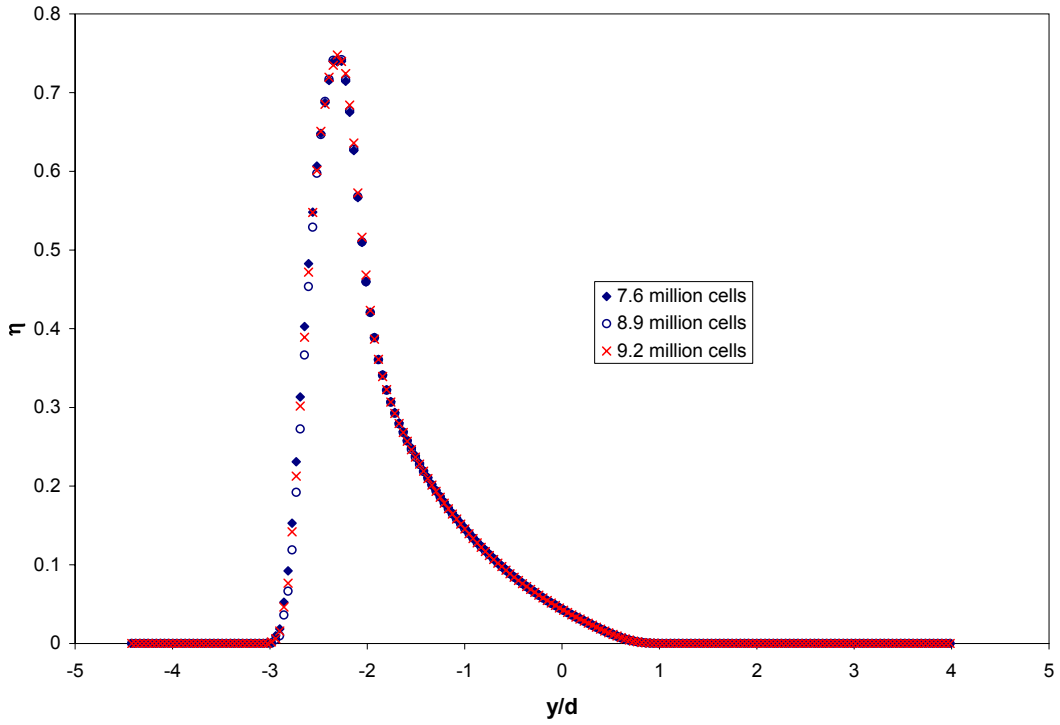


Fig. 8.3 Adiabatic effectiveness plots for several grids at  $x/d = 4$

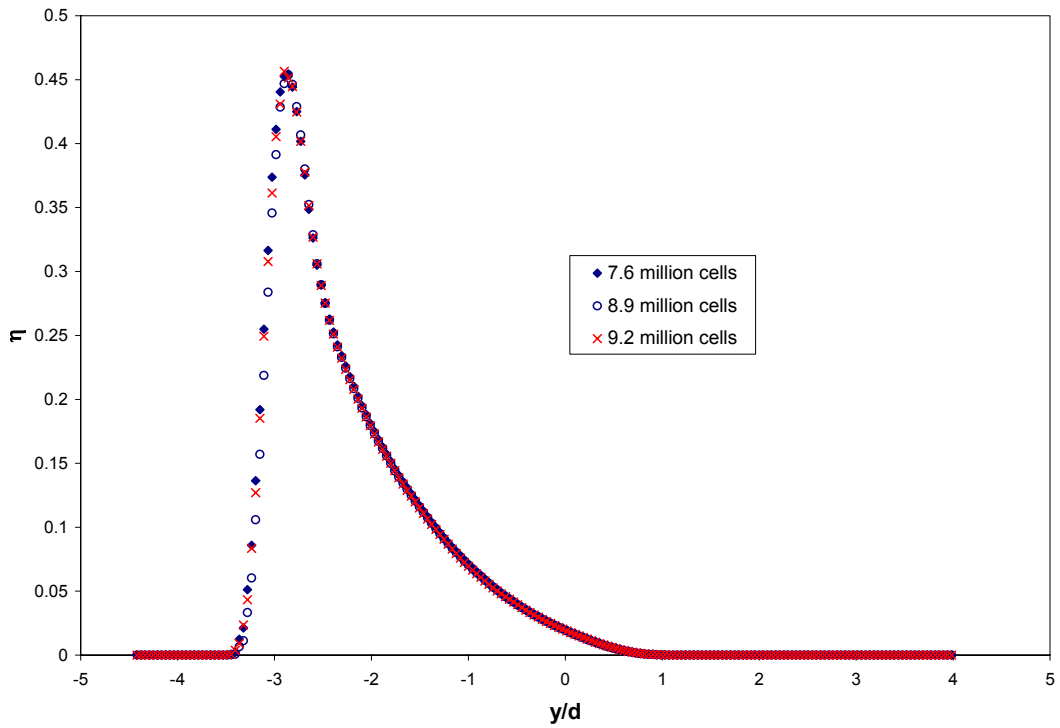
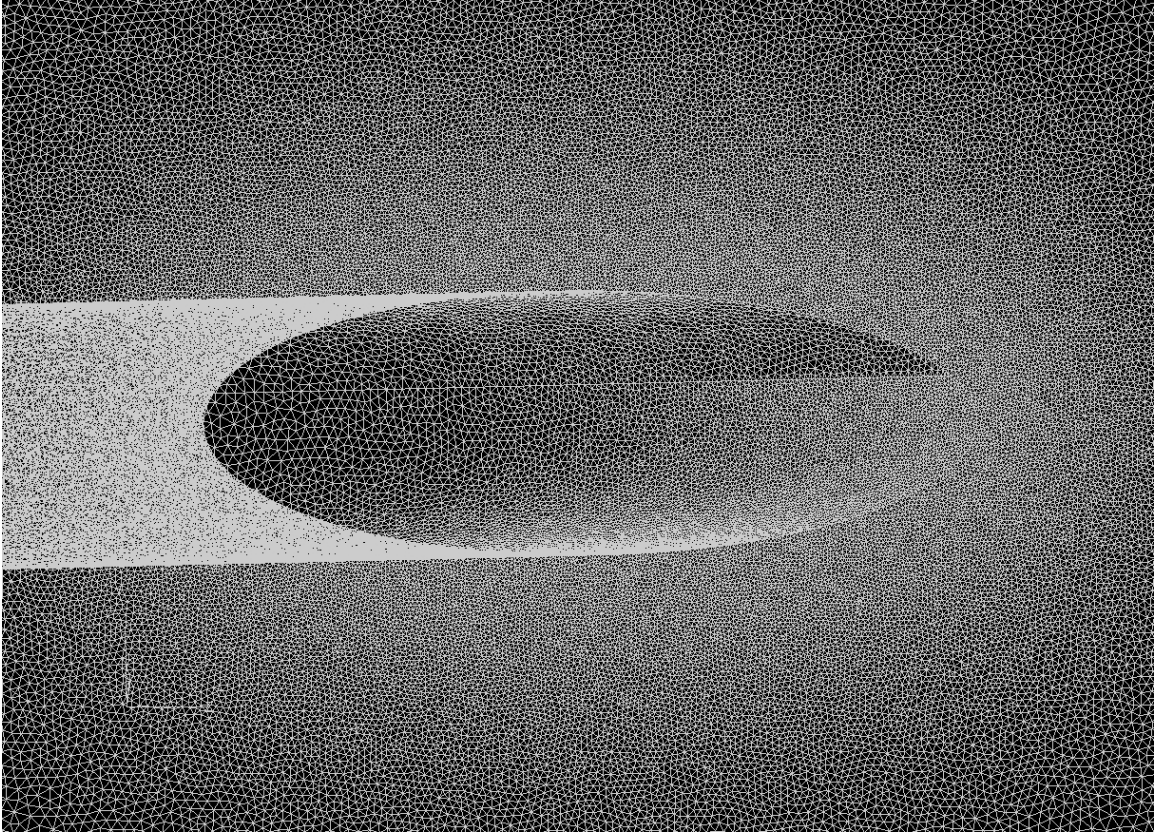


Fig. 8.4 Adiabatic effectiveness plots for several grids at  $x/d = 9$

The steady state results for  $M = 1$  were used to check the “wall  $z^+$ ” distribution on the 9.2 million cell grid. The “wall  $z^+$ ” distribution on a computational wall refers to the distance the nearest grid point off the wall lies from the wall. In order to resolve the boundary layer, we require that the first grid point off the wall is at a distance of order  $z^+ \approx 1$ . The maximum wall  $z^+$  was determined to be  $z^+ = 2.67$  along a small part of the intersection of the coolant hole with the outer radius of the leading edge where a sharp edge exists. Aside from this sharp edge, the wall  $z^+$  was approximately 1 or less than 1 except for a region approximately  $1 d$  downstream of the fore side of the coolant hole where the wall  $z^+$  had a maximum of approximately 1.8. This wall  $z^+$  distribution is deemed sufficient since where wall  $z^+ > 1$ , it is still well within the viscous sublayer, that is,  $z^+ < 5$ .

Having confirmed that the 9.2 million cell grid is both grid converged and has sufficiently close spacing near the wall to resolve a turbulent boundary layer, the remainder of the single hole computational studies employed this grid. Two renderings of the final grid are shown in Fig. 8.5 and Fig. 8.6.



**Fig. 8.5** Surface mesh on leading edge in vicinity of coolant hole

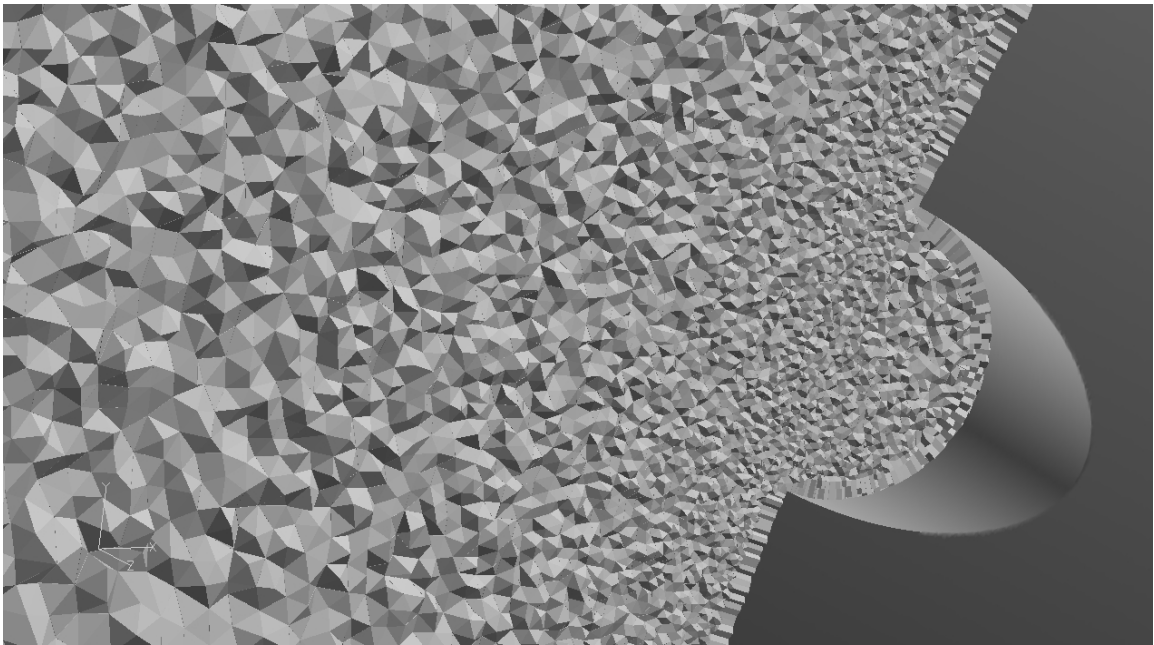


**Fig. 8.6** Fluid region mesh on streamwise plane bisecting intersection of the coolant hole with the leading edge

## 8.2 Time Step Convergence

Unsteady simulations were performed following the generation of a suitable grid. A second order implicit unsteady formulation was used for all unsteady simulations. Because the equations were segregated, splitting error could arise when advancing through time in addition to the second order temporal discretization error. An iterative time advancement scheme was employed that solved all equations iteratively at each time step in order to drive the splitting error to zero. In general, smaller time steps require fewer iterations at each time step. All scaled residuals were driven down to a maximum of  $10^{-6}$  before the solution was considered to be converged for a particular time step. Usually, the residual on  $\epsilon$  was the limiter, with the other residuals being at least an order of magnitude smaller.

Time step convergence was established by considering the temporal variation in adiabatic effectiveness at several points on the leading edge whose temperature is significantly influenced by the film cooling hole. These points are shown relative to the film cooling hole in Fig. 8.7. Unsteady simulations were performed for  $\bar{M} = 0.5$ ,  $f = 20$  Hz, DC = 50%. Thus the blowing ratio alternated between “on” at  $M = 1$  and “off” at  $M = 0$  with the blowing “on” for half of the time. An unsteady simulation was started using the steady-state  $M = 1$  results obtained in the process of establishing grid convergence. At  $t = 0$  the blowing ratio was set to  $M = 0$ . At  $t = 0.05$  s, the blowing was turned back on. The cycle was repeated several times in order to establish periodic steady state. It was found that periodic steady state conditions were in existence immediately because  $F \ll 1$  and the steady-state results for  $M = 1$  were used as the initial conditions for the unsteady simulation.

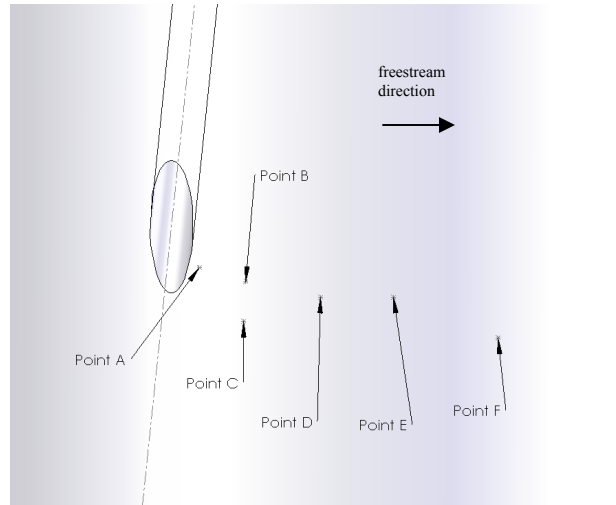


**Fig. 8.7 Surface points used in establishment of time step convergence**

A time step as low as  $2 \times 10^{-6}$  s was required for the solution to be sufficiently independent of time step. The true step change in the boundary condition at the inlet of the film cooling hole is quite likely to be responsible for the requirement of such a small time step. Fig. 8.8 shows the adiabatic effectiveness history of Point E for the  $2 \times 10^{-6}$  s time step and a time step of half of that, demonstrating that  $2 \times 10^{-6}$  s is sufficient. Several aspects of Fig. 8.8 are quite remarkable. The entire transient event took place over only 0.008 seconds (less than a fifth of the time that the coolant is turned “off”) and it took 0.001 seconds for the adiabatic effectiveness at Point E to respond to the step change in blowing ratio. Perhaps the most striking observation is the sharp increase in adiabatic effectiveness that increased the adiabatic effectiveness 16% over the steady state value for a short period of time during the transient event associated with turning off the coolant. Unusual dynamics associated with pulsed jets are already apparent. A more complete time history of the adiabatic effectiveness is presented in Fig. 9.7 in the context of the results as opposed to the current context of time step convergence.

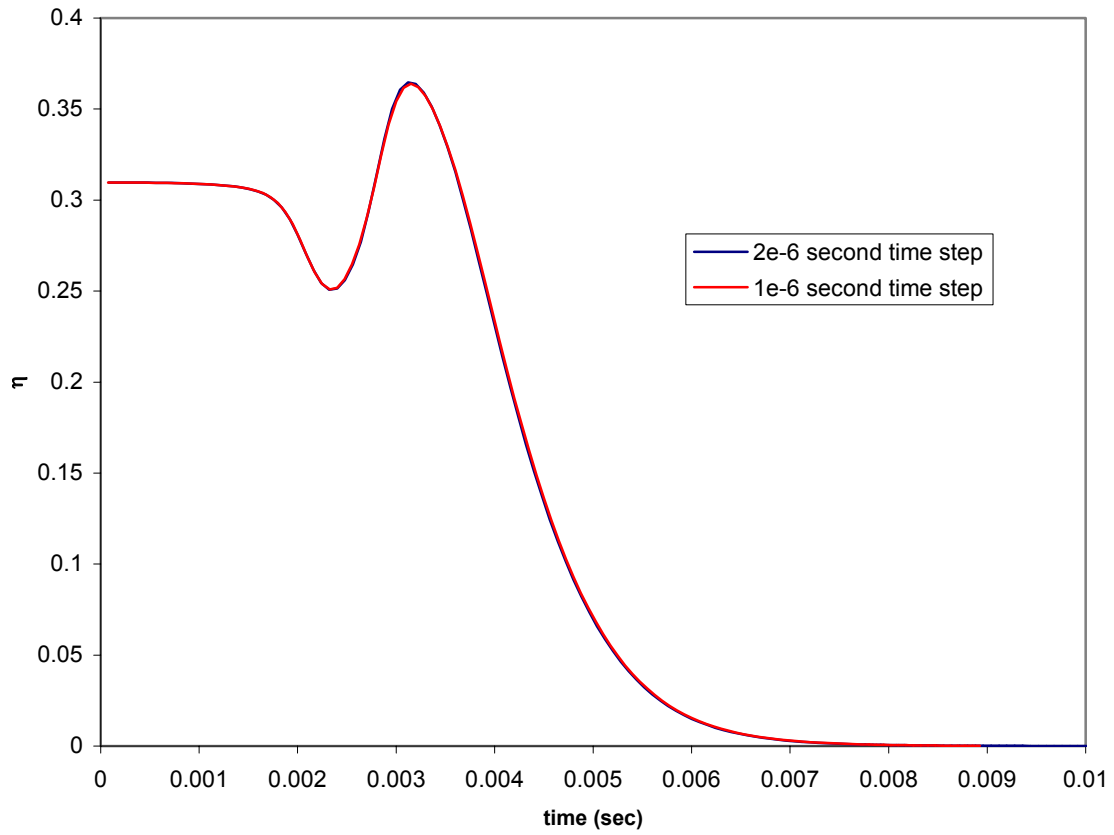


**Fig. 8.8 Adiabatic effectiveness histories at Point E obtained using two different time steps**

## 9. Computational Results

In order to gain an understanding of the physics behind pulsed film cooling flows, computational simulations were performed using the techniques described in Chapter 8.

### 9.1 Steady Jet Results

Adiabatic effectiveness contours for the steady  $M = 0.50$  jet are shown in Fig. 9.1. The axis of the hole is such that the coolant has velocity components in the positive  $z$  direction and the negative  $y$  direction. The freestream flow causes the coolant to turn in the positive  $x$  direction immediately upon exiting the coolant hole. The adiabatic effectiveness contours are similar to the experimental results shown in Fig. 5.10 on page 90; however, the contours are wider (in the spanwise direction) in the contour plot of the experimental data than predicted with the computational simulation. The narrower contours of the computational data are compensated somewhat by the fact that they extend farther downstream than in the experimental data set. It will be shown in Fig. 9.5 that the spanwise averaged adiabatic effectiveness is in excellent agreement with the experimental data of Chapter 5. Interestingly, a similar observation can be made through a comparison of the computationally acquired adiabatic effectiveness data (utilizing the  $k-\omega$  turbulence model) of Lin and Shih (2001) to the analogous experimental data of Cruse et al. (1997). That comparison also shows the computational adiabatic effectiveness contours are narrower, but extend farther downstream than with the experimental data set. Again, the spanwise averaged adiabatic effectiveness of the computational simulation was in excellent agreement with the experimental data. Although it is often instinctive to treat experimental data as the benchmark to which CFD data must conform, these differences may be attributed to the unaccounted and unavoidable spanwise thermal conduction in the physical experimental models that is absent in the perfectly adiabatic virtual computational model. In Fig. 9.1 we can see that there are high temperature gradients in the spanwise ( $y$ ) direction while there are relatively gentle gradients in the streamwise ( $x$ ) direction. When the experiment is run on a physical model with low, but nonzero, thermal conductivity, there is unavoidable smearing of the contours in the direction of the thermal gradients, or the spanwise direction. That is, the peak adiabatic

effectiveness at a given  $x$  location is reduced, but the adiabatic effectiveness adjacent to the peak in either  $y$  direction is elevated. Thanks to the gentle thermal gradients in the  $x$  direction, the result is that the spanwise averaged adiabatic effectiveness of the experiment agrees with the computational simulation. Although every effort was made in the present study to account for the effects of conduction in the experimental data, the conduction correction was one-dimensional; higher order conduction corrections were not feasible.

Heat transfer coefficient ratio,  $h_f/h_0$ , and net heat flux reduction,  $\Delta q_r$ , are shown for the  $M = 0.50$  case in Figs. 9.2 and 9.3, respectively. For the purpose of determining the heat transfer coefficient ratio,  $h_0$  was determined using the same leading edge cooling hole geometry, but with  $M = 0$  just as in the experimental data of Chapter 5. A classic fork-tine like pattern in the heat transfer coefficient ratio is evident downstream of the coolant hole. (The fork tines refer to the two regions of elevated heat transfer coefficient extending downstream of the hole.) Although these fork tines were not evident in the analogous experimental data shown in Fig. 5.25, the magnitudes of the peak  $h_f/h_0$  at each  $x/d$  location are in decent agreement. The absence of fork tines in the experimental data *may* be attributable to spanwise thermal conduction (which is expected to be greater than that without the heat flux plate since the heat flux plate itself has much higher thermal conductivity than the foam substrate), but it is also possibly a result of limitations on the ability of CFD to accurately predict  $h$  distributions. The predictions of peak  $h_f/h_0$  are generally within 5%, which is decent for CFD. In Fig. 9.1, the region of elevated adiabatic effectiveness is biased toward the leeward (lower region in the figure) end of the coolant hole; thus, in Fig. 9.2 the top tine of elevated heat transfer coefficient, where the adiabatic effectiveness is not as high, causes a region of negative net heat flux reduction, i.e. a net heat flux increase, as seen in Fig. 9.3. In Fig. 9.2 a small region immediately upstream of the hole as the boundary layer approaches the jet and extending on the leeward side of the hole experiences a decrease in heat transfer coefficient due to film cooling.

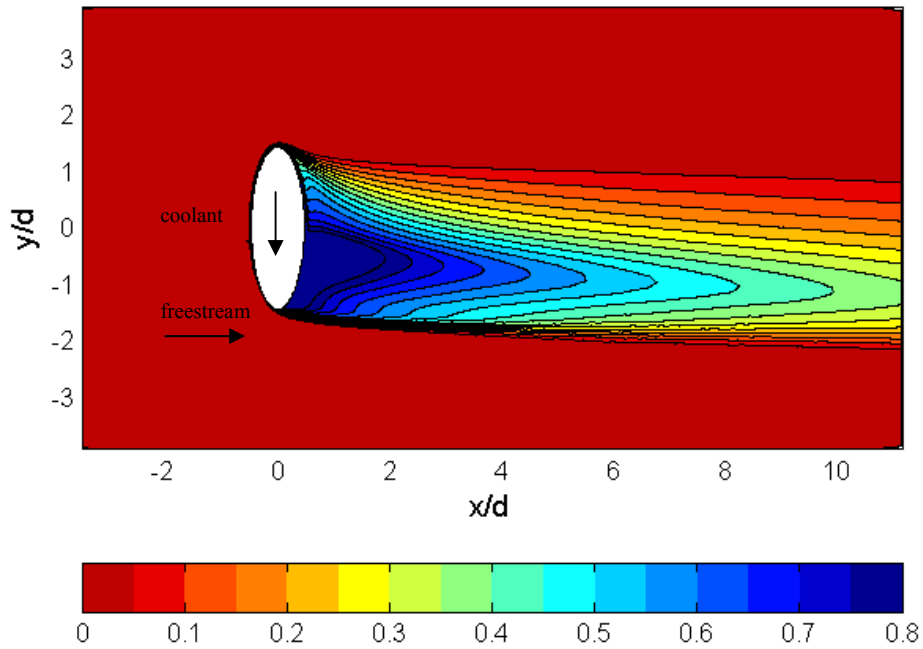


Fig. 9.1 Steady  $M = 0.50$  adiabatic effectiveness,  $\eta$  (arrows indicate direction of coolant and freestream)

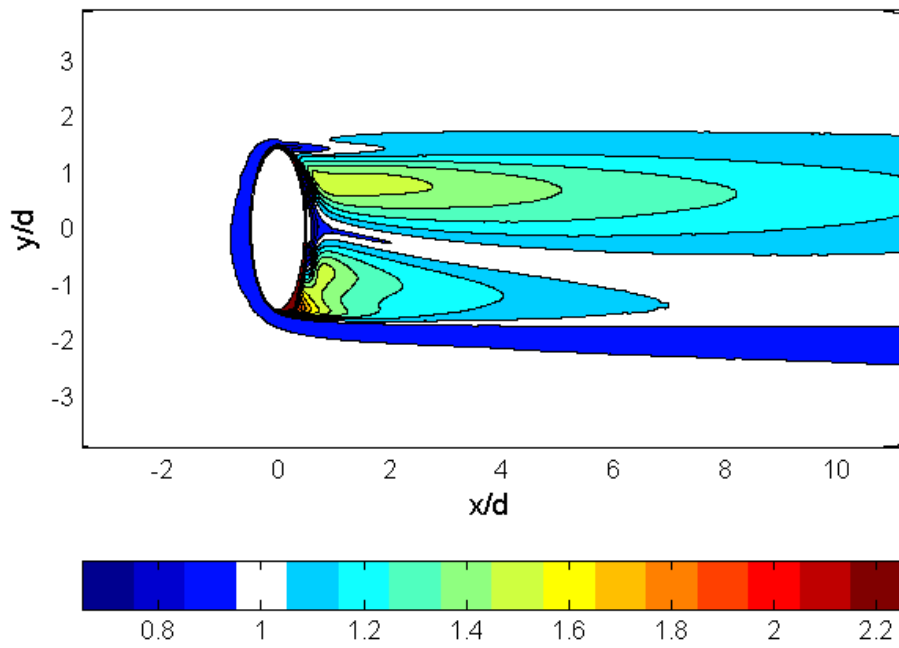


Fig. 9.2 Steady  $M = 0.50$  heat transfer coefficient ratio,  $h_f/h_0$

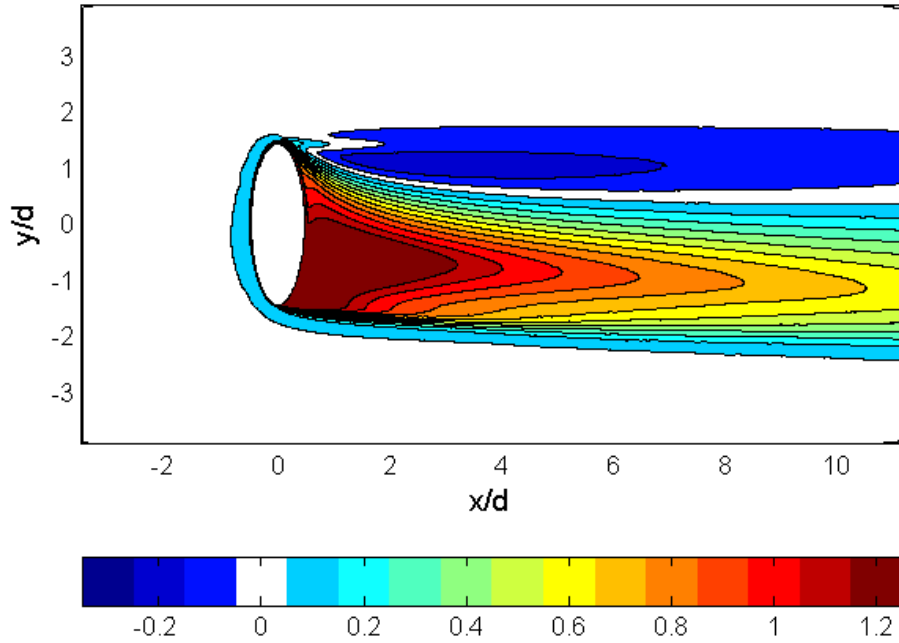


Fig. 9.3 Steady  $M = 0.50$  net heat flux reduction,  $\Delta q_r$

Adiabatic effectiveness contours for the steady  $M = 0.25$  jet are shown in Fig. 9.4. Since the  $M = 0.25$  jet has a lower blowing rate relative to the freestream, the coolant turns in the direction of the freestream faster than the higher  $M$  jet and with less lift-off.

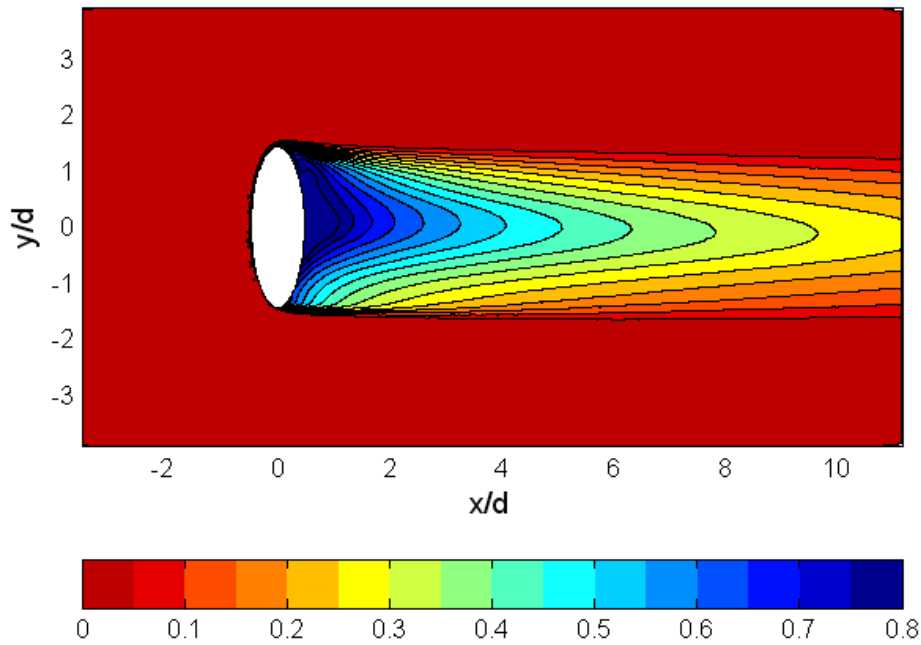
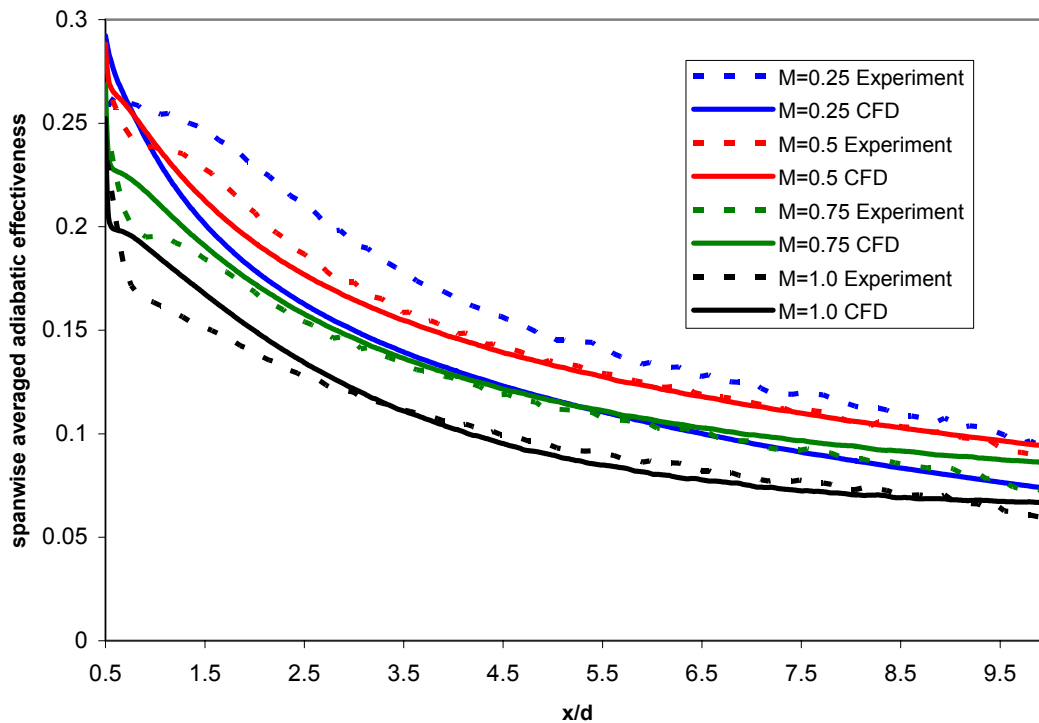


Fig. 9.4 Steady  $M = 0.25$  adiabatic effectiveness,  $\eta$

Spanwise averaged adiabatic effectiveness computational data are compared to experimentally acquired data in Fig. 9.5. The spanwise averaging extent was  $7.86 d$ , typical of hole spacing on a turbine blade leading edge and the same as used in the experimental data reduction. The experimental data compared very well for  $M \geq 0.5$ , particularly for  $x/d > 2$ . The worst comparison was between the  $M = 0.25$  data sets. The computational  $M = 0.25$  case underpredicted spanwise averaged  $\eta$  by  $\Delta\eta = 0.05$  at  $x/d = 2$ , decreasing to  $\Delta\eta = 0.03$  at  $x/d = 9$ . The higher  $M$  cases performed very well by comparison. The reason for the discrepancy with the  $M = 0.25$  data is apparent through a comparison of Fig. 9.4 and Fig. 5.15 on page 94; the latter figure shows the experimentally acquired adiabatic effectiveness contours. The experimental data (acquired in both the wind tunnel and the water channel) show that the coolant actually divides into multiple fingers extending downstream of the coolant hole. Although the physics of this phenomenon remain shrouded by some mystery, the phenomenon appears to arise from a flow instability that occurs only with creeping flow out of the coolant hole.



**Fig. 9.5 Comparison of computational and experimental steady spanwise averaged adiabatic effectiveness**

It was hypothesized that the inability of the computational model to simulate the fingers of coolant that occur at  $M = 0.25$  is related to shortfalls of the  $k-\epsilon$  turbulence model. In order to test this hypothesis, a computational simulation utilizing the large eddy simulation (LES) turbulence model was performed on the same grid used for the  $k-\epsilon$  simulations. Although the blowing ratio,  $M$ , was held constant, the LES simulation is an unsteady simulation that directly simulates the largest turbulent eddies while modeling only the smaller ones. The spatial  $\eta$  contours acquired through the LES simulation are shown in Fig. 9.6. The LES simulation correctly predicted the existence of coolant fingers at this blowing ratio, but overpredicted the magnitude of  $\eta$ . In fact, the spanwise averaged  $\eta$  from the LES simulation was high by  $\Delta\eta > 0.05$ . An LES simulation was also performed for  $M = 0.50$ , for which the coolant fingers were correctly not predicted. Again, the spanwise average magnitude of  $\eta$  was overpredicted by the LES simulation, this time by  $\Delta\eta \approx 0.015$ . Although the LES model better predicted whether or not coolant fingers exist, the generally poor predictions of the adiabatic effectiveness

magnitudes lends credence to the  $k-\varepsilon$  model for these CFD simulations in general. The inability of the present techniques to accurately model the steady  $M = 0.25$  case forces us to dispense with this data for the remainder of this document.

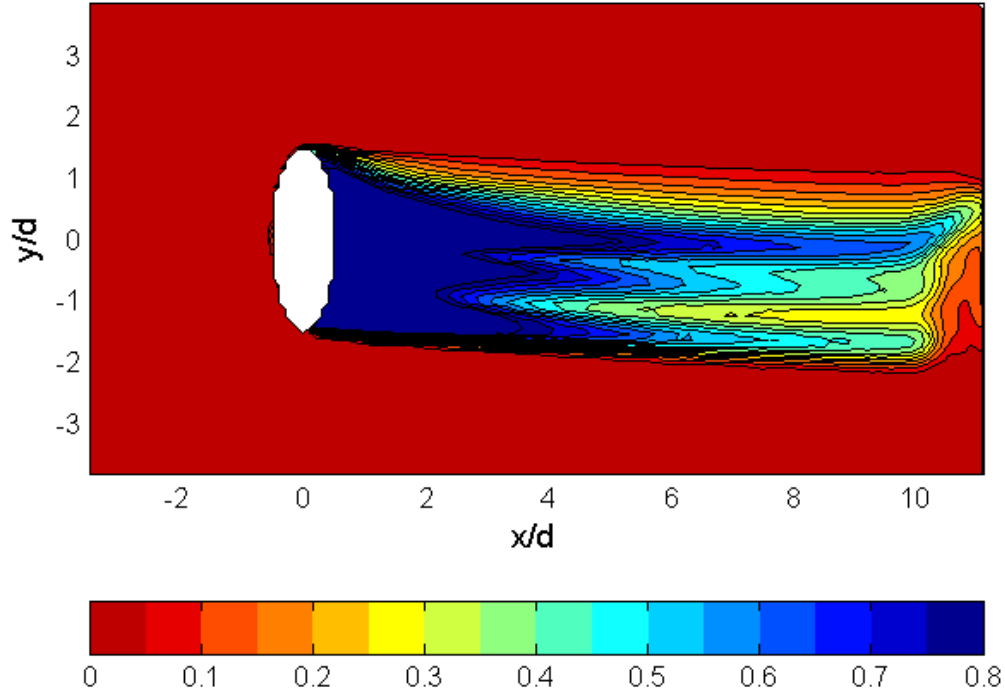


Fig. 9.6 Steady  $M = 0.25$  adiabatic effectiveness,  $\eta$ , acquired through LES simulation

## 9.2 Pulsed Jet Results

This section presents the results of the computational simulations involving pulsed jets.

### 9.2.1. Low Frequency Pulsed Jet Results

Low frequency simulations were performed at  $F = 0.151$ , nearly equal to the  $F = 0.148$  condition used with the wind tunnel and water channel experiments described in Sections 5.2 and 7.2, respectively. For all cases, the duty cycle was  $DC = 50\%$  with square wave pulsations. In actual engine conditions, this nondimensional frequency would correspond to a dimensional frequency in the vicinity of 3.5 kHz. The pulsed cases differ from each other only in the minimum and maximum blowing ratios, each with  $\bar{M} = 0.5$  or  $\bar{M} = 0.25$ .

Figure 9.7 shows adiabatic effectiveness histories for the points shown in Fig. 8.7 on page 181 for the case in which the blowing is pulsed between  $M = 1$  and  $M = 0$

( $\overline{M} = 0.5$ ). The transient events take place over only approximately one unit of nondimensional time (less than a fifth of the time that the coolant is turned “off”). Indeed, transient events lasting approximately one unit of nondimensional time would be expected since it takes one unit of nondimensional time for the freestream to travel one leading edge diameter. Likewise, it takes a discernable amount of time for the adiabatic effectiveness to respond to the step change in blowing ratio, with longer amounts of time required farther downstream from the coolant hole. Perhaps the most striking result is the 27% overshoot in the adiabatic effectiveness at Point F over the steady state value for a short period of time after turning on the coolant (at  $T \approx 1$ ). Similar overshoots occur at other points as well.

From Fig. 9.7, it is evident that the frequency is low enough that the film cooling jet is “on” long enough for steady-state to be attained, i.e., the state of the flow in the region of the entire cylindrical leading edge at  $T = 3.31$  is identical to that which it would be if steady film cooling were used. This aspect of the flow caused periodic steady state to be attained for the very first cycle, provided the initial condition was the steady jet flow field, as indicated earlier.

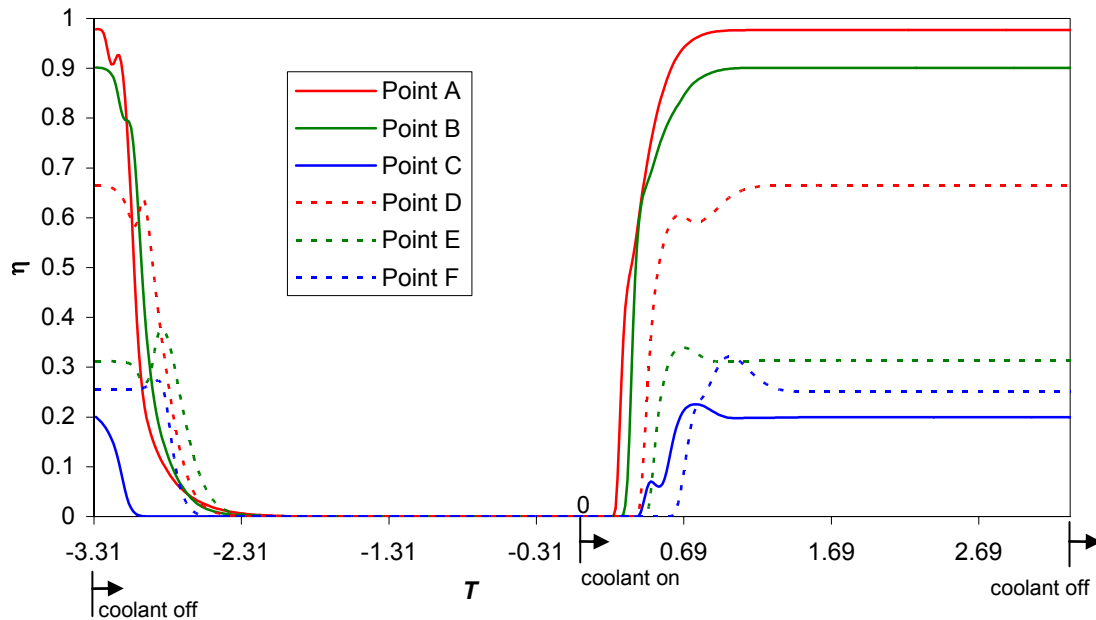
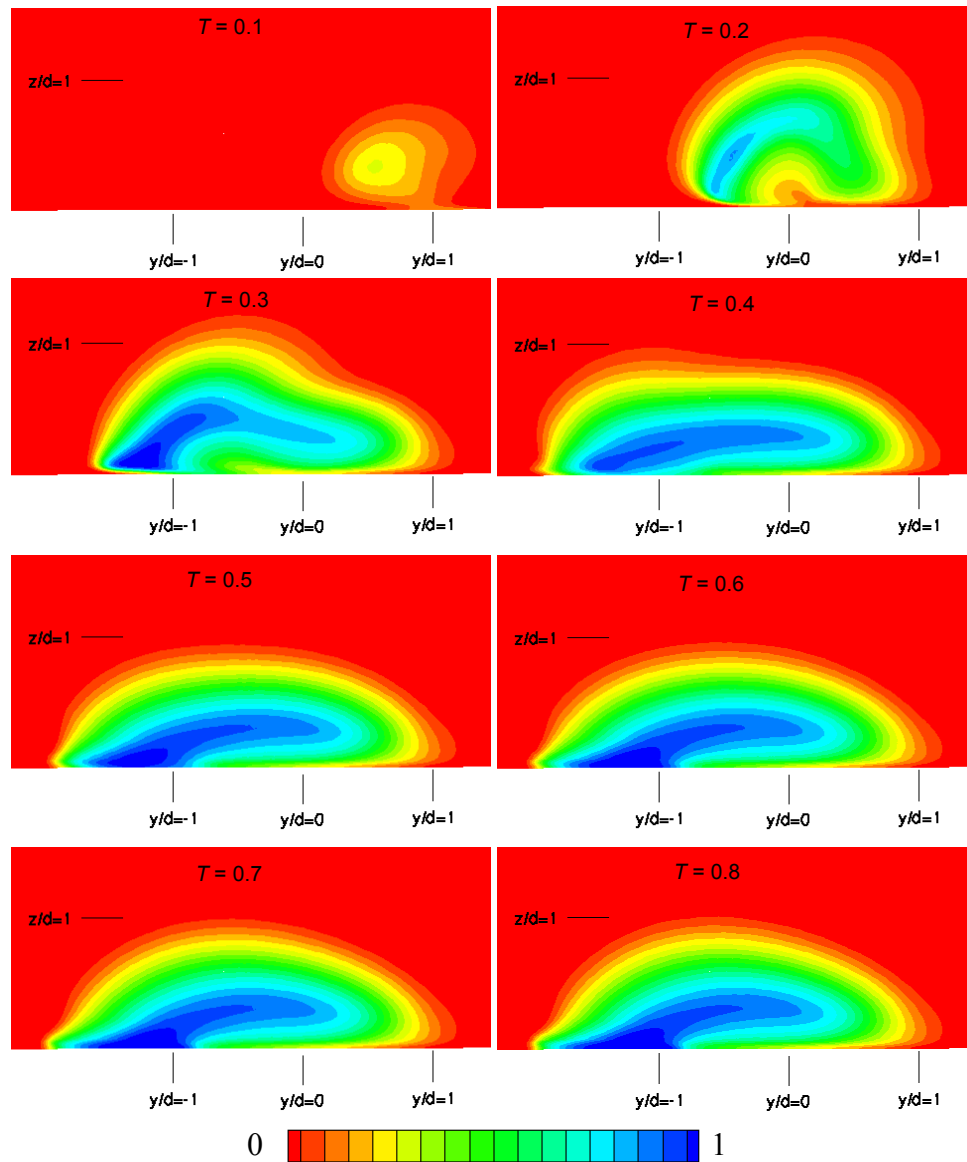


Fig. 9.7 Temporally resolved adiabatic effectiveness for several points on leading edge

In order to investigate jet lift-off during the steady-state transient start-up event, Fig. 9.8 shows nondimensional temperature contours for fluid in a plane normal to the surface at  $x/d = 1$  for the transient startup event for the case of coolant pulsed between  $M = 1$  and  $M = 0$ . The time period  $0.1 \leq T \leq 0.8$  was selected based on the time period over which the transient event occurs in the near hole region (Points A, B, and C) from Fig. 9.7. The blowing ratio switches from  $M = 0$  to  $M = 1$  at  $T = 0$ . By  $T = 0.8$ , the temperature profile at  $x/d = 1$  has nearly reached steady state and there is little change during the interval  $0.8 \leq T \leq 3.3$ . At  $T = 0.2$  the coolant penetrates the freestream beyond  $1 d$  from the surface at  $x/d = 1$  before it settles. This initial over-penetration of the coolant jet prior to settling at a quasi-steady state condition was also observed in the experimental flow visualization results in Section 7.2. Note in Fig. 9.8,  $T = 0.8$ , as the contours at  $x/d = 1$  have reached steady-state, the coolest region of fluid at  $y/d = 0$  is lifted off of the surface by a third of a hole diameter. This jet lift-off is indicative of inefficient use of coolant at  $M = 1$ .



**Fig. 9.8 Nondimensional temperature distribution,  $\theta$ , for fluid in plane intersecting surface at  $x/d = 1$  for transient jet startup for the case of pulsed coolant between  $M = 1$  and  $M = 0$ ,  $\overline{M} = 0.50$**

The corresponding adiabatic effectiveness contours are shown in Fig. 9.9. Because the surface is modeled as adiabatic, the surface temperature of the CFD model directly follows the adiabatic wall temperature, a fluid property, rather than some damped temperature that would occur on a conducting physical model. In Fig. 9.9, the region of nonzero  $\eta$  at  $T = 0.1$  is due to seepage of coolant out of the hole (also see  $T = 0.1$  in Fig. 9.8) as a result of continuous mixing between the fluid in the coolant hole and the external flow during the period that the coolant is off. After the coolant jet is turned on

( $T = 0.1$  through  $T = 0.5$ ), the momentum of the jet increases and the region of elevated  $\eta$  moves to the lower end of the coolant hole. As this occurs, the region of elevated  $\eta$  from the coolant seepage during the off-period shrinks until it disappears at  $T = 0.4$ . The adiabatic effectiveness in that region is actually higher while the coolant jet is off than while the coolant jet is on. For comparison, recall that the adiabatic effectiveness contour plot with steady film cooling and matched average blowing ratio,  $M = 0.5$  is shown in Fig. 9.1. The steady adiabatic effectiveness contours are generally greater than with pulsed film cooling at any time during the pulsed film cooling cycle, although certain localized points may benefit from pulsing, particular those downstream of the lower part of the coolant hole, where the higher momentum  $M = 1$  jet gives greater  $\eta$  than at  $M = 0.5$ .

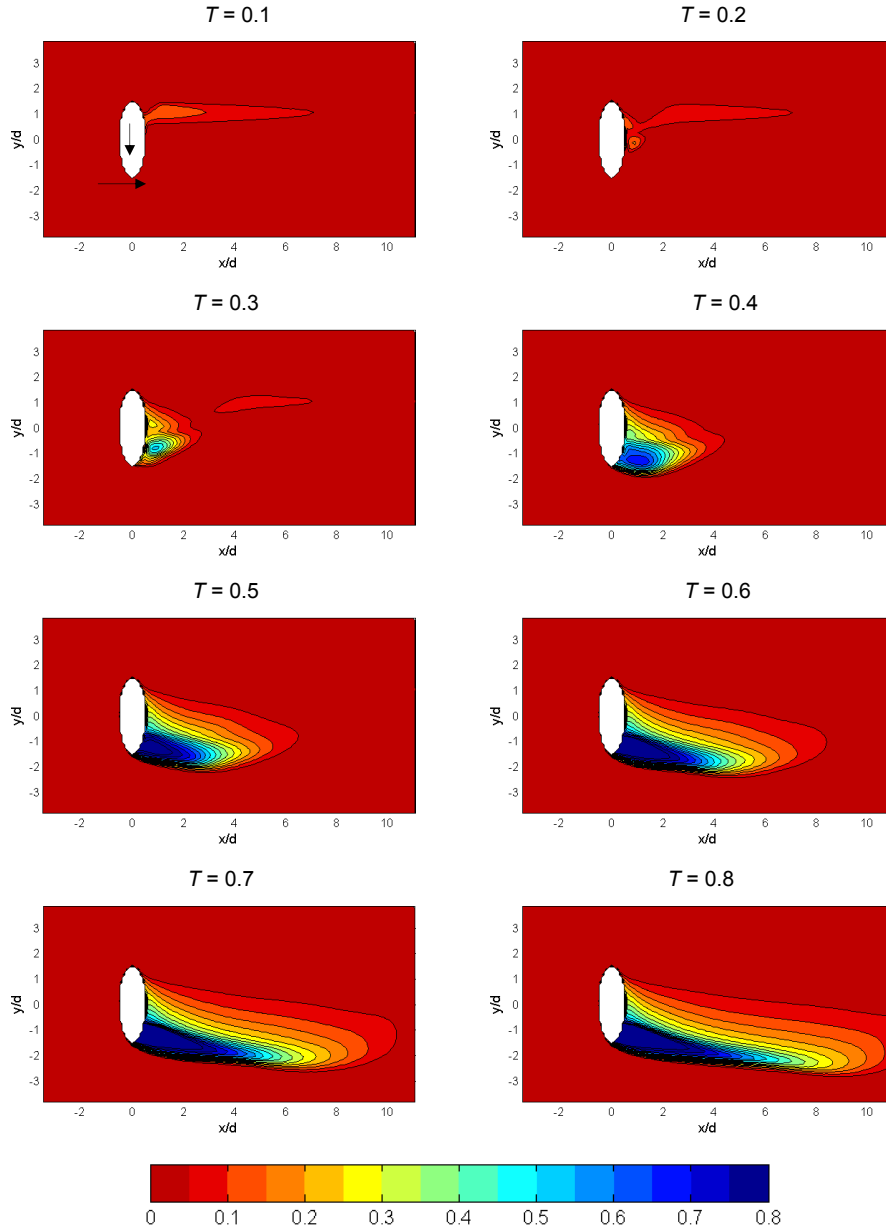


**Fig. 9.9** Adiabatic effectiveness contours for transient jet startup for the case of pulsed coolant between  $M = 1$  and  $M = 0$ ,  $\bar{M} = 0.50$  (arrows indicate direction of coolant and freestream)

Heat transfer coefficient ratio,  $h_f / h_0$ , contours for the transient startup event for the pulsed case between  $M = 1$  and  $M = 0$ , are shown in Fig. 9.10. The heat transfer coefficient generally increases during the course of the transient event. Immediately evident by comparing  $h_f / h_0$  in Fig. 9.10 to  $\eta$  in Fig. 9.9 at  $T = 0.8$ , which is nearing steady state condition, is that of the two times of elevated  $h_f / h_0$ , the more severe one is

protected by the highest levels of adiabatic effectiveness; however, the region of the top tine has much less protection from the film coolant. Recall that the  $h_f/h_0$  contour plot with steady film cooling at  $M = 0.5$  is shown in Fig. 9.2.

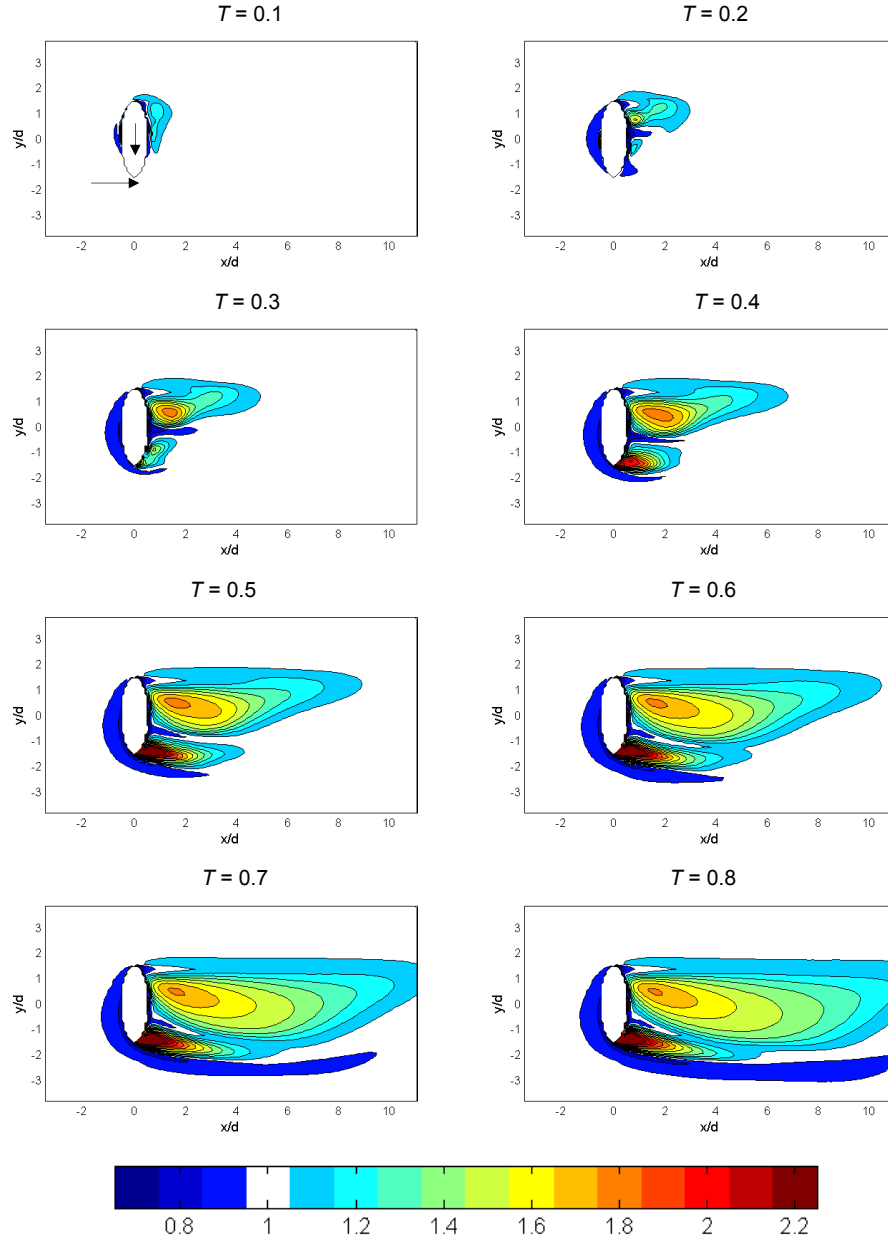


**Fig. 9.10**  $h_f/h_0$  contours for transient jet startup for the case of pulsed coolant between  $M = 1$  and  $M = 0$ ,  $\overline{M} = 0.50$  (arrows indicate direction of coolant and freestream)

With temporally resolved heat transfer coefficient distributions and adiabatic effectiveness data, we can compute the average net heat flux reduction, shown in Fig.

9.11. As one might expect from Figs. 9.9 and 9.10, there is a large region of negative net heat flux reduction (thus it is a region of net heat flux increase) where the heat transfer coefficient is elevated by the jet without a commensurate increase in adiabatic effectiveness. In this region the net heat flux is increased 20%. However, downstream of the lower part of the coolant hole, a favorable net heat flux reduction exists, with the 60% contour extending to  $x/d = 5$ . The coolant seepage from the top of the coolant hole during the time that the coolant jet is off results in an elevated  $\overline{\Delta q_r}$  downstream of the top of the coolant hole.

The role of the cross coupling term alone in influencing the net heat flux reduction is shown in Fig. 9.12. The region in which this term accounts for an effect greater than 5% is narrow, but extends to  $x/d = 4$ . Immediately adjacent to the coolant hole, the term accounts for a 50% net heat flux reduction. It is also important to note that this term has a beneficial effect wherever  $h_f$  and  $\eta$  fluctuate in phase, as is generally the case. Although not shown, the erroneous average net heat flux reduction that would have been obtained by improperly substituting  $\overline{h_f}$  and  $\overline{\eta}$  into Eq. (3.11) would be given by the difference of the values reported in Figs. 9.11 and 9.12.

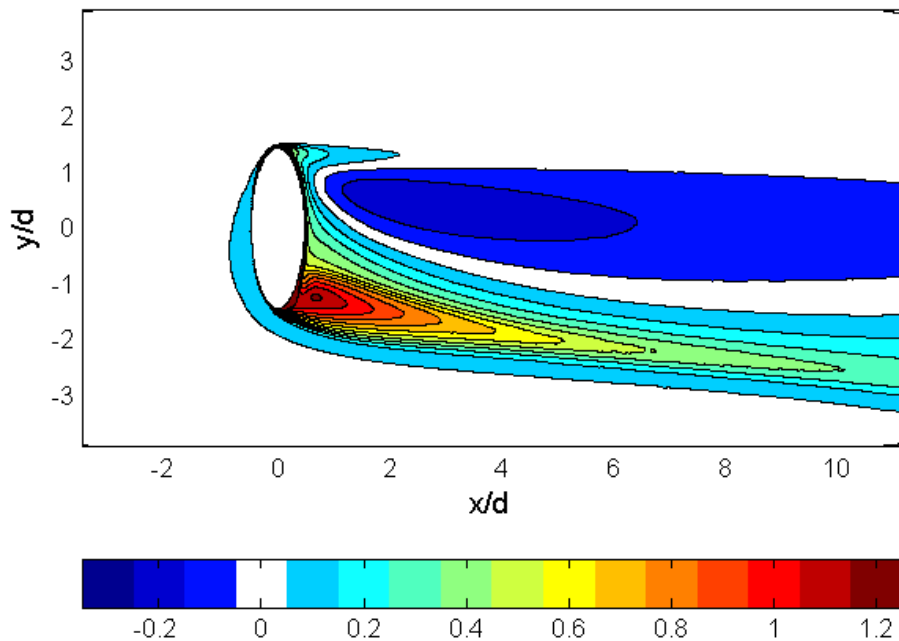
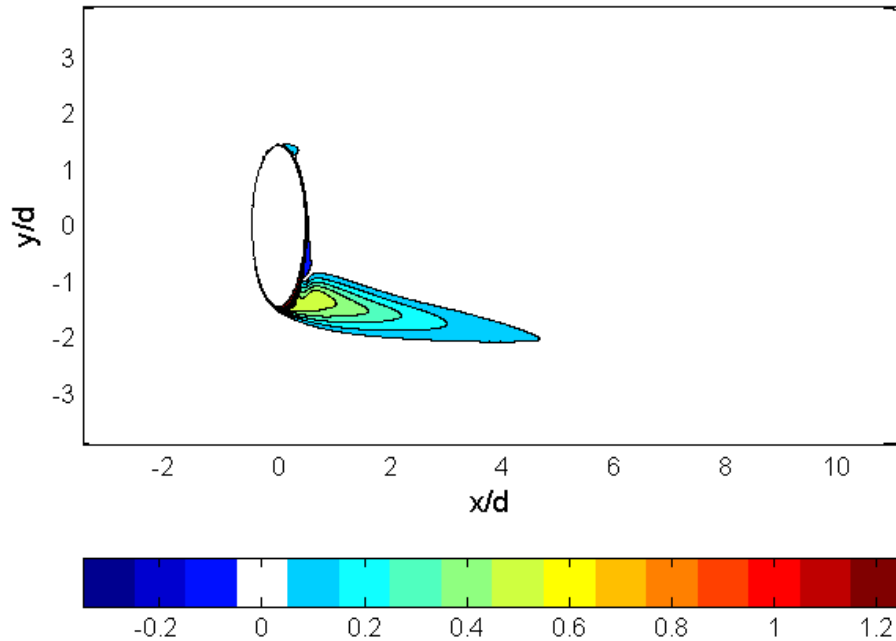


Fig. 9.11 Average net heat flux reduction,  $\overline{\Delta q_r}$ , for the case of pulsed coolant between  $M = 1$  and  $M = 0$ ,  $\overline{M} = 0.50$ ,  $\overline{M} = 0.50$



**Fig. 9.12 Influence of cross coupling term alone,  $\overline{h_f' \eta'} / (h_0 \phi)$ , on average net heat flux reduction for the case of pulsed coolant between  $M = 1$  and  $M = 0$ ,  $\overline{M} = 0.50$**

Net heat flux reduction results for a pulsed case with  $\overline{M} = 0.25$  is shown in Fig. 9.13. This case, in which coolant is pulsed between  $M = 0.5$  and  $M = 0$  has net heat flux reduction inferior to the steady jet at the same average blowing ratio. Although we have no reliable computational data for the steady jet at  $M = 0.25$ , we know from the experimental data that the steady computational data at  $M = 0.25$  underpredicts net heat flux reduction. Since the pulsed jet at  $\overline{M} = 0.25$  performs poorer than the underpredicted steady jet, we know that pulsing in this case is detrimental relative to the steady jet. As with the case of coolant pulsed between  $M = 1$  and  $M = 0$ , a small region of elevated  $\overline{\Delta q_r}$  is evident downstream of the top of the coolant hole due to coolant seepage during the  $M = 0$  period.

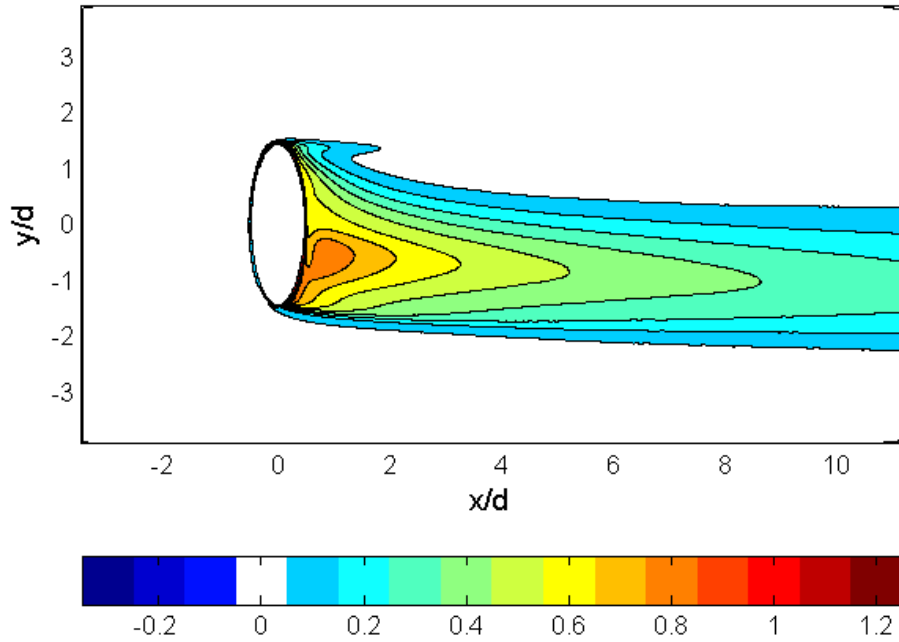


Fig. 9.13 Average net heat flux reduction,  $\overline{\Delta q_r}$ , for the case of pulsed coolant between  $M = 0.5$  and  $M = 0$ ,  $\overline{M} = 0.25$

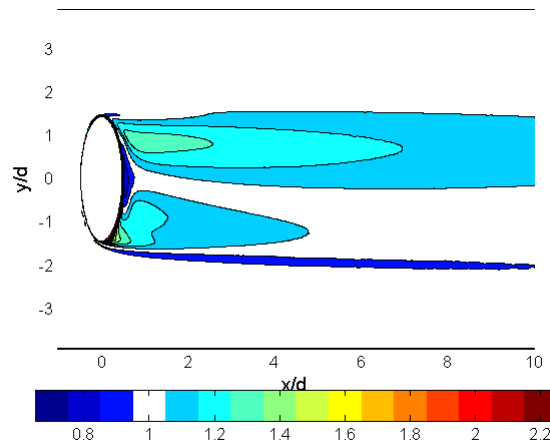


Fig. 9.14 Heat transfer coefficient ratio,  $\overline{h_f / h_0}$ , pulsed coolant between  $M = 0.5$  and  $M = 0$ ,  $F = 0.151$ ,  $\overline{M} = 0.25$

In order to more generally characterize the performance of the various cooling schemes, adiabatic effectiveness results were spanwise averaged and plotted in Fig. 9.15. The region of spanwise averaging was taken to be  $-3.93 < y/d < 3.93$ , typical of the spacing between coolant holes on an actual blade.

The net spanwise heat flux reduction (calculated via Eq. (4.49)) is shown in Fig. 9.16. Because performance of steady film cooling with respect to blowing ratio in terms of the net heat flux reduction is peaked in nature with an optimum blowing ratio, alternating between two blowing ratios at a low frequency such that steady state arises during the cycle gives poorer performance than with steady coolant at the average blowing ratio.

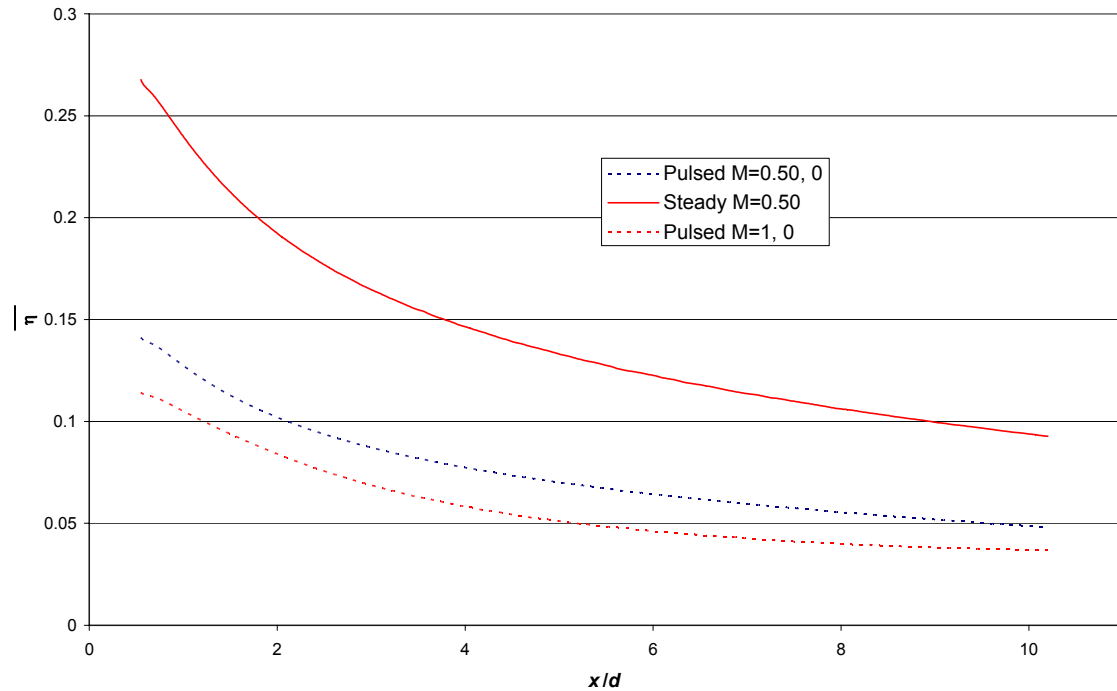


Fig. 9.15 Spanwise averaged  $\bar{\eta}$ ;  $M = A, B$  indicates pulsing between  $M = A$  and  $M = B$

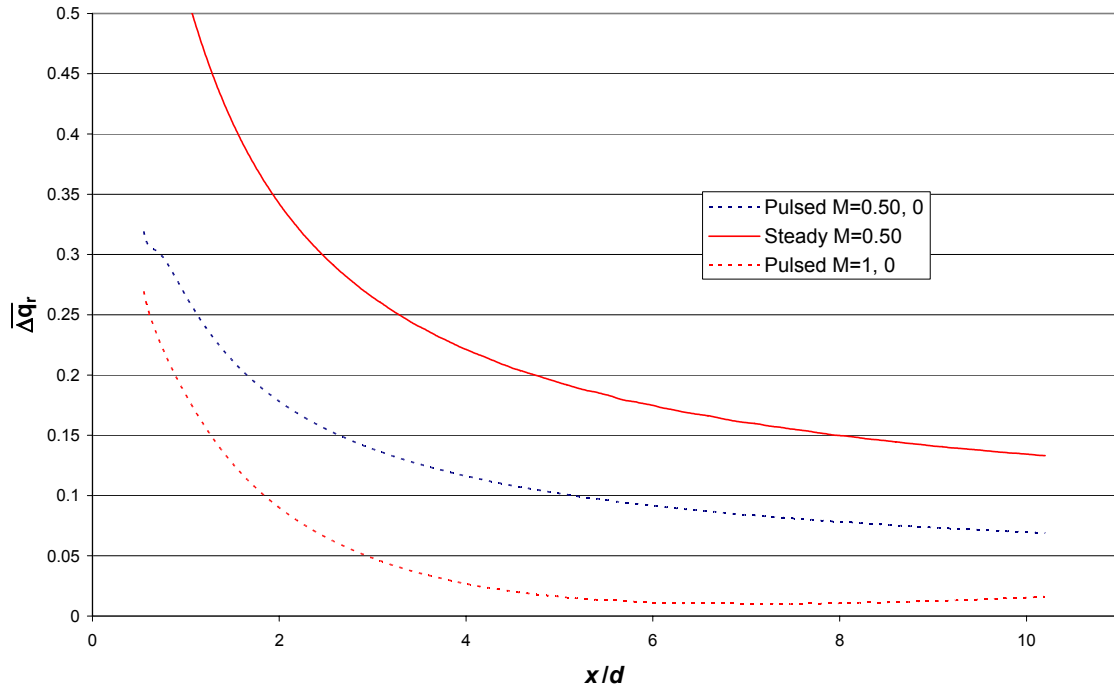


Fig. 9.16 Net spanwise heat flux reduction  $\overline{\Delta q_{r,span}}$  ;  $M = A, B$  indicates pulsing between  $M = A$  and  $M = B$

### 9.2.2. Low Frequency Performance Prediction

As discussed in Section 3.6, with low frequency unsteadiness ( $F \ll 1$ ), the flow field changes slowly and is quasi-steady. If the blowing rate is a discontinuous function (such as a square wave), the dwell time in between step changes is much longer than the time during which the rapid transients occur. In either case, the flow transients are unimportant with  $F \ll 1$  and one must only consider the fractional time spent at each quasi-steady blowing rate.

If  $Z$  is a performance parameter that is some measure of a steady film cooling scheme and  $Z$  is known as a continuous function of steady mass flux ratio,  $M$ , the average  $Z$  with unsteady mass flux ratio,  $M(t)$ , may be calculated through Eq. (3.73) or Eq. (3.77), repeated here:

$$\overline{Z} \approx \frac{\omega}{2\pi} \int_0^{2\pi/\omega} Z(M(t)) dt \quad (3.73)$$

$$\bar{Z} \approx \sum_{i=1}^n \frac{\Delta t_i}{2\pi/\omega} \delta(M - M_i) Z(M_i) \quad (3.77)$$

The quasi-steady nature of film cooling flow at low pulsing frequencies thereby removes some of the more complex unsteady flow physics from the problem of predicting the performance of a pulsed scheme. No such technique exists for high frequency pulsed cases in which the transient effects account for a significant amount of the flow time. A purpose of the current research is to determine how several pulsed film cooling schemes perform at higher frequencies such that the transient startup and shutdown of the film cooling jets account for the majority, if not all, of the duration of a cycle.

In Fig. 9.17 the spanwise averaged  $\bar{\eta}$  for the case of the jet pulsed between  $M = 1$  and  $M = 0$  at  $F = 0.151$  is compared to the performance predicted with Eq. (3.77) using only the steady state  $M = 1$  data (along with the trivial steady state  $M = 0$  data.) Evidently, the frequency is indeed low enough at  $F = 0.151$  that the simple low frequency prediction of Eq. (3.77) can be utilized with reasonable accuracy. Thus, there was impetus to determine the behavior of a film cooling jet that is left neither “on” nor “off” long enough for the quasi-steady “on” or “off” regimes to be attained.

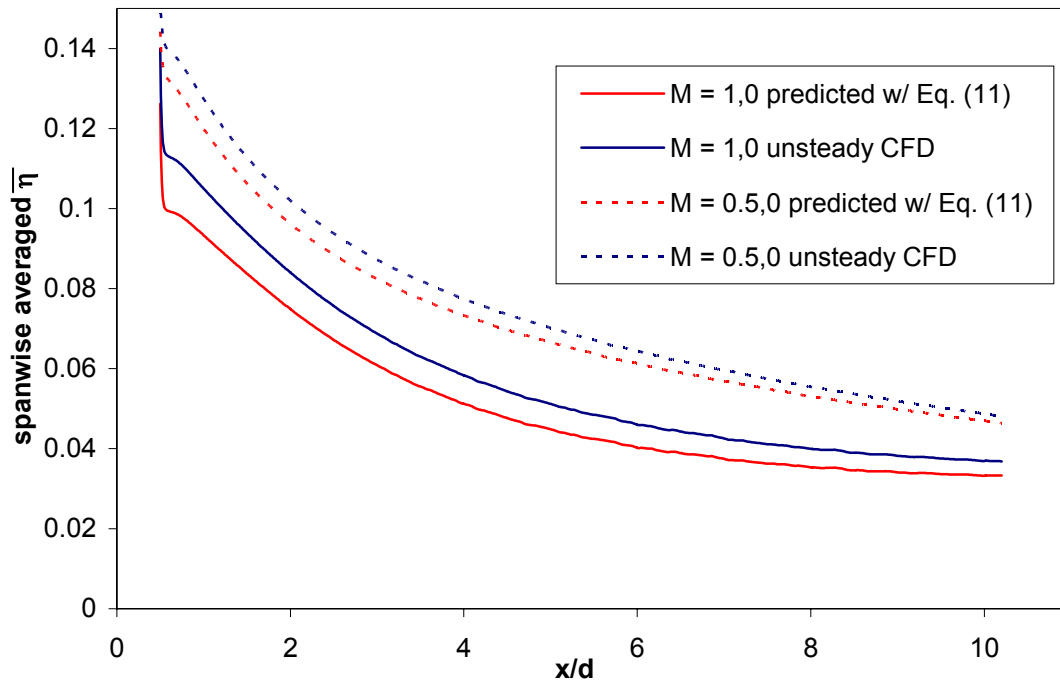


Fig. 9.17 Spanwise averaged  $\bar{\eta}$  for the case of a jet pulsed between  $M = A$  and  $M = B$  (indicated by  $M = A, B$ ) at  $F = 0.151$  compared to the prediction from Eq. (3.77).

Since the performance of steady film cooling dropped dramatically for blowing ratios greater than  $M = 0.5$ , the utilization of any amount of coolant at those higher, less efficient blowing rates for any amount of time caused a decrease in the performance of the pulsed film cooling schemes relative to steady film cooling at the two tested average blowing ratios of  $M = 0.5$  and  $M = 0.25$ .

A plot of the area-averaged net heat flux reduction as a function of steady blowing ratio for the leading edge geometry as obtained through the experimental methodology of Chapter 4 is shown in Fig. 5.46 on page 107. The concave-down nature of the performance curve in the vicinity of the peak performance ( $0.1 < M < 0.75$ ) is responsible for the degradation due to pulsing for the cases presented in Section 9.2.1. Any hope for the net heat flux reduction performance of a pulsed film cooling scheme to be superior to the performance of a steady jet with the same average coolant consumption requires the performance curve relative to a steady blowing ratio to have an interval on which the curve is concave-up. Such a region exists for  $M > 1.0$  as evident in Fig. 5.46. Pulsed

film cooling in that region, although superior to steady film cooling at matched  $\overline{M}$  would still be inferior to steady film cooling at say,  $M = 0.5$  (which would save a great deal of coolant if all other parameters are held constant), but if other design constraints (perhaps due to internal cooling requirements and the impracticality of machining more external coolant holes) prevent one from lowering the blowing ratio to  $M = 0.5$ , then pulsing the coolant may be desirable from a thermal management perspective.

### 9.2.3. The Frequency Dependence of Pulsed Jets

Ekkad et al. (2006) found that their measurements of the average performance of a film cooling jet was independent of the pulsing frequency they used. The frequency range that was tested by Ekkad et al. was  $0.035 < F < 0.14$ . Having now illuminated the mathematics of the average performance of a low frequency pulsed film cooling jet and the independence of said performance on frequency (see Eq. (3.77)), we are prepared to return our attention to the issue of frequency dependence. We now benefit from the knowledge that in order for there to be any possibility of frequency dependence,  $F$  must be large.

At a duty cycle of  $DC = 50\%$  and pulsing between  $M = 1$  and  $M = 0$ , additional simulations were performed at nondimensional frequencies of  $F = 0.604, 0.755, 3.02,$  and  $6.04$ . In Fig. 9.8 we observed jet lift-off immediately following the instantaneous start-up of the film cooling jet. In order to determine if this could be alleviated through a more gradual startup, a sawtooth waveform was run in addition to the square wave at  $F = 0.755$ . The waveforms are shown in Fig. 9.18.

Spanwise net heat flux reduction data for this variety of pulsing conditions are presented in Fig. 9.19. It is evident in Fig. 9.19 that all pulsing schemes performed poorer than the steady  $M = 0.5$  jet. As expected, the sawtooth wave outperformed the square waves, in part due to reduced liftoff at the jet startup event, but also because the jet spends more time at the more optimal blowing ratios in the vicinity of  $M = 0.50$ , rather than the far from optimal steady blowing ratios of  $M = 0$  and  $1$  (the steady  $M = 1$  results are also shown in Fig. 9.19;  $\Delta q_r$  for  $M = 0$  is, by definition, zero.) A remarkable characteristic in Fig. 9.19 is the relative independence of the net heat flux reduction on

the pulsing frequency up to  $F = 3.02$ . However, from  $F = 0.755$  to  $F = 3.02$ , the net heat flux reduction drops by up to approximately 0.05 in the vicinity near the hole, but the differences become insignificant at  $x/d = 4$ . However, when the pulsing frequency was increased to  $F = 6.04$ , the net heat flux reduction improved at nearly all spanwise locations by up to approximately 0.05 relative to the  $F \leq 0.755$  cases.

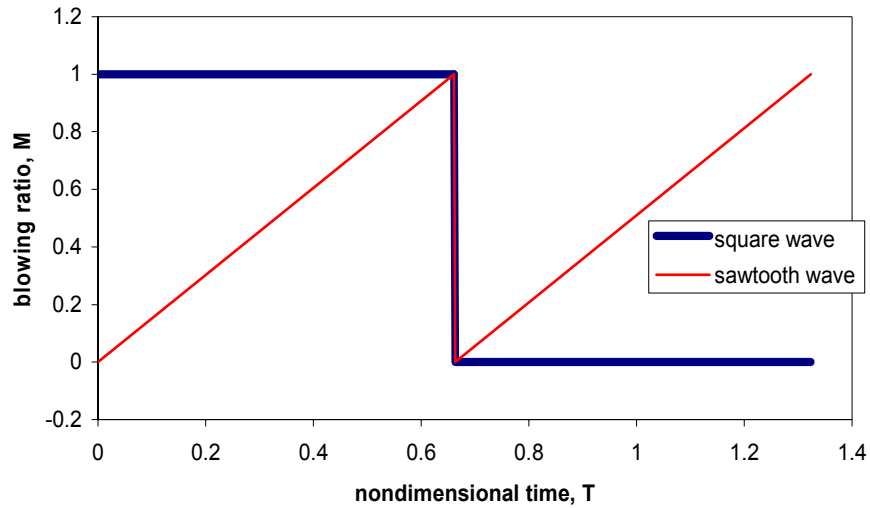


Fig. 9.18 Square and sawtooth waves used for pulsing between  $M = 1$  and  $M = 0$  at  $F = 0.755$ . Both have average blowing ratio,  $\bar{M} = 0.5$

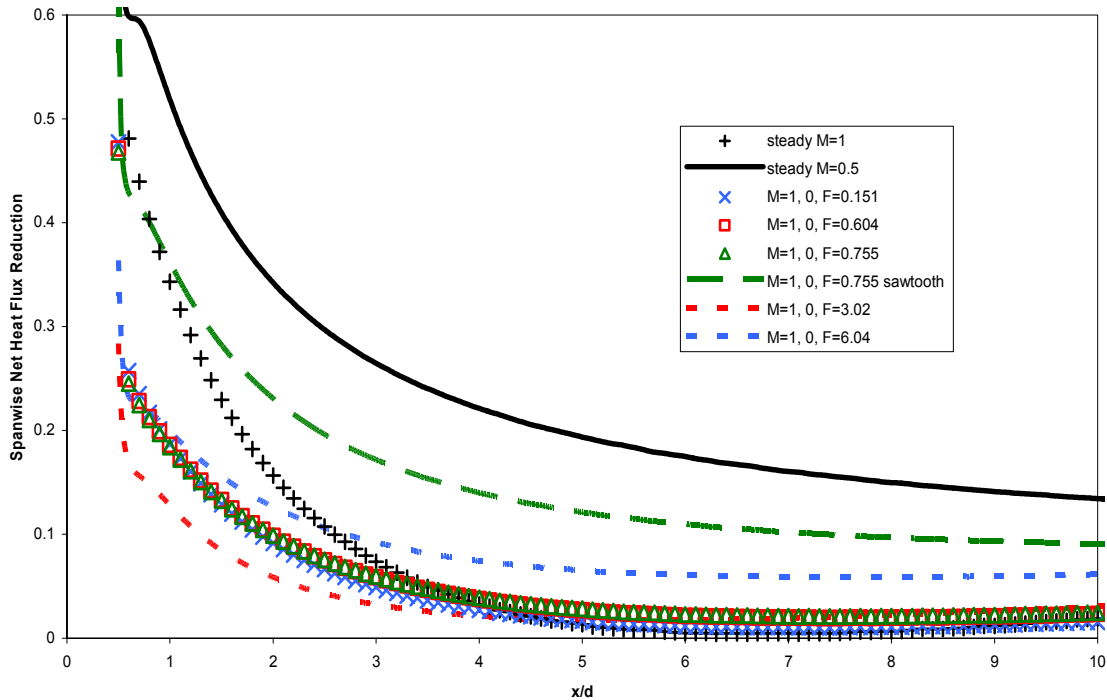
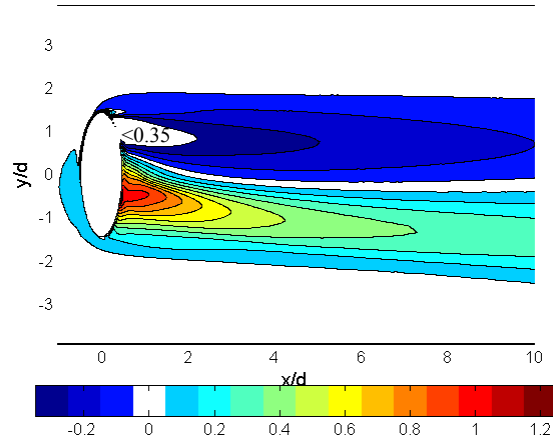


Fig. 9.19 Spanwise net heat flux reduction,  $\overline{\Delta q_{r,span}}$ , for  $\bar{M} = 0.5$  at several  $F$ .  $M = A, B$  indicates pulsing between  $M = A$  and  $M = B$ . Steady  $M = 1$  results also shown.

Kartuzova et al. (2008) also document similar non-monotonic performance with respect to frequency on a flat plate with their CFD simulations of adiabatic effectiveness. At  $\overline{M} = 0.25$  (pulsed between  $M = 0$  and 0.5) the adiabatic effectiveness at a nondimensional frequency equivalent to  $F = 3.55$  was lower than that at  $F = 0.222$ . However, their  $F = 18.7$  case had higher  $\overline{\eta}$  than their  $F = 0.222$  case.

The net heat flux reduction contours with high frequency square wave pulsing are shown in Figs. 9.20 and 9.21. In each of these high frequency cases, the lobes of higher positive  $\overline{\Delta q_r}$  are mid-hole relative to the  $F = 0.151$  case in Fig. 9.11. Although the region with negative  $\overline{\Delta q_r}$  in Fig. 9.21 with  $F = 6.04$  is more severe than the  $F = 3.02$  case in Fig. 9.20 (and with a greater degradation than the  $F = 0.151$  case— see Fig. 9.11), it is more than offset by a greater positive  $\overline{\Delta q_r}$  in the region downstream of the lower part of the hole. The relatively poor film cooling performance in the region downstream of the upper part of the hole in Fig. 9.21 is due to a higher  $\overline{h_f} / h_0$  at  $F = 6.04$  than at the lower pulsing frequencies. Another important difference between the  $\overline{\Delta q_r}$  results for the  $F = 6.04$  case and all lower frequencies is the presence of two lobes of positive  $\overline{\Delta q_r}$  in Fig. 9.21. The upper (primary) lobe extends downstream of the hole at  $y/d \approx 0.9$ . As we follow this lobe downstream, the peak of the lobe follows a curve that increases in  $y/d$  slightly before it decreases in  $y/d$  monotonically through  $x/d = 10$ . The lower lobe of positive  $\overline{\Delta q_r}$  extends downstream of the lower tip of the coolant hole at  $y/d \approx 1.4$ .



**Fig. 9.20** Average net heat flux reduction,  $\overline{\Delta q_r}$ , for pulsed coolant between  $M = 1$  and  $M = 0$ ,  
 $F = 3.02$ ,  $\overline{M} = 0.50$

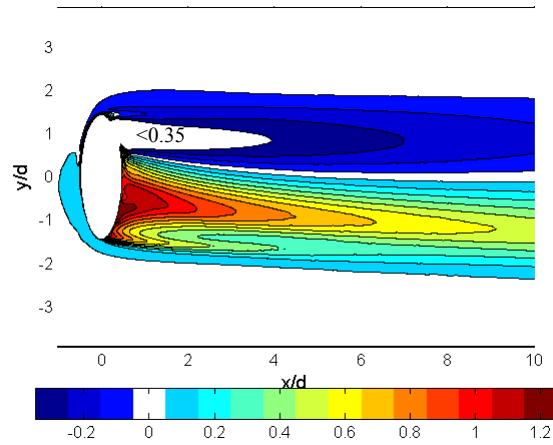


**Fig. 9.21** Average net heat flux reduction,  $\overline{\Delta q_r}$ , for pulsed coolant between  $M = 1$  and  $M = 0$ ,  
 $F = 6.04$ ,  $\overline{M} = 0.50$

The flow of coolant at  $F = 6.04$  clearly has different dynamics than at  $F = 0.151$ . Figure 9.22 shows the adiabatic effectiveness contours at several points in time throughout the cycle at  $F = 6.04$ . Whereas the  $F = 0.151$  jet has enough time in the “on” and “off” states to reach a quasi steady state in the region  $x/d < 10$ , the  $F = 6.04$  jet has insufficient time to reach anything remotely close to steady state at anytime during its very short cycle. The freestream travels only  $1/F$  leading edge diameters = 3.1 hole diameters per cycle. Indeed, undulations of a wavelength of approximately  $3d$  are evident in Fig. 9.22. Immediately after the jet is turned off ( $T = -0.083$ ), coolant at the

exit of the coolant hole continues to exit because mixing occurs between the coolant at the hole exit and the freestream. Before this coolant at the exit can be completely eradicated, the coolant is switched back on ( $T = 0$ ). The result is a more constant flow of coolant whose average spanwise performance (see Fig. 9.19) is more like a steady jet than at lower frequency pulsing. The shapes of the contours, however, are much different due to the unsteadiness in the jet.

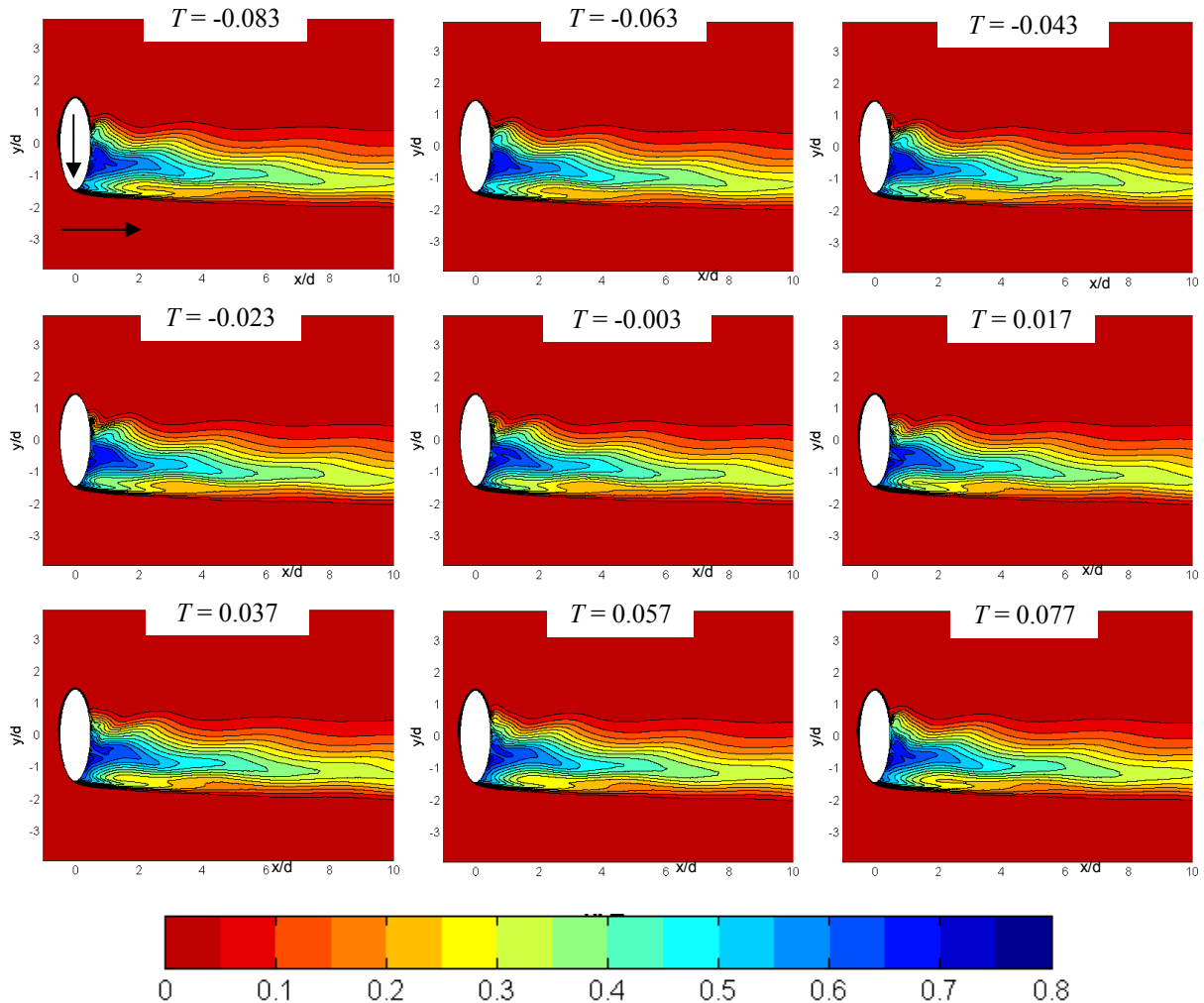


**Fig. 9.22** Adiabatic effectiveness contours through a cycle for  $F = 6.04$  jet pulsed in square wave,  $DC = 50\%$ . Total cycle time is  $1/F = 0.166$ . Jet turns off at  $T = \pm 0.083$  and on at  $T = 0$ .

Also evident from Fig. 9.22 is the fact that the aforementioned two lobes of elevated  $\overline{\Delta q_r}$  are a consequence of the adiabatic effectiveness contours. The coolant exits the cooling hole in two distinct regions at this high frequency of  $F = 6.04$  as shown in Fig. 9.23. The coolant turns off at  $T = -0.083$  in Fig. 9.23. At  $T = -0.037$  warm

freestream fluid has entered the right hand side of the coolant hole, eventually surrounding a pocket of cool fluid that remains in the coolant hole, evident at  $T = 0.003$ , just after the coolant turned back on. This cool pocket of fluid proceeds down the coolant hole followed by the warm fluid that surrounded it. This cool pocket of fluid is responsible for the lower lobe of elevated adiabatic effectiveness visible in all frames of Fig. 9.22.

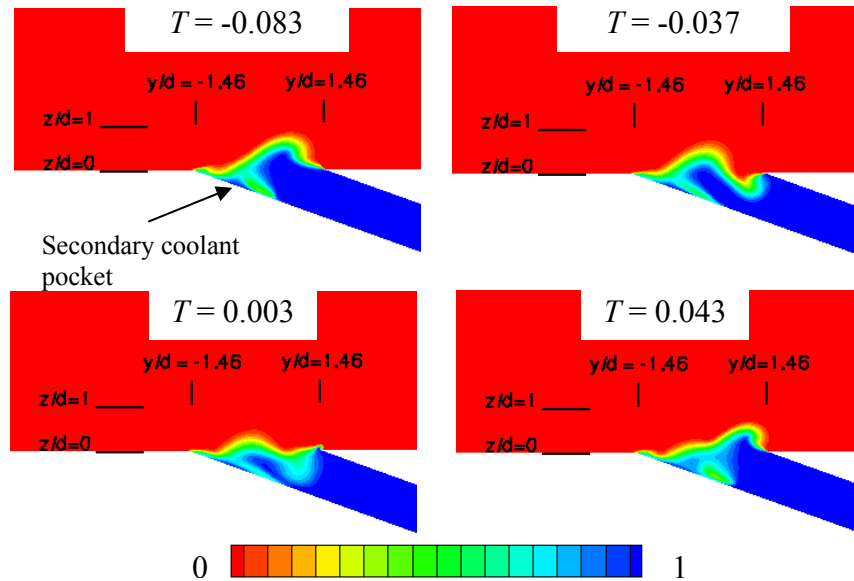


**Fig. 9.23** Nondimensional temperature distribution,  $\theta$ , of fluid in plane intersecting surface at  $x/d = 0$  for several points in time for pulsed coolant between  $M = 1$  and  $M = 0$  at  $F = 6.04$ . Total cycle time is  $1/F = 0.166$ . Jet turns off at  $T = \pm 0.083$  and on at  $T = 0$ .

Additional simulations were performed at an average blowing ratio of  $\bar{M} = 0.25$  with square wave pulsing between  $M = 0.5$  and  $0$ . Figure 9.24 shows the spanwise net heat flux reduction for the  $\bar{M} = 0.25$  cases. Similar to the  $\bar{M} = 0.50$  cases, the performance was not highly dependent on frequency and the  $F = 3.02$  case had somewhat lower net heat flux reduction than the lower frequency cases and the  $F = 6.04$  case performed slightly better than the lower frequency cases. Although not shown, the adiabatic effectiveness contours for the  $F = 6.04$  case do not exhibit the double tine phenomenon observed at  $\bar{M} = 0.5$ .

Contours of the net heat flux reduction for  $F = 3.02$  are shown in Fig. 9.25 in contrast with the net heat flux reduction for  $F = 0.151$  in Fig. 9.13. In Fig. 9.25 the lobe

of positive  $\overline{\Delta q_r}$  is shifted toward the top of the hole for the higher frequency case and has higher magnitude— a trend opposite what was observed at  $\overline{M} = 0.50$ . The shift in position is due primarily to a shift in the position of the area of elevated adiabatic effectiveness, but the change in magnitude results from a decrease in the magnitude of the lower tine of elevated  $\overline{h_f} / h_0$  as shown in Fig. 9.26. The top tine of elevated  $\overline{h_f} / h_0$  has a higher magnitude than at low frequency pulsing (see Fig. 9.14), more than offsetting the beneficial effect realized in the lower region, resulting in decreased spanwise averaged  $\overline{\Delta q_r}$  in Fig. 9.24 for the high frequency pulsed case.

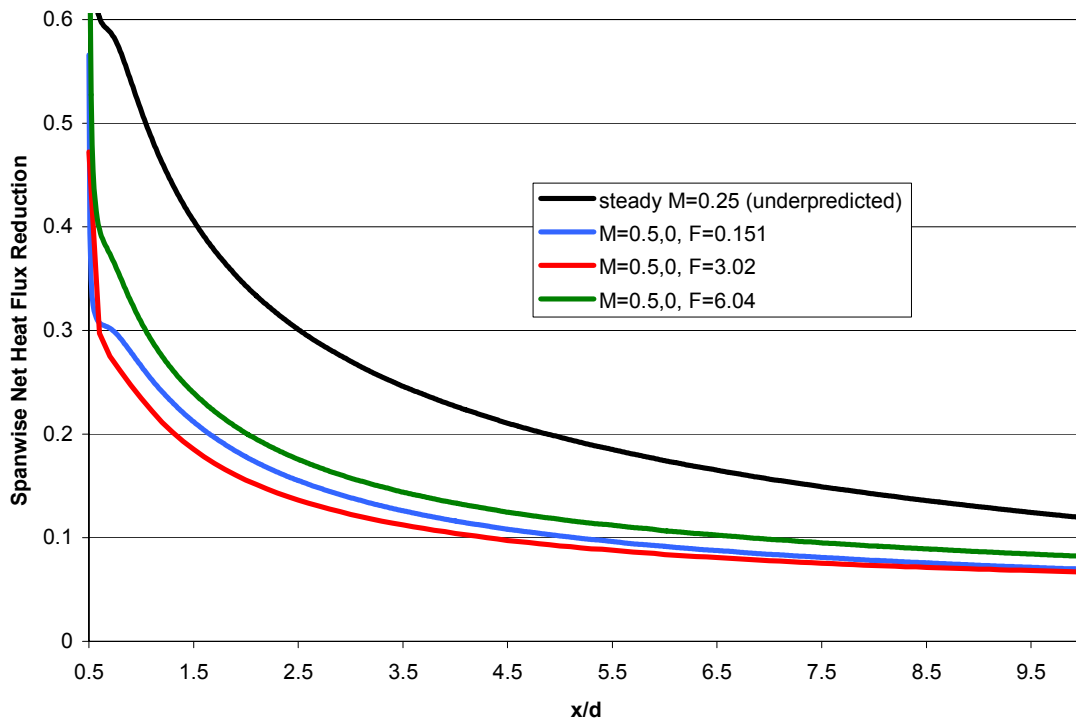
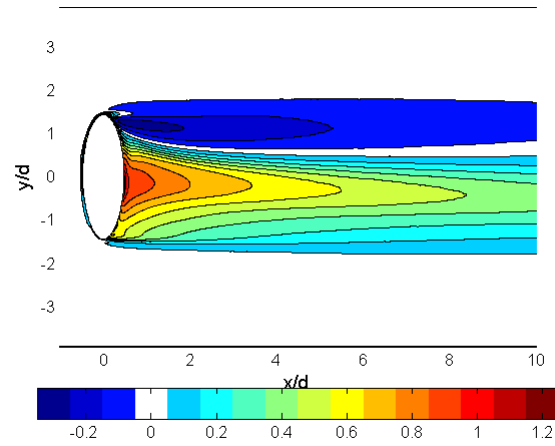
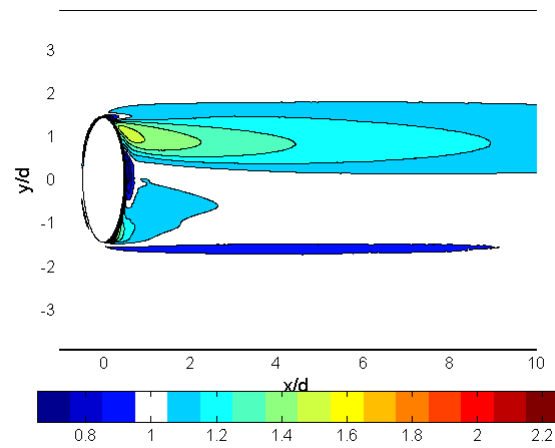


Fig. 9.24 Spanwise net heat flux reduction,  $\overline{\Delta q_{r,span}}$ , for  $\overline{M} = 0.25$  at several frequencies.  $M = A, B$  indicates pulsing between  $M = A$  and  $M = B$ .



**Fig. 9.25** Average net heat flux reduction,  $\overline{\Delta q_r}$ , pulsed coolant between  $M = 0.5$  and  $M = 0$ ,  $F = 3.02$ ,  $\overline{M} = 0.25$



**Fig. 9.26** Heat transfer coefficient ratio,  $\overline{h_f}/h_0$ , pulsed coolant between  $M = 0.5$  and  $M = 0$ ,  $F = 3.02$ ,  $\overline{M} = 0.25$

In conclusion, several pulsing frequencies were examined at average blowing ratios of  $\overline{M} = 0.25$  and  $0.50$ . Although pulsing the coolant is detrimental to the net heat flux reduction compared to steady jets, the performance of high frequency jets ( $F > 3$ ) was found to differ from the performance of the jets at low frequency ( $F < 0.8$ ). The low frequency jets all had similar performance that was predictable through a time-weighted averaging of the performance of a steady jet. This simple technique was demonstrated at a frequency of  $F = 0.151$ .

Because the transient startup and shutdown events account for a significant (if not the entire) cycle time at high pulsing frequencies, the performance cannot be predicted as accurately through a time weighted average of the performance of a steady jet. At both average blowing ratios tested,  $\overline{M} = 0.50$  and  $0.25$ , the performance deteriorated when the pulsing frequency was increased from  $F = 0.755$  to  $3.04$  where the complexity of the unsteady fluid dynamics began to have significant influence on the film cooling performance. The trend reversed when the pulsing frequency was raised as high as  $F = 6.04$  for the  $\overline{M} = 0.50$  case, yielding results superior to the low frequency pulsed jet all the way to  $x/d = 10$ , but still inferior to the steady  $M = 0.50$  jet.

The  $F = 6.04$  jet had behavior that differed markedly from lower frequency jets. The interaction of the coolant at the hole exit with the freestream fluid caused two nearly steady distinct streams of coolant to exit the cooling hole. This second stream of coolant appears to improve the adiabatic effectiveness. Although the dynamics of the jet at this high frequency are rather complex, as the pulsing frequency is increased, the performance may start to behave more like a steady jet; however, higher frequency simulations were not conducted with the current computational model to test this hypothesis.

The low frequency prediction technique predicts that the performance of a low frequency pulsed scheme is poorer than the steady scheme when pulsing occurs in the vicinity of a concave-down region of the net heat flux reduction plotted against steady blowing ratio. Inspired by this and the slightly better performance of the  $F = 6.04$  jet relative to lower frequencies, we would like to understand how a  $F = 6.04$  jet pulsed between at  $\overline{M} = 1$  (both through pulsing between  $M = 1.5$  and  $0.5$  as well as  $M = 1.25$  and  $0.75$ ) compares with a steady jet at  $M = 1$ . By drawing straight lines between the two blowing ratios involved in the pulsed schemes, in the steady experimental NHFR data in Fig. 5.46, we can determine that such jets would perform comparably according to the low frequency prediction technique. The results of the CFD simulations are presented in Fig. 9.27. Because  $F = 6.04$ , we would not expect the pulsed cases to match up exactly with the low frequency prediction technique. The higher amplitude pulsed case has a spanwise averaged heat load of approximately 5% higher than the steady jet; however, the lower amplitude pulsed case yields almost identical heat load, with a slightly lower

heat load ( $\approx 1\%$ ) than the steady jet for  $x/d < 3$ . The lower amplitude pulsed case performs more similarly to the steady jet because the deviations in blowing ratio are not as far from the mean. This finding is the only CFD simulation performed as part of this research in which the spanwise net heat flux reduction was found to be higher for a pulsed case than the corresponding steady case.

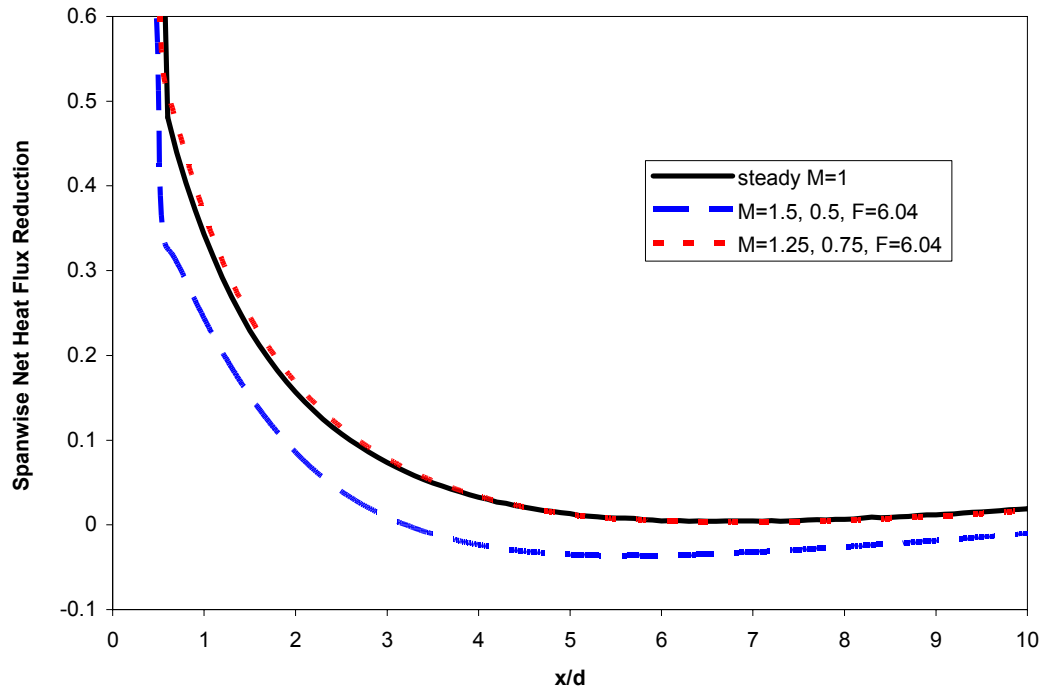


Fig. 9.27 Spanwise net heat flux reduction,  $\overline{\Delta q_{r,span}}$ , for  $\overline{M} = 1.0$  at  $F = 6.04$ .  $M = A, B$  indicates pulsing between  $M = A$  and  $M = B$ .

### 9.3 Computational Simulation of a Row of Holes

The aforementioned simulations of a single hole leave open the possibility of coolant hole interaction from a row of coolant holes. The method of superposition described in such references as Muska et al. (1976) and Sellers (1963) describes how one can predict the performance of a film cooling scheme using multiple sources of film coolant through knowledge of the performance of the individual sources of film coolant. Although the technique is valid for regions on the surface that are influenced by both sources of film coolant, the technique requires that the multiple sources are spaced

sufficiently far that the only interaction is an additive one. In this section we shall examine a spanwise row of film cooling holes spaced  $7.86 d$  apart.

The mesh used for the single hole simulations was modified such that the spanwise extent was only  $7.86 d$  instead of  $209 d$  as in the original grid. Periodic boundary conditions were placed on the spanwise boundaries such that a leading edge of infinite span with an infinite number of film cooling holes is formed. The domain was re-meshed such that the grid resolution was at least that of the original grid that was verified to be grid independent. The final mesh had 9.9 million cells, more than the original despite the smaller domain size owing to a conservative meshing philosophy.

The  $F = 6.04$  case was run with the blowing ratio alternating between  $M = 1$  and 0. The spanwise averaged  $\bar{\eta}$  results of the row of holes are compared to the single hole results in Fig. 9.28. The difference in spanwise averaged  $\bar{\eta}$  is negligible, with a maximum difference of  $\Delta\bar{\eta} = 0.006$ . Slightly higher values of  $\bar{\eta}$  for the row of holes would be expected, since a spanwise component of the coolant velocity could cause some coolant to depart the region over which spanwise averaging takes place. The row of holes corrects that problem with coolant entering the region from a neighboring jet. This coolant that traverses to a neighboring region does not imply jet interaction, only a limitation of the region selected for spanwise averaging with the single hole.

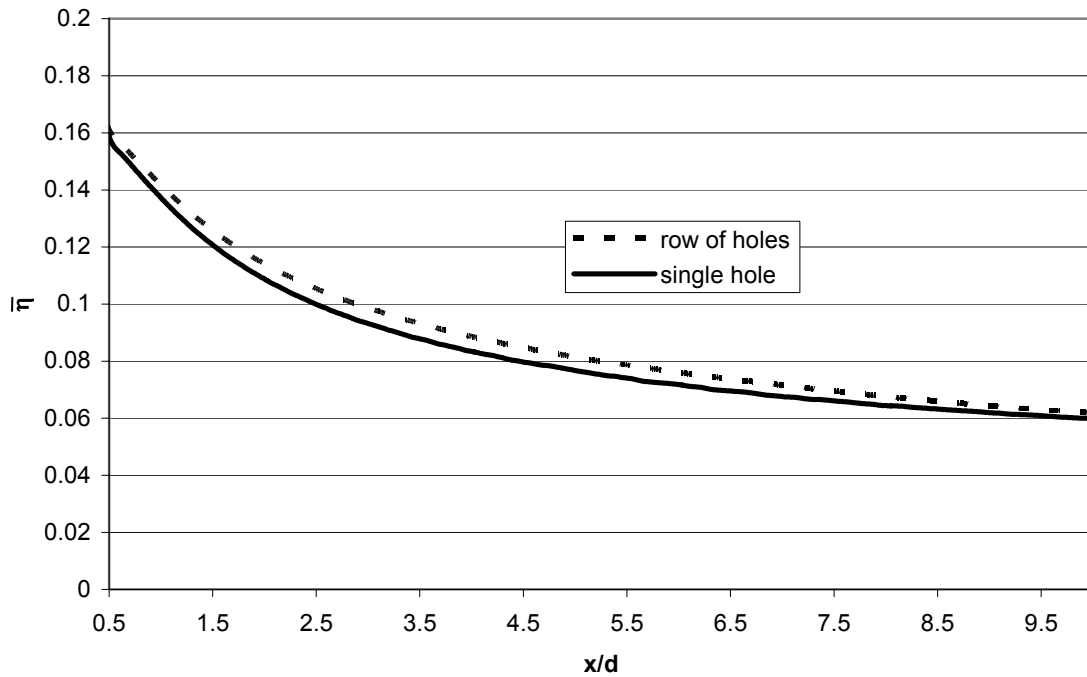


**Fig. 9.28** Spanwise averaged  $\bar{\eta}$  for a row of holes compared with a single hole with pulsed coolant between  $M = 1$  and  $M = 0$ ,  $\bar{M} = 0.5$ ,  $F = 6.04$

The lack of interaction between the neighboring jet domains suggests that the spacing of  $7.86 d$  is large relative to the spanwise extent of the influence of the coolant jets at the blowing ratio of  $M = 1$ . At slightly higher blowing ratios, one would also expect negligible interaction. At very high blowing ratios, the spanwise velocity of the jet would be sufficient to cause a significant amount of coolant to cross the boundaries of spanwise averaging. Even in that case, the effect would be mostly an additive effect, easily predictable with superposition.

## 10. Conclusion

In this chapter, the results of the previous chapters are briefly summarized. Recommendations for future research are also given.

### 10.1 Summary of Work

Increasing interest in the use of pulsed jets as a means of active flow control on turbine blades requires an understanding of the impact this would have on film cooling performance. Even without intentional pulsing, natural unsteadiness from wake passage causes unsteady film cooling behavior. A higher-order understanding of the influence of film cooling unsteadiness can only benefit the practice of modern gas turbine design.

Calculation of the net heat flux reduction with steady film cooling requires knowledge of  $\eta$  and  $h_f$  in addition to  $h_0$  for a baseline non-film-cooled case for comparison. This technique has been used for decades, but until presently, no research has considered how the technique must differ with unsteady film cooling. Some researchers have simply attempted to use average values,  $\bar{\eta}$  and  $\bar{h}_f$  with the traditional form of the net heat flux reduction equation (Eq. (3.11)). In the present study we show that to determine the net heat flux reduction with  $\bar{\eta}$  and  $\bar{h}_f$ , one would also need to take into account the cross-coupling of  $\eta$  with  $h_f$  through the term,  $\overline{h_f'\eta'}$ . One may then properly compute the net heat flux reduction with Eq. (3.25). Although  $\bar{\eta}$  is difficult, but not impossible, to measure experimentally, it is very simple to measure computationally where a perfectly adiabatic boundary condition can be applied. Instead of experimentally measuring  $\bar{\eta}$ , one may alternatively measure the unsteady coupled adiabatic effectiveness,  $\gamma$ , in lieu of both  $\bar{\eta}$  and  $\overline{h_f'\eta'}$ .  $\gamma$  is shown to be relatively simple to measure, but requires careful experimental design such that surface temperature fluctuations on the model are negligible. This may be accomplished by ensuring that  $C = \frac{k}{\bar{h}\sqrt{\alpha/\omega}} \rightarrow \infty$  for the experimental apparatus. This requirement must be balanced with a requirement for low  $k$ , so  $C$  must be made large primarily through selection of a

material with large  $\rho$  and  $c$  along with proper scaling such that  $\omega$  is sufficiently large. Incidentally, a measurement of  $\bar{\eta}$  would require  $C=0$ . Although sufficiently low  $C$  would be possible to obtain a measurement approximating  $\bar{\eta}$ , under most circumstances, it would be simpler to design the experiment for large  $C$  and measure  $\gamma$  instead. Furthermore, a measurement of  $\bar{\eta}$  would still be insufficient to determine the net heat flux reduction without  $\overline{h_f' \eta'}$ , another parameter that would be difficult to measure. It is worth stressing that care must be taken with the experimental design for if  $C$  is neither sufficiently large nor sufficiently small, the measurements will yield neither  $\bar{\eta}$  nor  $\gamma$ .

The aforementioned experimental technique to determine the net heat flux reduction due to pulsed film cooling was performed on a simulated film-cooled leading edge region in a wind tunnel. The experimental study first considered the steady film cooling jet. The optimum blowing ratios were all  $M \leq 0.5$ , with the largest area-averaged  $\Delta q_r$  of 28% attainable at  $M=0.25$  with  $Re_D=60k$  and low freestream turbulence. High freestream turbulence decreased  $\Delta q_r$  by between 3% and 5% at both Reynolds numbers. The peak values of  $\Delta q_r$  at  $Re_D=60k$  outperformed the peak values at  $Re_D=30k$  at both freestream turbulence intensities by between 4% and 6%. Switching from low to high freestream turbulence caused  $Fr$  to be 18% and 12% higher at the hole location for the  $Re_D=60k$  and  $30k$  cases, respectively. On the other hand, the  $Fr_f / Fr_0$  ratios were up to 10% higher at low freestream turbulence. At low  $M$ , turbulence tended to degrade  $\eta$  since coolant that would have been close to the surface was mixed more with the freestream. At high  $M$ , the opposite was true, with the increased turbulent mixing causing some lifted-off coolant to return to the surface and improve  $\eta$  over what it was at low freestream turbulence. As a result, film cooling provided better net heat flux reduction at high turbulence than at low turbulence for  $M \geq 1$ ; however, the adiabatic effectiveness afforded by the coolant in this high  $M$  regime was not sufficient to compensate for the higher Frössling numbers caused by the film cooling. This resulted in  $\Delta q_r < 0$  at high  $M$ .

The flow visualization experiments and the computational simulations both showed that square wave film cooling pulsations at  $F = 0.15$  (approximately 3.5 kHz at engine scale, similar to the natural blade passing frequency) are slow enough that the majority of the time (~70%) the entire surface experiences conditions very similar to either the steady-state “on” or “off” conditions of the jet; individual points experiences quasi-steady conditions for over 80% of the time. The wind tunnel experiments for measuring net heat flux reduction did not have square wave pulsations; however, it was a reasonable hypothesis that at  $F = 0.15$ , the flow was quasi-steady. For quasi-steady, low frequency flows, a simple technique to predict the performance of a pulsed film cooling scheme was developed that requires only the shape of the pulsed film cooling waveform and the performance of steady film cooling as a function of blowing ratio. Since the average net heat flux reduction with pulsed film cooling was predicted very accurately with the low-frequency prediction technique, the hypothesis of quasi-steady flow was confirmed.

At the higher nondimensional pulsing frequencies ( $F \geq 0.6$ ), there was some frequency dependence of the results. This was evident by comparing cases with different frequencies, but similar waveform shapes. The frequency dependence implies that the low frequency prediction technique would be less applicable in this frequency range. Generally, the lower frequency cases performed better than the higher frequency cases that were studied.

The quasi-steady behavior of the film cooling jet implies that the more time the jet spends in the vicinity of the optimum steady blowing ratio, the better the jet performs. Indeed, this was found to be true. In the event that over the range of acceptable average blowing ratios the heat flux reduction performance curve as a function of steady  $M$  is concave-up, pulsing the jet is likely to yield better performance than a steady jet at matched average blowing ratio. In fact, the particular leading edge geometry tested in this study has a concave-up performance curve at  $M > 1$ . Sure enough, at high  $\overline{M}$ , some pulsed schemes did perform better than steady blowing, in excellent agreement with the predicted performance.

The flow visualization of the steady jets in the water channel revealed that for  $M \leq 0.5$ , the coolant propagation is essentially laminar at  $Re_D = 30k$ . This laminar coolant behavior was characterized by the coolant dividing into fingers at multiple spanwise locations and remaining very close to the surface. These fingers of coolant are expected to be responsible for fingers of elevated adiabatic effectiveness observed with the wind tunnel experiments. The flow visualization also revealed that the steady jets do not necessarily imply a steady flow-field. Indeed, the coolant propagation had small magnitude unsteadiness that would not be expected to cause a significant departure from the steady form of the net heat flux reduction equation (Eq. (3.11)) that would require use of the unsteady form (Eq. (3.25)).

The pulsed coolant resulted in enormous unsteadiness in the film cooling flow. At low frequency ( $F \leq 0.294$ ), the film cooling jet had ample time to reach quasi-steady states during the “on” and “off” portions of the cycle time. In all cases, the fairly sudden jet turn-on resulted in an amount of coolant penetrating farther into the freestream than the remainder of the coolant to exit the coolant hole. In the case of the low frequency jets, this over-penetrating coolant was virtually insignificant relative to the remainder of the coolant, implying that the low frequency prediction technique would be applicable. Transient events accounted for only approximately 30% of the cycle time at  $F = 0.148$ . At the highest frequency of  $F = 1.195$ , the over-penetrating coolant accounted for the majority of the coolant, owing to the short time remaining during the pulse for additional coolant to exit at a quasi-steady state. In fact, one could argue that there is no quasi-steady state achieved during the short pulses with  $F = 1.195$ . This additional coolant that penetrates far into the freestream affords little thermal protection and is a decent explanation for the poor net heat flux reduction observed at  $F = 1.20$  from the wind tunnel experiments.

Computational simulations afforded time resolved thermal data for the film cooled surface since the computational surfaces have no heat capacity or thermal conductivity causing the surface temperature response to lag changes in the flow field. Furthermore, computational simulations lend themselves to direct spatial measurements of the instantaneous surface temperature, a difficult experimental feat. The cross coupled

term in the unsteady form of the net heat flux reduction equation was demonstrated to have a 50% effect on net heat flux adjacent to the hole with decreasing importance out to  $x/d = 4.5$  for the case of coolant pulsed between  $M = 1$  and  $M = 0$ . Neglecting this term could lead to very large errors in  $\overline{\Delta q_r}$ . Because  $h$  and  $\eta$  tend to fluctuate in phase, the positive nature of the term would cause an analysis neglecting it to underestimate the net heat flux reduction.

Spatial and time resolved adiabatic effectiveness and heat transfer coefficient data demonstrate that net heat flux was generally increased by pulsing the film coolant at  $F = 0.151$  and  $DC = 50\%$ . The heat transfer coefficient was only marginally affected by pulsing, with small reductions occurring particularly in cases for which the coolant was turned off during the cycle, evidently due to nonlinearity in the behavior of heat transfer coefficient with steady blowing ratio. The poorer net heat flux reduction performance of the pulsed schemes was rooted primarily in reduced adiabatic effectiveness, which in the more severe cases was cut in half by pulsing. The pulsing frequency is slow enough that transient events account for only approximately 30% of the total period, suggesting that the behavior of a pulsed scheme is dominated by the average of the behavior of the two blowing ratios between which the coolant fluctuates. The percentage of time that transient events occur is in agreement with the observations from the experimental flow visualization in Section 7.2.

Computational simulations of high frequency jets ( $F \geq 3$ ) found that the physics of the jet behavior change remarkably and the low frequency prediction technique becomes less accurate. At  $F = 3.02$ , the performance of the jet decreased relative to the low frequency cases (which had performances nearly frequency independent according to the low-frequency prediction technique). At  $F = 6.04$ , the performance of the jet was better than the low frequency cases. The jet behavior, while still unsteady, was much more like a steady jet, without the coherent breaks in the film cooling jet. In fact, the coolant was expelled from the coolant hole almost continuously at this high frequency due in part to a pocket of coolant that got trapped between the main coolant flow and some freestream fluid that entered a portion of the coolant hole during the “off” part of the cycle.

## 10.2 Recommendations for Future Work

The experimental and computational work presented in Chapters 4 through 9 describe the influence of pulsed film cooling from a single film cooling hole using the general theory of pulsed film cooling net heat flux reduction developed in Chapter 3. Although this present study afforded an in-depth analysis of pulsed film cooling, more work remains to fully understand the behavior of pulsed film cooling in engine representative conditions.

### 10.2.1. Low Frequency Predictions with Steady Data Sets from Other Configurations

At sufficiently high  $\overline{M}$ , pulsed film cooling schemes were found to be superior to steady cooling at matched  $\overline{M}$  with the leading edge geometry and flow conditions used in the present study; however, these pulsed cases were inferior to steady cooling at lower blowing ratios. There certainly may be design constraints that require the use of large  $\overline{M}$ , making pulsing beneficial, but there may be other film cooled components that may benefit more directly from pulsed film cooling, without requirements that the blowing ratio is higher than the optimum for external film cooling. The low frequency prediction technique described in Section 3.6 and demonstrated in Sections 5.3 and 9.2.2 may be used with existing sets of steady film cooling data for a variety of geometries to predict the likely effects of pulsed film cooling. For example, McCall and Branam (2009) performed a computational study of the net heat flux reduction performance on a steady film cooled surface with uniform concave curvature in the spanwise direction and no streamwise curvature. The geometry was selected to simulate the interior of a converging-diverging nozzle. The concave upward curvature of their  $\Delta q_r$  data as a function of steady  $M$  for all  $M$  studied suggest that there may be a clear benefit of pulsing with that geometry per the low frequency theory of Section 3.6.

### 10.2.2. Pulsed Film Cooling from Multiple Rows of Film Cooling Holes

A row of holes was briefly examined in Section 9.3 in which we found that the spacing between those holes was sufficiently far that the holes did not interact; however,

examination of multiple rows of film cooling holes was not performed. The behavior of film cooling from a row of film cooling holes with another upstream is almost certainly going to be affected by the upstream row, regardless of the distance in practical turbine scales.

Appendix B describes an extension of a steady superposition technique described by Muska et al. (1976) and Sellers (1963) such that it may be applied to unsteady film cooling flows. This technique would allow one to predict the performance of a film cooling scheme consisting of multiple sources of film coolant through knowledge only of the performance of the individual sources of film coolant.

Future work may begin with mining existing steady film cooling data on geometries more closely matching actual turbine components with multiple rows of film cooling holes. The steady data may then be used with the low-frequency prediction technique described in Section 3.6 to predict the unsteady fluctuations in  $\eta$  and  $h_f$ . The data may then be applied through the the unsteady superposition theory in Appendix B. Several phase angles could be studied while accounting for the natural phase angle due to the time it takes for coolant from an upstream row to come into contact with the downstream row. The net heat flux reduction predicted through Eq. (3.25) could then be compared to the net heat flux reduction attainable through steady film cooling at matched average coolant consumption.

Higher fidelity simulations may be performed that do not rely on the low-frequency assumption through the use of CFD or wind tunnel experiments. Flow visualization experiments may be useful to confirm the relative phases of the various rows of holes.

### **10.2.3. Full Coverage Pulsed Film Cooling**

As an extension of the work addressing multiple rows of holes in Section 10.2.2, simulation of turbine components with full film cooling might be useful. Research such as that by Abhari (1996) have considered the effects of rotor-stator interactions of the blowing rates of coolant issued from a fully cooled model. Experiments or computational simulations of the film cooling performance with the appropriate waveforms and phase

shifts for each row of coolant holes would afford realistic data on the influence of natural unsteadiness on the film cooling behavior for the entire blade.

#### **10.2.4. Modulation of Film Cooling Flow**

In the event that intentional pulsing of the film coolant would be beneficial for either cooling, flow control, or both, a method to intentionally pulse the coolant would need to be devised. Such a coolant modulation technique might instead be useful for countering the influence of unsteadiness due to wake passage. The method would need to be efficient enough to not overwhelm the benefit of modulation. Once a practical pulsing method is developed, the actual waveforms achievable with the method would need to be tested for their net heat flux reduction behavior.

#### **10.2.5. Examination of Other Sources of Unsteadiness**

The techniques developed in Chapter 3 allow determination of the net heat flux reduction on a film cooled component with unsteady  $T_{aw}$  and  $h$ . Although the present focus has been on fluctuations in those parameters caused by unsteady  $M$ , the techniques may be used to deal with unsteady  $T_{aw}$  and  $h$  that result from virtually any form of unsteadiness one may encounter in a convective heat transfer scenario. For example, a hypothetical wake passage that does not affect  $M$  might still affect  $\eta$  and  $h$  due to hydrodynamic effects. In another hypothetical example,  $T_{aw}$  would be unsteady if  $T_\infty$  is unsteady, even if  $T_c$  and  $M$  are steady. In this event, a redefinition of  $\eta$  that employs a constant reference value of  $T_\infty$  would allow continued use of Eq. (3.25) in its unaltered form.

## Appendix A Pulsed Jet Waveforms for Net Heat Flux Reduction Experiments

In order to report the behavior of pulsed film cooling, it is necessary to describe how the blowing ratio was varied in time. Due to the mechanical nature of the solenoid valves used in these experiments, the waveforms were found to be much more complex than simply “on” or “off.” Additionally, the various duty cycles, pulsing frequency, and intermediate poppet replacement resulted in such varied behavior, that the description of these waveforms necessitates its own appendix in this document.

A complete set ( $\gamma$  and  $\overline{h_f}$ ) of experiments were conducted with the solenoid valves as they were supplied. Following characterization of the waveforms of the flow from the coolant hole, the poppets were replaced and the waveforms were recharacterized. A second complete set of experiments were then conducted with the modified wave forms. The two sets of data are designated “partial valve closure” and “complete valve closure,” using the acronym VC to refer to “valve closure.” The duty cycles given refer to the percentage of time the valve controller intended for the valve to be in the “on” state relative to the total time of operation. As will be evident, the intentions of the valve controller were not necessarily what the valves did (especially during the partial VC experiments), and even less related to the flow at the outlet of the film cooling hole, located approximately 1.7 m from the solenoid valves.

The waveforms were characterized by placing a hot film anemometer probe (confirmed to have sufficiently high frequency response) at the exit of the coolant hole and pulsing the coolant with zero freestream velocity. The average coolant mass flow rate was set to the approximate value it would be for a particular value of  $\overline{M}$  at a freestream Reynolds number of  $Re_D = 60000$ . The velocity measured by the anemometer was normalized according to this value of  $\overline{M}$  such that the data presented in the figures in this section is  $M(t)$  at  $Re_D = 60000$ . Of course, the same coolant velocity profiles were used in the experimentation at  $Re_D = 30000$ , for which  $\overline{M}$  and  $M(t)$  would simply be doubled relative to the scales shown in the figures. Data was acquired at 10 kHz for

10 seconds. For example, at a pulsing frequency of 20 Hz, this corresponds to 200 cycles, each cycle resolved by 500 data points. The velocity data was then phase averaged over the entire 10 seconds of data.

The average measured velocity of the coolant was generally approximately 10% higher than the calculated bulk average velocity of the coolant because the hot film probe measures a velocity of the coolant near the centerline of the hole. The 10% value was not universal, however, since the turbulence characteristics influence the velocity profile at the exit of the hole. The measured velocity as a function of time was converted to a virtual  $M$  as a function of time by normalizing the velocity by the average velocity and multiplying the result by the target average blowing ratio.

### **A.1 Partial Valve Closure, 20 Hz, DC = 25%**

Several waveforms obtained with the valves in the partial VC configuration at 20 Hz,  $DC = 25\%$  are shown in Figs. A.1 through A.4. With the exception of  $\bar{M} = 0.25$  in Fig. A.1, the waveforms were very similar, characterized by two periods of elevated  $M$ , with one being about 60-70% larger than the other.

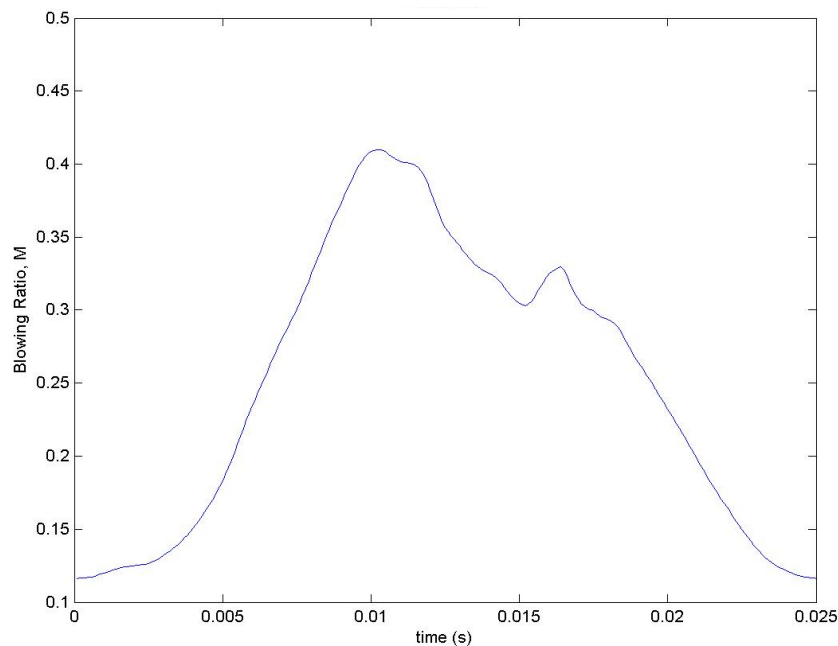


**Fig. A.1  $M(t)$  for  $\bar{M} = 0.25$ , 20 Hz,  $DC = 25\%$ , partial VC ( $M$  calculated based on  $Re_D = 60000$ ; double  $M$  for  $Re_D = 30000$ )**

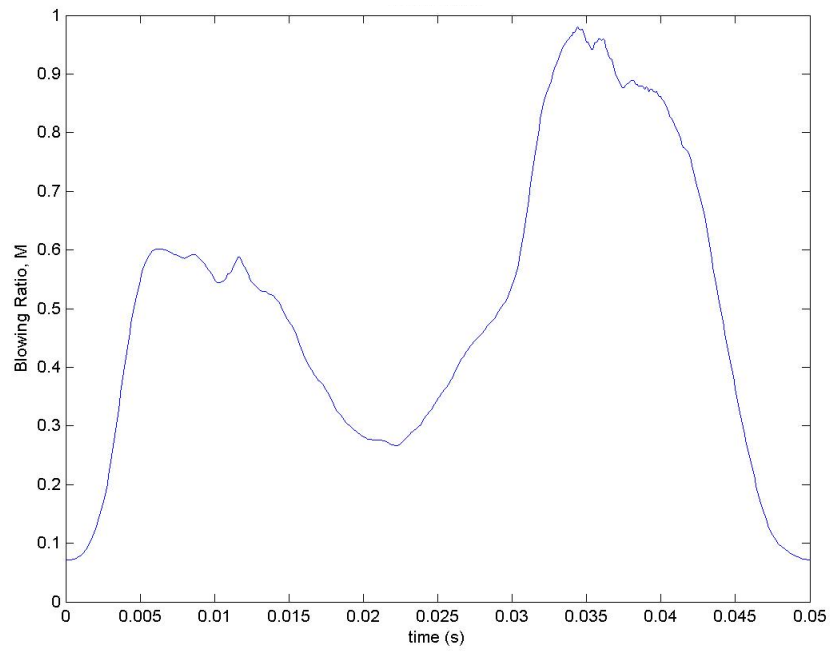


**Fig. A.2  $M(t)$  for  $\overline{M} = 0.50$ , 20 Hz,  $DC = 25\%$ , partial VC ( $M$  calculated based on  $Re_D = 60000$ ; double  $M$  for  $Re_D = 30000$ )**

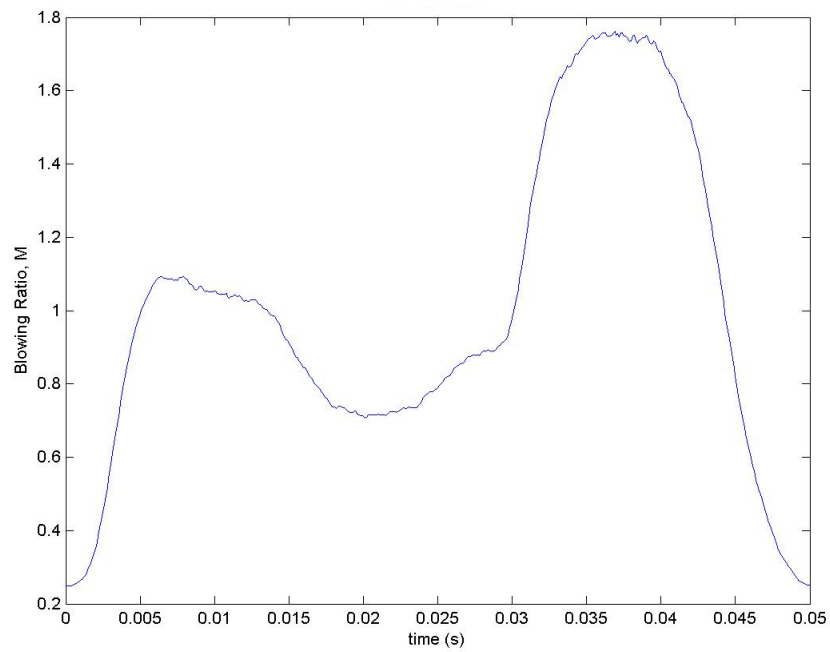


**Fig. A.3  $M(t)$  for  $\overline{M} = 1.0$ , 20 Hz,  $DC = 25\%$ , partial VC ( $M$  calculated based on  $Re_D = 60000$ ; double  $M$  for  $Re_D = 30000$ )**

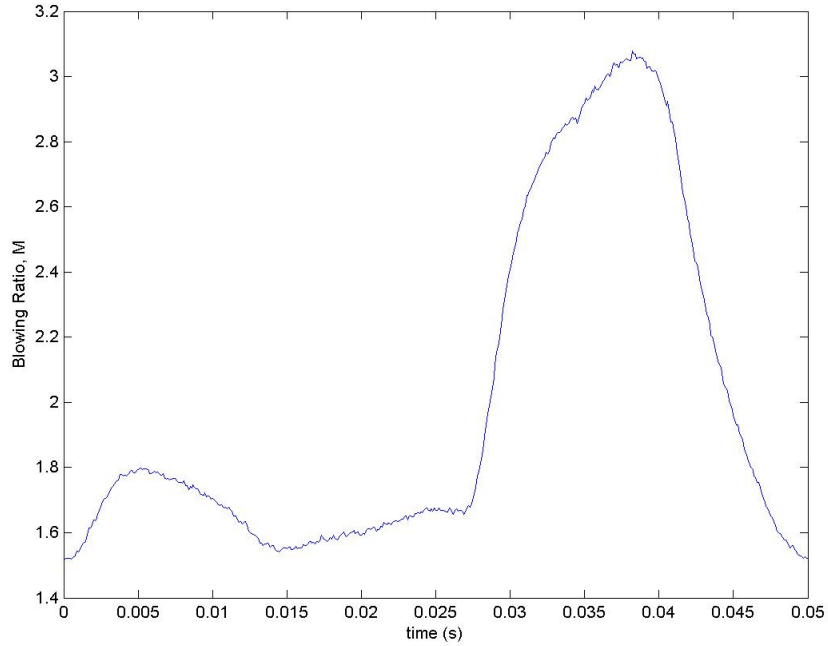


**Fig. A.4**  $M(t)$  for  $\overline{M} = 2.0$ , 20 Hz,  $DC = 25\%$ , partial VC ( $M$  calculated based on  $Re_D = 60000$ ; double  $M$  for  $Re_D = 30000$ )

## **A.2 Partial Valve Closure, 20 Hz, $DC = 50\%$**

Blowing ratio waveforms for the partial VC configuration at 20 Hz,  $DC = 50\%$  are shown in Figs. A.5 through A.8. Again, the waveforms were very similar with the exception of the  $\overline{M} = 0.25$  case.

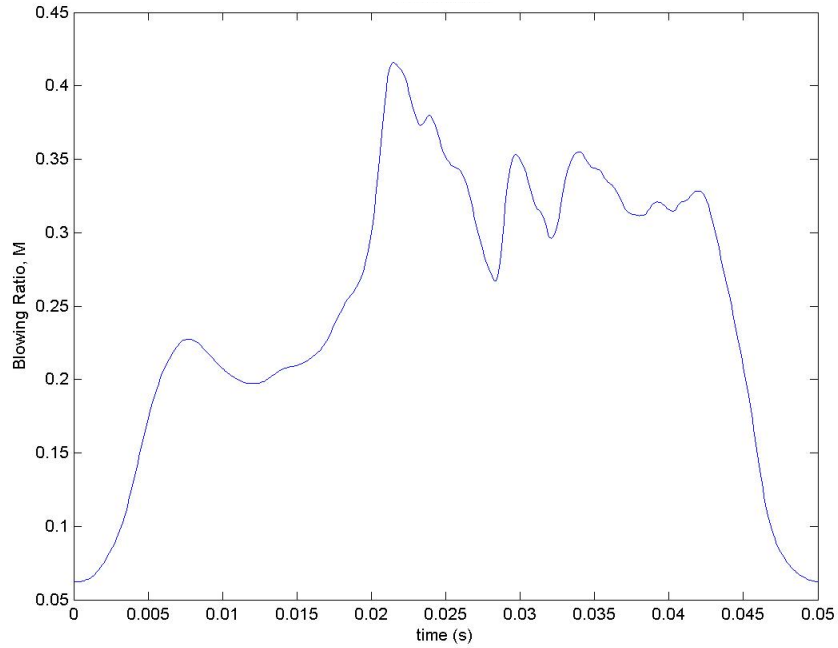


**Fig. A.5  $M(t)$  for  $\overline{M} = 0.25$ , 20 Hz, DC = 50%, partial VC ( $M$  calculated based on  $Re_D = 60000$ ; double  $M$  for  $Re_D = 30000$ )**

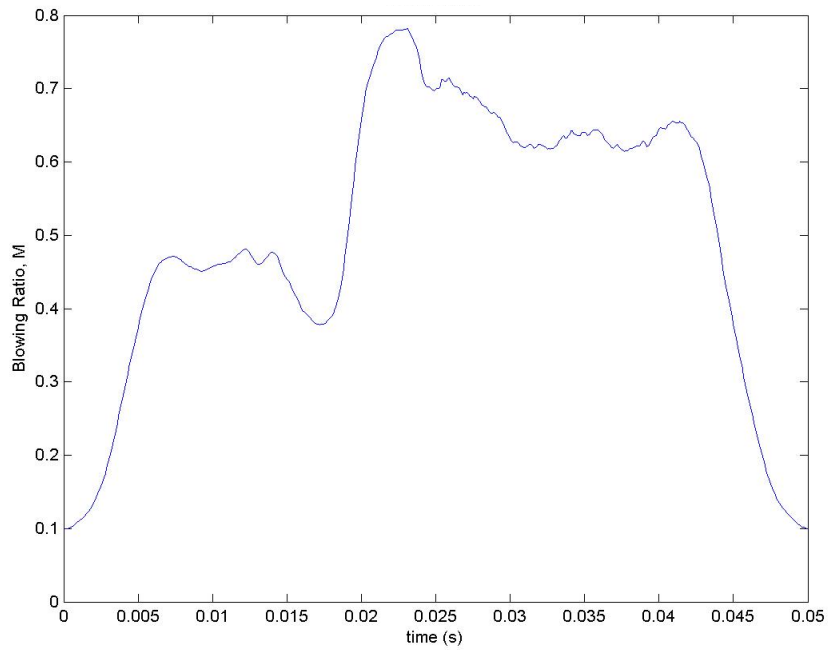


**Fig. A.6  $M(t)$  for  $\overline{M} = 0.50$ , 20 Hz, DC = 50%, partial VC ( $M$  calculated based on  $Re_D = 60000$ ; double  $M$  for  $Re_D = 30000$ )**

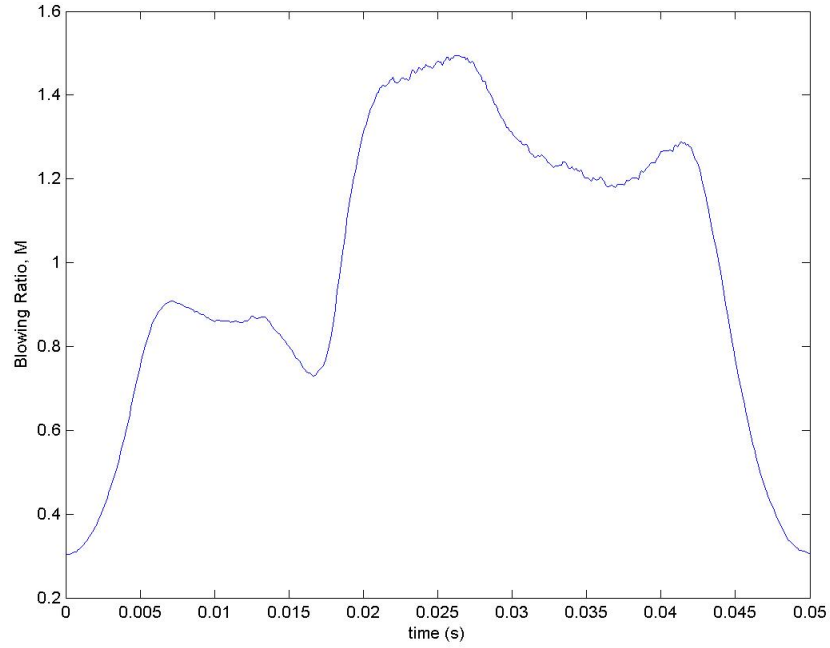


**Fig. A.7**  $M(t)$  for  $\overline{M} = 1.0$ , 20 Hz, DC = 50%, partial VC ( $M$  calculated based on  $Re_D = 60000$ ; double  $M$  for  $Re_D = 30000$ )

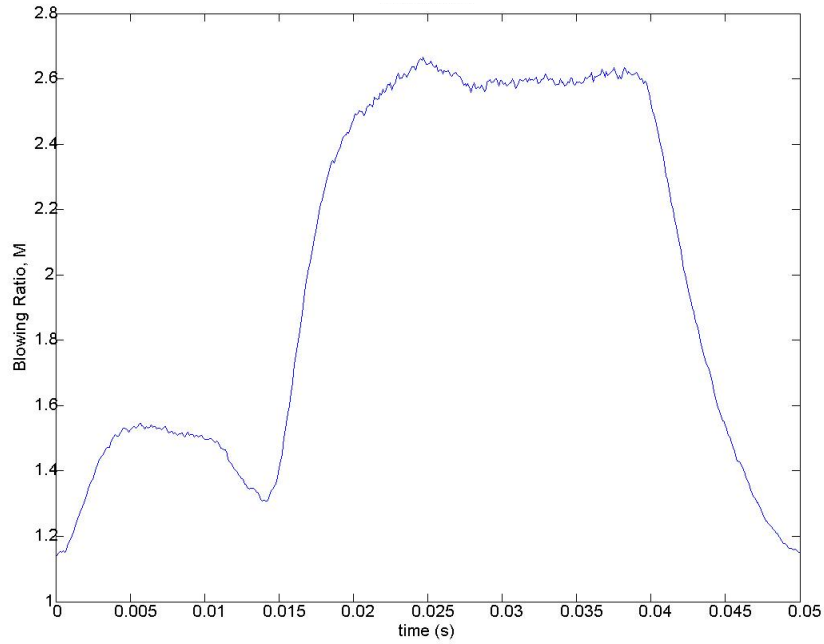


**Fig. A.8**  $M(t)$  for  $\overline{M} = 2.0$ , 20 Hz, DC = 50%, partial VC ( $M$  calculated based on  $Re_D = 60000$ ; double  $M$  for  $Re_D = 30000$ )

### A.3 Partial Valve Closure, 20 Hz, DC = 75%

Blowing ratio waveforms for the partial VC configured valves pulsed at 20 Hz, with a duty cycle of 75% are presented in this section (see Figs. A.9 through A.12). As usual, the  $\bar{M} = 0.25$  (see Fig. A.9) case had a somewhat different appearance than the higher blowing ratios.

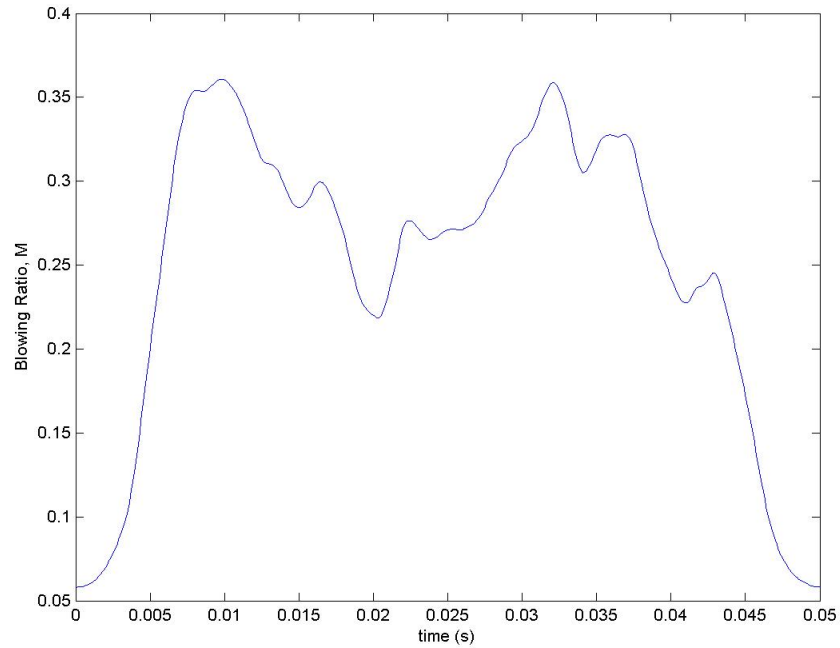
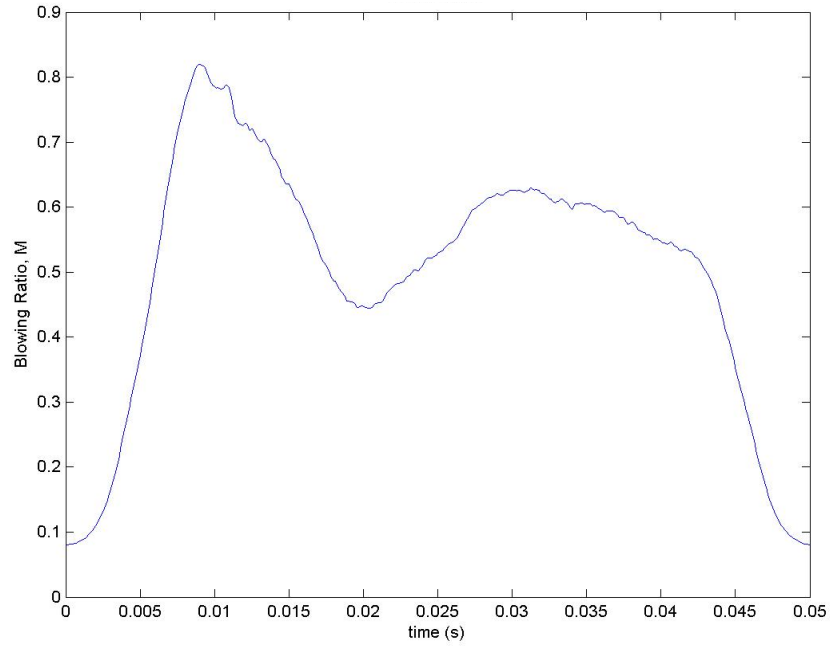
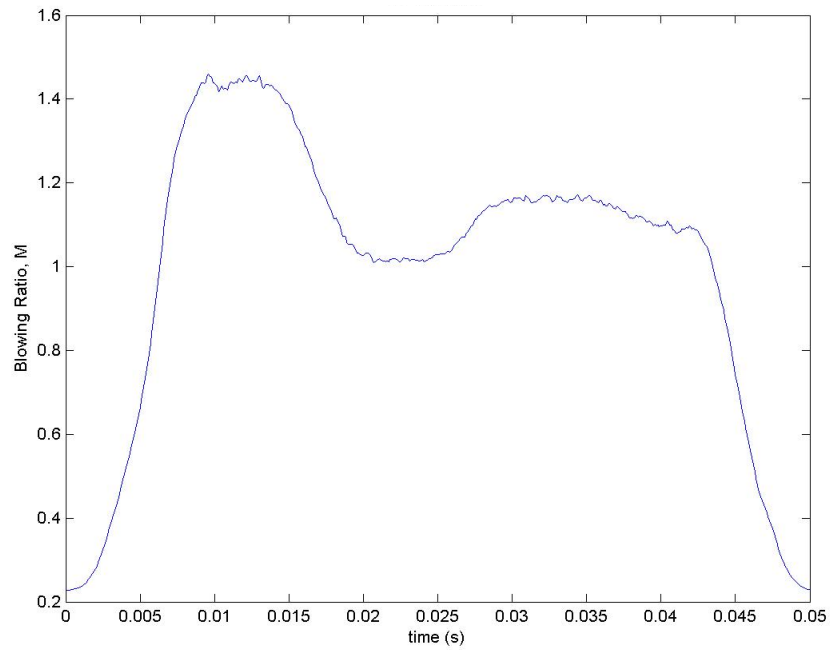


Fig. A.9  $M(t)$  for  $\bar{M} = 0.25$ , 20 Hz, DC = 75%, partial VC ( $M$  calculated based on  $Re_D = 60000$ ; double  $M$  for  $Re_D = 30000$ )



**Fig. A.10**  $M(t)$  for  $\overline{M} = 0.50$ , 20 Hz,  $DC = 75\%$ , partial VC ( $M$  calculated based on  $Re_D = 60000$ ; double  $M$  for  $Re_D = 30000$ )



**Fig. A.11**  $M(t)$  for  $\overline{M} = 1.0$ , 20 Hz,  $DC = 75\%$ , partial VC ( $M$  calculated based on  $Re_D = 60000$ ; double  $M$  for  $Re_D = 30000$ )

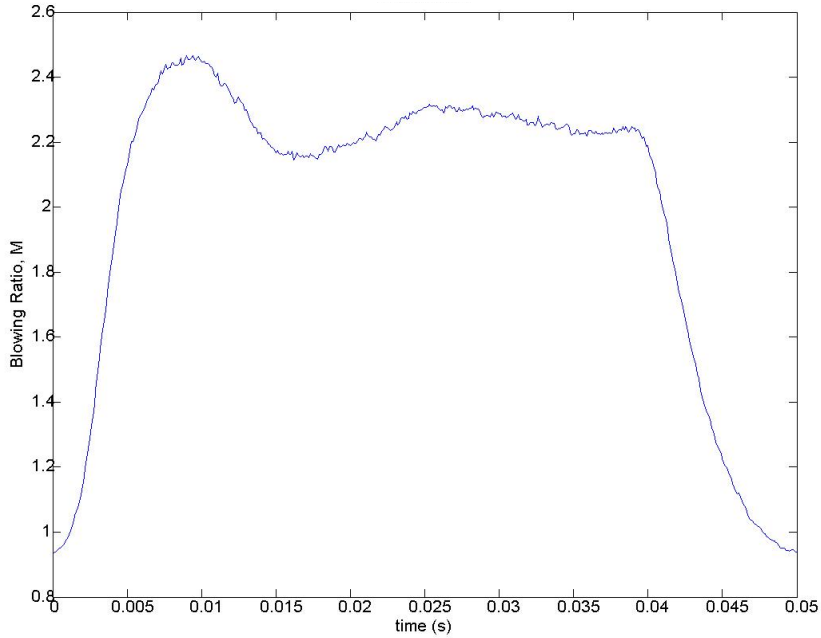


Fig. A.12  $M(t)$  for  $\bar{M} = 2.0$ , 20 Hz, DC = 75%, partial VC ( $M$  calculated based on  $Re_D = 60000$ ; double  $M$  for  $Re_D = 30000$ )

#### **A.4 Partial Valve Closure, 40 Hz, DC = 50%**

Blowing ratio waveforms for the partial VC configured valves pulsed at 40 Hz at a duty cycle of 50% are presented in this section in Figs. A.13 through A.16. At this frequency, the valves were not left in either the “on” or “off” states long enough for the unsteadiness in the waveform to appear (likely a consequence of sonic waves traveling between the valves and the hole exit- see Section A.5 for a more detailed description of one way this occurs.) Also note that the  $\bar{M} = 0.25$  case shown in Fig. A.13 was similar in shape to the higher average blowing ratio cases.

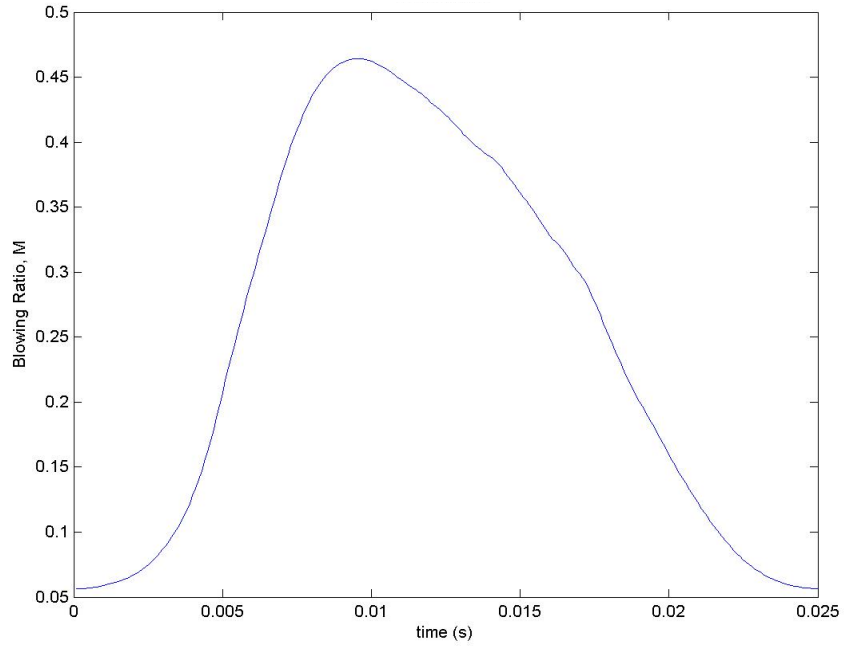


Fig. A.13  $M(t)$  for  $\overline{M} = 0.25$ , 40 Hz,  $DC = 50\%$ , partial VC ( $M$  calculated based on  $Re_D = 60000$ ; double  $M$  for  $Re_D = 30000$ )

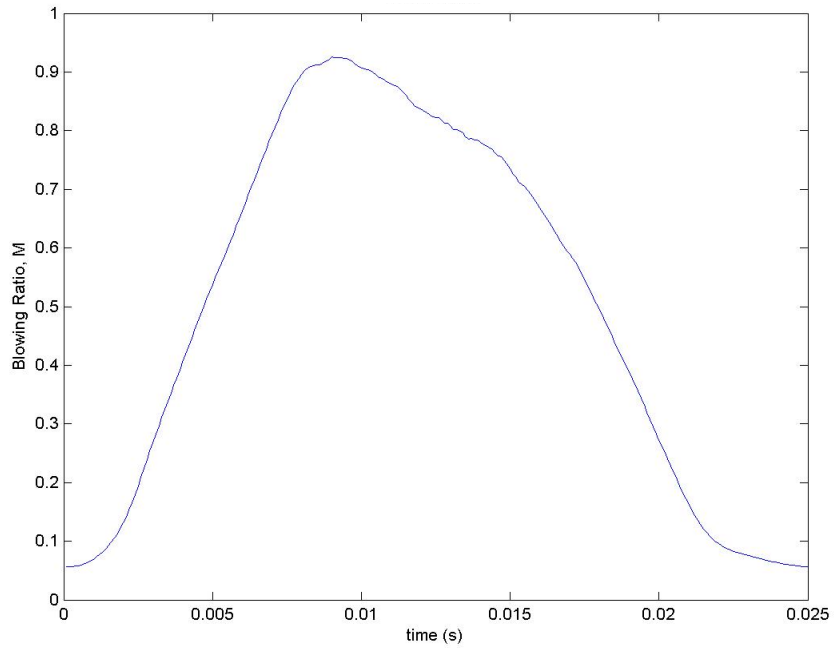
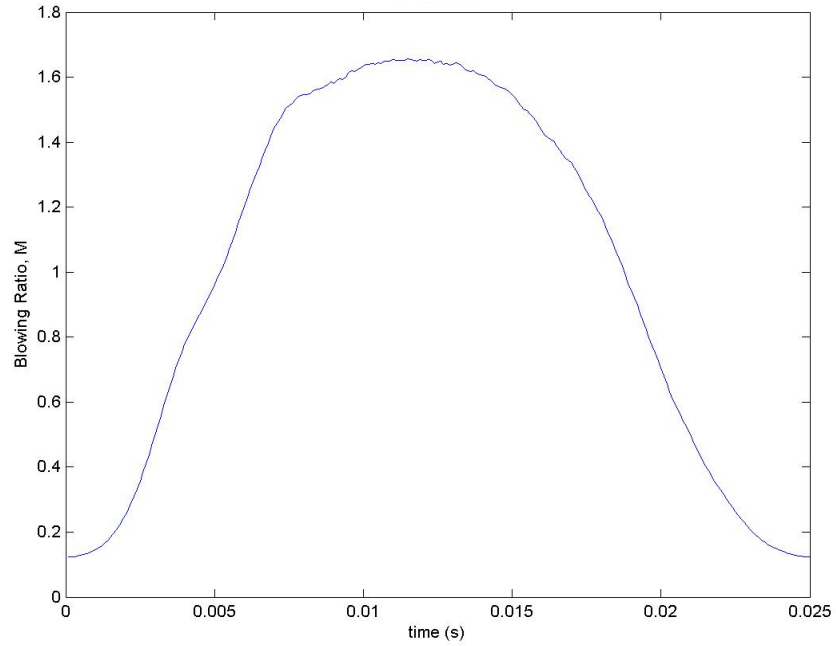
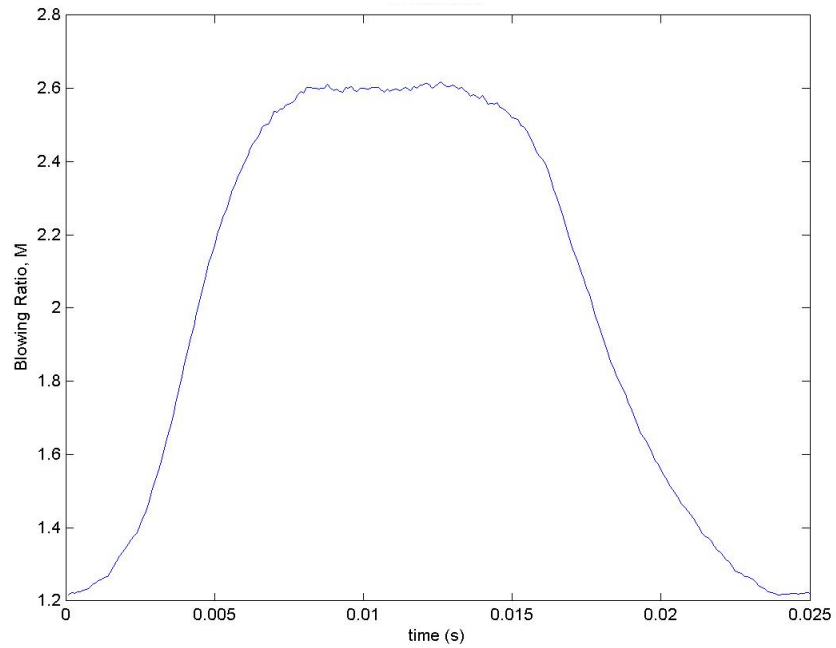


Fig. A.14  $M(t)$  for  $\overline{M} = 0.50$ , 40 Hz,  $DC = 50\%$ , partial VC ( $M$  calculated based on  $Re_D = 60000$ ; double  $M$  for  $Re_D = 30000$ )



**Fig. A.15**  $M(t)$  for  $\overline{M} = 1.0$ , 40 Hz,  $DC = 50\%$ , partial VC ( $M$  calculated based on  $Re_D = 60000$ ; double  $M$  for  $Re_D = 30000$ )



**Fig. A.16**  $M(t)$  for  $\overline{M} = 2.0$ , 40 Hz,  $DC = 50\%$ , partial VC ( $M$  calculated based on  $Re_D = 60000$ ; double  $M$  for  $Re_D = 30000$ )

### **A.5 Complete Valve Closure, 20 Hz, DC = 50%**

Replacement of the solenoid valve poppets along with cleaning the valves allowed the poppets to seat appropriately, completely blocking the flow when in the “off” position. A consequence of suddenly opening and closing valves is the possibility of shock waves and expansion waves propagating through the coolant line.

For the complete VC, 20 Hz,  $DC = 50\%$  case, the anemometer recorded a rise in velocity that lasted approximately 0.01 s immediately following the drop in velocity associated with the closing of the valves. Following that rise in velocity, the velocity would again drop and rise again briefly before the velocity would drop and rise due to the opening of the valves. Because a single wire hot film anemometer cannot measure flow direction, the possibility of reversed flow must always be considered when analyzing hot film anemometry data.

We shall consider the fluid flow between the solenoid valves and the exit of the coolant hole. If we suppose that the flow could start instantaneously at the valve when it opens, as it would if we suddenly started moving a piston at the location of the valve, a shock wave would be sent down the length of the coolant tube to the hole exit. The ratio of the pressures ahead of and behind the shock would be dictated only by the velocity of the fluid at the piston. If we were to suddenly move a piston at the location of the valve at 10 m/s (corresponding to a blowing ratio of approximately  $M = 0.9$ ), we would have a pressure ratio of 1.04 and the shock would propagate at approximately the speed of sound. The pressure behind the shock is therefore about 4% higher than the pressure at the outlet of the hole, a higher pressure than is necessary to push that amount of coolant through the coolant line. Because the flow is low speed, we would expect the pressure just inside the coolant hole to be equal to the atmospheric pressure, given enough time for the flow to reach steady state after the shock passes. Due to the 4% higher pressure inside the coolant hole immediately after the shock passes, we would expect the flow rate to overshoot the steady-state flow rate briefly after the shock wave exits the coolant hole. When the valve is suddenly closed (or a piston suddenly stopped), an expansion wave must propagate through the coolant line at approximately the speed of sound. Suddenly stopping the flow that was originally at 10 m/s would result in a pressure ratio of 0.96

between the pressure behind and ahead of the expansion wave. Once the expansion wave exits the coolant hole, the pressure in the coolant line is lower than atmospheric pressure, forcing air back into the coolant hole.

With this expectation of a flow reversal at the coolant hole exit in mind, it is clear that the first rise in velocity magnitude immediately following the decrease in velocity as the expansion wave passes must indicate flow back into the coolant hole. Figures A.17 through A.19 present the blowing ratio as a function of time, depicting a negative blowing ratio after the expansion wave exits the cooling hole. The highest average blowing ratio achievable in this configuration was  $\overline{M} = 1.25$ , lower than with the partial VC configuration because more pressure is required to drive an equivalent flow through the valves since they are closed for a large period of time. In fact, this is why the 25% duty cycle was forgone in the complete VC configuration.

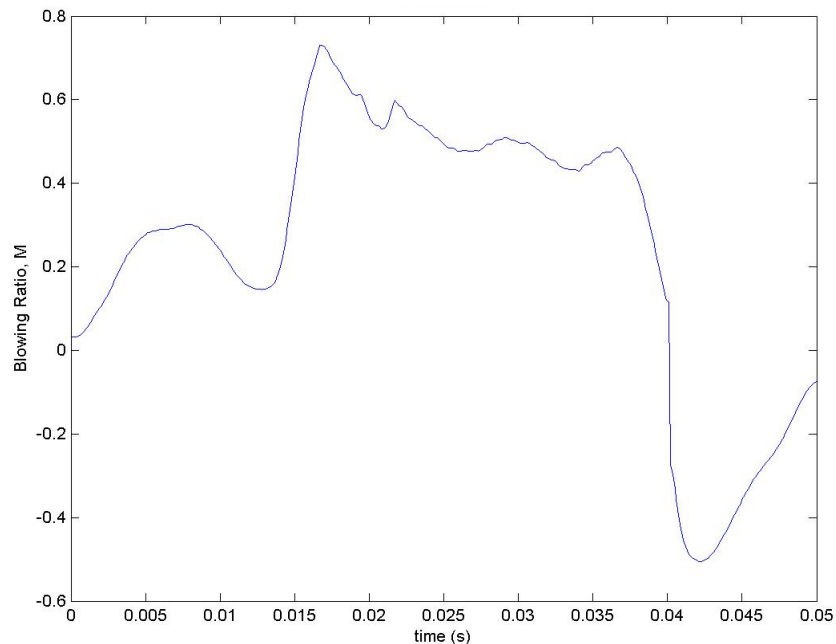


**Fig. A.17  $M(t)$  for  $\overline{M} = 0.25$ , 20 Hz, DC = 50%, complete VC ( $M$  calculated based on  $Re_D = 60000$ ; double  $M$  for  $Re_D = 30000$ )**

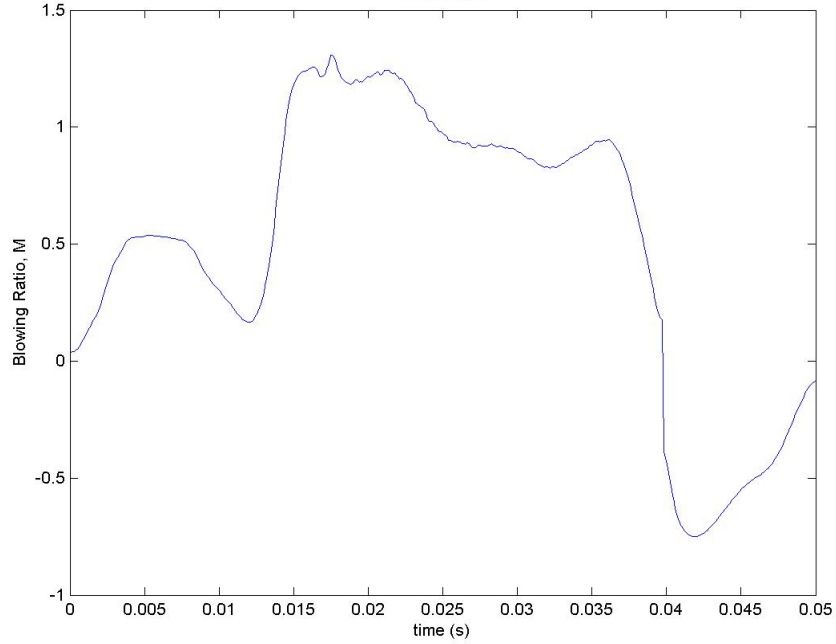


**Fig. A.18**  $M(t)$  for  $\overline{M} = 0.50$ , 20 Hz,  $DC = 50\%$ , complete VC ( $M$  calculated based on  $Re_D = 60000$ ; double  $M$  for  $Re_D = 30000$ )

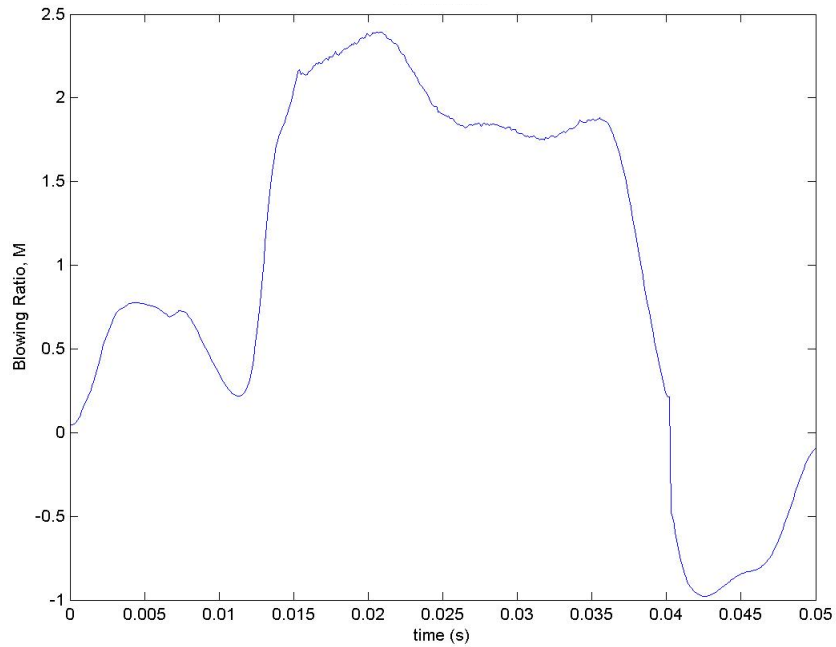


**Fig. A.19**  $M(t)$  for  $\overline{M} = 1.0$ , 20 Hz,  $DC = 50\%$ , complete VC ( $M$  calculated based on  $Re_D = 60000$ ; double  $M$  for  $Re_D = 30000$ )

Despite the aforementioned theoretical reasons for the negative velocity occurring after the valve was closed, the ambiguity of the direction of the flow was further resolved by changing the position of the hot-film probe and observing differences in the waveforms. Figure A.20 shows the approximate location of the hot-film probe used for the data acquisition of all of the results presented in Appendix A along with a second position used only for ambiguity resolution. In the secondary position, the magnitude of the elevated velocity magnitude occurring from approximately  $0.04 \text{ s} < t < 0.05 \text{ s}$  in Figs. A.17 through A.19 had much lower magnitude than in the normal probe location; however, the recorded velocity magnitudes were similar during  $0.00 \text{ s} < t < 0.04 \text{ s}$ . This observation confirms the hypothesis that the velocity is negative (into the hole) during  $0.04 \text{ s} < t < 0.05$ . The extreme curvature of the streamlines as fluid enters a cavity results in very low fluid velocities relative to the velocity in the core of the jet at the outlet of the cavity. Consider, for example, a home HVAC (heating, ventilation, and air condition) system. When the system is running, a strong breeze can be felt, say 10 cm away from a vent outlet at or near the vent centerline, but very little, breeze can be felt 10 cm away from the air intake along its centerline, even though continuity requires that the mass flow into the air intake matches the mass flow out of all of the vents. A much higher velocity would be measured if the flow were tested 10 cm into the air intake despite the fact that the velocity measured at a vent exit would be relatively independent of whether the velocity were measured 10 cm out of or 10 cm inside the vent. This relative change in velocity at an inlet compared to an outlet gives us a technique to determine the sign of the velocity measured at the normal probe location at the outlet of the coolant hole.

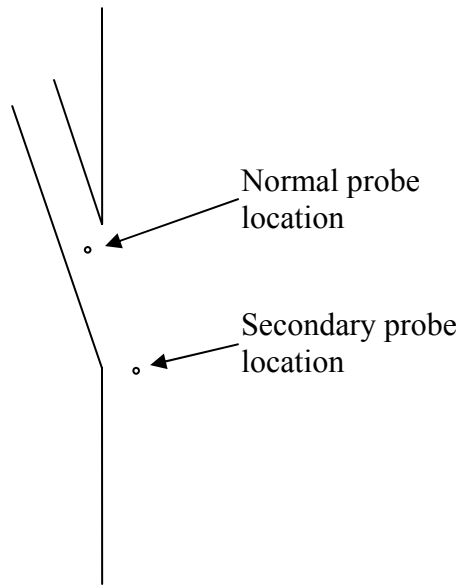


**Fig. A.20** Approximate locations of hot-film probe

### **A.6 Complete Valve Closure, 20 Hz, DC = 75%**

This section presents the blowing ratio waveforms for the valves in the complete VC state at 20 Hz with a duty cycle of 75%. The waveforms are shown in Figs. A.21 through A.24. Just as with the  $DC = 50\%$  case, an expansion wave exits the coolant hole and a flow reversal occurs immediately after the exit of the expansion wave. The waveforms for all of the average blowing ratios are similar; however, the magnitude of the reversed flow is not linearly proportional to the average blowing ratio.

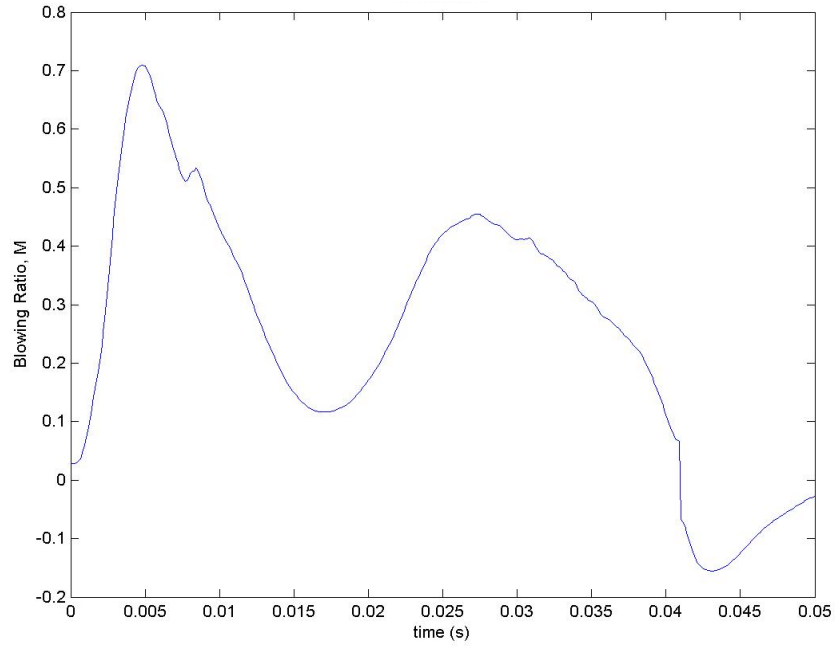


**Fig. A.21**  $M(t)$  for  $\overline{M} = 0.25$ , 20 Hz, DC = 75%, complete VC ( $M$  calculated based on  $Re_D = 60000$ ; double  $M$  for  $Re_D = 30000$ )

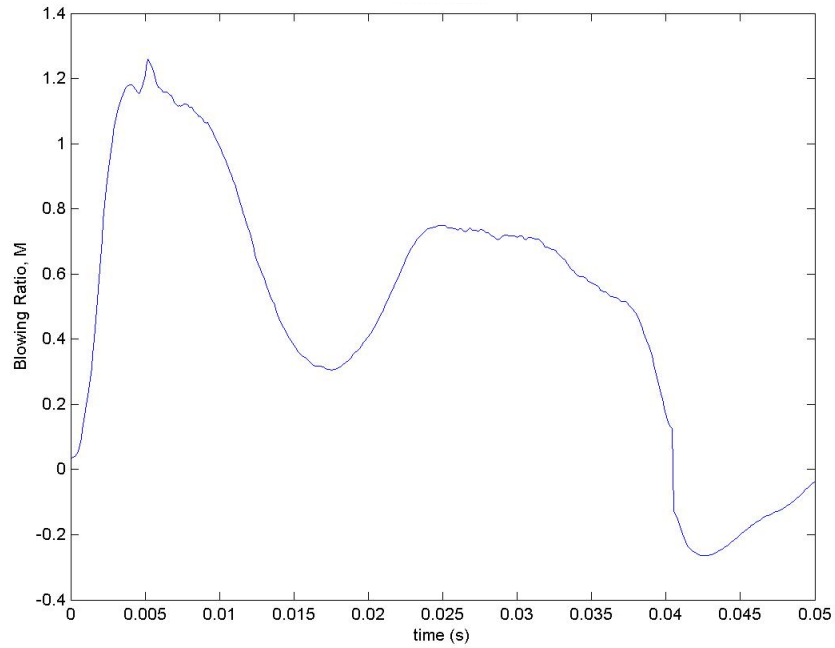


**Fig. A.22**  $M(t)$  for  $\overline{M} = 0.50$ , 20 Hz, DC = 75%, complete VC ( $M$  calculated based on  $Re_D = 60000$ ; double  $M$  for  $Re_D = 30000$ )

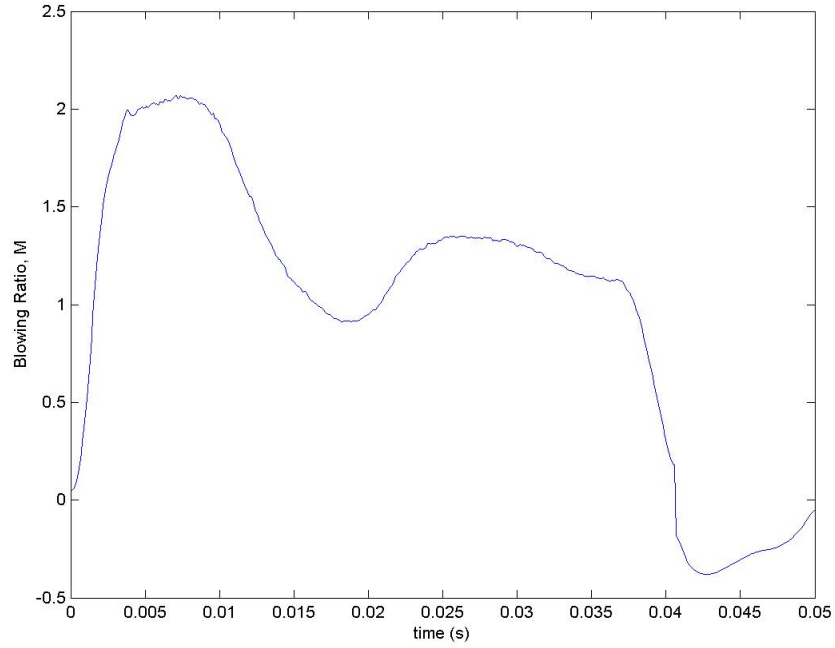


**Fig. A.23**  $M(t)$  for  $\overline{M} = 1.0$ , 20 Hz,  $DC = 75\%$ , complete VC ( $M$  calculated based on  $Re_D = 60000$ ; double  $M$  for  $Re_D = 30000$ )

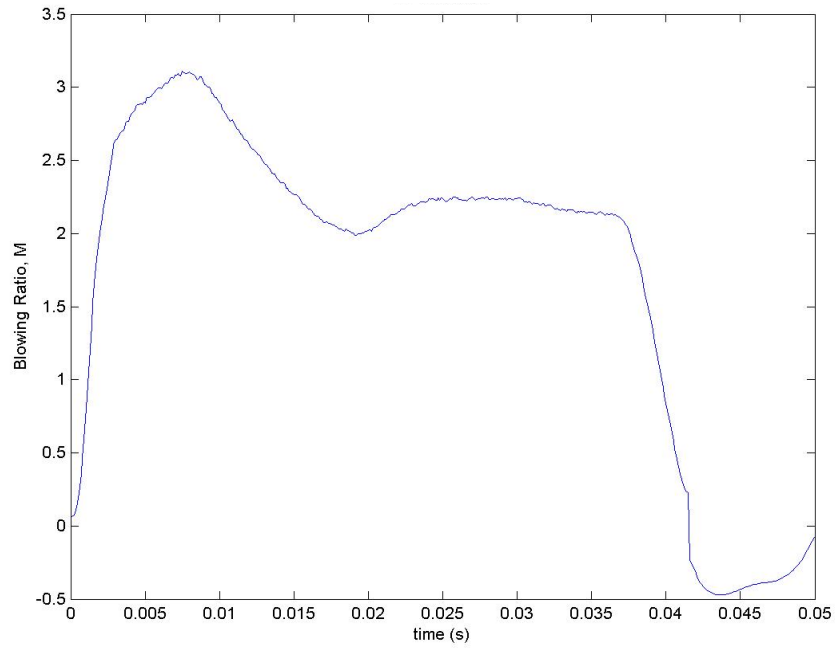


**Fig. A.24**  $M(t)$  for  $\overline{M} = 1.75$ , 20 Hz,  $DC = 75\%$ , complete VC ( $M$  calculated based on  $Re_D = 60000$ ; double  $M$  for  $Re_D = 30000$ )

### A.7 Complete Valve Closure, 80 Hz, DC = 50%

The blowing ratio waveforms for the complete VC configuration at 80 Hz,  $DC = 50\%$  are presented in Figs. A.25 through A.27. The waveforms at 80 Hz are very smooth, attributable to the short duration of “on” and “off” times for the valves. Note that the entire cycle time is only slightly longer than the amount of time it takes for a sonic wave to make a round trip between the coolant jet exit and the valves. It appears, especially for  $\bar{M} > 0.25$ , that the coolant velocity at the hole exit never goes completely to zero.

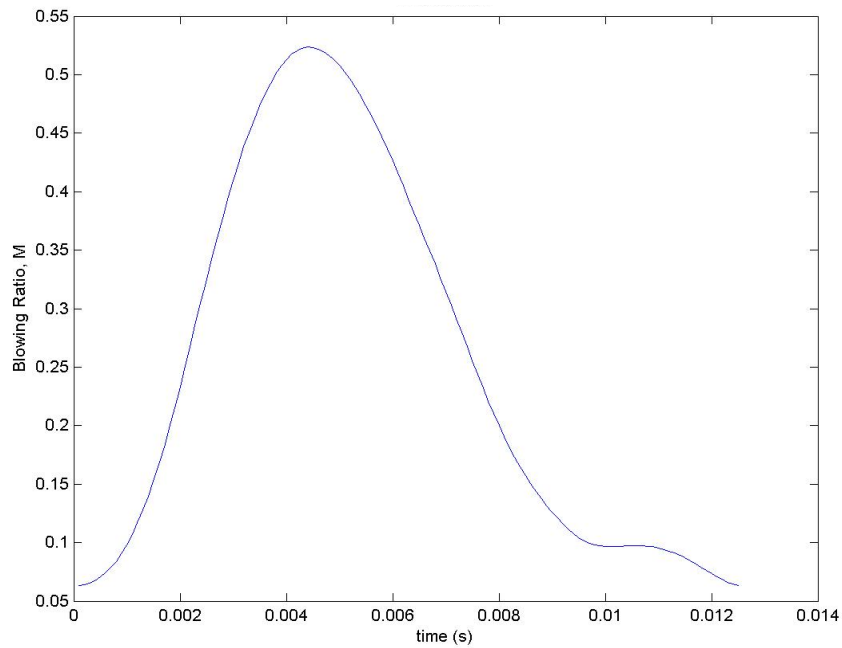
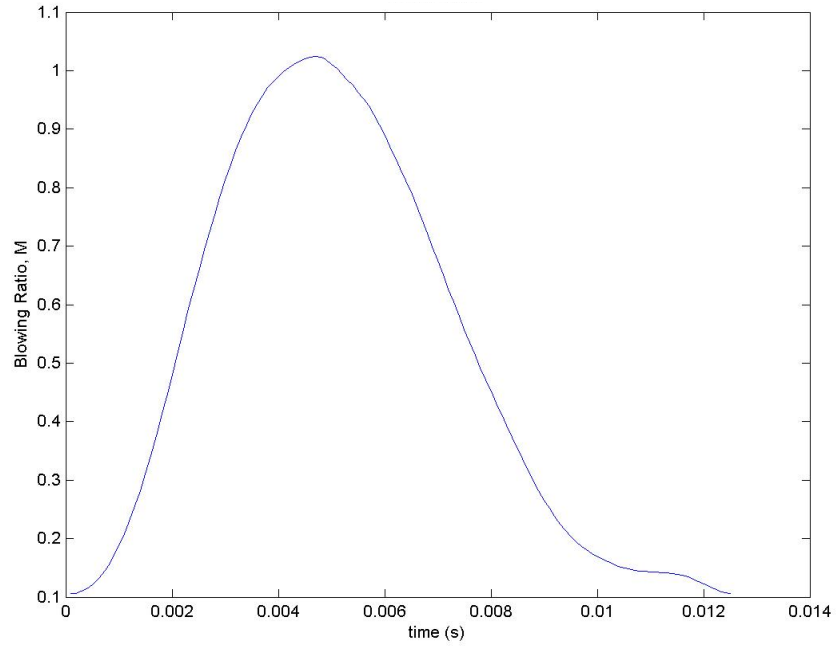
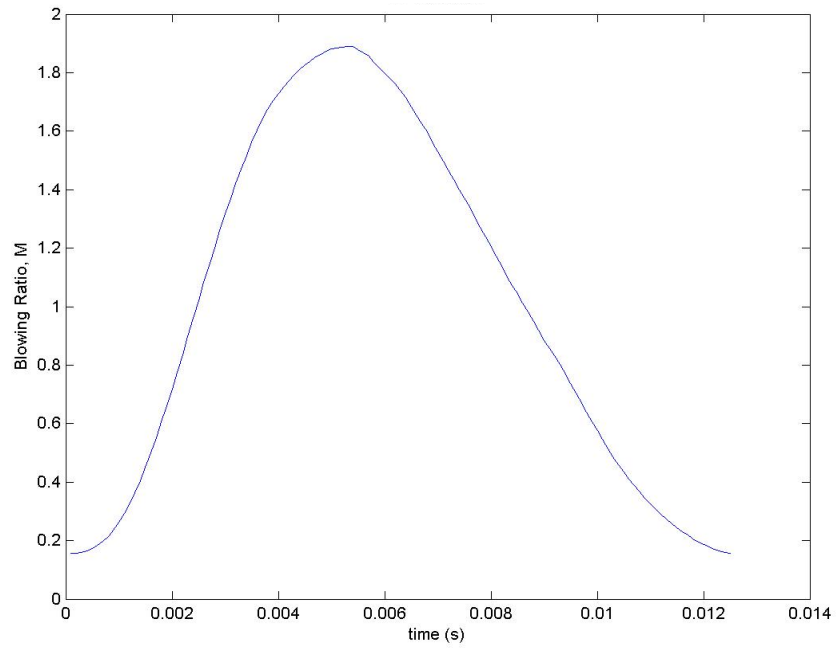


Fig. A.25  $M(t)$  for  $\bar{M} = 0.25$ , 80 Hz,  $DC = 50\%$ , complete VC ( $M$  calculated based on  $Re_D = 60000$ ; double  $M$  for  $Re_D = 30000$ )



**Fig. A.26**  $M(t)$  for  $\overline{M} = 0.50$ , 80 Hz,  $DC = 50\%$ , complete VC ( $M$  calculated based on  $Re_D = 60000$ ; double  $M$  for  $Re_D = 30000$ )



**Fig. A.27**  $M(t)$  for  $\overline{M} = 1.0$ , 80 Hz,  $DC = 50\%$ , complete VC ( $M$  calculated based on  $Re_D = 60000$ ; double  $M$  for  $Re_D = 30000$ )

## Appendix B Multiple Row Superposition Theory for Pulsed Film Cooling

The method of superposition described by Muska et al. (1976) and Sellers (1963) allows one to predict the adiabatic effectiveness of a film cooling scheme using multiple sources of film coolant through knowledge of the performance of the individual sources of film coolant. With this method of superposition, we assume that the region of interest downstream of the downstream row of holes (row 2) has an effective  $T_\infty$  replaced by the adiabatic wall temperature resulting from the upstream row (row 1). This is plausible since without row 2, the adiabatic wall temperature would be  $T_{aw,1}$  whereas it would be  $T_\infty$  with neither row operating. With row 2 operating alone, the adiabatic effectiveness would be written:

$$\eta_2 = \frac{T_\infty - T_{aw,2}}{T_\infty - T_c} \quad (\text{B.1})$$

With row 1 also operating, the adiabatic effectiveness downstream of row 2 would become:

$$\eta_2 = \frac{T_{aw,1} - T_{aw,2}}{T_{aw,1} - T_c} \quad (\text{B.2})$$

Since the  $\eta_1$  analog to Eq. (B.1) is

$$\eta_1 = \frac{T_\infty - T_{aw,1}}{T_\infty - T_c}, \quad (\text{B.3})$$

we may write  $T_{aw,1}$  in Eq. (B.2) in terms of  $\eta_1$ :

$$\eta_2 = \frac{T_\infty - \eta_1(T_\infty - T_c) - T_{aw}}{T_\infty - \eta_1(T_\infty - T_c) - T_c} \quad (\text{B.4})$$

We now solve Eq. (B.4) for the adiabatic effectiveness due to both rows of film cooling holes,  $\eta = (T_\infty - T_{aw}) / (T_\infty - T_c)$ .

$$\eta = \eta_1 + \eta_2 - \eta_1\eta_2 \quad (\text{B.5})$$

Note that if the adiabatic effectiveness from either row is zero, Eq. (B.5) reduces to the adiabatic effectiveness due to the other row alone. This technique has been tested successfully by such researchers as Muska et al. (1976) and Robertson (2004) at various levels of freestream turbulence and surface roughness. The technique is limited in that the rows of coolant holes must be spaced sufficiently far apart that hydrodynamic interactions are negligible because Eq. (B.5) accounts only for thermal interactions.

We shall use superposition of adiabatic effectiveness as a starting point to consider the influence of multiple rows of pulsed film cooling holes. As in Section 3.2, we shall consider temporal adiabatic effectiveness as a sum between its mean and the zero-mean fluctuating component (see Eq. (3.17)). We shall rewrite Eq. (B.5) in that fashion.

$$\eta = (\bar{\eta}_1 + \eta_1') + (\bar{\eta}_2 + \eta_2') - (\bar{\eta}_1 + \eta_1')(\bar{\eta}_2 + \eta_2') \quad (\text{B.6})$$

Taking the mean of Eq. (B.6), we obtain

$$\bar{\eta} = \bar{\eta}_1 + \bar{\eta}_2 - \overline{\eta_1 \eta_2} - \overline{\eta_1' \eta_2'} \quad (\text{B.7})$$

The zero-mean fluctuating component of adiabatic effectiveness becomes

$$\eta' = (1 - \bar{\eta}_1)\eta_2' - (1 - \bar{\eta}_2)\eta_1' \quad (\text{B.8})$$

The similarity between Eq. (B.7) and Eq. (B.5) suggests that average adiabatic effectiveness values may be substituted into Eq. (B.5) as long as  $\overline{\eta_1' \eta_2'}$  is subtracted from the result. Note that if the phasing between the individual fluctuations in  $\eta$  is such that  $\eta_1$  and  $\eta_2$  fluctuate out of phase,  $\overline{\eta_1' \eta_2'} < 0$ , thereby tending to improve  $\bar{\eta}$ . This phasing may be accomplished by either inducing a phase shift of the pulsations of one row relative to the other, but such a phase shift may be unnecessary due simply to the time it takes for the coolant from the upstream row to reach the downstream row.

As we found in Section 3.2, we must also understand the behavior of the unsteady heat transfer coefficient to predict the influence of film cooling on the net heat flux reduction. I am unaware of a thorough study of a method of superposition as it relates to

heat transfer coefficient, although a reasonable approach is to assume that the row that results in the largest heat transfer coefficient augmentation dominates since heat transfer augmentation due to film cooling is due primarily to additional turbulence created by the film cooling jets. This approach could be written,

$$\frac{h_f}{h_0} \approx \begin{cases} h_{f,1} / h_0, & \text{if } h_{f,1} > h_{f,2} \\ h_{f,2} / h_0, & \text{otherwise} \end{cases} \quad (\text{B.9})$$

This model for the behavior of  $h_f$  implies that  $h_f'$  must be smaller than or equal to the fluctuations in  $h_{f,1}$  and  $h_{f,2}$ , that is:

$$h_f' \leq h_{f,1}' \quad (\text{B.10})$$

and

$$h_f' \leq h_{f,2}' \quad (\text{B.11})$$

In the event that  $h_{f,1}$  and  $h_{f,2}$  fluctuate out of phase, then it would be possible for  $h_f'$  to become very small despite large fluctuations in  $h_{f,1}$  and  $h_{f,2}$ , particularly if they fluctuate as square waves. Remember that Eq. (B.7) suggests that out-of-phase fluctuations are desirable for  $\bar{\eta}$ . We end up having competing effects in terms of net heat flux reduction given by Eq. (3.25), repeated here:

$$\overline{\Delta q_r} = 1 - \frac{\overline{h_f}}{h_0} \left( 1 - \frac{\overline{\eta}}{\phi} \right) + \frac{\overline{h_f' \eta'}}{h_0 \phi} \quad (\text{3.25})$$

In Eq. (3.25), strong in-phase fluctuations between  $h_f'$  and  $\eta'$  are desirable to achieve large  $\overline{\Delta q_r}$ . The decrease of  $h_f'$  that is likely to occur with out-of-phase fluctuations between  $\eta_1$  and  $\eta_2$  may tend to offset the benefits of improved  $\bar{\eta}$ .

## References

- Abhari, R. S., "Impact of Rotor-Stator Interaction on Turbine Blade Film Cooling," *Journal of Turbomachinery*, Vol. 118, pp. 123-133, 1996.
- Adami, P., Montomoli, F., Belardini, E., Martelli, F., "Interaction Between Wake and Film Cooling Jets: Numerical Analysis," ASME Paper No. GT2004-53178, 2004.
- Allegheny Ludlum, "Technical Data Blue Sheet- Allegheny Ludlum Stainless Steel Type 301," Allegheny Ludlum Corporation, 1998.
- Ammari, H. D., Hay, N., Lampard, D., "The Effect of Density Ratio on the Heat Transfer Coefficient from a Film Cooled Flat Plate," *Journal of Turbomachinery*, Vol. 112, pp. 444-450, 1990.
- ASM International, "ASM Specialty Handbook: Nickel, Cobalt, and Their Alloys," ASM International, 2000.
- Bevington, P., Robinson, K., *Data Reduction and Error Analysis*, McGraw-Hill, 2003.
- Compton, D. A., and Johnston, J. P., "Streamwise Vortex Production by Pitched and Skewed Jets in a Turbulent Boundary Layer," *AIAA Journal*, Vol. 30, No. 3, 640-647, 1992.
- Coulthard, S., Volino, R., Flack, K., "Effect of Jet Pulsing on Film Cooling- Part I: Effectiveness and Flow-Field Temperature Results," *Journal of Turbomachinery*, Vol. 129, pp. 232-246, 2007.
- Coulthard, S., Volino, R., Flack, K., "Effect of Jet Pulsing on Film Cooling- Part II: Heat Transfer Results," *Journal of Turbomachinery*, Vol. 129, pp. 247-257, 2007.
- Cruse, M. W., Yuki, U. M., and Bogard, D. G., "Investigation of Various Parametric Influences on Leading Edge Film Cooling," ASME Paper 97-GT-296, 1997.
- Ekkad, S. V., Han, J. C., Du, H., "Detailed Film Cooling Measurements on a Cylindrical Leading Edge Model: Effect of Free-Stream Turbulence and Coolant Density," *Journal of Turbomachinery*, Vol. 120, pp. 799-807, 1998.
- Ekkad, S. V., Ou, S., Rivir, R. B., "Effect of Jet Pulsation and Duty Cycle on Film Cooling From a Single Jet on a Leading Edge Model," *Journal of Turbomachinery*, Vol. 128, pp. 564-571, 2006.
- Fluent Inc., *Fluent User's Guide*, Release 6.2, Lebanon, New Hampshire, 2005.

- Giedt, W. H., "Investigation of Variation of Point Unit Heat-Transfer Coefficient Around a Cylinder Normal to an Air Stream," *Transactions of the ASME*, Vol. 71, p. 375, 1949.
- Gompertz, K., Pluim, J., Bons, J., "Separation Control Authority of Vortex Generating Jets in a Low-Pressure Turbine Cascade with Simulated Wakes," AIAA Paper No. 2009-377, 2009.
- Han, J. C, Dutta, S., and Ekkad, S. V., *Gas Turbine Heat Transfer and Cooling Technology*, Taylor & Francis, 2000.
- Harrison, K. and Bogard, D., "CFD Predictions of Film Cooling Adiabatic Effectiveness for Cylindrical Holes Embedded in Narrow and Wide Transverse Trenches," ASME Paper No. GT2007-28005, 2007.
- Incropera, F., and DeWitt, D., *Fundamentals of Heat and Mass Transfer*, 4<sup>th</sup> ed., John Wiley & Sons, New York, 1996.
- Kaplan, S., Altman, A., Ol, M., "Wake Vorticity Measurements for Low Aspect Ratio Wings at Low Reynolds Number," *Journal of Aircraft*, Vol. 44, No. 1, pp. 241-251, 2007.
- Kartuzova, O., Danila, D., Ibrahim, M., Volino, R., "CFD Simulation of Jet Pulsation Effects on Film Cooling of Flat Plates," ASME Paper No. GT2008-50284, 2008.
- Kays, W. M., and Crawford, M. E., *Convective Heat and Mass Transfer*, 2<sup>nd</sup> ed., McGraw-Hill, New York, 1980.
- Keith, F., *The CRC Handbook of Mechanical Engineering*, CRC Press, 1998.
- Kline, S. J., and McClintock, F. A., "Describing Uncertainties in Single Sample Experiments," *Mechanical Engineering* vol. 75, 1953.
- Leylek, J. H. and Zerkle, R. D., "Discrete-Jet Film Cooling: A Comparison of Computational Results with Experiments," *Journal of Turbomachinery*, Vol. 116, pp. 358-368, 1994.
- Lin, Y. L. and Shih, T. I. P., "Film Cooling of a Cylindrical Leading Edge With Injection Through Rows of Compound-Angle Holes," *Journal of Heat Transfer*, Vol. 123, pp. 645-654, 2001.
- M'Closkey, R. T., King, J. M., Cortelezzi, L., Karagozian, A. R., "The Actively Controlled Jet in Crossflow," *Journal of Fluid Mechanics*, Vol. 452, pp. 325-335, 2002.

- Marcum, D. L., "Advancing-Front/Local-Reconnection (AFLR) Unstructured Grid Generation," *Computational Fluid Dynamics Review*, 1998.
- Mattingly, J. D., Heiser, W. H., Pratt, D. T., *Aircraft Engine Design*, AIAA Education Series, American Institute of Aeronautics and Astronautics, Virginia, 2002.
- McCall, J. and Branam, R., "Effects of Radial Curvature on Net Heat Flux Reduction in a Film-Cooled Rocket," AIAA Paper 2009-1586, 2009.
- McManus, K. R., Legner, H. H., and Davis, S. J., "Pulsed Vortex Generator Jets for Active Control of Flow Separation," AIAA Paper 94-2218, 1994.
- Mick, W. J. and Mayle, R. E., "Stagnation Film Cooling and Heat Transfer Including Its Effect Within the Hole Pattern," *Journal of Turbomachinery*, Vol. 110, pp. 66-72, 1988.
- Mills, A. F., *Heat Transfer*, Second Edition, Prentice Hall, New Jersey, 1999.
- Moore, K., "Large Scale Visualization of Pulsed Vortex Generator Jets," M. S. Thesis, Wright State University, 2005.
- Muska, J. F., Fish, R. W., and Suo, M. "The Additive Nature of Film Cooling from Rows of Holes," *ASME Journal of Engineering for Power*, Vol. 98, pp. 457-464, 1976.
- Muldoon, F. and Acharya, S., "Computations of Pulsed Film-Cooling," ASME Paper No. GT2007-28156, 2007.
- Panton, R. L., *Incompressible Flow*, 2<sup>nd</sup> ed., Wiley, New York, 1996.
- Pietrzyk, J. R., Bogard, D. G., Crawford, M. E., "Hydrodynamic Measurements of Jets in Cross flow for Gas Turbine Film Cooling Applications," *Journal of Turbomachinery*, Vol. 111, pp. 139-145, 1989.
- Robertson, D. R., "Roughness Impact on Turbine Vane Suction Side Effectiveness," M. S. Thesis, University of Texas at Austin, 2004.
- Rutledge, J. L., "Suction Side Roughness Effects on Film Cooling Heat Transfer on a Turbine Vane," M. S. Thesis, University of Texas at Austin, 2004.
- Sellers, J. P. "Gaseous Film Cooling With Multiple Injection Stations," *AIAA Journal*, Vol. 1, No. 9, pp. 2154-2156, 1963.
- Sen, B., Schmidt, D. L., Bogard, D. G., "Film Cooling With Compound Angle Holes: Heat Transfer," *Journal of Turbomachinery*, Vol. 118, pp. 800-806, 1996.

Walters, D. K., and Leylek, J. H., "A Systematic Computational Methodology Applied to a Three-Dimensional Film-Cooling Flow field," *Journal of Turbomachinery*, Vol. 119, pp. 777-785, 1997.

Webster, D. R., and Longmire, E. K., "Vortex Rings from Cylinders with Inclined Exits," *Physics of Fluids*, Vol. 10, No. 2, pp. 400-416, 1997.

Wilson D. G. and Korakianitis T., *The Design of High-Efficiency Turbomachinery and Gas Turbines*, 2<sup>nd</sup> ed., Prentice Hall, New Jersey, 1998.

Wolff, S., Fottner, L., Ardey S., "An Experimental Investigation on the Influence of Periodic Unsteady Inflow Conditions on Leading Edge Film Cooling," ASME Paper No. GT2002-30202, 2002.

### **Vita**

James (Jay) Lloyd Rutledge was raised in El Paso, Texas where he graduated valedictorian from Hanks High School in May 1998. He earned his Bachelor of Science in Mechanical Engineering with Highest Honors at the University of Texas at Austin in December 2002, at which point he was commissioned in the United States Air Force. He earned his Master of Science in Mechanical Engineering from the University of Texas at Austin in May 2004 before an assignment at Kirtland Air Force Base, New Mexico with the Air Force Research Laboratory Space Vehicles Directorate. In September 2006 he entered the Graduate School of Engineering and Management at the Air Force Institute of Technology.

# REPORT DOCUMENTATION PAGE

*Form Approved*  
OMB No. 074-0188

The public reporting burden for this collection of information is estimated to average 1 hour per response, including the time for reviewing instructions, searching existing data sources, gathering and maintaining the data needed, and completing and reviewing the collection of information. Send comments regarding this burden estimate or any other aspect of the collection of information, including suggestions for reducing this burden to Department of Defense, Washington Headquarters Services, Directorate for Information Operations and Reports (0704-0188), 1215 Jefferson Davis Highway, Suite 1204, Arlington, VA 22202-4302. Respondents should be aware that notwithstanding any other provision of law, no person shall be subject to a penalty for failing to comply with a collection of information if it does not display a currently valid OMB control number.

**PLEASE DO NOT RETURN YOUR FORM TO THE ABOVE ADDRESS.**

<b>1. REPORT DATE (DD-MM-YYYY)</b> 10-09-2009		<b>2. REPORT TYPE</b> Doctoral Dissertation		<b>3. DATES COVERED (From – To)</b> Sept 2006 – Sept 2009	
<b>4. TITLE AND SUBTITLE</b>  Pulsed Film Cooling on a Turbine Blade Leading Edge			<b>5a. CONTRACT NUMBER</b>		
			<b>5b. GRANT NUMBER</b>		
			<b>5c. PROGRAM ELEMENT NUMBER</b>		
<b>6. AUTHOR(S)</b>  James L. Rutledge, Captain, USAF			<b>5d. PROJECT NUMBER</b>		
			<b>5e. TASK NUMBER</b>		
			<b>5f. WORK UNIT NUMBER</b>		
<b>7. PERFORMING ORGANIZATION NAMES(S) AND ADDRESS(S)</b>  Air Force Institute of Technology Graduate School of Engineering and Management 2950 Hobson Way WPAFB, OH 45433-7765			<b>8. PERFORMING ORGANIZATION REPORT NUMBER</b>  AFIT/DS/ENY/09-S03		
<b>9. SPONSORING/MONITORING AGENCY NAME(S) AND ADDRESS(ES)</b>  Dr. Richard Rivir Air Force Research Laboratory Propulsion Directorate 1950 Fifth Street, Building 18 WPAFB, OH 45433-7251			<b>10. SPONSOR/MONITOR'S ACRONYM(S)</b>  AFMC AFRL/RZ		
			<b>11. SPONSOR/MONITOR'S REPORT NUMBER(S)</b>		
<b>12. DISTRIBUTION/AVAILABILITY STATEMENT</b>  APPROVED FOR PUBLIC RELEASE; DISTRIBUTION UNLIMITED					
<b>13. SUPPLEMENTARY NOTES</b>  This material is declared a work of the U.S. Government and is not subject to copyright protection in the United States.					
<b>14. ABSTRACT</b> Unsteadiness in gas turbine film cooling jets may arise due to inherent unsteadiness of the flow through an engine or may be induced as a means of flow control. The traditional technique used to evaluate the performance of a steady film cooling scheme is demonstrated to be insufficient for use with unsteady film cooling and is modified to account for the cross coupling of the time dependent adiabatic effectiveness and heat transfer coefficient. The addition of a single term to the traditional steady form of the net heat flux reduction equation with time averaged quantities accounts for the unsteady effects. An experimental technique to account for the influence of the new term was devised and used to measure the influence of a pulsating jet on the net heat flux in the leading edge region of a turbine blade. High spatial resolution data was acquired in the near-hole region using infrared thermography coupled with experimental techniques that allowed application of the appropriate thermal boundary conditions immediately adjacent to the film cooling hole. The turbine blade leading edge was simulated by a half cylinder in cross flow with a blunt afterbody. The film cooling geometry consisted of a coolant hole located 21.5° from the leading edge, angled 20° to the surface and 90° from the streamwise direction. Investigated parameters include pulsation frequency, duty cycle, and waveform shape. Separate experiments were conducted in a water channel to provide visualization of the unsteady coolant propagation behavior. Further insight into the flow physics was obtained through computational simulations of the experimental apparatus. The computational results afforded time resolved flow field and net heat flux reduction data unobtainable with the experimental techniques. A technique to predict the performance of an unsteady film cooling scheme through knowledge of only the steady film cooling behavior was developed and demonstrated to be effective.					
<b>15. SUBJECT TERMS</b>  Film Cooling, Turbine, Unsteady, Pulsed, Heat Transfer					
<b>16. SECURITY CLASSIFICATION OF:</b>		<b>17. LIMITATION OF ABSTRACT</b>	<b>18. NUMBER OF PAGES</b>	<b>19a. NAME OF RESPONSIBLE PERSON</b>	
a. REPORT	b. ABSTRACT			Dr. Paul King	
U	U	UU	275	<b>19b. TELEPHONE NUMBER (Include area code)</b>  (937) 255-6565 ext 4559	

Standard Form 298 (Rev. 8-98)  
Prescribed by ANSI Std. Z39-18

